MAY 1978

ORO 5178-78-2
UC 62

STMPO-560

SOLAR CENTRAL RECEIVER

HELIOSTAT FIELD ANALYSIS

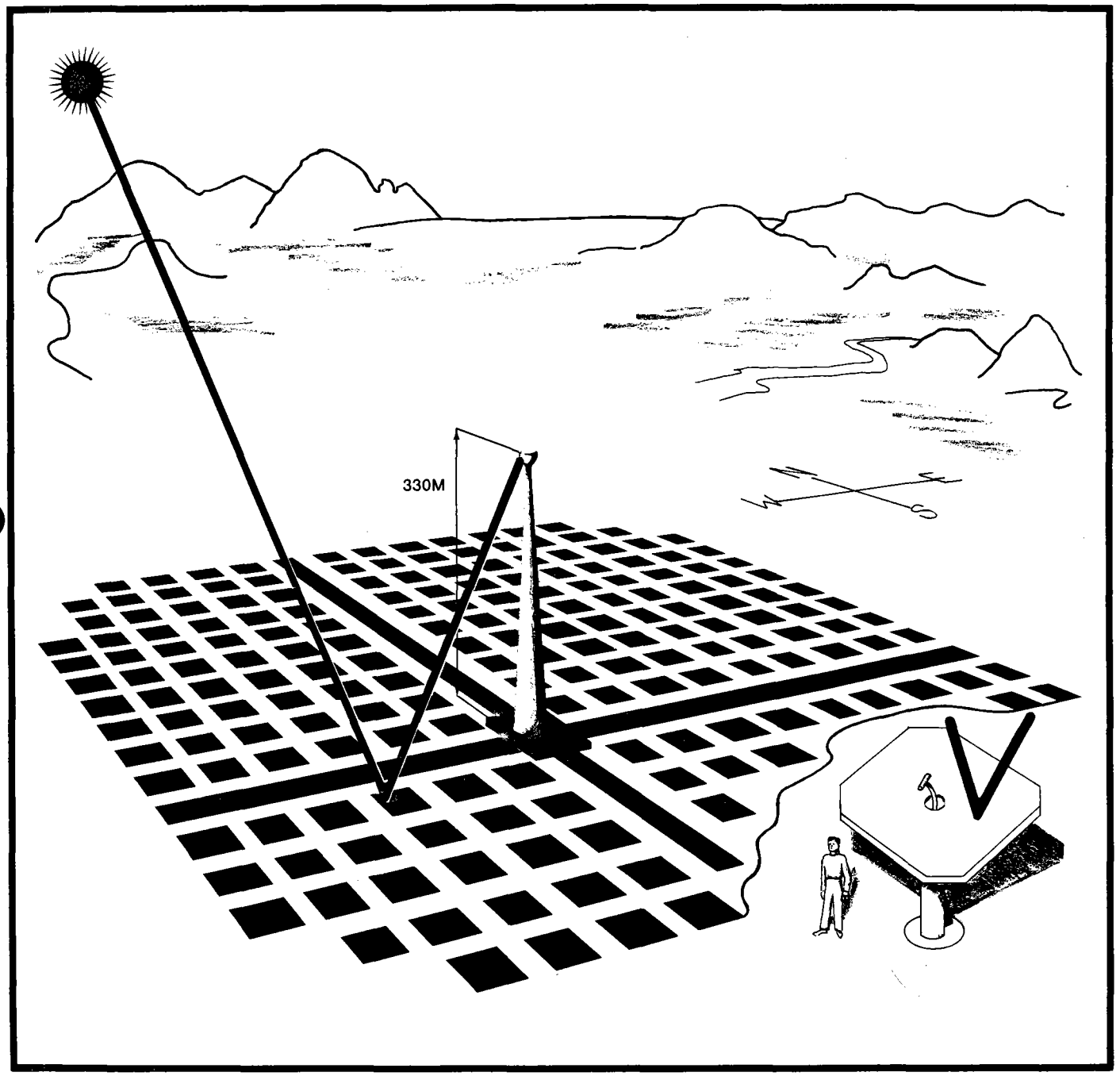

FINAL REPORT—Part II

Heliostat Field Analysis

Prepared by the
Energy Laboratory, University of Houston
Under ERDA Grant No. EG-76-G-05-5178

UH

University of Houston

Notice

Printed in the United States of America
Available from
National Technical Information Service
U. S. Department of Commerce
5285 Port Royal Road
Springfield, Virginia 22161

May 1978

ORO 5178-78-2
UC 62

LIQUID METAL COOLED SOLAR CENTRAL RECEIVER FEASIBILITY STUDY AND

HELIOSTAT FIELD ANALYSIS

STUDY TEAM
Lorin L. Vant-Hull
F. W. Lipps
M. D. Walzel
A. C. Meyers, III.
C. L. Pitman
A. K. Detwiler, III.

Energy Laboratory
UNIVERSITY OF HOUSTON

FINAL REPORT
PART II.
HELIOSTAT FIELD ANALYSIS
including
Parametric Studies
Net Energy Analysis
Locating the Sun
The Sodium Heat Engine

Forward

This report is the final document in a series of reports on Solar Tower, or Central Receiver, studies, issued by the University of Houston. Funded work on this subject began in June of 1973 under NSF/RANN grant SE/GI-39456, "Solar Thermal Power Systems Based on Optical Transmission." This work, was supported by subcontracts to McDonnell Douglas Astronautics Company and Rocketdyne. Studies consisted of developing a conceptual design, performing a technical and feasibility study, and building and testing a model heliostat ($14m^2$). During the course of this work the basis of the computer codes described in the present report were formulated.

The following reports were prepared under this study and are available from NTIS under the title "Solar Thermal Power Systems Based on Optical Transmission" NSF/RANN/SE/GI-39456.

Report	Code	Accession No.	Cost
Progress Report No. 1	PR/73/4	PB 237 005	$ 9.50
No. 2	PR/74/2	PB 244 436/AS	7.50
Technical Report No. 1	TR/75/2	PB 253 166/AS	6.00
No. 2	TR/75/2	PB 252 667/LL	9.00
Final Report	FR/75/3	PB 253 167/AS	11.00

* TR #1 describes receiver analysis and tests.
* TR #2 describes heliostat design and tests.

At the conclusion of this feasibility study funding was requested for a two part effort;

1) To continue University of Houston development of computer capabilities.

2) To study the feasibility of an advanced receiver system.

In June 1976 a grant was received from DOE (then ERDA) No. EG-76-G-05-5178 to perform a Feasibility Study of a Solar Thermal Power System. Under this award a number of reports have also been completed carrying the title

"Liquid Metal Cooled Solar Central Receiver Feasibility Study and Heliostat Field Analysis." These are also available from NTIS.

Report	Accession No.	Cost
Executive Summary of Semi-Annual Report	ORO 5178-77-1	4.00
Final Report, Part I.	ORO 5178-78-1	6.75
Final Report, Part II.	ORO 5178-78-2	10.50

Other than the first progress report PR/73/4, a limited number of each of these reports is available from the Energy Laboratory, University of Houston, Texas, 77004 at the same cost, plus 30 percent for overseas air-mail. Charles Pitman's masters thesis from which section 3 of the current report is derived, is also available from the Energy Laboratory, University of Houston, upon request on letterhead stationery.

The Department of Energy program manager for most of the work reported above has been George Kaplan; the Technical Monitor on the recent work has been Lee Radosevitch of Sandia Laboratories, Livermore, California.

TABLE OF CONTENTS

Note that each self-contained section contains a table of contents, a list of figures and tables, and a list of references or a bibliography.

LIST OF ILLUSTRATIONS AND TABLES

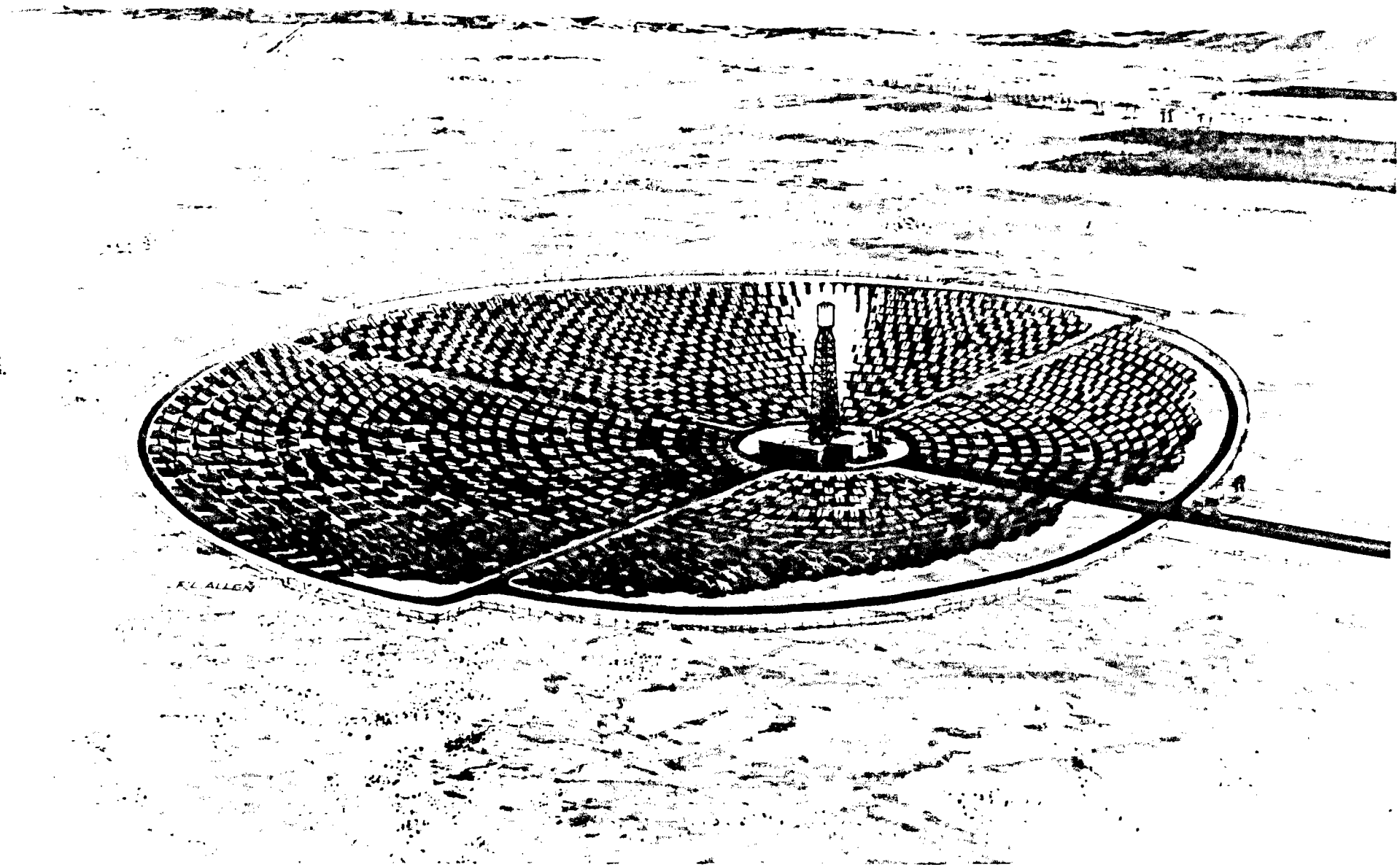

Figure 1- Artists Concept of a 10 MW_e Pilot Scale Solar Central Receiver System

Introduction

The University of Houston provided program direction and computational support to the feasibility study of the advanced liquid metal-cooled central receiver system study reported in Part I. of the final report ORO 5178-78-1, issued in October 1977 through NTIS. In addition, a number of other tasks related to the solar central receiver program have been under way at the University and are reported here in separate sections.

Two of these tasks, the Slope and Latitude Study and the Net Energy Analysis, are based on a specific design for a water/steam commercial 100 MW_e Solar Tower System; consequently, substantial work on these tasks was delayed until a reasonably final definition of the design and component costs for the system became available. This infomation was obtained in May 1977 from the McDonnell-Douglas team (of which the University of Houston was a member) as input to the final report on the two-year preliminary design study for the 10 MW_e pilot plant. In order that these relatively definitive results might be used in our analysis rather than results from the 1973-75 conceptual design study, a one year extension in time was negotiated. While work on these tasks was in progress, we were encouraged by DOE's selection of the design used in our analysis, i.e., proposed by the MDAC team, as the baseline design for the 10 MW_e pilot plant. Consequently, our results will be representative of the early central receiver facilities. As the design studies continue with DOE funding for low cost heliostats, advanced central receiver system, and other studies; we expect improvement in costs and net energy distributions within the subsystems with consequent decreases in both dollar and energy costs for the total system. The technique we describe will

nevertheless remain valid and can easily be applied to new designs. As the first order effect is expected to be an improvement in system efficiency, direct scaling will be applicable.

The third section of the report consists of excerpts from a master's thesis entitled Locating the Sun. This thesis analyzes the nomenclature, information and techniques scattered through a wide array of astronomical and celestial mechanics references and presents the techniques and mathematics required for adequate computer tracking of the sun. Higher order effects which are not specifically included in the computer code presented here are also described and discussed along with an estimate of the error associated with ignoring each effect.

The final section of this report consists of a brief description of the Sodium Heat Engine under development by the Ford Scientific Laboratory. A system is conceptualized in which a sodium-cooled receiver furnishes heat to a SHE cooled by a steam bottoming cycle. System efficiencies are computed under a variety of assumptions, and some design consideration formulated.

Executive Summary.

Section 1, Slope and Latitude Study.

Since 1973 a series of computer codes related to the Solar Central Receiver have been developed at the University of Houston. The procedure by which these codes are used to design an optimized central receiver system is described. All identified factors affecting performance of the heliostats are included, as are atmospheric attenuation, and receiver optical and thermal losses. In addition, the codes provide for a complete parametric cost model of the system. Based on this information, iteration of the optimization procedure produces a design having the lowest figure of merit (the capital cost per magawatt hour of energy produced in one year). The design is balanced in the sense that the heliostat spacing in the field is varied to trade among the various losses to produce the most effective field.

The optimization procedure is used to define a baseline system according to the exact tower height and receiver configuration used in defining the commercial water/steam baseline system in the Central Receiver Solar Thermal Power System, Phase I, Preliminary Design Study of the MDAC team. The Barstow 10 MW_e pilot plant shown in Figure 1 is a scaled version of this design. The baseline system resulting from our current optimization studies is about 40 percent larger than the preliminary design because more favorable cost and loss models are used than those available for use in defining the Phase I. design.

From this baseline a number of variations are considered, and the results of these variations are summarized in Figure 2. Results show that, while they strongly affect the detailed design, neither field

slope nor site latitude is a significant consideration in the performance of an external receiver system with a surrounding field. However, the total annual direct beam sunlight is of great significance, for the figure of merit is essentially inversely proportional to the available sunlight. Hence, while a site in the northern or eastern portions of the U.S. might convert sunlight to electricity with nearly the same efficiency as one in the southwestern deserts, only about two-thirds to three-fourths as many cloud free hours are typically available and the cost per kilowatt hour is correspondingly higher. As can be seen in Figure 2, other variations from the baseline configuration have somewhat less effect; the optimization acts to mitigate the effects of an imposed change in costs or performance of any subsystem. Thus, a 20 percent variation in heliostat cost changes the figure of merit of the optimized system by only about 13 percent.

Significant variations in the output power level for the optimized system can be accomplished by changing the receiver elevation. For a given receiver size and elevation, the power level can be modified by changing the input figure of merit or by redefining the boundary line of the field (trim control). Both approaches lead to suboptimum fields but are very convienient methods for preliminary design work. In most cases, the power level changes primarily because of changes in the reflector area. The energy collected per unit area remains relatively constant, as shown in Figure 3.

The optimization procedure described here provides a powerful tool for perfroming system trades or investigating the effects of design changes. We anticipate extensive use of these capabilities.

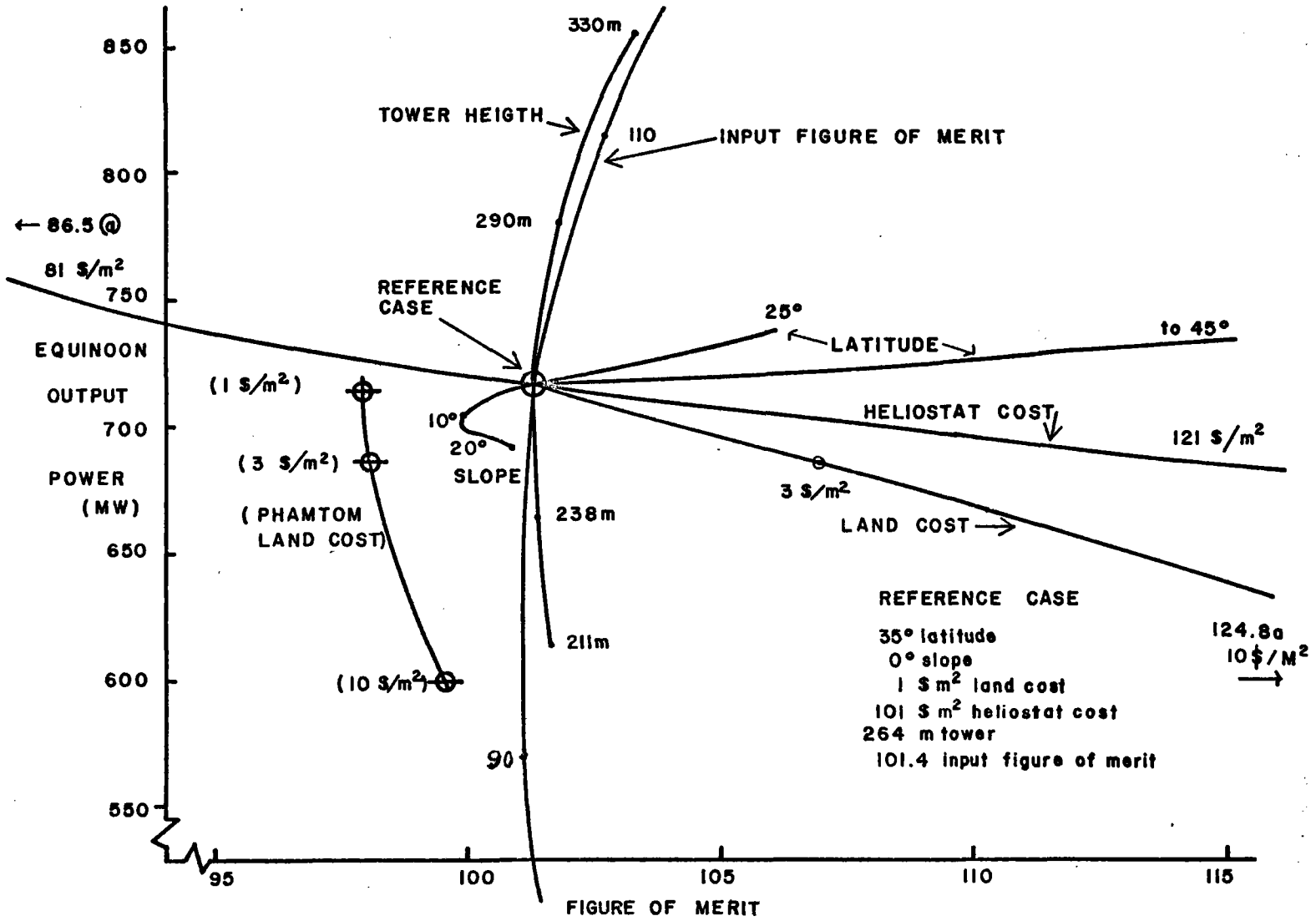

Figure 2 System Size vs. Output Figure of Merit for Parametric Variations from the Reference or Baseline Case

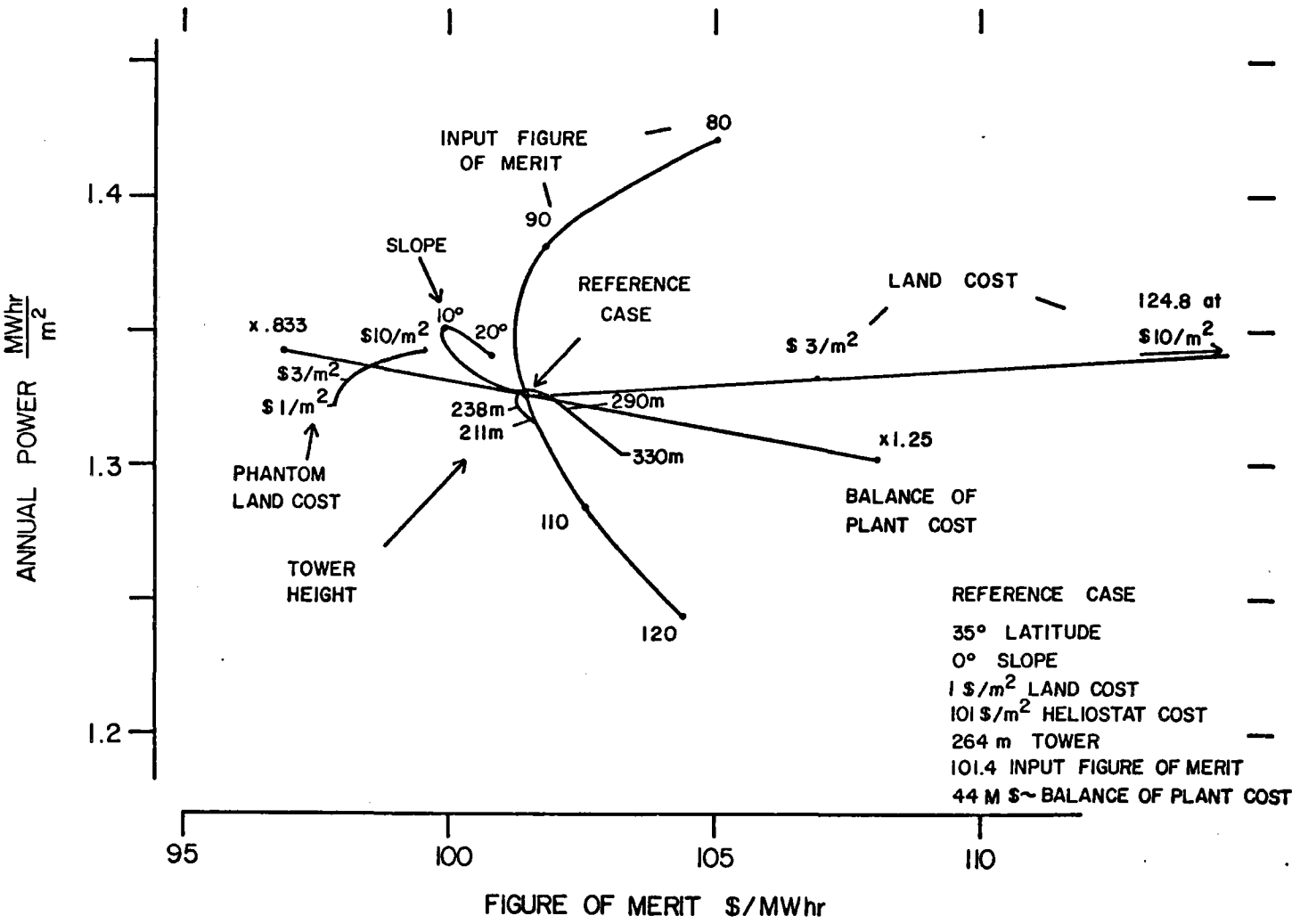

Figure 3 Annual Power per Unit of Reflector Area vs. Output Figure of Merit for Parametric Variations from the Reference or Baseline Case

Section 2, Net Energy Analysis

A heretofor unanswered question concerning the Solar Central Receiver asks, "what is its energy payback", or "by what factor is the energy expended in building the entire thermal collection system multiplied during the operating life of the plant?" Essentially we have carried out a "cost" analysis on the plant where the unit of cost is not the dollar, but the kWhr. This analysis is made relatively more difficult because energy cost accounting is not routinely done. Consequently, it has been necessary to conduct extensive literature searches and analyses to obtain the input numbers. To begin our analyses, we have determined the weight of each class of material used in each subsystem of the MDAC team's design for the Central Receiver. Next the energy content of each class of raw material, of fabrication and of transportation has been determined and summed for each subsystem, as shown in table 1. Finally in table 2, the total system energy content is evaluated and compared to the energy generated. The result shows that the energy cost can be regenerated as heat in 6 months or as electricity in 18 months. As the design life of the system is 30 years, the energy amplification factor is 20, assuming all the required energy must be provided as electricity.

Section 3, Locating the Sun

Open loop tracking of the heliostats under computer control is the currently preferred approach for the Central Receiver. To implement this tracking system the location of the sun must be known at all times with an accuracy appreciably better than 0.1 degrees. The naive approach of ignoring the eccentricity of the earth's orbit around the sun (i.e.,

NET ENERGY REQUIRED FOR 100 MW_e COMMERCIAL PLANT
(THERMAL COMPONENT WITHOUT STORAGE)

Part	Item	Weight (Metric Tons)	Energy Required - MWHt Unit	Total
One Heliostat	Steel	1.38	8.60	
	Glass	.61	1.97	
	Concrete	6.73	2.18	
	Other	.15	1.67	
	Transportation		2.28	
	Wiring		1.81	
	Manufacturing & Construction (15%)		2.78	
	Total - one heliostat		21.3	
Heliostats	22,940 Complete Heliostats			488,622
Receiver				
	Incoloy 800 Steel	154.2	1,406	
	Structural Steel	1,072.3	6,695	
	Transportation		718	
	Manufacturing and Construction (26%)		2,279	
	Total for Receiver			11,098
Riser & Downcomer				
	Steel	182	1,135	
	Transportation		105	
	Manufacturing and Construction (10%)		124	
	Total for Heat Transport			1,364
Tower				
	Concrete	41,757	13,517	
	Steel	1,266	7,899	
	Transportation		5,170	
	Manufacturing & Construction (10%)		124	
	Total for Tower			29,245
Total Net Energy Required to Build Plant (Without Storage)				530,329
Number of Days Needed to Provide Equivalent Energy:			Thermal	145
	(446K MWH_e/yr)		Electric	435

NET ENERGY REQUIRED FOR COMPLETE COLLECTION SYSTEM
FOR 100 MW_e COMMERCIAL PLANT
Annual Electric Production = 445K MW_e/yr

Part	Energy Required MWH_t	Number of Days Needed to Provide Equivalent Energy	
		Thermal	Electric
Collection System			
Heliostat	488,622	133.6	400.8
Receiver	11,098	3.0	9.1
Riser & Downcomer	1,364	.4	1.1
Tower	29,245	8.0	24.0
Subtotal	530,329	145.0	435.0
Thermal Storage System			
Caloria HT43	103,610	28.3	85.0
Rest of System (Materials, Manufacturing, Transportation and Construction)	24,657	6.7	20.2
Subtotal	128,267	35.0	105.2
NUMBER OF DAYS NEEDED TO PROVIDE EQUIVALENT ENERGY FOR COMPLETE SYSTEM (Total 658,596 MWH_t)		180.0	540.2
Days After Start-up System Completely Paid for - Capital Energy Cost		180.0	540.2
Energy Amplification Factor (30 year lifetime)		61	20.3

use of the "mean sun") is shown to result in errors as large as two degrees. While such errors are not troublesome when we design systems or predict system performance, they are of significance when we attempt to compare measured and predicted solar insolation models. Ignoring orbital considerations would preclude adequate computer controlled heliostat tracking, even for periods of as short as a day.

As a consequence, a computer code has been written which accounts in for the ellipticity of the solar orbit. As well as describing this orbit, all deviations in the position of the sun from that which the code predicts are described and analyzed. Consequently, the current code can be used with confidence at the design level of accuracy, or the appropriate corrections can be investigated without recourse to tomes on celestial mechanics, spherical geometry, and astronomy. A more detailed discussion is found in the original master's thesis.

The report also investigates the effect of solar location errors resulting from the use of the "mean sun" when comparing measured and predicted insolation. Errors of one to two percent in the daily total insolation result, arising mainly from rather large errors near sunset coupled with errors in the predicted length of the day.

Section 4, The Sodium Heat Engine.

The Sodium Heat Engine is a sort of thermal battery with no moving parts. Sodium ions at 800°C migrate through Beta Alumina, recombine with electrons which have passed through the "load", evaporate, are condensed at 400°C, and are electromagnetically pumped to the receiver

where they are reheated at 800°C. This system is described in more detail, and a conceptual design presented of a large scale system in which such a heat engine is cooled by a steam bottoming cycle. Overall efficiencies of over 50 percent seem possible. We are participating with the Ford Scientific Laboratory in further study of the Sodium Heat Engine.

SECTION I

SLOPE AND LATITUDE STUDY

Heliostat Field Analysis

F. W. Lipps and L. L. Vant-Hull

Abstract

The RCELL computer program provides a cellwise method for the economic optimization of central receiver systems. This program contains a cost and performance model for each element of the Solar Central Receiver Energy Collection System and can output nearly complete performance data for an economically optimized collector field. The optimal collector system is defined as that heliostat configuration which produces the lowest figure of merit. (collector system capital cost divided by the annual energy collected--$/aMWH_t$) for a given tower-receiver subsystem. In the current study the collector field utilizes radial stagger neighborhoods (i.e., the peak through feature) although alternate arrays are available. In this case the program adjusts the radial and azimuthal spacing coordinates in each cell to balance the losses in an optimum way.

While the RCELL program is completely general and can be applied to any heliostal-receiver system, we will give specific results for the MDAC 100 MW_e commercial baseline system with an external cylindrical water/steam receiver. Specifically, we compare performance for several latitudes, field slopes, tower heights, heliostat costs, land costs, and input figures of merit. While these results apply specifically to the MDAC configuration, the trends identified have general applicability to similar systems.

In the Latitude Study, we compare optimized systems at latitudes 25°, 35°, and 45° including weather models for appropriate parts of northern Mexico and the western U.S.A. Although collector efficiencies are comparable, the figures of merit are sensitive to the available direct beam insolation and are: 106.2 $/aMWH_t$ at 25°, 101.5 $/aMWH_t$ at 35° and 147.3 $/aMWH_t$ at 45°. In the Slope Study, we compare fields of 0° slope, 10° slope, and 20° (up to the north) slope at 35° latitude. The 10° slope gives

the best performance by one percent. The Tower Height Study shows that total thermal power at equinox noon is proportional to the 3/4 power of tower height for optimized systems; however, if all dimensions are scaled, the square law still prevails. The Heliostat Cost Study compares optimized systems using heliostat costs equal to 81.00 $/m^2$, 101.25 $/m^2$, and 121.50 $/m^2$. Results show total system costs increasing as expected but not as rapidly as heliostat cost due to the optimization. The Land Cost Study shows that the figure of merit increases 20 percent due to a 10-fold increase in land cost (i.e., 1.08 $/m^2$ to 10.00 $/m^2$). The Input Figure of Merit Study shows the extent to which the input figure of merit can be used to adjust the system size without seriously disturbing the optimization.

Table of Contents

LIST OF ILLUSTRATIONS

LIST OF TABLES

1.1 PURPOSE OF THE SLOPE AND LATITUDE STUDY

In 1973 our first efforts towards a computer model for the Central Receiver System were directed towards parametric results. (By seeking analytic results and clever program constructions, we were able to avoid the Monte-Carlo approach which provides an accurate model but no hope of optimization). System performance could be obtained as a function of the input parameters, but so many geometric parameters might have to be assumed that the dependence on any one parameter might not at all represent the behavior of the optimized system. For example, we find that the total system power varies with tower height to the 3/4 power for an optimized system, instead of the square as naively expected. Consequently, there is a vast difference between parametric studies with and without optimization. This paper represents the first effort to report the basic parametric dependence of the optimized Central Receiver System.

Our results relate to the 100 MW_e water-steam system developed by DOE during the preliminary design phase (1975-1977). . These results are based on cost data generated by the McDonnell Douglas team (MDAC) as of 1977; completion of these studies was delayed in order to utilize these improved cost estimates. We are reporting results for variations of slope, latitude, heliostat cost, land cost, tower height, and the input figure of merit estimate, as compared to a single baseline system.

The baseline system is detailed in section 1.5a. The focal height of the receiver is 264 meters. The external cylindrical receiver is 25.5 m in length and has a diameter of 17 m. There is a Hi-Lo aiming strategy suitable for the water-steam receiver. The results given here depend on MDAC component cost estimates and therefore leave open the question of comparison to other designs.

Several additional studies, not considered here, would be appropriate applications of our optimization methods. These include (1) studying the option of ganging several towers to a single prime mover; (2) varying receiver parameters such as temperature, losses, size cost, or configuration (cylinder, flat panel, cavity, etc); and (3) varying heliostat size, shape, guidance errors, or surface figure (including the counting of segments, stress, focusing, surface ripples, etc). Several of these studies are being carried out under other DOE funded contracts. We anticipate discussing these results in our future reports and papers.

1.2 INTRODUCTION TO THE OPTIMIZATION PROCEDURE

We are concerned with the optical behavior of the collector field and its interaction with the receiver. Our computer model of this behavior considers methods leading to an economically optimized design of the collector field. We will discuss:

1. The nature of the desired optimization and the resulting figure of merit.
2. The economic model for the commercial system.
3. The energy loss model
4. Design requirements.
5. Basic variables of the collector field geometry and various practical subsets.
6. Mathematical formulation of the optimization and its computerized solution.
7. Optimized collector field geometry.

The collector field contains a large number of heliostats whose locations with respect to the receiver and with respect to each other create an intricate design problem. Heliostat location is measured with respect to the base of the tower. An optimized set of heliostat coordinates provides an optimized collector field for present purposes.

The towertop receiver is designed to absorb solar energy and to deliver this energy to an electric utility for electric power production. The best economic measure of performance for this composite system is a suitably adjusted busbar cost estimate for the output electric power.

An effort to optimize the collector field geometry via busbar cost would make the collector field design too difficult and much too dependent on the design of the thermal storage system, on the turbogenerator system, and capacity displacement credits. It is desirable to consider the tower-top receiver a source of thermal energy which can be "sold" to the utility system; therefore, the cost of thermal energy at the base of the tower can be used as a suitable figure of merit for the optimization of the collector field.

Specifically, we assume a figure of merit equal to system cost (heliostat field, receiver, tower, piping, and coolant pumps) divided by net annual thermal energy delivered at the base of the tower. The use of annual thermal energy implies that thermal energy is always useful to the utility. This assumption would be invalid for a seasonal application such as irrigation pumping. Although it is not uniformly valid for utilities, it should be valid in an energy hungry community if the power plant is assumed to incorporate three to six hours of thermal storage. In the future, we may consider ways of biasing the energy towards desirable times, but for the present we accept the verdict of the system performance analysis. By system cost, we mean cost traceable to the energy collection and transporation system prior to delivery of the energy at the base of the tower. The heliostat field is a major cost item and thus a worthy object for optimization.

The source of energy, i.e., the insolation, and the loss model for our system are factors in the optimization. At a specific site, the system collects direct beam solar insolation which is influenced by local weather conditions and the site latitude. We are not concerned, however, with the specific details of the insolation record, but instead, with predictable average insolation behavior to help determine the outcome of investment decisions. Consequently, it is reasonable to use our analytic insolation model with a

"percent of possible insolation" factor. The following list cites reasons for energy loss:

1. Percent of possible insolation due to local weather conditions.
2. Heliostat related factors: reflectivity, dust, guidance errors, and malfunction.
3. Shading and blocking losses due to neighboring heliostats.
4. Start up and shut down losses due to wasted insolation and heat.
5. Atmospheric transmission losses between heliostat and receiver.
6. Receiver related factors: interception, absorptivity, emissivity, convection, and conduction.
7. Parasitic energy requirements for heliostat guidance and coolant pumping.

The central receiver system concept is an optical concept and can therefore be optimized over many design variables not included in the collector field layout. Heliostats are optimized for mass production cost savings and performance under reasonable loads. This is basically a mechanical problem and the resulting heliostat design is an input to the collector field problem. For a specific study, heliostat size is usually fixed. Although the tower design is also basically a mechanical problem, the tower height must be adjusted so the associated collector field is large enough to satisfy the name plate power requirements for the utility power plant. As an overly tall tower presents an excessive cost, the tower height becomes a by-product of the collector field optimization.

The receiver design also affects the optical performance of the system. For our purposes, the receiver design is assumed given. Receiver size was optimized at an earlier stage when various receiver geometries were considered. The specified receiver size is adequate to handle the required power, and its configuration is appropriate for the anticipated variation in flux distribution with time. To reduce the peak flux level, the receiver has been sized in fact somewhat larger than is required to intercept the design level power from an optimized field. Consequently, it is possible to employ an aiming strategy, redistributing the flux to reduce the excessively high peak values on the north side. The enlarged size makes it possible to vary the aim strategy for a specified field to optimize the receiver interception. In this study we adopt the Hi-Lo aim strategy wherein alternate heliostats are aimed so the outer edge of their beams grazes the upper and lower edges of the receiver. An earlier 3-point aim involved an arbitrary upwards or downwards shift of heliostat aims by 7.5 m and produced inferior results. See Table 1.2.1

Table 1.2.1 Interception Performance Averages for MDAC External Cylindrical Receivers

System	Aiming Strategy	Interception	Flux Spillage
Commercial	3 Point	95.8%	4.2%
Commercial	Hi-Lo	97.0%	3.0%
Pilot	Hi-Lo	98.0%	2.0%

The receiver design is complicated by many considerations, certain of which impact the collector optimization. The receiver must be large enough to intercept effectively the beams projected from the heliostat field, but small enough that thermal losses are not excessive. Like any heat transfer device, it has a flux density limit beyond which some form of damage or malfunction will occur, and the heliostat field design must be sensitive to this

limitation. To date we have considered cylindrical or flat external receivers composed of a number of panels, each having an input and an output manifold with sensors and controls. Flow control must be positive and, for two phase flow, a limited range of flow control is possible. Consequently, we must maintain a minimum panel power at all times during useful operations. Furthermore, the manifolds will fail to distribute flow satisfactorily to each of the tubes in a given panel if the flux gradient across the panel is excessive, resulting in a maximum flux gradient limit. While the above discussion is directed at external receivers, similar considerations apply to the heat transfer surfaces in the interior of a cavity, although the cavity designer has somewhat more latitude in positioning the surfaces.

The design procedure for an optimized heliostat field requires the following steps:

1) Set scale of system by specifying the total thermal power at the design point, typically equinox noon.

2) Scale receiver dimensions to satisfy the flux density limit, assuming that adjustments will be made in the aiming strategy.

3) Estimate tower height.

4) Optimize the collector field.

5) Adjust the aiming strategy to reduce bright spots on the receiver.

6) Adjust the trim of the field to satisfy panel power minimum, if necessary. At 35° latitude, the southern field tends to be weak and becomes weaker as latitude increases. A slight departure from optimization may be required here, although the problem may also be solved through the use of preheat panels in the southern quadrant of the receiver.

7) Scale tower height and collector field to achieve exactly the desired system power level.

8) Generate final heliostat coordinates. We must give a complete list of coordinates for roughly 20,000 heliostats allowing for free turning of the heliostats, roads, tower exclusion, and heliostat access ways. Each heliostat must have a designation suitable for use by the surveyors and to define the subsequent control connections.

We assume that the heliostats are identical and that the centers of the heliostats are coplanar so that the collector field is flat, although it may have a slope. Allowance for contours in the collector field is a step beyond the current state of the art. The intersection of the tower center line with the plane of the heliostats determines a natural origin for the coordinates of the heliostats in the collector field. The complete list of heliostat coordinates can be visualized as a set with the following additional structure. Let H be a heliostat in the set of heliostats S so that the list of heliostat coordinates $\hat{L}$ can be expressed as:

$$\hat{L} = \{(x_H, y_H) \mid H \in S\},$$

where (x_H, y_H) gives the coordinates of heliostat H. Now let H be identified by a pair of integers (i,j) such that

$$H \leftrightarrow (i_H, j_H),$$

i.e., H is one-to-one correspondence with (i_H, j_H). Consequently, the list of coordinates can be written as

$$\hat{L} = \{[x(i,j), y(i,j)] \mid (i,j) \in S\},$$

and the mapping from S to the collector field is given by the functions x(i,j) and y(i,j) which are determined by the optimization procedure. If the coordinates are expressed in units of heliostat width, we can visualize the coordinate mapping as an actual layout process in which the heliostats are moved from a storage area where they are kept in a state of rectangular closest packing so that their coordinates are (i_H, j_H) in heliostat units. Currently we expect that i will be a circle label and j will be an azimuth label.

Historically, we have approached the collector field design by assuming the simplest possible layout and gradually adding variables, but never allowing a chaotic solution to occur. In general, the optimization is non-unique and leads to chaotic solutions similar to dislocations in a crystal. This type of result is to be expected from a straight forward, rigorous minimization of the figure of merit. For example, if L is an arbitrary set of heliostat coordinates and F is the figure of merit, the optimization implies that

$$\hat{F} = \underset{\{L\}}{\text{MIN}}\ F(L) = (\hat{L}),$$

where $\hat{L}$ is the optimized coordinate set. The function F(L) is difficult to construct for several reasons:

1. There are many independent variables.
2. Insolation averages must be performed numerically.
3. Instantaneous reflected power from each heliostat is a function of the heliostat coordinates which has at least eight analytic branches. (We expect non-analytic behavior from every shading and blocking event. Normally, eight neighbors can contribute events, hence eight branches.)

However, F(L) can be defined as follows: Let

$$F(L) = C(L)/E(L),$$

where C(L) is the dollar cost of the system and E(L) is the net annual thermal power delivered at the base of the tower. C(L) is determined by the economic model. E(L) is determined by the optical model of the system. We can write

$$E(L) = a\, E_o(L) - b,$$

and then

$$E_o(L) = \sum_{H \varepsilon S} \eta_H g_H(L) A_H,$$

where

A_H is the reflective area of a heliostat,

$g_H(L)$ is the annual total thermal energy reflected by heliostat H in a field specified by L,

η_H is the receiver interception factor for heliostat H, which is assumed to be time independent for purposes of simplicity, and

$E_o(L)$ is the annual thermal power incident on the receiver.

The coefficients a and b contain all other losses so that E(L) becomes the net thermal energy delivered at the base of the tower.

Currently, our computer facility is able to generate quantities such as $E_o(L)$ for a collector field only if the summation is limited to several hundred terms. Consequently, we are forced to a system of representative heliostats, which is called the "cell-wise approximation for large collector fields." The expression for $E_o(L)$ is replaced by

$$E_o(L) = \sum_c n_c \eta_c g_c(D_c) A_H,$$

where n_c is the number of heliostats in a cell c. Consequently,

$$\eta_c g_c(D_c) = \eta_H g_H(L),$$

where H is the representative heliostat for cell c. The variables D_c are the displacements of the appropriate neighbors with respect to the representative heliostat. Hence, D_c is a function of L, but not vice-versa in general.

The cell-wise optimization procedure presented in Reference 4 and Appendix I (Section 1.7 and 1.8 of this report) starts with the above expression for $E_o(L)$. Unfortunately, it leads to a solution for the displacements and not for the coordinates themselves. Fortunately, the results for the displacements vary smoothly from cell to cell. The use of representatives implies that each heliostat in a cell has a similar neighbor. This assumption greatly reduces the number of independent displacements. In practice, we solve for two components, a radial x component and an azimuthal y component, as in Figure 1.2.1. The results show y nearly constant throughout the collector field and x nearly independent of azimuth with respect to the tower. Furthermore, x can be represented as a quadratic function of the tower elevation angle. Figure 1.2.1 defines cornfield and staggered neighborhoods.

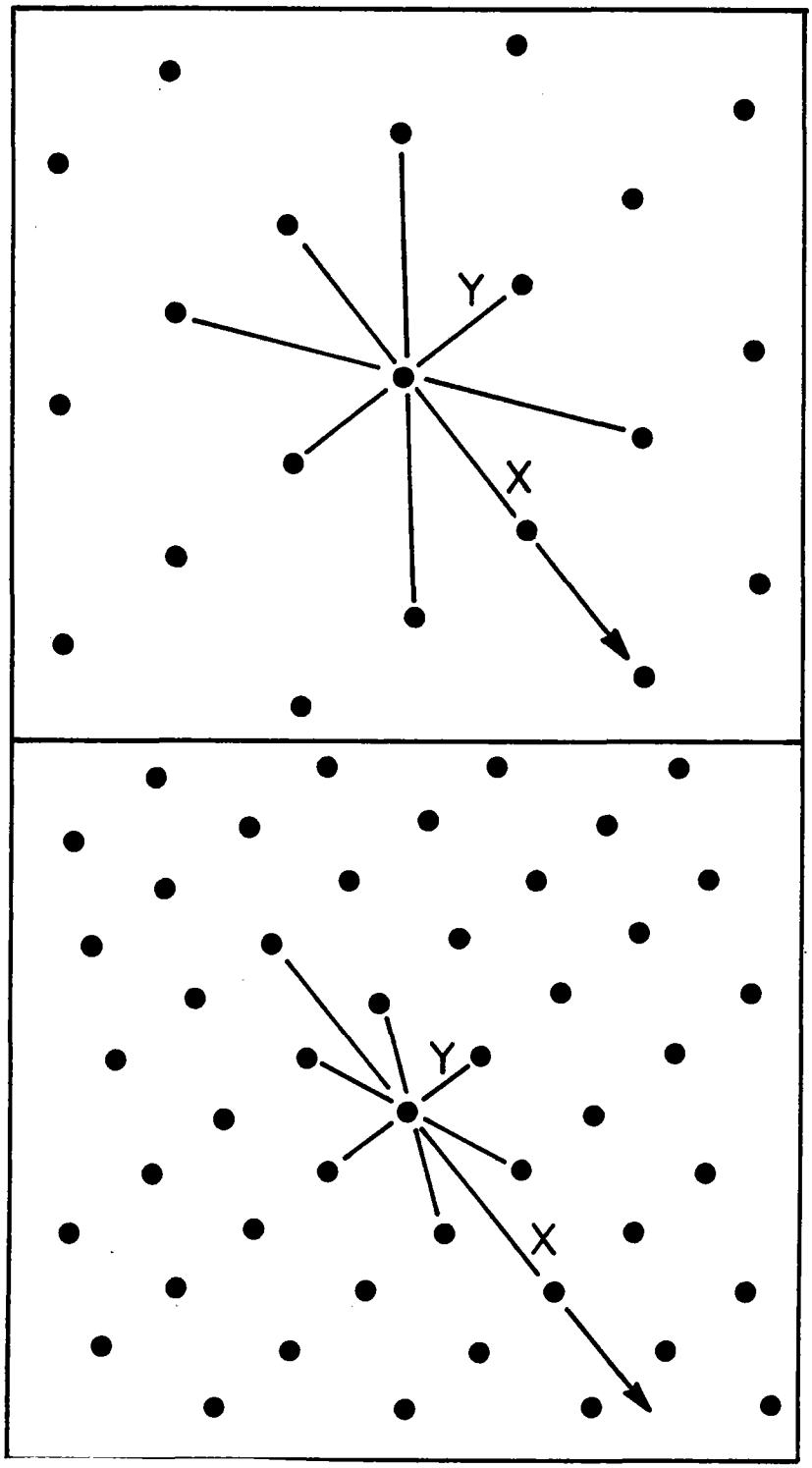

Figure 1.2.1 Cornfield and Radial Stagger Neighborhoods. The arrow points to the tower for radial alignment, or north for N-S alignment. The upper figure shows a cornfield configuration and the lower figure shows a staggered configuration. For radial staggers, x becomes the radial spacing parameter and y becomes the azimuthal spacing parameter. (In some cases we will replace x with R and y with z for mnemonic ease)

1.3 DETAILS OF CENTRAL RECEIVER MODEL

The model contained in the computer code must necessarily describe a specific system design in sufficient detail to respond to all data requirements of the code. In the ensuing pages we describe the components of the particular system we have chosen for this study. The code is, in fact, very general, and nearly every item of data described below is subject to operator control. Thus, although the study described here is based on a design involving a very specific cylindrical external receiver, changes in the program controls and input data, along with minor modifications in the code, will allow studies of flat receivers or apertures of cavities facing in any direction, etc. Variations in the heliostat configuration, the field configuration, or the cost and loss models are equally easy to implement.

The computer model of the Central Receiver System contains the following components, where the values quoted here define the baseline system used in this study:

1. The Astronomical Model
   a. Diurnal motion of sun using an eccentric earth orbit but not including lunar perturbations or effects of longitude. A discussion of the diurnal motion appears in Section 3.
   b. Insolation model for cloudless sky via an analytic fit on Allen's clear air data. [5] This model includes air mass, water vapor, and altitude effects. Air mass is calculated for a spherical earth.
   c. Daily and annual integrals based on a sample of times. We use 19 samples per day and 7 days per year. The

daily sample starts and stops at a specified elevation angle 10° above the astronomical horizon or 5° above the plane of the heliostat field, whichever is the more restrictive. The 19 daily samples are spaced less densely near noon where few shading or blocking events occur. The seven days sampled include the solstices and are uniformly spaced at monthly intervals. The sample includes the autumnal equinox but not the vernal equinox, which is represented by symmetry with allowances for varying earth distance.

2. The Site and Weather Model

   a. Latitude, slope, and altitude of site.

   b. Visual range for redirected sunlight. The loss due to atmospheric scattering is approximated by a linear function of the slant range based on a computation using the NOAA Lo Tran II program.[6]

   c. Monthly turbidity factors for incoming sunlight. Available direct beam sunlight predicted by Allen's clear air model is attenuated by $\exp(-T\ m_r)$, where m_r is the relative air mass and T is the estimated turbidity factor.[7]

   d. Monthly percent of possible sunlight hours.

   e. Monthly mean precipitable water content of atmosphere from Weather Bureau Technical Paper No. 10, 1949. See Table 1.5c.3 for details of these models.

   f. Elevation of sun required for operation.

3. The Collector Field Model

A cell model is used with uniformly spaced representative heliostats in each cell and a variable number of heliostats per cell. Currently RCELL requires an east-west symmetry in the collector field. The field arrays have variable dimensions but represent the east half field only.

The collector field has an outer boundary optimized by RCELL (See Appendix II) and a fixed inner boundary. The inner boundary represents a subtower exclusion which must occur for tower supported cylindrical receivers. The optimization procedure could also determine the inner boundary; however, the cell structure in the collector field is too crude for good results. Furthermore, the number of heliostats on the inner boundary is too small to influence the optimization significantly.

The collector field is constrained to allow access and free turning for the heliostats. This constraint is called mechanical limits. RCELL maintains mechanical limits for both initial and final heliostat spacing coordinates. For the heliostat used in this study, this means that the separation of radial, azimuthal, and diagonal neighbors must exceed 1.4844 heliostat widths.

The results given below come from studies using a 14 x 8 field array corresponding to a 14 x 15 array of cells for the complete field. All cells can have heliostats, but the effective population of heliostats is inside the field boundary, i.e., the Trim line. Cells <u>on</u> the boundary are split into fourths to increase the accuracy of the system performance estimates.

4. The Heliostat Model

We assume a flat heliostat with a square profile and no canting. Allowance is made for slotting according to the 1977 MDAC design. The area of glass is 37.226 m^2/heliostat, but this has little effect upon the optimization. The heliostat mounting is Alt-azimuthal. The heliostat width is 6.5024 m. The code contains provisions for any of the common mounting schemes (polar, pitch-roll, etc.)

5. The Shading and Blocking Model

The subroutine used in RCELL processes multiple events for regular N-Gons, in this case square heliostats.[8] A complete set of first and second nearest neighbors is included. The set of neighbors slopes with the field if slope is used. An alternate subroutine can be used if the heliostat is rectangular. These subroutines are generalized by operating in coordinates normalized by the heliostat width, 6.5m in this case.

6. The Guidance Error Model

The guidance error model relates to image formation and interception fractions and, consequently, to RCELL optimizations. Many factors contribute to guidance error. For our purposes, all heliostat induced errors are represented by a Gaussian distribution having 1 σ standard error for the deflection of the redirected rays, taken as 3.7 mrad for present purposes. The images are also determined by the solar disk and the heliostat size and shape. We use the exact geometry of the MDAC heliostat for image purposes, but any

other heliostat configuration can be easily substituted. The sun is 4.66 mrad in radius at 1 AU and is modeled using moments up to the sixth order to fit the limb darkening.

7. The Image Model

The Image Generator used in this study is based on Walzel's two dimensional Hermite polynomial approximations method [9] which represents the heliostat geometry exactly to the sixth order. The results given below depend on the assumption that interception fractions are time independent so that the equinox noon results can be used for the whole year. This appears to be a valid assumption for flat or nearly flat heliostats with an aspect ratio (length/width) of approximately unity. See reference 10.

8. The Receiver Model

The results given below relate to the 100 MW_e water/steam system with a solar multiple of 1.7 which will have an external cylindrical receiver. Of course any size or shape receiver can be modeled. The receiver model used here has receiver nodes on a 17 x 24 array, one column for each of 24 vertical panels in the receiver and 17 nodes along each panel. The receiver dimensions are 25.5 m tall by 17 m diameter. The design power level for this receiver is 532 MW_t absorbed of which approximately 25 MW_t is lost due to convection and infrared radiation. We use a baseline focal height of 264 m in this study, primarily for historical reasons. In fact, for the system defined here, we find the optimum focal height corresponding to 532 MW_t, absorbed is about 211.2 m (the

smallest system considered in our study). Our results at higher power levels remain valid since we incorporate an appropriate scaling factor on receiver cost vs. power.

9. The Aiming Strategy

The results given below are based on a Hi-Lo aiming strategy in which the aim points of alternate heliostats are shifted vertically to reduce the peak flux. This strategy gives a reasonably flat flux density profile in the vertical direction without spilling much flux at the top or the bottom. See page 1-40 for details.

10. The Energy Loss Model

a. Heliostat Reflectivity including dust *

Reflectivity = .94; Dust factor = .97

b. Heliostat outage including heliostats deleted due to roads or heliostats which will be effectively lost in converting an optimized field to a relizable configuration*

Outage factor = .98

c. Scattering of reflected rays between heliostat and receiver (i.e., visual range) *

Transmission =

$$1.0 - (.01 + \text{Range}/20\ \text{km})\sqrt{50\ \text{km}/\text{visual range}}$$

d. Receiver absorptivity and its angular dependence *

Absorptivity = $.95\alpha(\theta)$;

$$\alpha(\theta) = \begin{cases} 1 & .5 \leq \cos\theta \leq 1 \\ .395 + 1.21\cos\theta & 0 \leq \cos\theta < .5 \end{cases}$$

e. Reradiation and convection by receiver *

1.16 MW_t/boiler panel; 0.58 MW_t/heater panel in present study

f. Thermodynamic cycle efficiency

g. Pump power and other parasitic losses

* Starred items are included in this optimization procedure.

Items e, f, g, and the solar multiple define the required thermal power level.

II. The Cost Model for the Thermal Component

McDonnell Douglas has developed a detailed cost model for the "Nth" commercial 100 MW_e solar central receiver plant resulting from the preliminary design study of 1975-1977. This design is reported in Vol. VII of their final report on DOE contract SAN 1108, submitted in June 1977. The cost model used in that report was obtained as a computer output dated 77/05/19. In detailed discussions of this model, the various costs were allocated on the basis of their dependency on various parameters of the thermal collection component of the Solar Tower System. The categories of interest are:

"Fixed" (F), such as calibration equipment or master controller.

"Height Dependent" (H), such as tower or vertical plumbing.

"Reflector Area" (A), such as heliostats, shipping containers, or field assembly.

"Power" (P), such as receiver or plumbing.

This analysis was carried out in June, 1977, and represents a consistent cost model as of that date. Sandia revisions of this cost model are not extensive or large, and sufficient detail is not available from the Sandia reports to allow the proper apportioning of the charges among the various categories. Consequently, the decision was made essentially to retain the MDAC cost model.

In Table 1.3.1, the various items are listed by Work Breakdown Statement (WBS) Number, Title, Total Cost, and the cost distribution among F, H, A, and P. Summarizing the items in the table, we find the grand total cost for the solar component of a mass produced commercial water/steam plant delivering up to 506.4 MW_t of steam at 510°C at the base of the tower is $124.22 million in 1977 dollars with no allowance for contingency, interest during construction, or escalation. This system has a solar multiple of 1.7 (sufficient power is delivered at the design point to power a 170 MWe turbine generator) and represents current technology for a water/steam cooled receiver. It is reasonable to assume that evolution of the design of the heliostats and of the receiver system would lead to a still lower cost system, partially through reductions in the thermal power required and partially through design related cost reductions. For our purposes, the absolute cost per kilowatt statistic is not of particular concern, but we use the breakdown into categories for optimization purposes. Doubling or halving all costs uniformly would not influence the outcome of our analysis; the crucial requirement is that costs be internally consistent, i.e., generated by use of a coherent costing methodology. Thus, we achieve a fixed cost for this plant of $\$4.97 \times 10^6$, a cost dependent upon heliostat area of $\$88.25 \times 10^6$ for a collector area of 871,615 m^2, or $\$101.25$ m^2, and a cost of $\$3.76 \times 10^6$ for acquisition and preparation of the heliostat field of approximate area 3.48 km^2, or $\$1.08/m^2$.

Costs for the receiver, riser, downcomer, feedwater pumps, tower, and foundation depend on the height and power and can be represented by the formula

Table 1.3.1 Solar Thermal Component Cost Breakdown for the N^{th} Commercial Central Receiver Plant

May, 1977 Baseline: 506.5 MW_t of Steam @ 510° C

F: Fixed Costs -- multiplier = 1

A: Reflector Area dependent costs -- multiplier = A/A_o where A_o = 871,615 m^2

H: Receiver Height dependent costs -- multipliers are h_1 = (H-9m)/255; h_2 = (H + 19 m)/283; and h_3 = (H-22m)/242;

P: Power Level dependent costs -- multiplier = $\rho = (P/P_o)^{0.62}$ where P_o = 506.5 MW_t

*: Actually a field area dependent cost -- multiplier = $A/\phi A_o$ where $\phi \sim .25$

WBS	Title	Total Cost x $10^6	F x $10^6	A x $10^6	H x $10^6	P x $10^6
4000.1	Land and Preparation	3.76	0	3.76*	0	0
4190.1	Collector Equipment (open loop control)					
.11	Reflective Unit	19.44		19.44		
.12	Drive Unit	30.17		30.17		
.13	Calibration Unit	.10	.10			
.14	Field Controller	3.93		3.93		
.15	Foundation & Site Prep.	7.73		7.73		
.16	Design/Engineering	1.74	1.74			
.17	Transportation to Site	.76		.76		
.18	Field Assly, Inst, C.O.	14.07		14.07		
.19	Lightning Protection	.00				
	Total 4190.1	77.94	1.84	76.10	0	0

Table 1.3.1 (Continued)

WBS	Title	Total Cost	F	A	H	P
4190.2	Receiver and Tower					
.21	Receiver Unit	14.01				14.01
.22	Steam Generator	.00				
.23	Riser & Horiz line	.71			.71 $h_1\rho$	
.24	Downcomer & Horiz line	1.48			1.48 $h_2\rho$	
.25	Tower	6.10			6.10 h_3	
.26	Foundation & Site	3.38			3.38 h_3	
.27	Design	.00				
	Total 4190.2	25.68	0.00	0.00	11.67 f(h,ρ)	14.01
4300.42	Feed Water Pumps	1.56				1.56
8100.20	Construction Mgnt	8.80		8.80		
8100.40	Solar Eng. & Design	2.70	1.35	1.35		
8100.50	Master Controller	1.78	1.78			
--	Helio. Handling Rigs	2.00		2.00		
	Total 4200+	16.84	3.13	12.15	0.00	1.56
GRAND TOTAL		124.22	4.97	88.25	11.67	15.57
				3.76*		

$$\{[14.01 + .71\,\frac{H-9}{255m} + 1.48\,\frac{H+19}{283m} + 1.56]\,(\frac{P}{P_o})^{.62}$$

$$+ (6.10 + 3.38)\,(\frac{H-22}{242m})^{1.9}\} \times (\$10^6)$$

Here, the costs of the receiver (14.01) and the feedwater pumps (1.56) are scaled with the power. The costs of the riser and downcomer are scaled by both power level and length of line while the costs of tower and foundation scale with the tower height to the 1.9 power. This 1.9 power law and the 0.62 power law for scaling with steam power represent correlations with design data. Correlations with design data for a similar system employing a sodium cooled receiver have given exponents of 1.8 and 0.8; the above relation is nevertheless used throughout this study. The power P is evaluated at equinox noon assuming 950 W/m^2 of insolation for design purposes. The influence of scaling the receiver and plumbing costs with the power level will be considered again in section 1.5g of this report.

Finally, several variations on the scheme for delivering guidance power and control commands to the heliostats have been considered. The current choice seems to be adequate and produces a low but realistic cost for wire and installation. In this scheme, armored cable is laid in trenches costing $6.10/m to open and close. Power and signal cables are run together from the tower outward and are connected serially to field controllers on each circle. Each field controller services ~75 heliostats on a circle with a single

series connected data link costing $4.54/m and a power line costing $8.06/m. With heliostats about 15 m apart and after allowance for the radial runs, this cost amounts to ∿ 285 $/heliostat, or $7.64/m^2.

12. The Figure of Merit and Optimization Procedure

The optimization procedure is described in detail in the next section. In addition to considering the performance of the heliostat field in its operation, it produces a cost benefit ratio for the optimized system. This ratio, which we designate as figure of merit, is the capital cost of the system divided by the annual energy produced ($/aMWH$_t$). The cost model has been discussed in item 11 of this section and the loss model in section 10. Subject to external constraints imposed on the design, the optimizer is operated iteratively to produce a converged figure of merit and an optimized design. At that point, the component costs are itemized and the net annual energy estimated.

The following items are typical of the external constraints which can be imposed:

1. Policy related choice of base time period
2. Definition of scale, i.e., Power at Equinox Noon, etc.
3. Mechanical constraints for heliostats and access
4. Flux limits for receiver
5. Flux gradient limits for receiver
6. Imposed field boundaries

1.4 OPERATION OF THE RCELL PROGRAM

Initial application of the RCELL program to a new study requires that values appropriate for the specific case be inserted for each of the variables defined in the preceding sections. In addition, there are several auxiliary inputs which must be decided upon. These include the field cell size, the field array size, the input figure of merit, a set of preliminary heliostat spacings, and the step size for the variation in heliostat spacing considered in the optimization process.

The field cell size is determined by the distance between representative heliostats at the center of each cell, and is specified in terms of the tower focal height. Typical values range from ½ to $\sqrt{6/2}$ of the focal height, giving cell areas of 1/4 to 6/4 of the focal height squared. The array size must be large enough to include all remote heliostats, the cell size must be small enough to provide adequate resolution of details in the structure of the collector field. As the array size increases, the number of cells increases and the CPU time increases. Each result given below represents at least one 10 minute run and several 30-second runs to converge the figure of merit (Honeywell 66/60 time).

The input figure of merit is an estimate of the total system cost divided by the annual thermal energy produced, expressed as $\$/aMWH_t$. As the optimization is iterative and converges rapidly, the heliostat cost in $\$/m^2$ is an adequate zero order estimate for the input figure of merit. The resulting output figure of merit provides a much better estimate for the next iteration. The step size for variations in heliostat spacings is generally held at 1/10. This gives a "patch" covering the range 0.85 to 1.15 times the input spacings. This is generally adequate for optimizer variations wtihout becoming too granular. However, if no knowledge

exists about the optimal heliostat spacings expected for the particular design, one may have to resort to a step size of 1/8 or 1/6 to find solutions. A reasonable equation for preliminary field layout sets the azimuthal separation at 2.1 mirror diameters and represents the radial spacings (also in mirror diameters) by the function

$$R = 60°/\theta - 1/3 + \theta/60°,$$

where θ is the local elevation angle to the center of the receiver.

Once all these preliminaries are out of the way operational procedures for RCELL are quite straightforward.

The data flow schematic in Table 1.41 shows the initial receiver run in which interception factors for the representative heliostats are calculated (120 in this case). The schematic closely resembles the program structure. This is a 30-second run because we assume uncanted flat heliostats. The model involving the generation of separate images from 12 canted flat segments requires six minutes for this run. Coefficients may be generated to represent the matrix of interception fractions and to replace the panel data file. The use of interception coefficients permit interpolation of the computed interception fractions which is necessary if a change of cell size is required by RCELL.

The data flow schematic for the optimization is shown in Table 1.4.2. The RCELL program used in this study provides the same functions but only approximates the structure of Table 1.4.2. The code has been updated, and it is desirable for clarity of presentation to picture the data flow as it appears in the revised code. The RCELL subroutine contains the shading and blocking model, the time integrals, and the optimum-finding procedure. Loop 3 can be recycled to converge the input figure of merit to the output figure of merit. This is required in order to get a reasonable estimate of system size (see section 5g).

Table 1.4.1 Data Flow Schematic For Initial Receiver Run

The dot precedes a program or subroutine. Data are enclosed by parentheses. The PANEL data file is generated by the scheme.

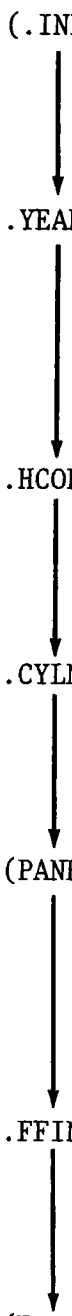

(.INPUTF) Input Program: contains heliostat design, etc.

.YEAR Main Program: includes insolation model, all basic unit vectors, cosine of incidence angle and shading and blocking.

.HCOEF Image Generator: includes solar limb darkening and guidance error model.

.CYLN Receiver Program: implements geometry of the receiver.

(PANEL) Output Data File: contains the panel interception factors for each cell in the heliostat field which can be input to RCELL.

.FFINT Linear Regression Analysis Program: provides for fitting matrix of interception fractions.

(FCOFS) Output Data File: contains coefficients from fit on interception fractions, which can replace PANEL file input to RCELL.

Table 1.4.2 Data Flow Schematic for Optimization Procedure

The RCELL linkage can be interated as often as required for optimizations.

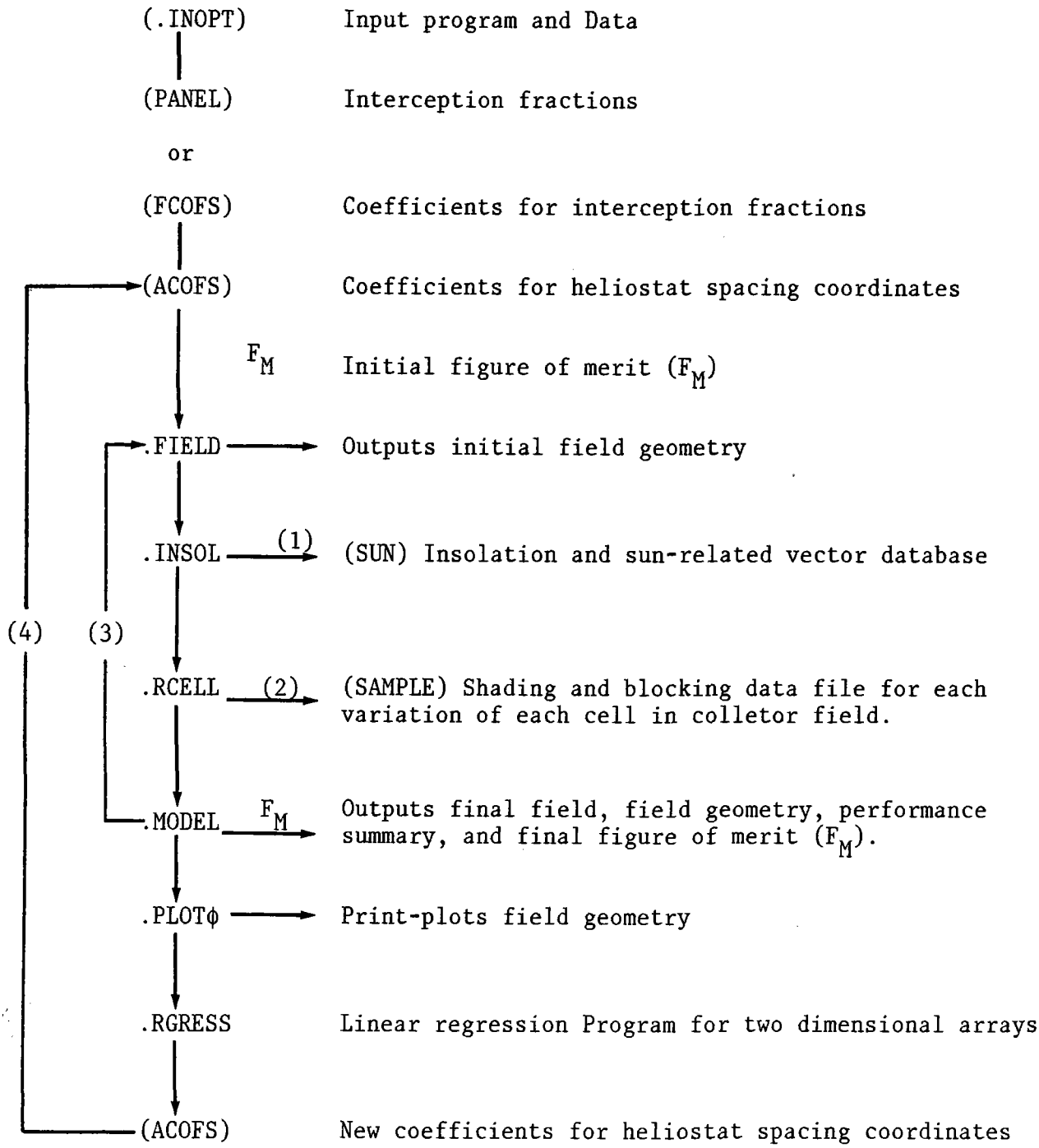

Steps 1 to 4 are described in the text.

The various input/output options and alternative iteration loops shown in table 1.4.2 are handled as follows:

(1.) An optional I/O arrangement which can save CPU time if it is utilized.

(2.) An optional I/O arrangement which must be used to save CPU time when converging the figure of merit or making changes in any parameter that does not enter into the SAMPLE data file.

(3.) Iteration to converge input figure of merit to equal the output figure of merit. Convergence rate is roughly one decade/ cycle.

(4.) Iteration to converge final collector field geometry. This cycle is not needed if all cells in the collector field contain optimized solutions within the domain of the variations, and if the scale of variation is 1/10 or less.

The figure of merit converges by roughly one decade/cycle and the convergence runs reuse the SAMPLE data so that only 30 seconds of CPU are required per cycle. LOOP 4 is needed for initiating studies of new configurations in which the input ACOFS data are far from satisfactory. At the point of closng loop 4, both the interception data and the heliostat spacing data are or can be in the form of coefficients for polynomial fits to the original data. Consequently, the cell size and the array size can be modified to meet the developing needs of the study with a minimum of inconvenience. For example, a small array of very large cells may be used to determine preliminary values for the ACOFS with much less investment in CPU time.

Earlier versions of RCELL required an input for the initial heliostat spacing coordinates. The output file could be edited to remove bad solutions. i.e., cells in which the optimizer locates the wrong branch of a curve or a local extreamum. The concept of bad solutions implies a fitting procedure, which, if implemented, generates the coefficients represented by ACOFS. Hence, we have restyled the program to input and output coefficients for the heliostat spacing coordinates. This provides us with a more robust optimizer in which an occasional bad solution is generally corrected by the fitting procedures. An excess of bad solutions near the tower can destroy the utility of the coefficients by distorting the fit for small slant ranges. If this happens, it is necessary to restart the solutions with a larger variation step size.

PLOTϕ provides a variety of alternative fits on the heliostat spacing coordinates. The best fitting set of coefficients can be input to RCELL in order to produce the most robust optimization procedure. On the other hand, the actual layout procedure is usually restricted to circles of heliostats. In keeping with the current concept of heliostat field layout, the fit on the radial spacing coordinate should not include azimuthal terms when used for layout purposes. If it should appear essential at some time to represent an azimuthal variation of the radial spacing, we would be tempted either to use a sector model or to search for an epicenter near the tower that would preserve the concentric circles. Such drastic action is not indicated by our present results for cylindrical receivers.

The RCELL program can be applied to any central receiver system currently under consideration via a reasonable variation of the inputs described here. In the near future, we anticipate increasing the output capabilities of RCELL to include flux density on the receiver at equinox noon

for the optimized system. It would be impractical to require annual summary output from RCELL. If desired, these results can be obtained from the YEAR program using ACOFS to generate heliostat spacing information representative of the optimized system.

The RCELL program has two serious limitations. First, it does not provide completely general variations of the local collector field in the vicinity of a representative heliostat. Having selected a specific configuration such as the radial stagger neighborhoods, we have two variables/representative instead of four. Second, if we assume circular fields in each cell, as implied, the optimum radial stagger neighborhoods in adjacent cells will not mate at the common cell boundary so that the heliostats on the boundary will be misrepresented. On the other hand, if we attempt to blend the cells across the boundaries, then the neighborhood of the representative will no longer be exactly radial stagger and, again, the situation will be misrepresented by the computer model. Clearly, constraints at the cell boundary are being ignored; this makes it possible to define an optimum in each cell which depends on the cell matching parameter but not on neighboring cells. Consequently, circular layouts using our ACOFS coefficients generate a system having a few less heliostats than were predicted by RCELL. This can be corrected in layout applications. But it also suggests the need for further theoretical work on the optimization.

1.5 RESULTS

1.5a The Baseline System and Optimization

The baseline system for our current parametric study closely resembles the 1977 MDAC 100 MW_e water/steam design with an external cylindrical receiver. Varied for the parametric study, the parameters were given the following values for the baseline case:

1) Slope of field = 0°
2) Latitude of Site = 35°N
3) Cost of Heliostats =101.25 $/m^2$
   (Second cost option in Performance Summary)
4) Cost of Land = 1.08 $/m^2$
5) Focal Height, H = 264 m

The optimum system for this case gives 722 MW_t at the base of the tower at equinox noon assuming 950 W/m^2 for the insolation. This is somewhat large for the DOE system, but our choice of 264 m focal height was based on an earlier cost model and a somewhat elementary optimization. The following performance summary Table 1.5a.1 contains the most useful data. ($M=10^6$)

Table 1.5a.1 Baseline System
PERFORMANCE SUMMARY AND COST BREAKDOWN

EQNOON POWER	=	722.043			IN MW - (SCALED TO 950 W/m^2)
ANNUAL POWER	=	1.775			IN MMWH
FIXED COSTS	=	4.970			IN $M
TOWER COST	=	9.480			IN $M
RECEIVER COST	=	19.069			IN $M for 950. EQUINOON POWER
LAND COST	=	6.153			IN $M
WIRING COST	=	4.695			IN $M
HELIOSTAT COST	=	108.657	· 135.821	· 162.986	IN $M
TOTAL COST	=	153.022	· 180.187	· 207.351	IN $M
FIGURE OF MERIT	=	86.216	· 101.521	· 116.826	IN $/MWH
		1st	· 2nd	· 3rd	Heliostat cost option
		81.00	· 101.25	· 121.50	Heliostat cost in $/m^2$

The boxed-in data in table 1.5a.1 represents a system optimized for the second heliostat cost option. The alternative heliostat cost options are output but do not represent the corresponding optimizations.

Table 1.5a.2 represents the number of heliostats per cell for the optimized baseline system as seen in a 14 x 8 array, which is standard for all results reported here. This array represents the eastern half of the field, with the tower in cell (0.0). Column 0 records the heliostats in half cells.

Table 1.5a.2 Number of Heliostats Cell for Baseline System

CELL	0	1	2	3	4	5	6	7
-8	0.	0.	0.	0.	0.	0.	0.	0.
-7	117.8	173.7	82.6	0.	0.	0.	0.	0.
-6	220.1	431.9	404.6	278.8	82.9	0.	0.	0.
-5	269.1	522.7	492.2	451.8	399.9	84.1	0.	0.
-4	329.4	640.4	595.1	536.6	461.1	295.3	0.	0.
-3	417.0	804.8	722.5	626.1	526.3	438.3	90.1	0.
2	547.3	1034.9	878.3	708.3	581.2	481.9	193.6	0.
-1	438.8	1132.5	1015.9	792.2	634.7	508.4	200.6	0.
0	0.	859.9	1087.6	816.2	637.2	513.3	91.2	0.
10	445.9	1138.3	994.1	764.8	614.9	488.8	0.	0.
2	529.4	1040.9	843.9	670.4	549.9	220.2	0.	0.
3	391.3	752.6	663.7	555.9	337.0	0.	0.	0.
4	288.0	552.9	376.4	108.0	0.	0.	0.	0.
5	57.7	0.	0.	0.	0.	0.	0.	0.

The cell width is 0.866H, or 228.63 m, and the cell area is 52,272 m^2.

Figure 1.5a.1 shows the locations of the representative heliostat in each cell of the eastern half field and compares the 14 x 8 array with several alternatives used previously. The tower locations tend to shift with latitude as indicated (although table 1.5c.5 shows the actual configuration of the optimized fields). The 8 x 4 array with double size cells provides a useful first step in dealing with new situations.

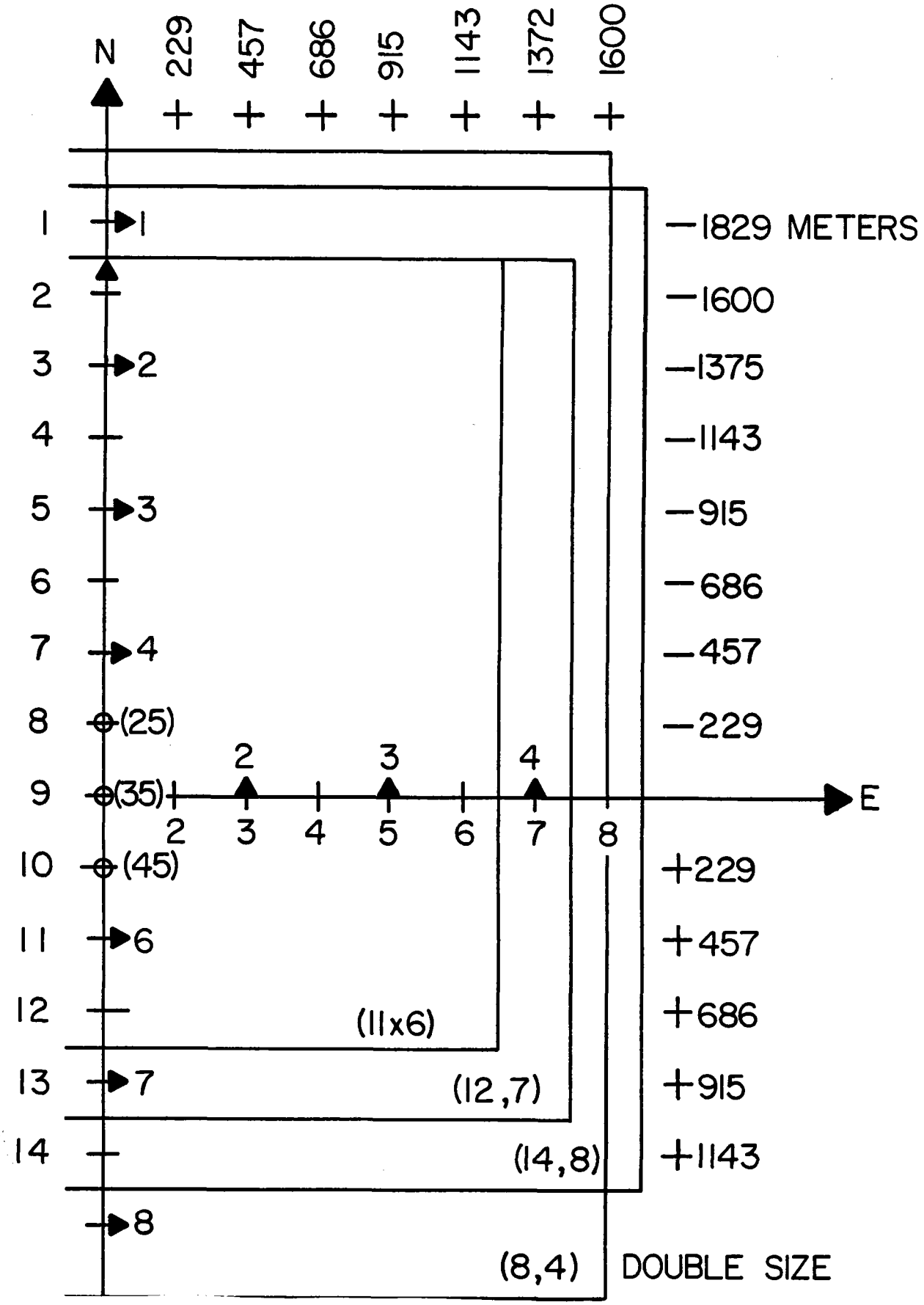

Figure 1.5a.1 Cell Structures for Eastern Half Field. This shows the region of collector field covered by various arrays. Horizontal and vertical cell counts refer to internal parameters. For output purposes, the subtower cell is (0,0). The cell center coordinates in meters refer to a tower height of 264 m.

The table of input data (1.5a.3) is complete, except for the weather data which is given in table 1.5b.4 of this section, and several cost scaling laws given in table 1.3.1.

Table 1.5a.3) RCELL Input Data for Baseline System.

PARAMETER ID = 14	FOR NUMBER OF COLUMNS - STEPS FROM NORTH
PARAMETER JD = 8	FOR NUMBER OF ROWS - STEPS TO EAST
JDVEQ = 2444320	JULIAN DAY OF VERNAL EQUINOX FOR MARCH 21,1980
XLAT = 35.	LATITUDE OF SITE IN DEGREES
EGRND = 0.0	SLOPE OF GROUND LEVEL IN DEGREES
ZGRND = 180.	AZIMUTH OF UPWARD SLOPE IN DEGREES
VR = 50.	VISUAL RANGE OF SITE IN KM
HS = 550.	ELEVATION OF SITE IN METERS
ESUNO = 10.0	ELEVATION OF SUN AT STARTUP IN DEGREES
NGON = 4	NUMBER OF SIDES FOR HELIOSTAT
NBOR = 8	NUMBER OF NEIGHBORS FOR HELIOSTAT
NTOW = 9	ROW NUMBER OF TOWER
IMAX = 19	NUMBER OF SAMPLE HOURS = 3,7,11 ...
JMAX = 7	NUMBER OF SAMPLE DAYS
IOPT = 2	HELIO COST OPTION
KORY = 1	EQUALS 1 FOR RADIAL , 2 FOR N-S ORIENTATION
LRAY = 2	EQUALS 1 FOR CORNFIELD 2 FOR STAGGERED ARRAY
NGEO = 4	NUMBER OF CELLS IN DISPLACEMENT ARRAY
NDIV = 10	NUMBER OF DIVISIONS FOR INTERPOLATOR
IAXIS = 1	INDEX OF MOUNTING SYSTEM, 1 FOR ALT-AZ
ISUN = 1	EQUALS 0 FOR UNIFORM WTS , 1 FOR SINE WTS
DMIR = 6.502413	WIDTH OF HELIOSTAT IN METERS
DMECH = 1.4844	MECHANICAL LIMIT IN DMIR UNITS
HGLASS = 37.226397	AREA OF GLASS/HELIOS IN m^2 (400.7 SQ. FT)
DGEO = 1./20	CELL SPACING FOR LOSS PRINTS
DTRIM = .090	TRIM CONSTANT FOR INTERPOLATION
REARTH = 6370.	RADIUS OF EARTH IN KILOMETERS
HATMOS = 8.430	HEIGHT OF ATMOSPHERE IN KILOMETERS

Table 1.5a.3 (concluded)

```
     CONTAINS CONSTANTS FOR COST MODEL ( 100 MWe)
CFIXD  =  4.970E6   FIXED COST IN $-INDEPENDENT OF TOWER HEIGHT
CHL(1) =    81.00   HELIO COST IN $/m2 FIRST OPT  NO SENSOR
CHL(2) =   101.25   HELIO COST IN $/m2 SECOND OPT  NO SENSOR
CHL(3) =   121.50   HELIO COST IN $/m2 THIRD OPT  NO SENSOR
CL     =     1.08   COST OF LAND IN $/m2
CW     =     3.50   PRORATED COST OF WIRING IN $/m2
BOILER =     1.16   CONV&RAD.  LOSSES IN MW PER BOILER PANEL
HEATER =      .58   CONV&RAD.  LOSSES IN MW PER PREHEAT PANEL
HYEARS =   3397     HOURS/YEAR FOR SUN ABOVE 10 DEG. AT LAT. 35
PREPAN =      2     HALF NUMBER OF PREHEAT PANELS IN PANPOW
KPANL  =      1     EQUALS FIRST PANEL FOR FINT
ABSOR  =  .95*.98   ABSORBTIVITY AND PERCENT ACTIVE HELIOSTATS
REFLT  =  .94*.97   REFLECTIVITY AND DUST
SNSHAD =   1.0      SENSOR SHADOW 1.0 OR .98
FRLOS  =  ABSOR*REFLT*SNSHAD
     COEFFICIENTS FOR COLLECTOR FIELD (35 DEG. LAT.)
COEFX1 =  63.45     FIRST RADIAL COEFFICIENT
COEFX2 =   -.6130   SECOND RADIAL COEFFICIENT
COEFX3 =    .02072  THIRD RADIAL COEFFICIENT
COEFY4 =   1.6748   FIRST AZIMUTHAL COOEFFICIENT
COEFY5 =   2.0823   SECOND AZIMUTHAL COOEFFICIENT
COEFY6 =   -.02016  THIRD AZIMUTHAL COOEFFICIENT
FMI    = 101.80     INITIAL FIGURE OF MERIT ($/MWH)

For reference, we also include a few definitions:
OPSOL  = (CW + CHL(IOPT))/FMI
     IN MWH/m2 for cell matching (here IOPT=2)
     NUMBER OF OPERATING RECEIVER PANELS
TOTPAN =   24 - 2* (KPANL-1)
EQLOSS = BOILER * (TOTPAN - 2*PREPAN) + HEATER * (2*PREPAN)
     MW OF LOSS AT EQUINOX NOON
ATLOSS = HYEARS * EQLOSS          MWH/year of LOSS
```

The matrix of interception fractions for the right half of the syMmetric field is shown in Table 1.5a.4. The matrix is equipped with horizontal and vertical averages, as shown in the set-off column and row. The figure to the right of the matrix is a contour print of the matrix showing contours of tenths, as indicated. The dots correspond to node centers in the collector field. The "T" locates the tower. North is the up direction and East is to the right on the page. This is the standard output format for field related matrices.

Interception fractions depend on the receiver model. The MDAC receiver is a cylinder 25.5 m long and 17 m in diameter, so that its total area is 1361.88 m^2. An optimized Hi-Low aiming strategy is used, which means that the population of each cell is split into two groups. One group aims high and the other low by the maximum amount compatible with the image size and the aspect of the cylinder.

In this strategy, aim points of alternate heliostats are adjusted upward or downward to the edge of the receiver. For flat heliostats the beam diameter is approximated by the root sum square of the heliostat width, the projected sun size, and the projected beam dispersion at the two sigma point. This aim strategy gives a sharper fall off in flux near the edge of the receiver and a less peaked distribution than one in which the heliostat aim points are uniformly moved a fixed number of meters up or down, and has less impact on the interception fractions because the larger beams from more distant heliostats are shifted less or not at all. This type of aiming strategy reduces the peak flux density as much as is possible in each case. The radiative, convective, and conductive losses for this receiver producing ~500°C superheated steam have been estimated by MDAC. Their estimates are represented by the input variables BOILER and HEATER, which correspond to 20.44 kW/m^2 and 11.22 kW/m^2 respectively for boiler and preheat panels.

Table 1.5a.4 Interception Fraction Matrix for Baseline Case Including Visual Range Effect

INTERCEPTION FACTORS FROM (LVH) RECIEVER PROGRAM ********** UNIVERSITY OF HOUSTON AND ERDA

0.537	0.532	0.518	0.495	0.465	0.429	0.389	0.345	0.
0.615	0.610	0.593	0.567	0.532	0.490	0.444	0.395	0.608
0.695	0.689	0.670	0.639	0.599	0.551	0.499	0.444	0.669
0.773	0.766	0.744	0.709	0.664	0.610	0.551	0.490	0.726
0.845	0.837	0.813	0.774	0.724	0.664	0.599	0.531	0.785
0.903	0.895	0.870	0.830	0.775	0.710	0.640	0.566	0.834
0.943	0.936	0.913	0.872	0.815	0.746	0.671	0.594	0.874
0.959	0.957	0.937	0.898	0.840	0.769	0.691	0.611	0.896
0.963	0.963	0.946	0.907	0.850	0.778	0.699	0.617	0.899
0.966	0.961	0.940	0.901	0.843	0.771	0.692	0.611	0.909
0.949	0.942	0.918	0.877	0.819	0.749	0.673	0.594	0.898
0.911	0.903	0.878	0.837	0.781	0.714	0.641	0.566	0.869
0.854	0.846	0.821	0.781	0.729	0.667	0.600	0.530	0.835
0.782	0.774	0.752	0.715	0.667	0.611	0.550	0.486	0.782
0.890	0.898	0.881	0.845	0.795	0.743	0.678	0.	0.854

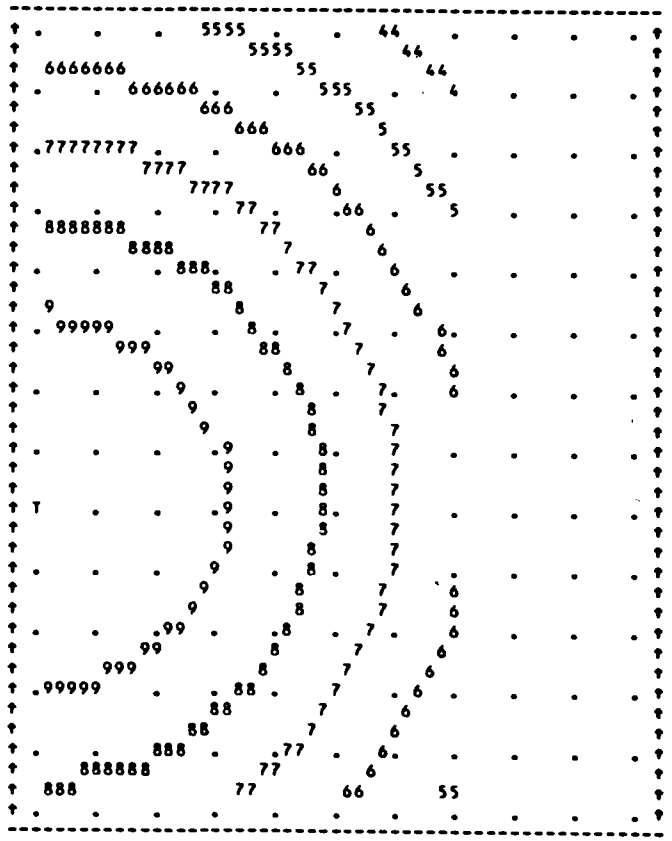

CONTUR INTERVAL = 0.100

The matrix of interception fractions shown above includes visual range effects (i.e., losses in transmission from the heliostat to the receiver) as well as flux spillage past the receiver, but not the thermal loses mentioned above.

The matrix of Lagrangian parameters shown in table 1.5a.5 gives the required performance level in $\$/aMWH_t$ for economically matched cells. These numbers are given by dividing OPSOL by the interception fractions for the particular cell.

The matrix of cell brightness in $aMWH_t/m^2$ is shown in table 1.5a.6. These numbers represent an integration over one year of reflected sunlight, ignoring all losses except cosine effects, shading, blocking, and weather.

The matrix of cell brightness in kW_t/m^2 at equinox noon, as shown in table 1.5a.7, represents one contribution to the integral over the year as mentioned above. At other hours the cell brightness is not symmetric.

The matrix of Loss fractions shown in table 1.5a.8 gives the fraction of loss due to shading and blocking. These fractions go to zero at or near the outer boundary of the field. Beyond the outer boundary, losses due to cosine and interception effects are so large that even with zero shading and blocking the performance does not reach the required level, and the cell is placed outside the trim line.

The matrix of ground coverage fractions shown in table 1.5a.9 represents the area of glass in a particular cell. Hence, the number of heliostats is proportional to the ground coverage, if we assume all heliostats are the same size.

The matrix of shape parameters shown in table 1.5a.10 represents the shape of the neighborhood in each particular cell. The numbers shown are given by the formula

Table 1.5a.5 Matrix of Lagrangian Variables for Baseline Case

LAGRANGIAN PARAMETERS FOR OPTIMIZAION **********

2.259	2.279	2.341	2.449	2.607	2.826	3.120	3.511	0.
1.970	1.988	2.044	2.139	2.280	2.473	2.730	3.069	1.995
1.743	..760	1.810	1.897	2.025	2.199	2.430	2.733	1.814
1.567	1.583	1.629	1.709	1.826	1.987	2.199	2.476	1.676
1.435	1.449	1.492	1.566	1.675	1.825	2.024	2.282	1.554
1.342	1.354	1.393	1.461	1.564	1.706	1.895	2.140	1.465
1.286	1.296	1.328	1.390	1.485	1.624	1.806	2.042	1.399
1.264	1.267	1.293	1.350	1.443	1.575	1.753	1.985	1.364
2.865	1.258	1.281	1.336	1.427	1.558	1.735	1.966	1.357
1.255	1.262	1.289	1.346	1.439	1.572	1.751	1.984	1.340
1.278	1.287	1.320	1.382	1.480	1.617	1.802	2.041	1.356
1.330	1.342	1.380	1.449	1.553	1.698	1.890	2.141	1.398
1.419	1.433	1.476	1.551	1.663	1.817	2.021	2.288	1.452
1.550	1.565	1.613	1.695	1.816	1.982	2.203	2.493	1.550
1.378	1.363	1.390	1.447	1.535	1.637	1.790	0.	1.438

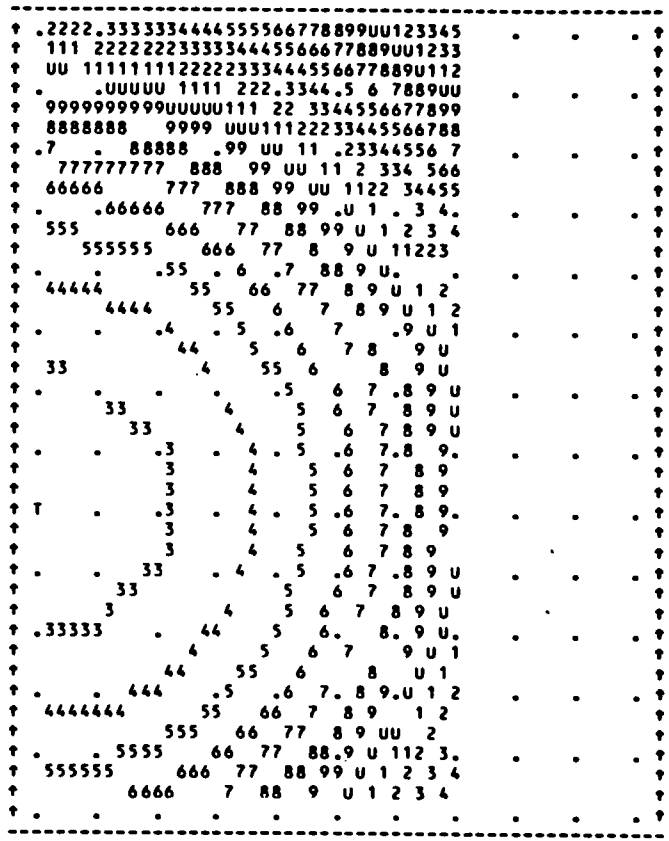

CONTUR INTERVAL = 0.100

Table 1.5a.6 Annual Power Matrix for Baseline Case

TOTAL ENERGY IN MWH/M2 FOR OPTIMUM SPACINGS

2.185	2.178	2.166	2.156	2.143	2.122	2.099	2.078	0.
2.184	2.169	2.161	2.159	2.139	2.113	2.088	2.066	2.172
2.156	2.150	2.147	2.137	2.120	2.100	2.075	2.052	2.146
2.153	2.145	2.126	2.105	2.087	2.079	2.059	2.035	2.121
2.154	2.135	2.110	2.079	2.061	2.044	2.037	2.009	2.100
2.125	2.121	2.097	2.052	2.026	2.007	1.992	1.974	2.074
2.094	2.093	2.046	2.011	1.977	1.950	1.942	1.933	2.033
2.072	2.024	1.983	1.935	1.897	1.886	1.890	1.888	1.967
2.195	1.934	1.882	1.856	1.843	1.834	1.842	1.838	1.875
1.894	1.841	1.779	1.782	1.783	1.789	1.795	1.791	1.808
1.740	1.696	1.695	1.714	1.724	1.740	1.748	1.747	1.711
1.659	1.647	1.648	1.657	1.678	1.690	1.699	1.704	1.655
1.610	1.613	1.622	1.627	1.635	1.643	1.656	1.665	1.616
1.573	1.576	1.584	1.596	1.600	1.610	1.620	1.631	1.573
1.958	1.939	1.916	1.906	1.899	1.899	1.916	0.	1.921

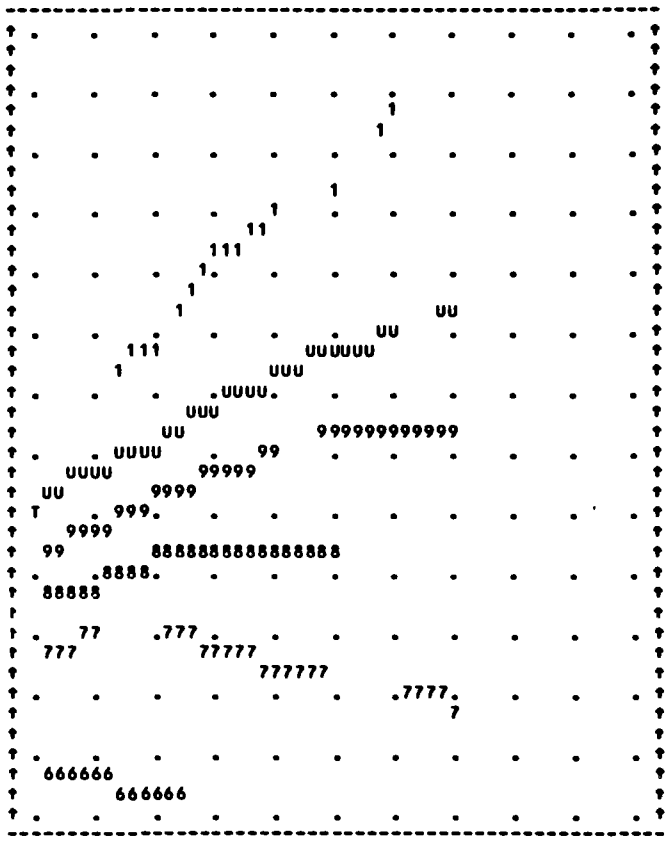

CONTUR INTERVAL = 0.100

Table 1.5a.7 Equinox Noon Power Matrix for Baseline Case

EQNOON POWER IN KW/M2 FOR OPTIMUM SPACINGS

0.735	0.734	0.731	0.726	0.719	0.712	0.705	0.697	0.
0.734	0.735	0.732	0.727	0.719	0.710	0.701	0.693	0.734
0.733	0.732	0.730	0.724	0.716	0.707	0.697	0.687	0.729
0.736	0.735	0.727	0.717	0.709	0.701	0.690	0.680	0.724
0.748	0.740	0.726	0.710	0.699	0.689	0.681	0.670	0.720
0.763	0.748	0.726	0.703	0.686	0.674	0.666	0.658	0.718
0.775	0.756	0.721	0.693	0.670	0.654	0.647	0.642	0.714
0.798	0.753	0.704	0.668	0.644	0.631	0.626	0.623	0.699
0.762	0.702	0.656	0.628	0.613	0.605	0.607	0.602	0.646
0.629	0.619	0.598	0.581	0.574	0.576	0.580	0.579	0.598
0.534	0.541	0.539	0.538	0.541	0.548	0.555	0.557	0.539
0.492	0.493	0.499	0.505	0.516	0.525	0.530	0.535	0.500
0.463	0.466	0.473	0.482	0.492	0.500	0.509	0.515	0.469
0.445	0.448	0.454	0.463	0.472	0.481	0.490	0.497	0.445
0.666	0.665	0.649	0.637	0.630	0.629	0.636	0.	0.648

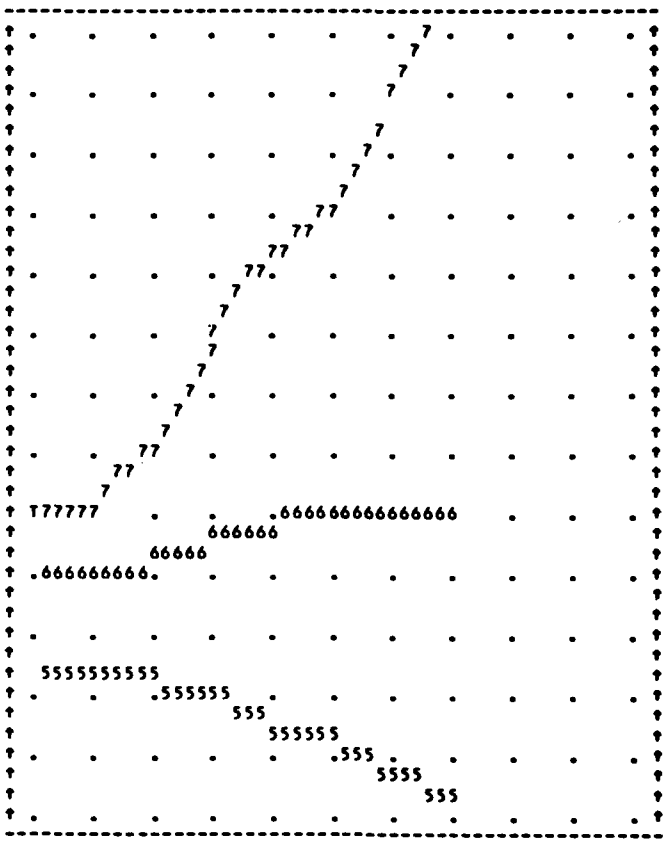

CONTUR INTERVAL = 0.100

Table 1.5a.8 Fraction of Energy Loss Matrix for Baseline Case with Optimum Spacing

FRACTION OF ENERGY LOST FOR OPTIMUM SPACINGS

0.008	0.009	0.010	0.008	0.006	0.006	0.006	0.005	0.
0.011	0.015	0.013	0.007	0.006	0.006	0.006	0.005	0.014
0.026	0.026	0.021	0.015	0.010	0.007	0.005	0.004	0.021
0.033	0.033	0.031	0.026	0.019	0.009	0.004	0.002	0.028
0.041	0.043	0.039	0.034	0.023	0.013	0.002	0.001	0.034
0.064	0.056	0.044	0.037	0.026	0.015	0.006	0.001	0.041
0.093	0.076	0.060	0.041	0.028	0.020	0.009	0.001	0.054
0.124	0.106	0.067	0.047	0.036	0.023	0.009	0.001	0.067
0.054	0.103	0.066	0.043	0.029	0.019	0.007	0.002	0.056
0.053	0.054	0.051	0.032	0.021	0.011	0.003	0.001	0.040
0.031	0.043	0.036	0.023	0.015	0.006	0.001	0.000	0.030
0.019	0.023	0.022	0.017	0.009	0.005	0.002	0.001	0.019
0.014	0.013	0.010	0.009	0.008	0.006	0.004	0.002	0.012
0.012	0.012	0.010	0.007	0.008	0.006	0.005	0.003	0.012
0.053	0.058	0.046	0.033	0.024	0.016	0.008	0.	0.041

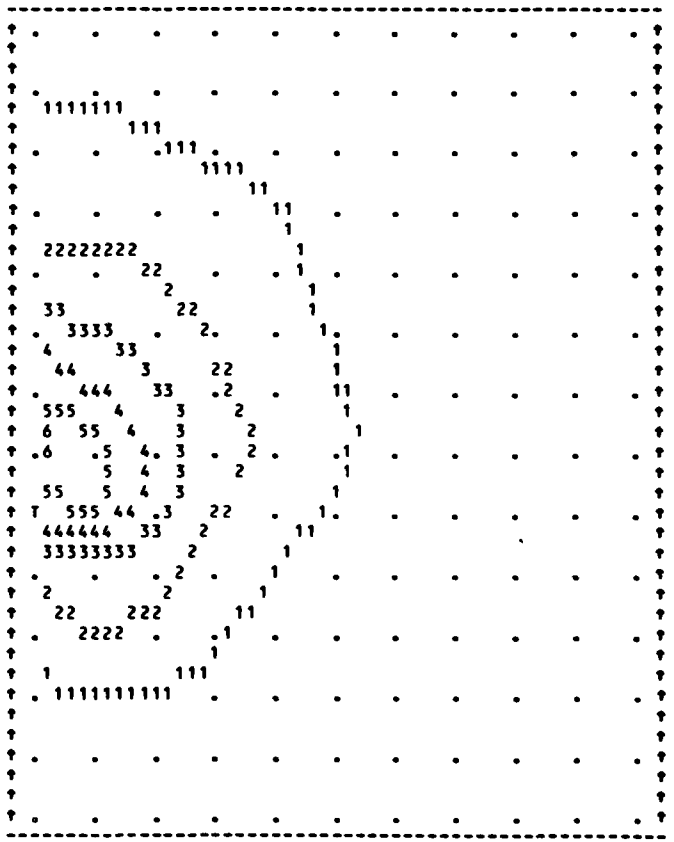

CONTUR INTERVAL = 0.020

Table 1.5a.9 Fraction of Ground Coverage Matrix for Baseline Case

FRACTION OF GROUND COVERED

0.100	0.099	0.097	0.093	0.088	0.082	0.077	0.072	0.
0.112	0.124	0.118	0.105	0.098	0.091	0.085	0.078	1.000
0.157	0.154	0.144	0.132	0.118	0.102	0.093	0.085	1.000
0.192	0.186	0.175	0.161	0.142	0.120	0.102	0.091	1.000
0.235	0.228	0.212	0.191	0.164	0.140	0.110	0.097	1.000
0.297	0.287	0.257	0.223	0.187	0.156	0.128	0.104	1.000
0.390	0.369	0.313	0.252	0.207	0.172	0.138	0.108	1.000
0.417	0.403	0.362	0.282	0.226	0.181	0.143	0.109	1.000
0.383	0.408	0.387	0.291	0.227	0.183	0.130	0.112	1.000
0.423	0.405	0.354	0.272	0.219	0.174	0.136	0.112	1.000
0.377	0.371	0.301	0.239	0.196	0.157	0.125	0.108	1.000
0.279	0.268	0.236	0.198	0.160	0.134	0.118	0.103	1.000
0.205	0.197	0.179	0.154	0.134	0.124	0.110	0.097	1.000
0.164	0.158	0.148	0.134	0.123	0.111	0.101	0.091	1.000
1.000	1.000	1.000	1.000	1.000	1.000	1.000	0.	0.235

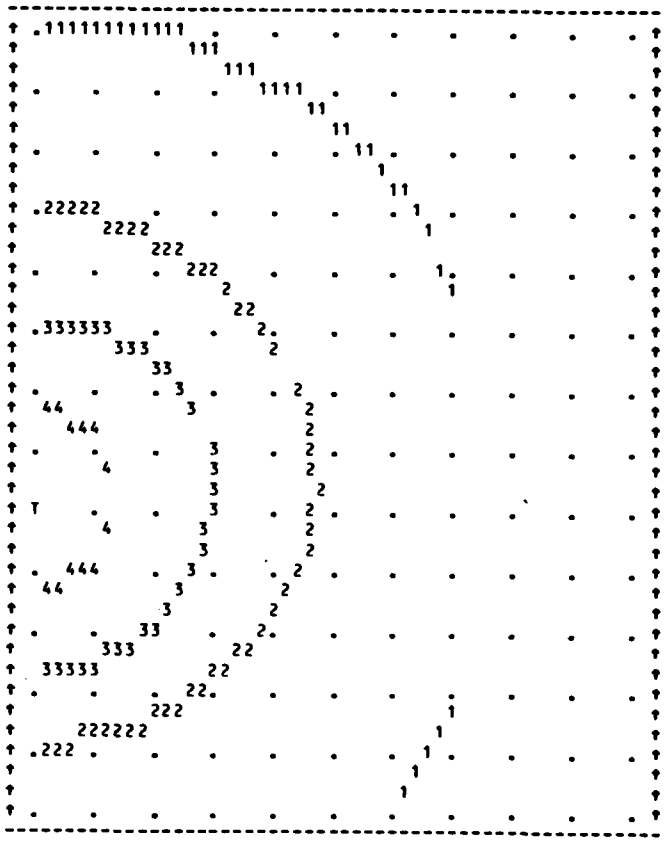

CONTUR INTERVAL = 0.100

Table 1.5a.10 Orthogonal Coordinate Matrix (X10) for Baseline Case

(T/10.) = ORTHOGONAL COORDINATE

2.348	2.384	2.512	2.711	3.022	3.397	3.846	4.373	0.
1.656	1.762	1.905	2.133	2.436	2.794	3.227	3.756	1.761
1.168	1.217	1.361	1.579	1.896	2.258	2.697	3.210	1.361
0.755	0.909	0.924	1.108	1.392	1.804	2.248	2.776	1.032
0.443	0.479	0.577	0.761	1.035	1.405	1.905	2.448	0.734
0.187	0.219	0.323	0.508	0.774	1.126	1.612	2.202	0.511
-0.022	0.031	0.145	0.330	0.594	0.944	1.429	2.045	0.329
-0.125	-0.060	0.011	0.207	0.473	0.840	1.333	1.983	0.222
0.245	-0.090	-0.028	0.180	0.452	0.800	1.222	1.853	0.212
-0.157	-0.125	0.022	0.238	0.499	0.846	1.313	1.858	0.160
0.104	0.109	0.139	0.329	0.602	0.990	1.471	1.991	0.274
0.152	0.226	0.341	0.532	0.830	1.183	1.639	2.165	0.382
0.379	0.450	0.613	0.868	1.160	1.440	1.881	2.413	0.515
0.702	0.777	0.903	1.145	1.409	1.775	2.225	2.772	0.702
0.249	0.222	0.299	0.476	0.715	0.985	1.391	0.	0.436

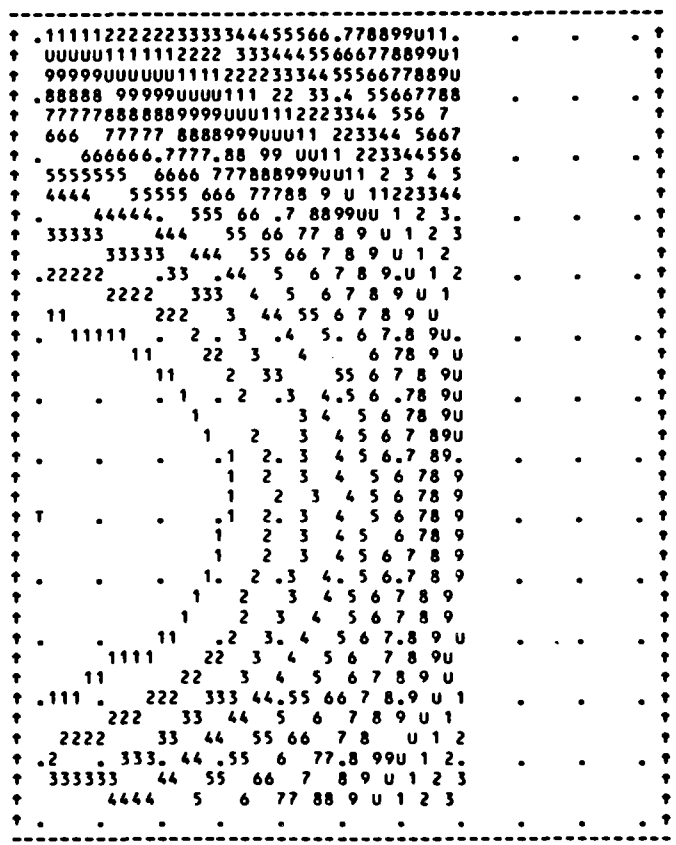

CONTUR INTERVAL = 2.000

$$T_1 = (X^2-Y^2)/20,$$

where X is the radial spacing coordinate, Y is the azimuthal spacing coordinate, and T_1 is 1/10 of the standard orthogonal variable for convenience of output. Notice that $T_1 = 0$ if X = Y, so that the neighborhoods become square. This occurs as we approach the base of the tower and shading becomes more important than blocking.

The matrix of radial spacing coordinates in units of heliostat width is shown in table 1.5a.11, and the matrix of azimuthal spacing coordinates in units of heliostat width shown in table 1.5a.12. The contours of radial spacing are nearly circular and concentric with the tower. On the other hand, the contours of azimuthal spacing are more irregular but the azimuthal spacing coordinates are nearly constant (i.e. ~2.0 heliostat widths). This situation suggests the possibility of reducing the X and Y matrices to a small number of coefficients by means of some appropriate fitting procedure. This has been acheived, and the resulting coefficents are given in table 1.5a.3 under the heading COEFFICIENTS FOR COLLECTOR FIELD. We are using the formulas (* = multiply)

$$X = COEFX1 * 1/\Theta + COEFX2 + COEFX3 * \Theta$$

and

$$\tan (Y/X) = Z = COEFY1 + COEFY2 * \Theta + COEFY3 * \Theta^2$$

where

$$\tan \Theta = H_T/(X_c^2 + Y_c^2)^{\frac{1}{2}}.$$

Table 1.5a.11 Radial Spacing Coordinate Matrix for Baseline Case

X = FIRST SPACING PARAMETER IN UNITS OF DMIR

7.268	7.318	7.494	7.759	8.156	8.610	9.123	9.691	0.
6.279	6.346	6.579	6.960	7.390	7.866	8.407	9.023	6.376
5.280	5.373	5.648	6.036	6.563	7.139	7.740	8.387	5.637
4.409	4.531	4.784	5.163	5.705	6.427	7.126	7.850	4.984
3.627	3.725	3.986	4.422	5.026	5.735	6.625	7.413	4.316
2.844	2.952	3.287	3.903	4.463	5.216	6.106	7.058	3.725
2.075	2.257	2.694	3.319	4.040	4.836	5.784	6.827	3.161
1.777	1.952	2.231	2.940	3.720	4.611	5.612	6.739	2.841
2.768	1.972	2.068	2.849	3.675	4.530	5.520	6.543	2.835
1.697	1.809	2.280	3.045	3.802	4.654	5.619	6.552	2.704
2.414	2.443	2.721	3.372	4.105	4.986	5.925	6.755	3.044
2.831	3.034	3.406	3.960	4.699	5.436	6.210	7.013	3.495
3.629	3.909	4.212	4.801	5.398	5.883	6.597	7.373	3.965
4.453	4.420	4.892	5.375	5.849	6.448	7.109	7.846	4.453
2.919	2.829	3.092	3.659	4.295	4.915	5.733	0.	3.462

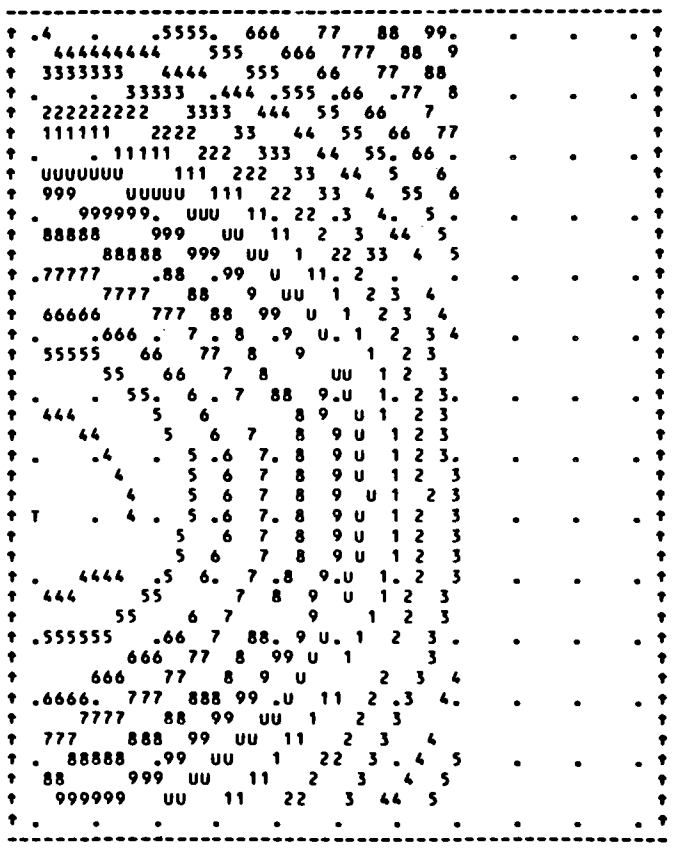

CONTUR INTERVAL = 0.500

Table 1.5a.12 Azimuthal Spacing Coordinate Matrix for Baseline Case

Y = SECOND SPACING PARAMETER IN UNITS OF DMIR

2.422	2.425	2.433	2.447	2.466	2.488	2.513	2.540	0.
2.508	2.243	2.275	2.403	2.425	2.450	2.478	2.509	2.333
2.127	2.131	2.164	2.204	2.271	2.413	2.444	2.478	2.162
2.084	2.088	2.100	2.120	2.167	2.287	2.413	2.473	2.118
2.070	2.073	2.085	2.084	2.134	2.190	2.406	2.448	2.099
2.084	2.081	2.082	2.077	2.105	2.163	2.248	2.403	2.099
2.177	2.117	2.090	2.103	2.106	2.122	2.208	2.387	2.120
2.378	2.237	2.182	2.123	2.094	2.109	2.197	2.399	2.185
1.663	2.304	2.199	2.126	2.112	2.127	2.456	2.396	2.190
2.451	2.402	2.182	2.123	2.115	2.174	2.307	2.399	2.245
1.935	1.944	2.153	2.188	2.191	2.252	2.385	2.410	2.084
2.232	2.165	2.188	2.246	2.342	2.426	2.404	2.426	2.219
2.365	2.348	2.340	2.385	2.439	2.411	2.429	2.470	2.352
2.406	2.411	2.425	2.448	2.455	2.467	2.458	2.473	2.406
2.202	2.179	2.158	2.139	2.143	2.156	2.250	0.	2.164

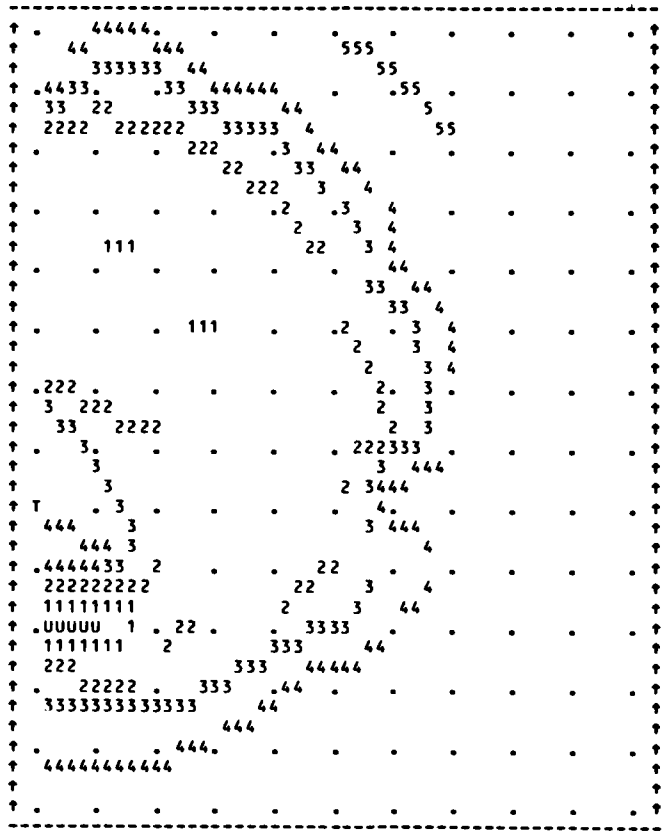

CONTUR INTERVAL = 0.100

H_T is the tower focal height and $(x_c, Y_c, -H_T)$ locates the cell center with respect to the center of the receiver, so that θ is the elevation angle for the receiver as seen from the cell center. The azimuthal spacing is obtained from Z:

$$Y = X * \tan^{-1}(Z).$$

The coefficients are obtained from the weighted least-squares fitting procedure, which weights according to the number of heliostats in the cell. Goodness of fit is the only justification required in the present case.

1.5b Results for Slope Study

In this section "slope" refers to the slope angle of a flat collector field which rises toward the north. These sloping fields are symmetric in the east-west direction and may shorten the effective length of summer days by producing an artificial horizon. The effective length of day in this study is limited to 10° above the astronomical horizon and 5° above the sloping plane, whichever is the more restrictive. Table 1.5b.1 shows that at 35° the 10° slope is non-restrictive; however, a small restriction occurs on days 93 and 124 if the slope is as large as 20°.

Table 1.5b.1 Total Direct Beam Comparison for Slope Study
(kWH/m^2/day and MWH/m^2/year)

Day of Year	93	124	155	186	216	246	276	Annual
0° Slope	9.452	8.974	8.384	7.345	6.367	5.383	4.687	2.609
10° Slope	9.452	8.974	8.384	7.345	6.367	5.383	4.687	2.609
20° Slope	9.263	8.888	8.384	7.345	6.367	5.383	4.687	2.598

For the external receiver, figure 1.5b.1 shows that the optimum slope is roughly 10° and the optimum is due to the amount of energy that can be collected rather than cost. We have assumed that land costs and heliostat

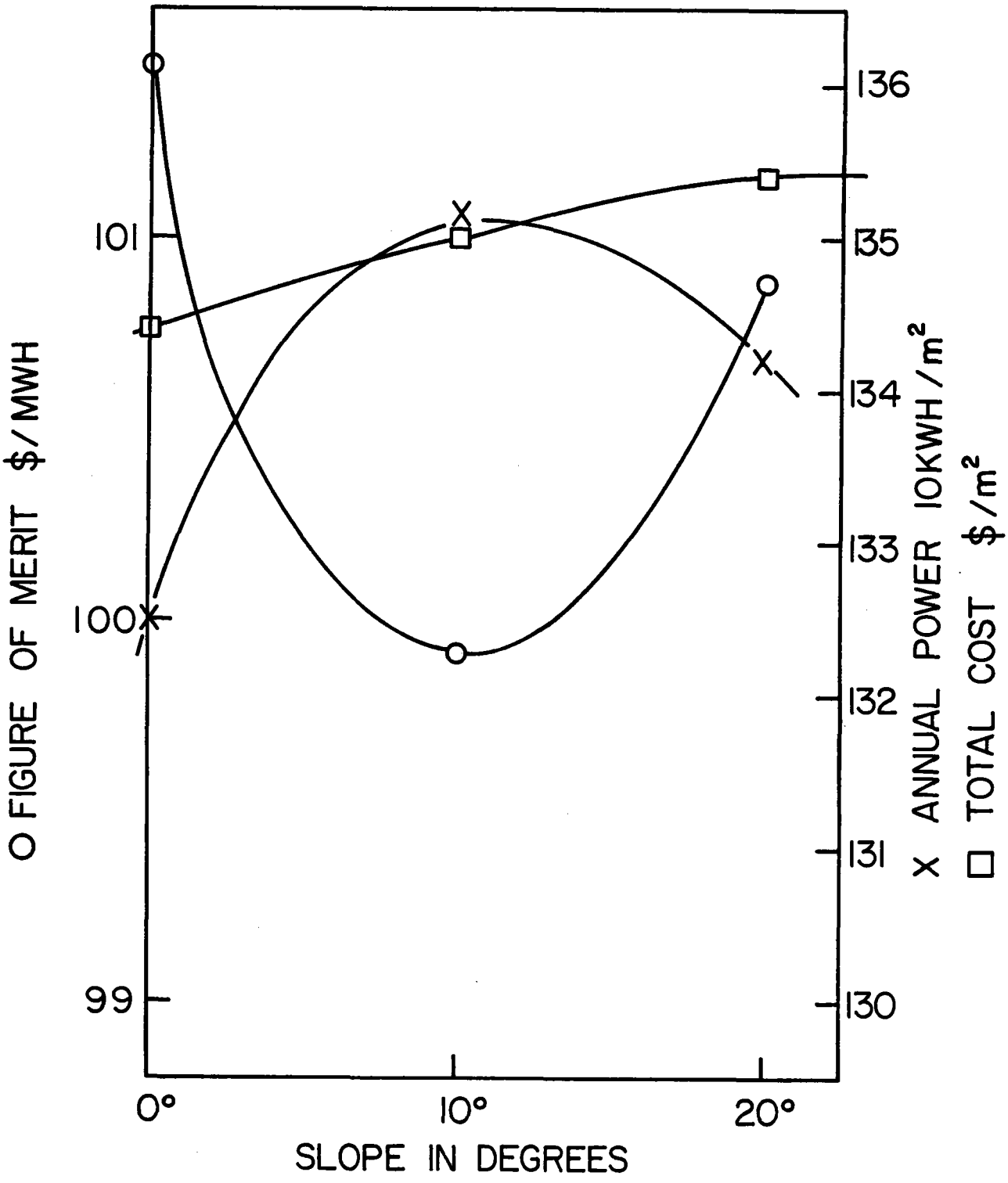

Figure 1.5b.1 Figure of Merit Versus Slope Angle. According to the figure of merit curve, the optimum slope is 10°, but see text for comments. The total cost in $/m^2 shows a gradual increase with slope; but the annual power/m^2 of glass shows a maximum at 10°.

installation costs are not specifically dependent on slope for small slope angles. This will not be true for slopes greater than 20°, and we feel that slopes greater than 20° should not be considered further for central receiver sites.

The 1.5 percent improvement in the figure of merit at 10° slope could be negated by a small increase in the cost of site preparation due to drainage or other sitework. However, it is more important to consider what a northern slope does to the collector field. Figure 1.5b.2 shows the meridian plane through a 25° sloping field. The sloping field is related to the level field by a rotation about the base of the tower at "b." The receiver is centered at "a" with focal height H above the level plane, but "a" has an effective height H' above the sloping plane through "ℓ" and "ℓ'." The point "c," which is the perpendicular projection of "a" onto this sloping field, becomes the center of the collector field for the sloping field. The distance $|bm| = |b\ell|$ but is greater than $|bn| = |c\ell|$. Heliostats at n and ℓ both see the receiver at a 20° elevation and, hence, will have similar blocking. Heliostats ℓ and m have the same slant range, but ℓ has an improved angle of incidence on the cylindrical receiver. For other locations in the collector field the comparison between level and sloping field will turn out somewhat differently.

Notice that the effective tower height for sloping fields is $H' < H$; consequently, to produce equal power the tower will be relatively more costly on sloping fields, in agreement with the decreasing number of heliostats reported in table 1.5b.2. Under optimized conditions, we do not expect any major reduction in blocking, due to slope. However, for sloping fields the shading losses are reduced for high suns and increased for low suns in summer. Since the low summer sun cut off does not occur for 10° slopes, it is

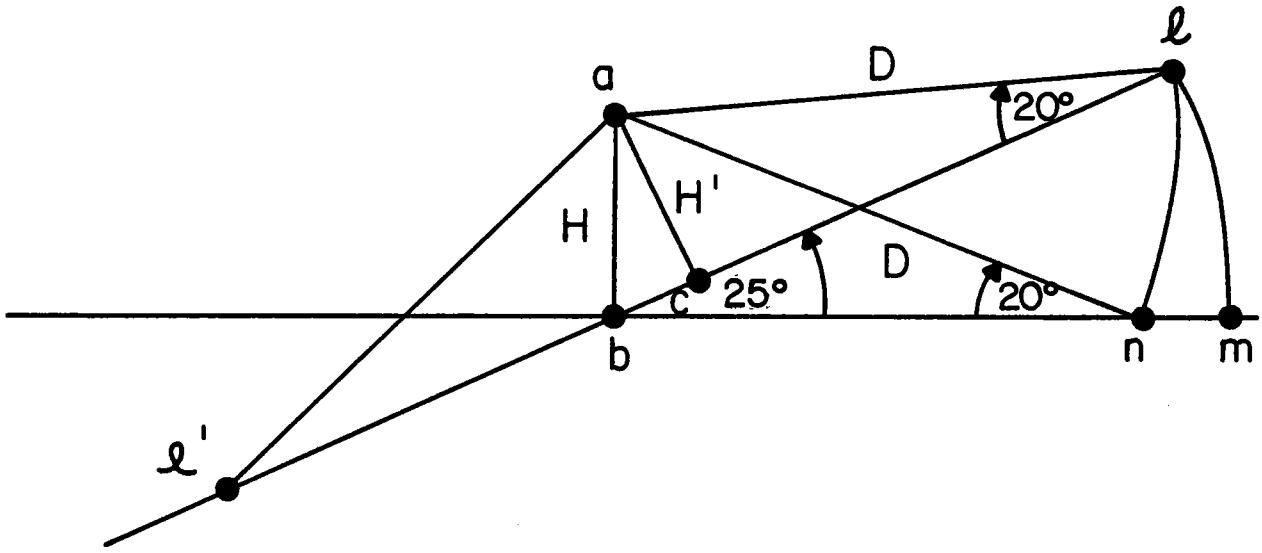

Figure 1.5b.2 Geometry of Sloping Field. The relationship between a sloping field and a level field is shown; H' is the effective tower height for the sloping field. The fact that H' < H for sloping fields is a handicap which may be overcome by reduced shading in some cases.

reasonable to expect a slight advantage for 10° slopes due to improved shading.

Figures 1.5b.(3-5) show the Total Energy contours for 0°, 10°, and 20° slopes. These results have reacted to the optimization process which reduces the shading advantage at 10° by compressing the field in order to maintain the effectiveness of the tower. As mentioned in Section 1-5a, these data include effects of cosine, shading, blocking and weather, but no other losses. (Note that the data reported here are not exactly comparable to the main body of this study. The figure of merit at 35° and 0° slope is about 0.07 percent low. This is due to a small change in the number of operational hours assigned and does not affect any comparisons made in the slope study).

The area of glass at 10° slope is 1.6 percent less than at 0° slope while the ground coverage remains unchanged. The peripheral cells eliminated had very low density, and the density in the interior cells has been increased somewhat, leading to slightly better average performance in this case.

In the 20° case, the total area of glass has decreased slightly more, but more glass is south of the tower due to an improvement in cosine for the southern field as slope increases. The net effect is a field of roughly the same size as a 10° slope, but the optimization process has reduced the density by 4 percent in order to compensate for worsened insolation at 20° slope.

A differential cost of $\$2.6 \times 10^6$ would cancel the advantage at 10° slope. This corresponds to an additional cost of about $1700 per acre or $4200 per hectare for preparing the sloping field and installing heliostats on it. The optimization results show in any case that slightly sloping fields need not be avoided.

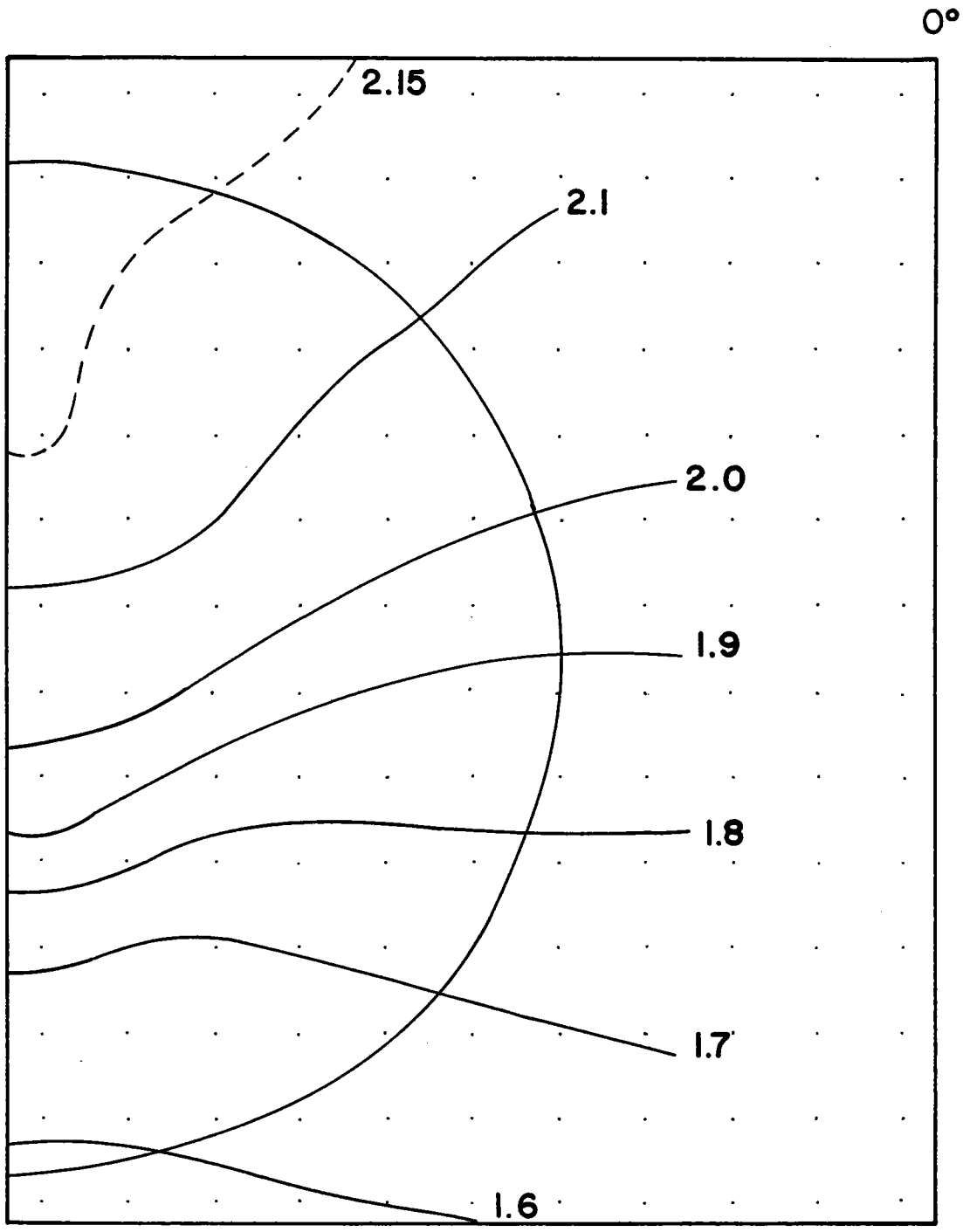

Figure 1.5b.3 Contours of Annual Power in $aMWH_t/m^2$ for 0° Slope. The "semicircle" represents the boundary of the right half-field and "T" shows the tower location.

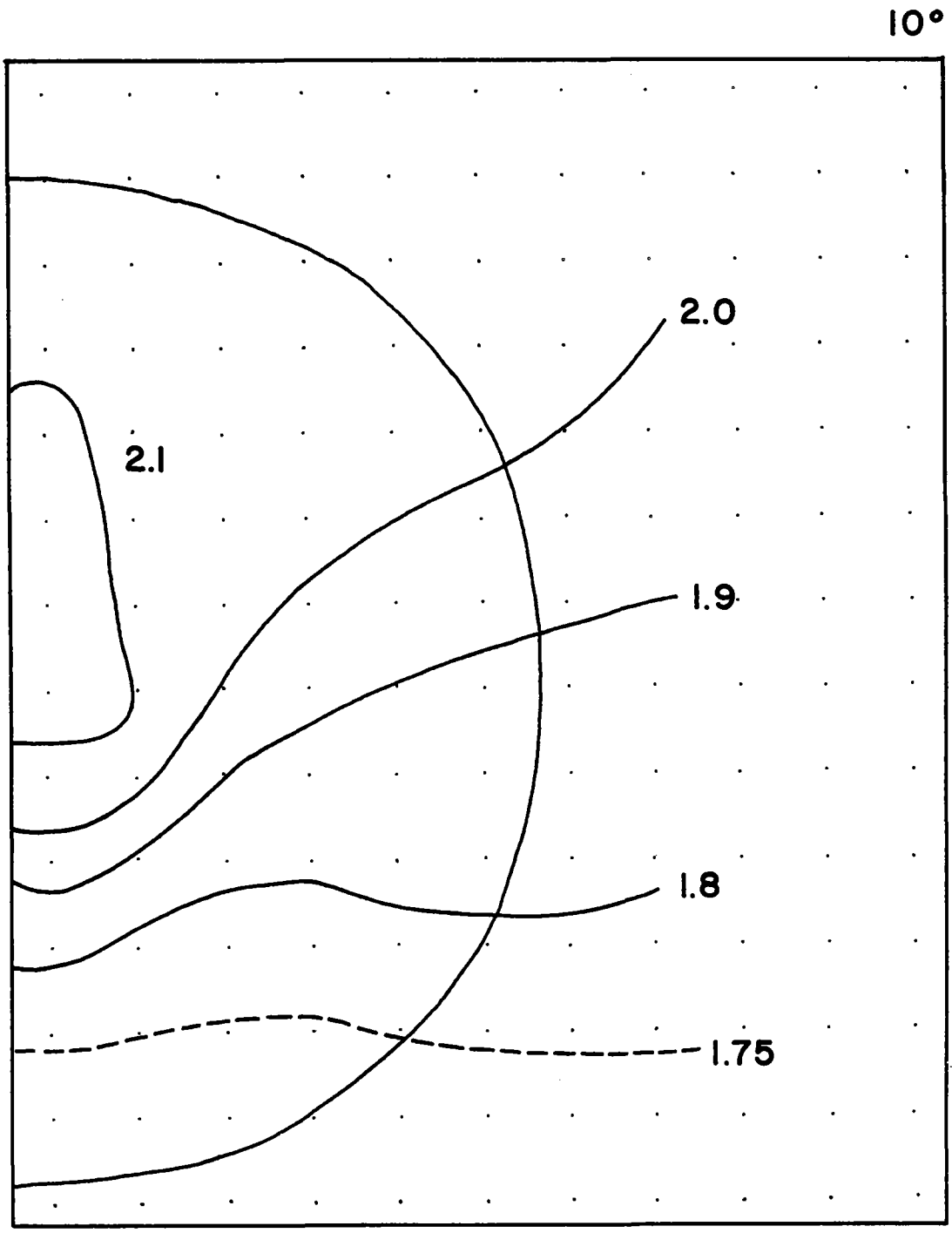

Figure 1.5b.4 Contours of Annual Power in aMWH$_t$/m^2 for 10° Slope.

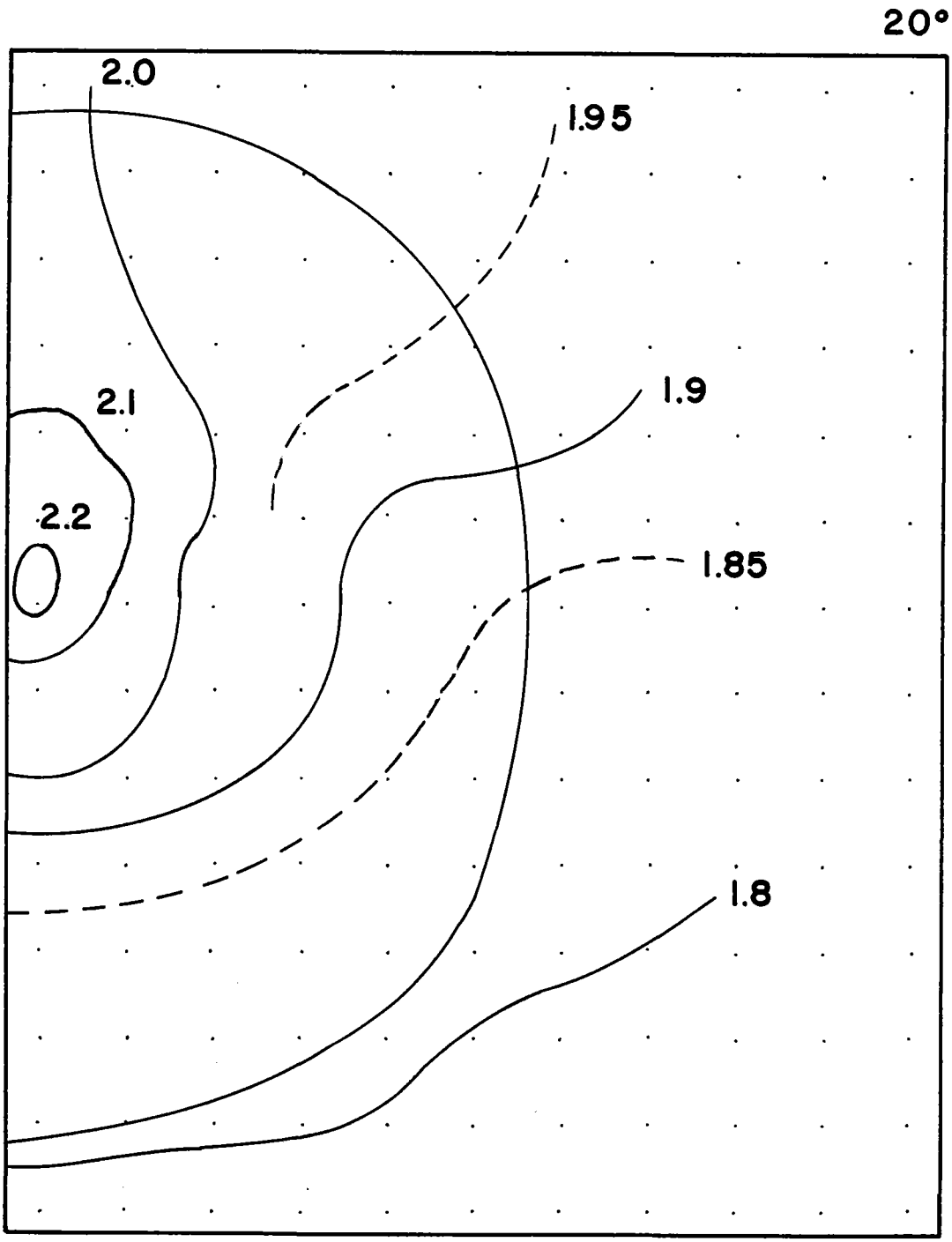

Figure 1.5b.5 Contours of Annual Power in aMWH$_t$/m^2 for 20° Slope.

fig 1.5b.5

Because the RCELL program is considered a design tool, it has been designed to output information of interest to both the design engineer and the systems engineer. Several of the standard outputs from RCELL are shown or summarized on the ensuing tables, where comparisons between the baseline and two alternate cases can be seen in detail. Table 1.5b.2 contains most of the cost data of interest, and is copied, with slight enhancements for clarity of comparison, from the optimizer summary page. The baseline cost model (with heliostat cost of $\$101.25/m^2$) described earlier is used thoughout these studies. Note that the main effect of the sloped field is to change the number of heliostats in the field.

Table 1.5b.2 Performance Summary for Slope

Slope in Degrees	0° Baseline	10°	20°
Equinox Noon Power (MW for 950 W/m^2)	717.61	704.01	691.27
Concentration	554.6	544.1	534.2
Annual Power			
MMWH/yr	1.764	1.746	1.710
$MWH/m^2/yr$	1.325	1.351	1.342
Fixed Cost (M$)	4.970	4.970	4.970
Tower Cost (M$)	9.480	9.480	9.480
Receiver Cost (M$)*	18.99	18.76	18.53
Land Cost (M$)	6.097	5.914	6.097
Wiring Cost (M$)	4.657	4.521	4.458
Heliostat Cost (M$)	134.73	130.79	128.95
Total Cost			
(M$)	178.92	174.43	172.49
($/$m^2$)	134.4	135.0	135.4
Number of Helios	35744	34699	34213
Area of Glass (km^2)	1.331	1.292	1.274
Ground Coverage	0.236	0.236	0.226
Figure of Merit			
($/aMWh)	101.45	99.92	100.88
	Baseline	-1.51%	-0.56%

*Here "receiver cost" includes cost of the riser and downcomer.

In table 1.5b.3 we depict the boundaries of the three fields. In the trim matrix a "4" represents a cell in which 4-fourths of the area is used, a "3" one in which 3-fourths of the area is used, etc.; 0 represents unoccupied cells. Note that the bottom lines of the table reveal the interesting fact that, with only 10° slope, the northernmost heliostat is level with the receiver. In Table 1.5b.4 ground coverage (heliostat density) values for the N-S column through the tower and for the E-W row through the tower are compared for the three cases. The 20° coverage is somewhat smaller in the south (larger blocking) and falls off somewhat faster to the east and west (perhaps due to the lower effective sun elevation on summer mornings and afternoons. For completeness the radial (table 1.5b.5) and azimuthal (table 1.5b.6) spacing data which go to make up the ground coverage are shown here. The larger radial spacing in the south and east for the sloping fields are more obvious here.

Weighted least square fits have been made to the spacing data, using number of heliostats per cell as a weighting factor. The coefficients to the fits are displayed in table 1.5b.7 for the three slopes. The fitting functions are those given on page 1-55; i.e., $X\theta$ and $Z = \tan Y/X$ are each fit with $C_1 + C_2\theta + C_3\,\theta^2$. (Note that as θ is the receiver elevation angle, large values of θ occur near the tower).

Table 1.5b.3 Trim Comparison for Slope Study
(shows east half field)

Slope	0°	10°	20°
Trim Matrix	0 0 0 0 0 0 0 0	0 0 0 0 0 0 0 0	0 0 0 0 0 0 0 0
	2 2 1 0 0 0 0 0	2 1 0 0 0 0 0 0	1 0 0 0 0 0 0 0
	4 4 4 3 1 0 0 0	4 4 4 3 0 0 0 0	4 4 4 2 0 0 0 0
	4 4 4 4 4 1 0 0	4 4 4 4 3 0 0 0	4 4 4 4 3 0 0 0
	4 4 4 4 4 3 0 0	4 4 4 4 4 3 0 0	4 4 4 4 4 2 0 0
	4 4 4 4 4 4 1 0	4 4 4 4 4 4 0 0	4 4 4 4 4 4 0 0
	4 4 4 4 4 4 2 0	4 4 4 4 4 4 1 0	4 4 4 4 4 4 1 0
	3 4 4 4 4 4 2 0	3 4 4 4 4 4 1 0	3 4 4 4 4 4 1 0
	0 3 4 4 4 4 1 0	0 3 4 4 4 4 1 0	0 3 4 4 4 4 1 0
	3 4 4 4 4 4 0 0	3 4 4 4 4 4 0 0	3 4 4 4 4 4 0 0
	4 4 4 4 4 2 0 0	4 4 4 4 4 2 0 0	4 4 4 4 4 3 0 0
	4 4 4 4 2 0 0 0	4 4 4 4 3 0 0 0	4 4 4 4 4 0 0 0
	4 4 3 1 0 0 0 0	4 4 4 2 0 0 0 0	4 4 4 3 1 0 0 0
	1 0 0 0 0 0 0 0	1 1 0 0 0 0 0 0	3 2 1 0 0 0 0 0
Heliostat Number	35,744	34,699	34,213

Elevation of Most Northern Heliostat From Center of Receiver

In Tower Heights	-1.0	+0.053	+ 1.072
In Degrees	-9.37°	+0.509°	+10.66°

Table 1.5b.4 Ground Coverage Values for Slope Study
(Data for column and row through tower only)

SLOPE	Column Data 0°	10°	20°	SLOPE	Row Data 0°	10°	20°
North	0.112	0.124	0.114	Tower	*	*	*
	0.154	0.159	0.162		0.408	0.431	0.409
	0.192	0.199	0.209		0.387	0.396	0.357*
	0.235	0.251	0.256		0.291	0.283	0.234
	0.297	0.318	0.305		0.227	0.208	0.211
	0.390	0.400	0.387*		0.183	0.159	0.161
	0.417	0.409	0.442	East	0.130	0.122	0.114
Tower	*	*	*				
	0.423*	0.402*	0.405				
	0.377	0.379	0.360				
	0.279	0.263	0.248				
	0.205	0.184	0.181				
South		0.141	0.129				

* Starred values are less accurate.

Table 1.5b.5 Radial Spacing Values for Slope Study

SLOPE	Column Data (in Heliostat Widths) 0°	10°	20°	SLOPE	Row Data (in Heliostat Widths) 0°	10°	20°
North	6.278	6.101	6.339	Tower	*	*	*
	5.316	5.121	5.131		1.872	1.657	2.311#
	4.409	4.247	4.118		2.068	2.184	2.615*
	3.627	3.421	3.276		2.849	2.943	3.565
	2.844	2.655	2.706		3.675	3.780	4.618
	2.075	2.034	2.389*		4.530	4.745	5.460
	1.777	1.865	2.509#	East	5.520	5.882	6.491
Tower	*	*	*				
	1.697*	1.991*	2.263				
	2.414	2.436	2.508				
	2.831	3.120	3.491				
	3.629	4.039	4.566				
South		5.036	5.685				

* Starred values are less accurate.
#. These cases show shape change with respect to neighboring cells.

Table 1.5b.6 Azimuthal Spacing Values for Slope Study

SLOPE	Column Data (in Heliostat Widths) 0°	10°	20°	SLOPE	Row Data (in Heliostat Widths) 0°	10°	20°
North	2.508	2.329	2.439	Tower	*	*	*
	2.149	2.158	2.124		2.304	2.463	1.863#
	2.084	2.088	2.049		2.199	2.038	1.886*
	2.070	2.051	2.099		2.126	2.116	2.110
	2.084	2.087	2.131		2.112	2.238	1.806
	2.177	2.162	1.904*		2.127	2.331	1.997
	2.378	2.310	1.587#	East	2.456	2.461	2.370
Tower	*	*	*				
	2.451*	2.202*	1.921				
	1.935	1.906	1.949				
	2.232	2.148	2.034				
South		2.489	2.409				

* Starred values are less accurate.
\# These cases show a shape change with respect to neighboring cells.

Table 1.5b.7 Field Coefficient for Slope Study

SLOPE	0°	10°	20°
Coefficient			
1) First Radial	64.9750	59.9779	63.1237
2) Second Radial	-0.7577	-0.3109	-0.4269
3) Third Radial	0.02553	0.01955	0.03064
4) First Shape	1.6931	7.8047	7.4582
5) Second Shape	2.1274	1.5734	1.4280
6) Third Shape	-0.02254	-0.01436	-0.01665

1.5c. The Latitude Study

The latitude study compares optimized central receiver systems at latitudes 25°, 35°, and 45°. Table 1.5c.1 shows a comparison of total direct beam insolation at normal incidence integrated over selected days and the whole year. The insolation model is based on Allen's clear air model plus a monthly weather model characteristic of the Western U.S., 100 to 120° longitude, shown in table 1.5c.3. After including site specific factors such as elevation of site, turbidity factor, mean precipitable water, and percent of possible sun, we no longer expect the natural insolation dependence on latitude. Consequently, the annual insolation at 25° is less than at 35° because of increased precipitable water and turbidity factor. The 45° insolation is greatly reduced by decreased percent possible sun due to clouds.

Table 1.5c.2 shows that receiver loss rates (i.e. EQLOSS in MW) are the same for all three latitudes, but the annual receiver loss (ATLOSS) depends on the number of hours of operation (HYEAR), as shown in the notes at the bottom of table 1.5a.3. HYEAR is actually the number of hours the solar elevation exceeds 10°, with no allowance for days with clouds. Consequently ATLOSS may be somewhat excessive at 45° latitude.

Figure 1.5c.1 shows a 50 percent variation in figure of merit with latitude for longitudes corresponding to western USA and northern Mexico. Most of this variation is due to the availability of insolation. In fact, if the figure of merit in each case is recomputed using the same value for the insolation at each latitude (a poor assumption), the remaining variation in the figure of merit is only 5 percent. Notice on this figure the plot of MWH/m^2 which represents annual thermal power available at the base of the tower divided by the total area of glass as given in table 1.5c.4.

Table 1.5c.1

Total Direct Beam Comparison for Latitude Study

(kWH/m^2/day and MWH/m^2/year)

Day of Year*	93	124	155	186	216	246	276	Annual
25° Latitude	7.913	7.995	7.548	6.989	6.357	5.658	5.068	2.467
35° Latitude	9.452	8.974	8.384	7.345	6.367	5.383	4.687	2.609
45° Latitude	7.197	7.208	6.454	5.409	4.180	2.968	2.657	1.869

*day 0 is vernal equinox

Table 1.5c.2

Loss Parameter Comparison for Latitude Study

Variable	VISUAL	ELEVAT	OPSOL	FRLOS	EQLOSS	HYEAR	ATLOSS
Units	km	Meters	MWH/m^2		MW	Hours	MWH/Yr
25° Latitude	50.0	1000.0	1.162	0.849	25.52	3764	96057
35° Latitude	50.0	550.0	1.212	0.849	25.52	3697	86691
45° Latitude	50.0	1550.0	0.837	0.849	25.52	3575	91234

Table 1.5c.3 Monthly Weather Data For Three Typical Areas for Latitudes 25°, 35°, and 45°N.*

Month	Percent Possible Sun			Centimeters of Mean Precipitable Water			Turbidity Factor		
	25°	35°	45°	25°	35°	45°	25°	35°	45°
JAN	75	75	56	1.78	1.52	0.76	.10	.05	.04
FEB	75	75	61	2.03	1.57	0.76	.10	.05	.04
MAR	80	80	62	1.78	1.52	0.76	.10	.05	.04
APR	85	85	61	2.54	1.65	1.14	.12	.07	.06
MAY	90	90	61	2.54	1.96	1.40	.12	.07	.06
JUN	90	90	67	3.30	1.78	2.03	.15	.07	.08
JUL	90	90	76	3.81	2.24	2.41	.15	.10	.08
AUG	92	92	74	4.06	2.67	2.16	.15	.10	.08
SEP	92	92	67	3.81	2.03	1.91	.15	.10	.08
OCT	92	92	60	2.54	1.91	1.27	.12	.07	.06
NOV	85	85	53	2.03	1.47	1.02	.10	.05	.04
DEC	75	75	56	1.91	1.52	0.76	.10	.05	.04
AVG	85	85	64	2.68	1.82	1.37	.12	.07	.06

* The 25° Latitude area represents northern Mexico.

35° Latitude area represents a combination of Barstow and Albuquerque data.

45° Latitude represents western U.S.A. east of the Cascades.

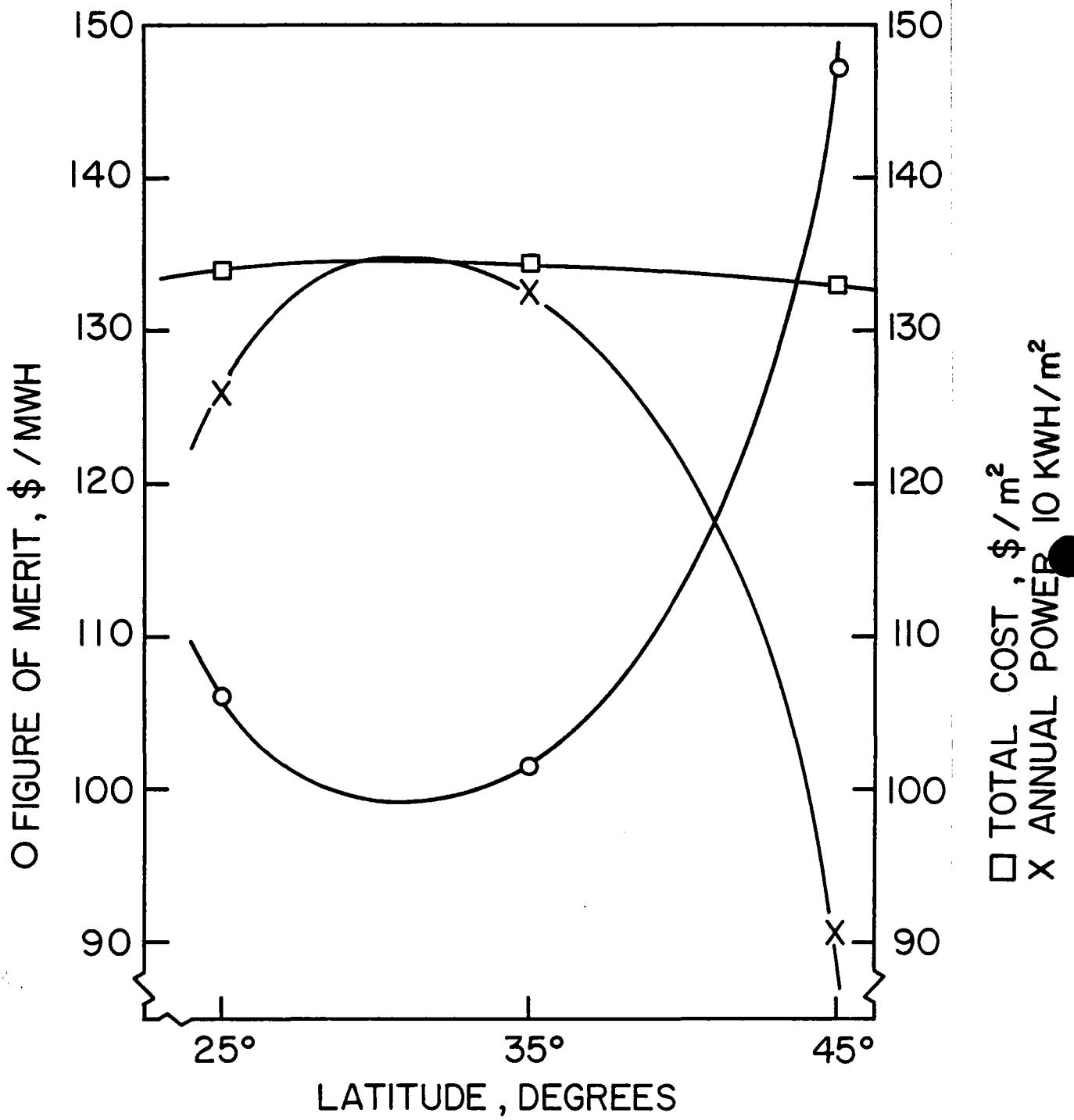

Figure 1.5c.1 Figure of Merit Versus Latitude. The figure of merit shows a minimum near 35° latitude having to do with the weather model--see discussion. The total cost in $\$/m^2$ and total annual power/m^2 are also shown. Notice that the cost is nearly independent of latititude as expected.

Table 1.5c.4 Performance Comparison for Latitude Study

Latitude in Degrees	25°	35° baseline	45°
Equinox Noon Power (MW for 950 W/m^2)	739.46	722.04	771.24
Concentration	571.5	558.0	596.1
Beam Insolation (MMWH/yr)	2.467	2.609	1.869
Annual Power (MMWH/yr.)	1.723	1.775	1.320
(MWH/m^2/yr.)	1.262	1.324	0.9035
System Efficiency (%)	51.2	50.7	48.3
Fixed Cost (M$)	4.970	4.970	4.970
Tower Cost	9.48	9.48	9.48
Receiver Cost (M$)	19.37	19.07	19.90
Land Cost (M$)	6.097	6.153	6.986
Wiring Cost (M$)	4.777	4.695	5.113
Heliostat Cost (M$)	138.21	135.82	147.91
Total Cost			
(M$)	182.89	180.19	194.36
($/$m^2$)	133.98	134.37	133.03
Number of Heliostats	36,667	36,035	39,243
Area of Glass $(km)^2$	1.365	1.341	1.461
Ground Coverage	0.242	0.235	0.226
Figure of Merit ($/MWH)	106.16 + 4.57%	101.52 baseline	147.25 + 45.05%

Several other interesting comparisons can be made at this point. In this study the cost of heliostats is 101.25 $/m^2, which is comparable to the total system cost divided by the area of glass in $/m^2. Table 1.5c.4 shows that the total cost/m^2 is roughly 134 $/m^2, so that the system cost is

$$134.0/101.25 = 1.323$$

times the cost of the heliostats. From an optimization point of view, cost should be thought of in terms of heliostats. The effectiveness of the collector field optimization depends more sensitively on energy utilization than on the number of heliostats when the total system cost is little more than the cost of the heliostats. Consequently, we expect to find that the number of heliostats (i.e., system size) is very sensitive to the input figure of merit. (See section 1.5g.)

The available thermal energy (annual average) in aMWH$_t$/m^2 can be compared to the annual direct beam energy. This type of comparison gives an overall system efficiency, which we see is relatively constant:

(25°) = 1.262/2.467 = 51.2%

(35°) = 1.324/2.609 = 50.7%

(45°) = 0.9035/1.869= 48.3%

Finally, the figure of merit can be compared to an ideal figure of merit for a loss-less system costing only heliostats. Let F* be the ideal figure of merit, so that

F* = 101.25 $m^2/2.609 MWH/m^2

= 38.81 $/MWH at 35° latitude, and the actual figure of merit is roughly 2.6 times F* (i.e., 1.323/50.7%).

For a more detailed comparison of the available energy from the collector field, see figures 1.5c.2-4 in which the total energy in aMWH$_t$/m^2 available from each cell has been converted to a contour map of the field for latitudes 25°, 35°, and 45°.

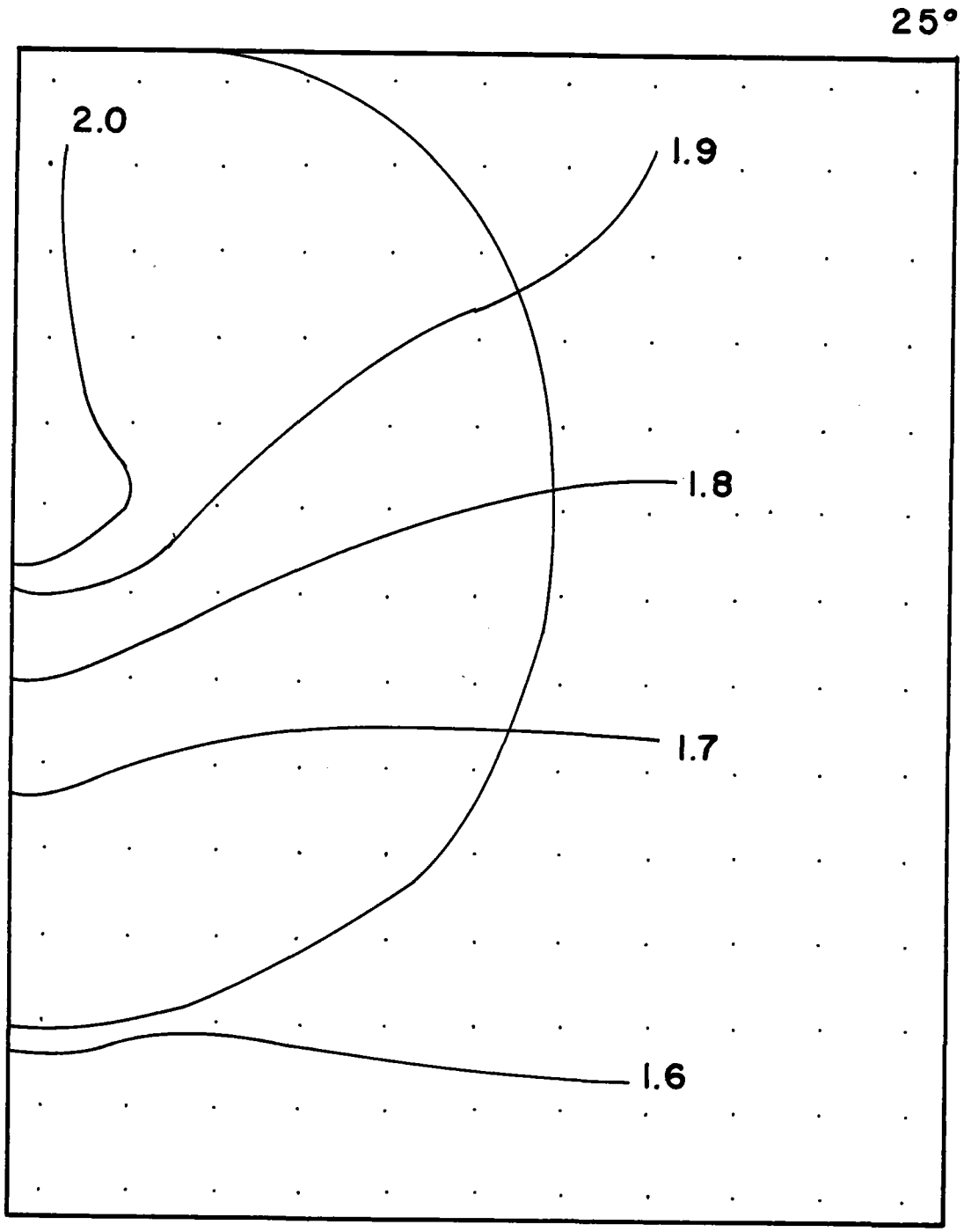

Figure 1.5c.2 Contours of Annual Power in $aMWH_t/m^2$ for 25° latitude. The "semicircle" represents the boundary of the right half field and "T" shows the tower location.

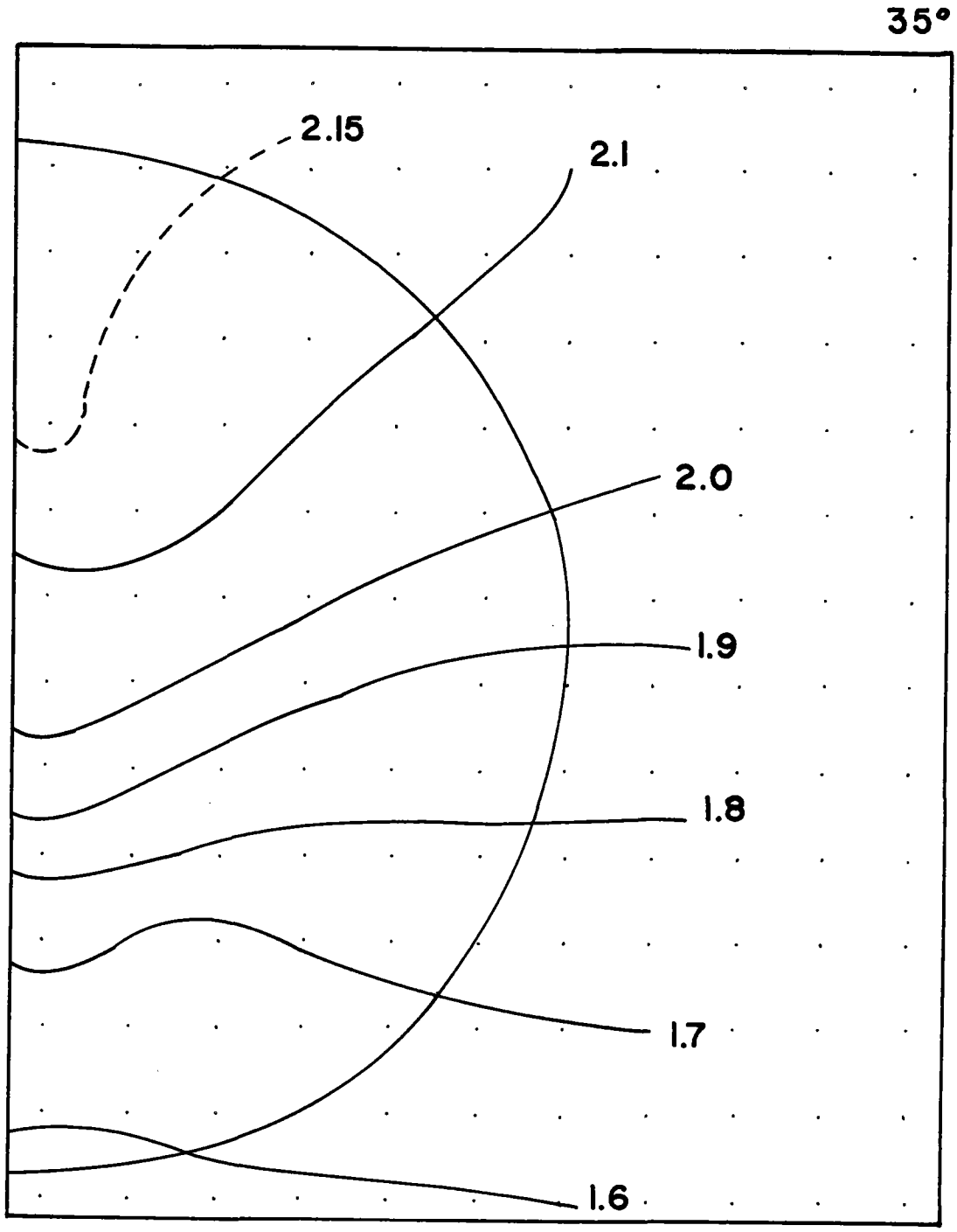

Figure 1.5c.3 Contours of Annual Power in aMWH$_t$/m^2 for 35° Latitude.

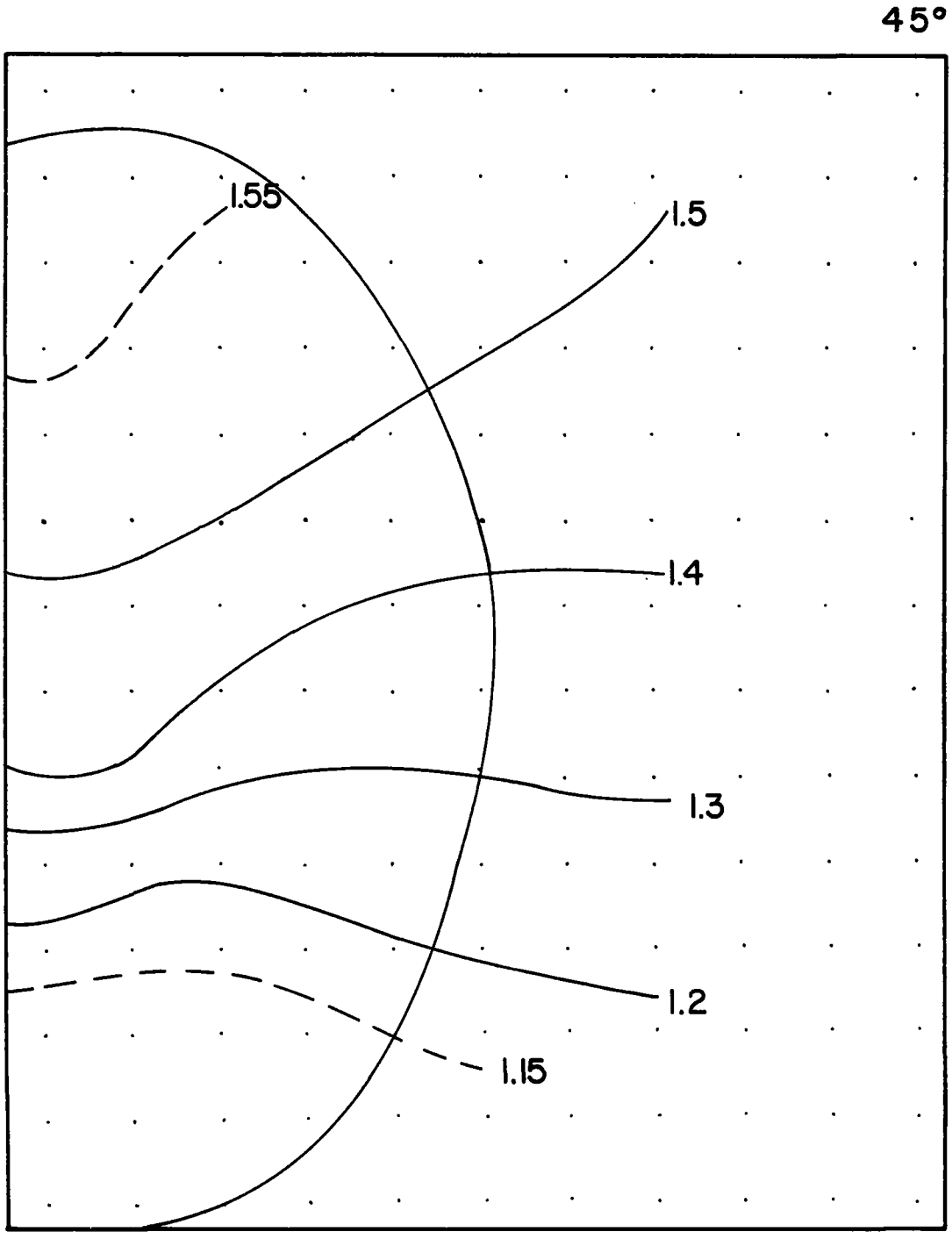

Figure 1.5c.4 Contours of Annual Power in aMWH$_t$/m^2 for 45° Latitude.

Tables 1.5c.4 and 1.5c.5 give summary data from the optimization runs at the three latitudes. Direct beam insolation and system efficiency have been added to table 1.5c.4 for comparison purposes. Note that numbers of heliostats increase at 45° to partially compensate for the reduced insolation, thus helping to overcome the fixed, tower, and receiver costs.

Tables 1.5c.6-8 give the ground coverage and spacing values for the N-S and E-W rows of heliostats centered on the tower. Finally table 1.5c.9 gives the coefficients resulting from a least squares fit on the spacing data for the whole field.

Table 1.5c.5 Trim Comparison for Latitude Study

LATITUDE	25°	35°	45°
Trim Matrix	0 0 0 0 0 0 0 0 0 0 0 0 0 0 0 0 0 0 4 4 4 2 0 0 0 0 4 4 4 4 3 0 0 0 4 4 4 4 4 3 0 0 4 4 4 4 4 4 0 0 3 4 4 4 4 4 2 0 0 3 4 4 4 4 1 0 3 4 4 4 4 4 0 0 4 4 4 4 4 3 0 0 4 4 4 4 4 0 0 0 4 4 4 3 0 0 0 0 2 2 1 0 0 0 0 0	0 0 0 0 0 0 0 0 0 3 2 1 0 0 0 0 0 4 4 4 3 1 0 0 0 4 4 4 4 4 1 0 0 4 4 4 4 4 4 3 0 0 4 4 4 4 4 4 4 1 0 3 4 4 4 4 4 4 2 0 0 3 4 4 4 4 4 1 0 3 4 4 4 4 4 4 0 0 4 4 4 4 4 4 2 0 0 4 4 4 4 4 3 0 0 0 4 4 3 1 0 0 0 0 1 0 0 0 0 0 0 0	0 0 0 0 0 0 0 0 0 4 4 3 1 0 0 0 0 4 4 4 4 4 3 0 0 0 4 4 4 4 4 4 2 0 0 4 4 4 4 4 4 4 1 0 4 4 4 4 4 4 4 2 0 3 4 4 4 4 4 4 3 0 0 3 4 4 4 4 4 3 0 3 4 4 4 4 4 4 1 0 4 4 4 4 4 4 3 0 0 4 4 4 4 4 2 0 0 0 4 4 4 3 1 0 0 0 3 3 2 0 0 0 0 0
Heliostat Number	36,667	36,035	39,243
Field Limits in Cell Widths			
North	6.50	7.17	7.50
East	5.67	5.67	6.17
South	5.00	4.67	5.17

Table 1.5c.6 Ground Coverage Values for Latitude Study
(Data for column and row through tower only)

Column Data				Row Data			
LAT	25°	35°	45°	LAT.	25°	35°	45°
N		0.112	0.128	T	*	*	*
	0.155	0.157	0.156		0.436	0.408	0.400
	0.191	0.192	0.187		0.400	0.387	0.373
	0.234	0.235	0.236		0.300	0.291	0.289
	0.302	0.297	0.296		0.228	0.227	0.226
	0.400	0.390	0.371		0.181	0.183	0.178
	0.412	0.417	0.422	E	0.130	0.130	0.142
T	*	*	*				
	0.457	0.423	0.432				
	0.404	0.377	0.390				
	0.292	0.279	0.268				
	0.213	0.205	0.237				
S	0.157	0.164	0.177				

* Starred values are less accurate.

Table 1.5c.7 Radial Spacing Values for Latitude Study

Column Data (in Heliostat Widths)				Row Data (in Heliostat Width)			
LAT.	25°	35°	45°	LAT	25°	35°	45°
N		6.278	6.267	T	*	*	*
	5.262	5.280	5.340		2.485	1.872	2.097
	4.376	4.409	4.517		2.045	2.068	2.165
	3.587	3.627	3.624		2.782	2.849	2.859
	2.817	2.844	2.823		3.644	3.675	3.669
	2.088	2.075	2.117		4.535	4.530	4.564
	2.338	1.777	2.415	E	5.499	5.520	5.522
T	*	*	*				
	2.559	1.697*	2.467				
	2.244	2.414	2.372				
	2.747	2.831	3.026				
	3.583	3.629	3.613				
S	4.619	4.453	4.550				

* Starred values are less accurate or indicate the subtower cell.

Table 1.5c.8 Azimuthal Spacing Values for Latitude Study

	Column Data (In Heliostat Widths)				Row Data (In Heliostat Widths)		
LAT	25°	35°	45°	LAT.	25°	35°	45°
N		2.508	2.192	T	*	*	*
	2.160	2.127	2.116		1.625	2.304	2.102
	2.106	2.084	2.084		2.153	2.199	2.179
	2.094	2.070	2.057		2.109	2.126	2.128
	2.067	2.084	2.107		2.116	2.112	2.121
	2.111	2.177	2.243		2.150	2.127	2.170
	1.830	2.378	1.726	E	2.469	2.456	2.246
T	*	*	*				
	1.505	2.451	1.651				
	1.944	1.935	1.904				
	2.193	2.232	2.170				
	2.308	2.365	2.057				
S	2.432	2.406	2.192				

* Starred Values indicate the subtower cell.

Table 1.5c.9 Field Coefficients for Latitude Study

LATITUDE	25°	35°	45°
Coefficient			
First Radial	76.4449	63.8487	70.9813
Second Radial	- 2.2353	- 0.7279	- 1.5478
Third Radial	0.06500	0.02548	0.04786
First Shape	- 3.9478	1.8291	- 2.7520
Second Shape	2.8616	2.1162	2.6250
Third Shape	- 0.04357	-0.02236	-0.03579

1.5d. The Heliostat Cost Study

Table 1.5d.1 gives the performance comparison for three different heliostat cost assumptions. Figure 1.5d.1 shows the figure of merit versus heliostat cost. The figure of merit increases by 34% for a 50% increase in the cost of heliostats $/m^2$. This shows that the optimization process is fighting against the increased cost of the heliostats by requiring more $aMWH_t/m^2$ as the cost increases. The heliostats are packed less densely in the interior of the field to reduce shading and blocking, while the trim line moves in to prevent excessive interception or cosine losses. The improved performance can be seen in figure 1.5e.2, which also shows a tendency for the improvement to saturate. The reduction in the number of heliostats has the effect of increasing the total collector cost per unit area of mirror. Thus in Figure 1.5e.3, the slope of the lower curve is greater than 45°.

To show the effect of the optimization from another point of view we have included an extra row of cost data in Table 1.5d.1 for the relative system cost (i.e., Total Cost/m^2 ÷ Heliostat Cost/m^2). The relative total system cost decreases as heliostat cost increases.

The optimization depends on relative costs; i.e., it is reasonable to scale the value of dollars in order to adjust the heliostat cost to a constant value, so that the result indicates the effects of higher or lower costs for the balance of the plant. As shown in table 1.5d.2, a 25% increase in balance of plant costs thus leads to a 6.6% increase in the figure of merit, while a 16.7% decrease in BOP costs leads to a 4.6% decrease in the figure of merit. The relative system costs and all performance figures are unchanged from the previous table.

Table 1.5d.1 Performance Comparison for Heliostat Cost Study

Cost of Heliostats in $\$/m^2$	81.00 -20%	101.25 Baseline	121.50 + 20%
Equinox Noon Power (MW for 950 W/m^2)	770.56	717.61	681.12
Concentration	595.5	554.6	526.4
Annual Power (MMWH/yr)	1.900	1.764	1.670
($MWH/m^2/yr$)	1.303	1.325	1.341
Fixed Cost (M$)	4.970	4.970	4.970
Tower Cost (M$)	9.48	9.48	9.48
Receiver Cost (M$)	19.89	18.99	18.36
Land Cost (M$)	6.774	6.097	5.631
Wiring Cost (M$)	5.104	4.657	4.358
Heliostat Cost (M$)	118.13	134.73	151.29
Total Cost (M$)	164.35	178.92	194.09
($\$/m^2$)	112.7	134.4	155.9
Relative to Heliostats	1.391	1.327	1.283
Number of Heliostats	39,175	35,744	33,449
Area of Glass $(km)^2$	1.458	1.331	1.245
Ground Coverage	0.232	0.236	0.239
Figure of Merit ($/MWH)	86.49	101.45	116.19
	-14.7%	baseline	+12.7%

Table 1.5d.2 Performance Comparison Using a Balance of Plant Costing for Heliostat Cost Study

Cost of Heliostats in $\$/m^2$	101.25	101.25	101.25
Cost Multiplier on Balance of Plant Relative to Baseline	1.25	1.	.833
Equinox Noon Power (MW for 950 w/m^2)	770.56	717.61	681.12
Concentration	595.5	554.6	526.4
Annual Power (MWH/yr)	1.900	1.764	1.670
($MWH/m^2/yr$)	1.303	1.325	1.341
Fixed Costs (M$)	6.213	4.970	4.142
Tower Cost (M$)	11.85	9.48	7.90
Receiver Costs (M$)	24.86	18.99	15.30
Land Costs (M$)	8.468	6.097	4.693
Wiring Costs (M$)	6.380	4.657	3.632
Heliostat Cost (M$)	147.66	134.73	126.08
Total Cost (M$)	205.43	178.92	161.74
($\$/m^2$)	140.9	134.4	129.9
Relative to Heliostats	1.391	1.327	1.238
Number of Heliostats	39,175	35,744	33,449
Area of Glass $(km)^2$	1.458	1.331	1.245
Ground Coverage	0.232	0.236	0.239
Figure of Merit ($/MWH)	108.11	101.45	96.82
	+6.6%	baseline	-4.6%

In table 1.5d.3 the variation in the boundary of the field and the number of heliostats in the field with heliostat cost are shown. more expensive heliostats lead to a smaller field, because those heliostats with a poor interception factor can no longer be afforded. Simultaneously, heliostat separations increase with cost, a fact which can be determined by evaluating the cost functions using coefficients provided in table 1.5d.4. The increase in ground coverage shown in tables 1.5d.1 and 2 results in spite of the decrease in local ground coverage because the outer, sparsely occupied region of the field is deleted.

Considering the lower curves in figures 1.5d.1-3, we find the figure of merit, the annual power production per m^2 and the total system cost divided by the mirror area plotted against the costs of heliostats. The first and third of these are closely linear functions of heliostat cost, while the annual power per m^2 tends to saturate at higher heliostat costs. This must occur as the available energy per m^2 is limited to the direct beam insolation (modified by the maximum average cosine of incidence).

Table 1.5d.3 Trim Comparison for Heliostat Cost Variation Study

Cost of Heliostats	81.00 $/m^2	101.25 $/m	121.50 $/m
	-20%	baseline	+20%
Trim Matrix	0 0 0 0 0 0 0 0 0 4 3 2 0 0 0 0 0 0 4 4 4 4 2 0 0 0 0 4 4 4 4 4 4 0 0 0 4 4 4 4 4 4 4 2 0 4 4 4 4 4 4 4 3 0 3 4 4 4 4 4 4 3 0 0 3 4 4 4 4 4 3 0 3 4 4 4 4 4 4 2 0 4 4 4 4 4 4 4 0 0 4 4 4 4 4 4 1 0 0 4 4 4 3 0 0 0 0 0 2 1 0 0 0 0 0 0 0	0 0 0 0 0 0 0 0 0 2 2 1 0 0 0 0 0 0 4 4 4 3 1 0 0 0 0 4 4 4 4 4 4 3 0 0 4 4 4 4 4 4 4 1 0 4 4 4 4 4 4 4 2 0 3 4 4 4 4 4 4 2 0 0 3 4 4 4 4 4 1 0 3 4 4 4 4 4 4 0 0 4 4 4 4 4 4 2 0 0 4 4 4 4 4 2 0 0 0 4 4 3 1 0 0 0 0 0 1 0 0 0 0 0 0 0 0	0 0 0 0 0 0 0 0 0 2 1 0 0 0 0 0 0 0 4 4 4 2 0 0 0 0 0 4 4 4 4 4 2 0 0 0 4 4 4 4 4 4 4 0 0 4 4 4 4 4 4 4 1 0 3 4 4 4 4 4 4 1 0 0 3 4 4 4 4 4 1 0 3 4 4 4 4 4 3 0 0 4 4 4 4 4 4 1 0 0 4 4 4 4 4 1 0 0 0 3 3 2 0 0 0 0 0 0 0 0 0 0 0 0 0 0 0
Heliostat Number	39,175	35,744	33,449

Table 1.5d.4 Field Coefficients for Heliostat Cost Study

Cost of Heliostat in $/m^2	81.00	101.25	121.50
Coefficient			
First Radial	64.3334	64.9750	64.0637
Second Radial	- 0.7669	- 0.7577	- 0.6093
Third Radial	0.02626	0.02553	0.02174
First Shape	2.0929	1.6931	2.0166
Second Shape	2.0871	2.1274	2.0877
Third Shape	- 0.02202	- 0.02254	- 0.02131

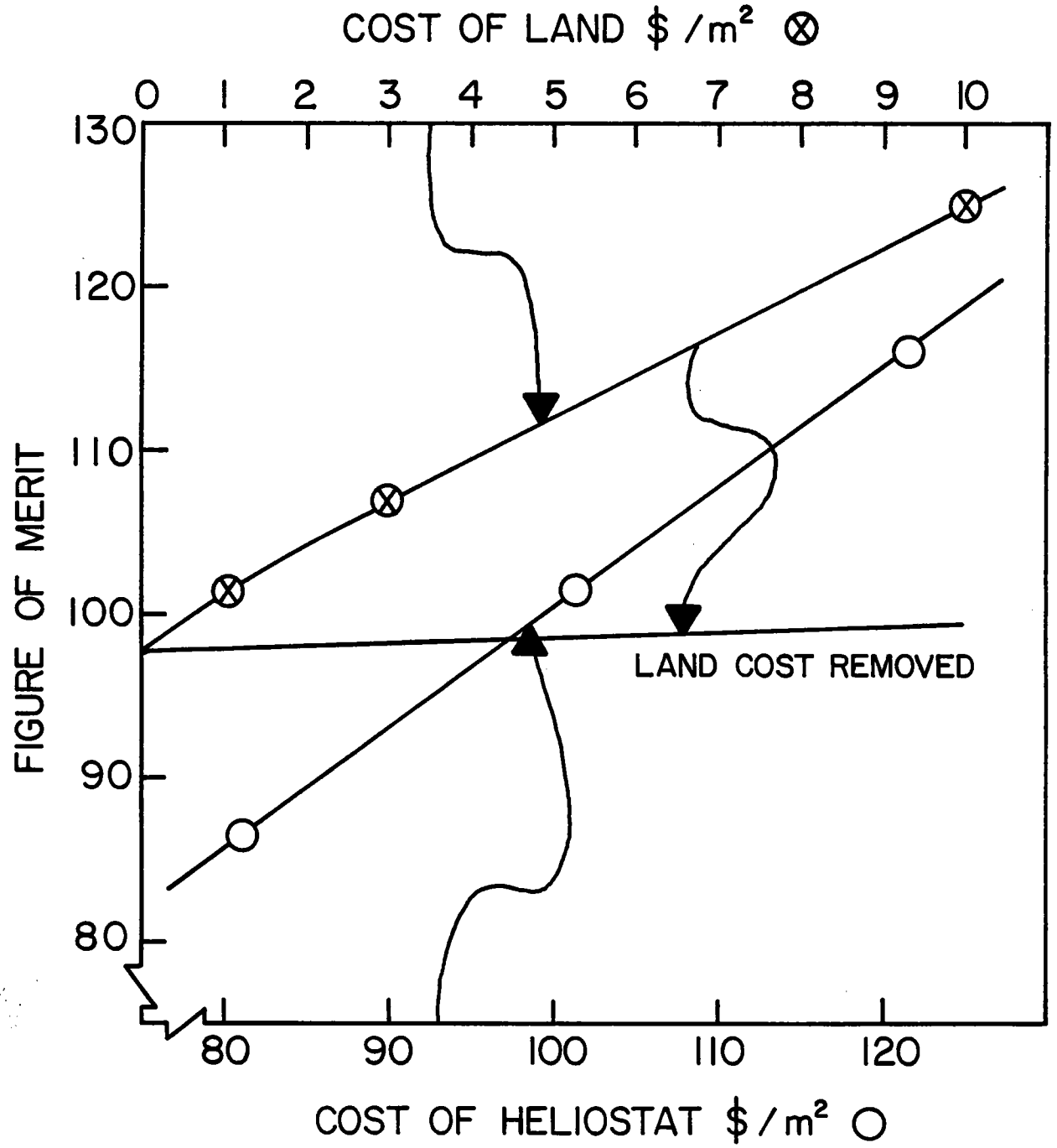

Figure 1.5d.1 Figure of Merit Versus Cost of Heliostat and of Land. The upper scale shows the cost of land in $\$/m^2$, and the lower scale shows the cost of heliostats in $\$/m^2$.

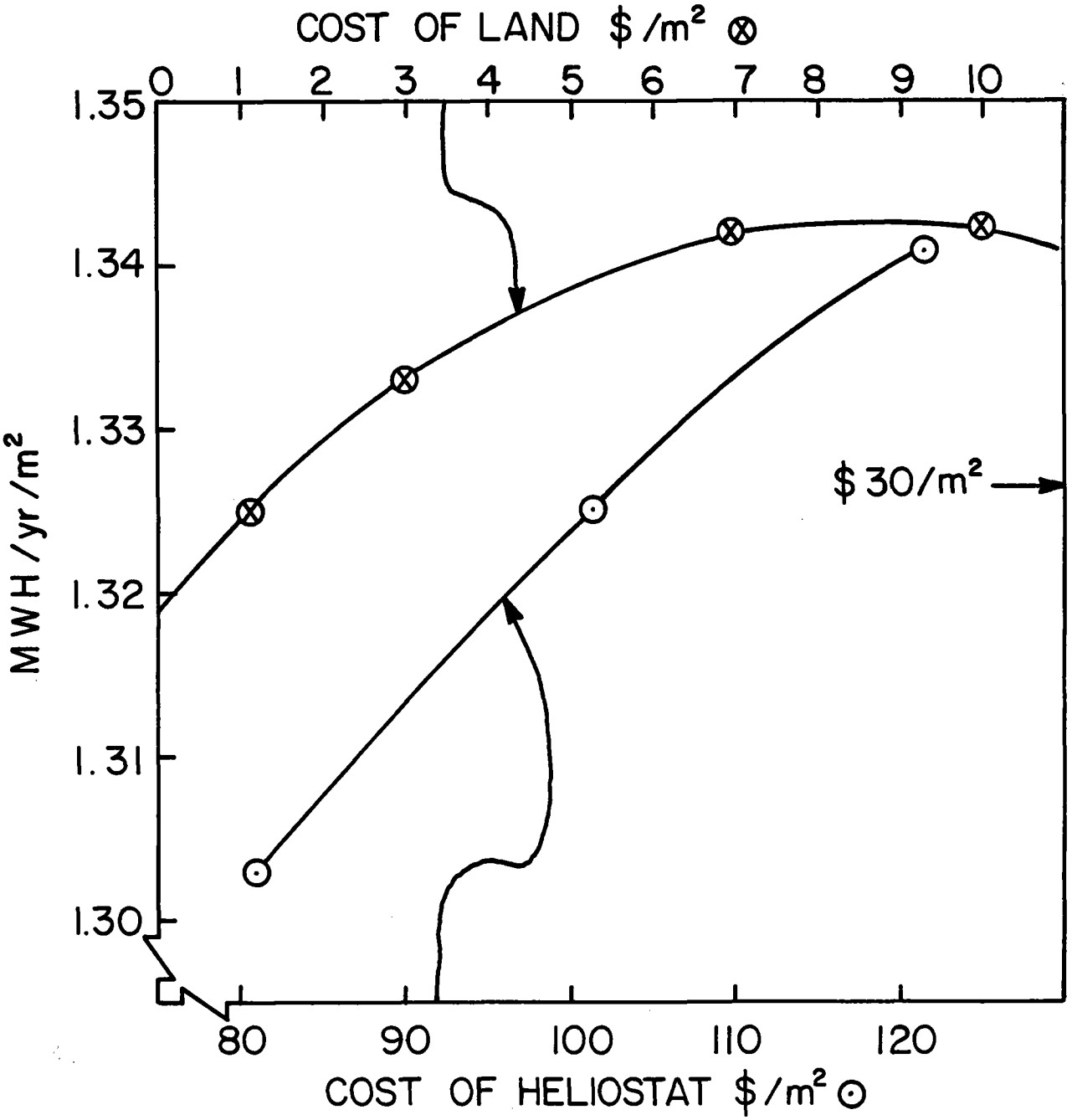

Figure 1.5d.2 Annual Power Versus Cost of Heliostats and of Land. The upper scale shows the cost of land in $/m^2$, and the lower scale shows the cost of heliostats in $/m^2$.

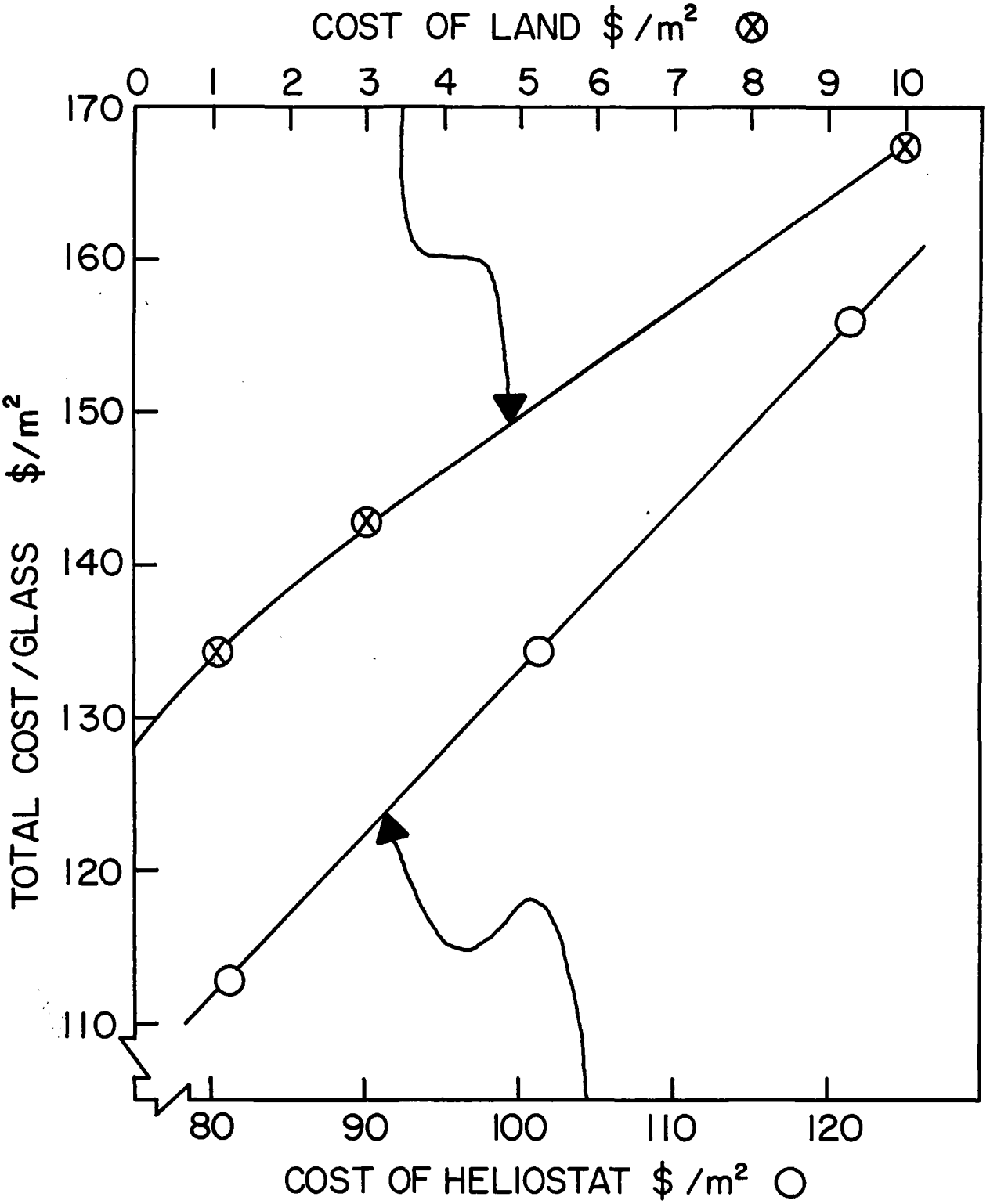

Figure 1.5d.3 Total Cost Versus Cost of Heliostats and of Land. The upper scale shows the cost of land in $\$/m^2$, and the lower scale shows the cost of heliostats in $\$/m^2$.

1.5e.3 The Land Cost Study

Land costs are included as a variable in this study because they affect the heliostat field differentially. In the dense portions of the field the ground coverage can be ~ 0.4. Hence 2.5 m^2 of land are required for each m^2 of mirror. However, in the outer reaches of the field the ground coverage may drop to 0.10. Here 10 m^2 of land are required for each m^2 of mirror. At \$1/m^2 this cost is negligible, but at \$10/m^2 it effectively doubles the cost of placing heliostats at the periphery of the field.

Table 1.5e.1 gives a performance comparison for central receiver systems assuming three different land costs. A ten-fold increase in land cost gives a 23% increase in figure of merit, a 25% increase in average ground coverage, and a 27% increase in MWH collected per m^2 of land each year. Figure 1.5d.1 (previous section) shows that the figure of merit is approximately a linear function of land cost through the range of interest. Figure 1.5d.2 indicates that the MWH/m^2 will go through an apparent maximum as land cost increases. This can be understood in terms of the optimization process which gains efficiency initially by eliminating the remote heliostats in sparsely populated cells. In general, these heliostats perform poorly because either the interception or mean cosine is in the range of 0.6 to 0.7. The worst performers are eliminated at \$3/m^2; at \$10/m^2 the other aspect of the optimization overrides the effects of trim variations; i.e., the higher figure of merit drives toward a higher density of heliostats in the interior of the field in an attempt to reduce the pro-rated cost of the tower facility per heliostat. This higher density results in greater shading and blocking losses and a net reduction in the average heliostat performance.

If the entire land cost is excluded, we see in figure 1.5d.1 that the denser field (\$10/m^2) land) suffers only a 1.7% increase in the figure of merit

Table 1.5e.1 Performance Comparison for Land Cost Study

Cost of Land in $\$/m^2$	1.08 baseline	3.00	10.00	30.00
Equinox Noon Power (MW for 950 W/m^2)	717.61	688.03	598.50	490.72
Concentration	554.6	531.7	462.5	379.2
Annual Power				
($MMWH/yr$)	1.764	1.685	1.451	1.173
($MWH/m^2/yr$)	1.325	1.333	1.342	1.326
Fixed Cost (M$)	4.970	4.970	4.970	4.970
Tower Cost (M$)	9.48	9.48	9.48	9.48
Receiver Cost (M$)	18.99	18.48	16.87	14.80
Land Cost (M$)	6.097	14.898	36.460	76.840
Wiring Cost (M$)	4.657	4.425	3.782	3.096
Heliostat Cost (M$)	134.73	128.02	109.42	89.55
Total Cost				
(M$)	178.92	180.27	180.98	198.75
($\$/m^2$)	134.4	142.6	167.4	224.7
Number of Heliostats	35,744	33,965	29,029	23,760
Area of Glass $(km)^2$	1.331	1.264	1.081	.8845
Ground Coverage	0.236	0.255	0.296	.345
Figure of Merit ($/MWH)	101.45	106.97	124.77	169.41
	baseline	+ 4.5%	+ 23.0%	+ 67.0%
Figure of Merit (assuming free land)	97.97	98.14	99.60	104.11
Land Area (km^2)	5.645	4.623	3.646	2.563
MWH_t/m^2(land)/yr	.3125	.3645	.3980	.4577

while the land use efficiency increases by 27%. Thus, if a limited amount of land is available, an artificially high land cost can be used to encourage the optimization procedure to use the available land most efficiently with only a second order effect on the cost of the balance of the system. In essence, if a premium is placed on land, a taller more expensive tower will provide greater energy recovery at only a small increase in non-land cost.

Tables 1.5e.2 - 3 show the decrease in the field boundary and the changes in the spacing coefficients associated with the higher land costs. The first shape coefficient shows considerable variation in this case.

Table 1.5e.2 Trim Comparison for Land Cost Variation Study

Cost of Land $/m^2	1.08	3.00	10.00
Trim Matrix	0 0 0 0 0 0 0 0 2 2 1 0 0 0 0 0 4 4 4 3 1 0 0 0 4 4 4 4 4 1 0 0 4 4 4 4 4 3 0 0 4 4 4 4 4 4 1 0 4 4 4 4 4 4 2 0 3 4 4 4 4 4 2 0 0 3 4 4 4 4 1 0 3 4 4 4 4 4 0 0 4 4 4 4 4 2 0 0 4 4 4 4 2 0 0 0 4 4 3 1 0 0 0 0 1 0 0 0 0 0 0 0	0 0 0 0 0 0 0 0 0 0 0 0 0 0 0 0 4 4 3 1 0 0 0 0 4 4 4 4 2 0 0 0 4 4 4 4 4 1 0 0 4 4 4 4 4 3 0 0 4 4 4 4 4 4 0 0 3 4 4 4 4 4 0 0 0 3 4 4 4 4 0 0 3 4 4 4 4 3 0 0 4 4 4 4 4 1 0 0 4 4 4 4 1 0 0 0 4 3 2 0 0 0 0 0 0 0 0 0 0 0 0 0	0 0 0 0 0 0 0 0 0 0 0 0 0 0 0 0 0 0 0 0 0 0 0 0 4 4 3 0 0 0 0 0 4 4 4 4 1 0 0 0 4 4 4 4 4 0 0 0 4 4 4 4 4 0 0 0 3 4 4 4 4 1 0 0 0 3 4 4 4 1 0 0 3 4 4 4 4 0 0 0 4 4 4 4 1 0 0 0 4 4 4 1 0 0 0 0 1 1 0 0 0 0 0 0 0 0 0 0 0 0 0 0
Heliostat Number	35,744	33,965	29,029

Table 1.5e.3 Field Coefficients for Land Cost Study

Cost of Land in $/m^2$	1.08	3.00	10.00
Coefficient			
First Radial	64.9750	64.5398	61.2642
Second Radial	- 0.7577	- 0.7833	- 0.6762
Third Radial	0.02553	0.02654	0.02626
First Shape	1.6931	2.2094	4.5297
Second Shape	2.1274	2.0751	1.8745
Third Shape	- 0.02254	0.02180	- 0.01874

1.5f The Tower Height Study

Table 1.5f.1 provides a performance comparison for central receiver systems of five different tower focal heights. As before, the receiver dimensions and heliostat size are maintained constant. An additional row of data is included in table 1.5f.1 for the average interception fractions, which show a decrease with increased tower focal height due to increased slant range. Interception averages shown here include flux spillage at the receiver and scattering of the reflected sunlight due to visual range effects, both of which increase with slant range.

The number of heliostats increases strongly with tower height, but the total cost/m^2 is nearly constant. Optimization causes the average ground coverage to increase with tower height in order to avoid excessive slant range and still pay for the increased tower cost. Apparently, this works well within the range of this study. Average ground coverage varies by 30% while the cost/m^2 varies by 0.34% and the figure of merit varies by ~ 2%, corresponding to tower height variations of 67%.

Figure 1.5f.1 shows an optimum tower height of roughly 250 m. This result is strongly dependent on the receiver size and aiming strategy. The Hi-Lo optimum aiming strategy accommodates slant range variations so that the minimum shown in Figure 1.5f.1 is broader than would be expected for a one point aim. A one point aiming strategy would give higher concentration ratios and less radiative and convective loss, but the peak flux would be quite high, typically 2MW/m^2.

Some improvement in the guidance system or the choice of a larger receiver would shift the optimum toward 330 m towers, 1000 times concentration, and 10^{10} thermal watts at noon power.

Table 1.5f.1 Performance Comparison for Tower Height Study

Tower Height in Meters	211.2 -20%	237.6 -10%	264.0 baseline	290.4 +10%	330.0 +25%
Equinox Noon Power					
(MW for 950/W/m^2)	615.69	669.83	722.04	781.25	854.92
Concentration	475.8	517.7	558.0	603.8	660.7
Annual Power					
(MMWH/yr)	1.524	1.652	1.775	1.916	2.090
(MWH/m^2/yr)	1.322	1.323	1.324	1.321	1.304
Fixed Cost (M$)	4.970	4.970	4.970	4.970	4.970
Tower Cost (M$)	6.204	7.760	9.480	11.362	14.485
Receiver Cost (M$)	16.846	17.970	19.070	20.288	21.885
Land Cost (M$)	6.142	6.139	6.153	6.336	6.550
Wiring Cost (M$)	4.037	4.370	4.695	5.080	5.612
Heliostat Cost (M$)	116.78	126.42	135.82	146.96	162.35
Total Cost					
(M$)	154.97	167.63	180.19	195.00	215.86
($/$m^2$)	134.41	134.21	134.37	134.39	134.66
Number of Heliostats	30,962	33,542	36,035	38,991	43,074
Area of Glass $(km)^2$	1.153	1.249	1.341	1.451	1.603
Ground Coverage	.203	.220	0.235	.247	.264
Figure of Merit ($/MWH)	101.68	101.44	101.52	101.78	103.28
	+ 0.16%	- 0.08%	baseline	+ 0.26	+ 1.73%
Avg. Interception	.867	.860	.854	.845	.828

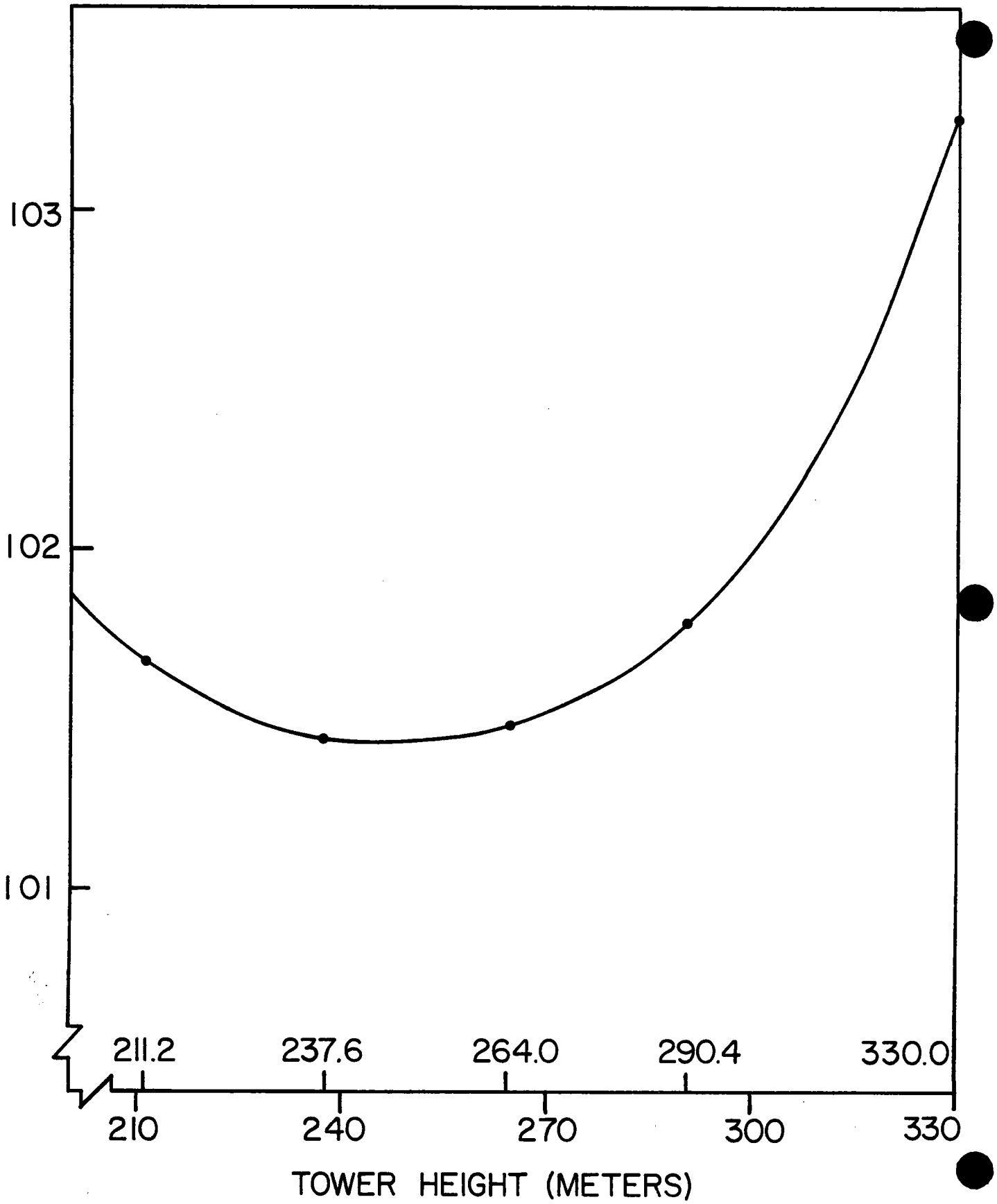

Figure 1.5f.1 The Figure of Merit Versus Tower Height

Figure 1.5f.2 shows a log-log plot of total thermal power at equinox noon (P_{EQ}) versus tower height. We estimate

$$P_{EQ} = 696.9\ (H_T/250)^{.736}\ MW_t,$$

or $$H_T = 250\ \ (P_{EQ}/696.9)^{1.359}\ \text{meters}$$

for optimized systems employing this cost model, aiming strategy, and receiver size. Changing any of these parameters will lead to a different set of coefficients; however, the simplicity and relatively wide range of applicability of this scaling law will facilitate the achievement of an optimized system having specified noon power. Thus, if one wished to use the baseline system components to produce 400 MW_t, the scaling law gives

$$H_T = 250\ (400.0/696.9)^{1.359} = 117.6\ \text{m}.$$

For 1000 MW_t we get H_T = 408.4 m, but in this case it will be cost effective to consider variations of receiver size or aiming strategy.

There is a significant difference in concept between this scaling law and the intuitively correct quadratic scaling law which results from a linear cost model and strict geometric scaling of a system. The quadratic law, applied to our current design optimized at H_T = 250 m, gives

$$P_{ED} = 696.9\ (H_T/250)^2\ MW_t.$$

In this case, the receiver and heliostats are also scaled by the same factor as the tower, and all component costs are assumed to scale as their areas. Thus, a 400 MW_t system of this type would require a tower height

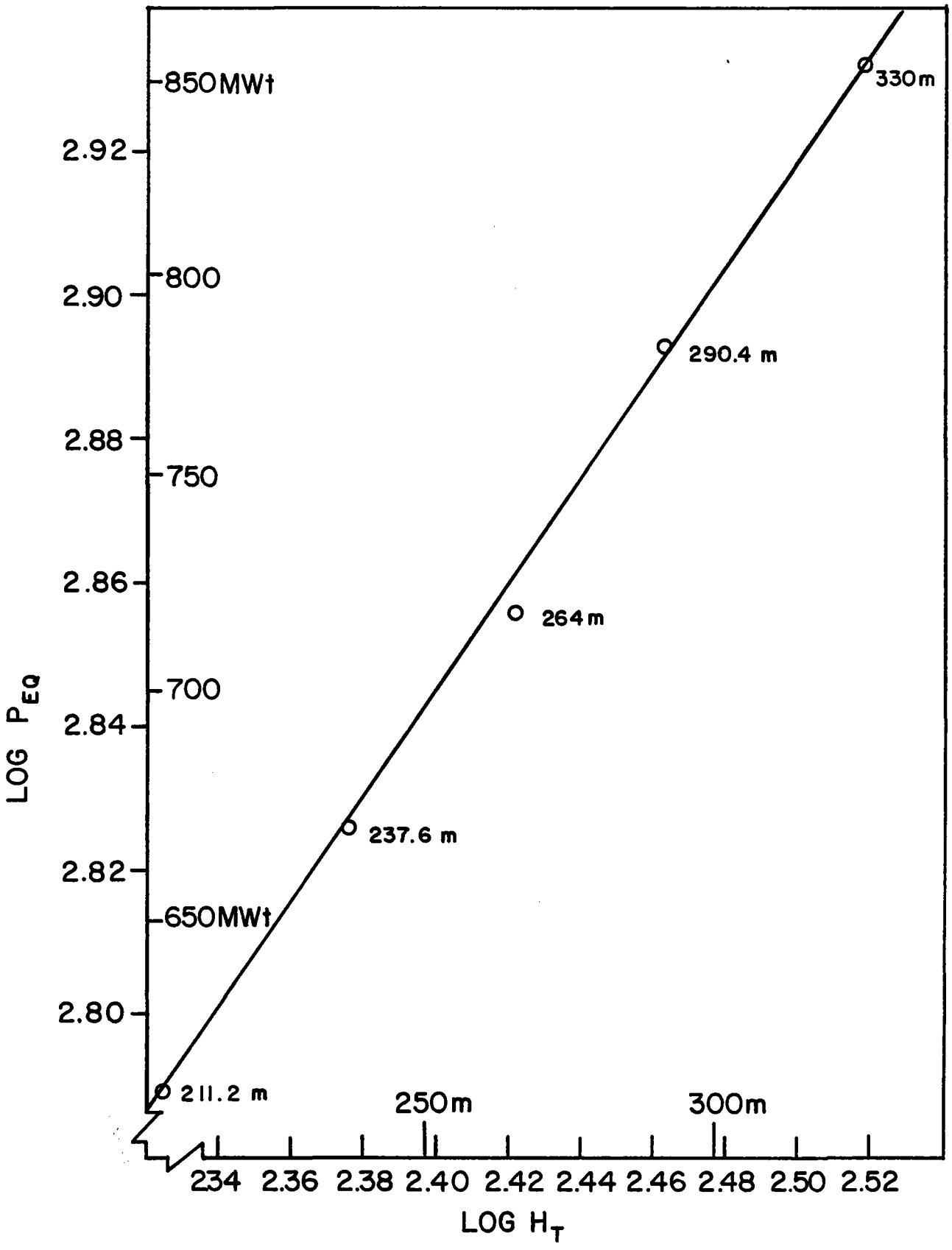

SLOPE = .736 INTERCEPT ON LOG E_T AXIS = 1.08

Figure 1.5f.2 Equinox Noon Power Versus Tower Height.

$$H_T = 250\ (400.0/696.9)^{\frac{1}{2}} = 189\ m.$$

However, the heliostats and receiver would also be reduced in linear dimension by the factor 0.758.

A combination of both scaling relations allows one to make a reasonable estimate of system size in many situations. For example, if the heliostat size were increased to 50 m^2 from the current 37.23 m^2 and one were willing to increase the receiver correspondingly, the quadratic scaling relationship gives a tower height of 290 m. Consequently,

$$P_{EQ} = 696.9\ (290/250)^2\ MW_t = 938\ MW_t$$

To return to a 250 m tower, with the larger heliostat and receiver, we apply the first scaling law in the form

$$P_{EQ} = 938\ (250/290)^{0.736}\ MWt = 840\ MW_t.$$

Table 1.5f.2 shows field boundaries for the various tower focal heights. Note that the cell size scales with the square root of tower height, while the cell area scales with the tower height, in this case cell area = 0.75 $(H_T)^2$. Thus, actual dimensions of the field increase with tower height as indicated by the land cost item in table 1.5f.1. The first matrix (of very small cells) is full to overflowing. Comparison with its neighbor indicates that a few more cells would be occupied if they were available. Because these are marginal cells and sparsely populated, they will have little effect on the results.

Field coefficients shown in table 1.5f.3 are reasonably well behaved. The most interesting noticeable exception is the first shape coefficient for the 330 m case. This change of two units in the constant term is compensated by changes in the θ and θ^2 terms in the interior of the field.

Table 1.5f.2 Trim Comparison for Tower Height Study

Tower Height	211.2 m	237.6 m	264.0 m
Cell Size	182.9 m	205.8 m	228.6 m
Trim Matrix	4 4 4 3 2 0 0 0 4 4 4 4 4 2 0 0 4 4 4 4 4 4 4 2 0 4 4 4 4 4 4 4 4 1 4 4 4 4 4 4 4 4 3 4 4 4 4 4 4 4 4 4 4 4 4 4 4 4 4 4 4 3 4 4 4 4 4 4 4 4 0 3 4 4 4 4 4 4 3 3 4 4 4 4 4 4 4 2 4 4 4 4 4 4 4 4 1 4 4 4 4 4 4 4 2 0 4 4 4 4 3 2 0 0 0 4 4 3 2 1 0 0 0 0	1 1 0 0 0 0 0 0 0 4 4 4 3 1 0 0 0 0 4 4 4 4 4 4 1 0 0 4 4 4 4 4 4 4 0 0 4 4 4 4 4 4 4 3 0 4 4 4 4 4 4 4 4 0 4 4 4 4 4 4 4 4 0 3 4 4 4 4 4 4 4 1 0 3 4 4 4 4 4 4 0 3 4 4 4 4 4 4 3 0 4 4 4 4 4 4 4 1 0 4 4 4 4 4 4 2 0 0 4 4 4 3 1 0 0 0 0 2 2 1 0 0 0 0 0 0	0 0 0 0 0 0 0 0 0 3 2 1 0 0 0 0 0 0 4 4 4 3 1 0 0 0 0 4 4 4 4 4 0 0 0 0 4 4 4 4 4 3 0 0 0 4 4 4 4 4 4 1 0 0 4 4 4 4 4 4 2 0 0 3 4 4 4 4 4 4 2 0 0 3 4 4 4 4 4 1 0 3 4 4 4 4 4 4 0 0 4 4 4 4 4 4 2 0 0 4 4 4 4 4 3 0 0 0 4 4 3 1 0 0 0 0 0 1 0 0 0 0 0 0 0 0
Heliostat Number	30,982	33,542	36,035

Tower Height	290.4 m	330.0 m
Cell Size	251.5 m	285.8 m
Trim Matrix	0 0 0 0 0 0 0 0 0 0 0 0 0 0 0 0 0 0 4 4 3 0 0 0 0 0 0 4 4 4 4 1 0 0 0 0 4 4 4 4 4 1 0 0 0 4 4 4 4 4 3 0 0 0 4 4 4 4 4 4 0 0 0 3 4 4 4 4 4 0 0 0 0 3 4 4 4 4 0 0 0 3 4 4 4 4 3 0 0 0 4 4 4 4 4 0 0 0 0 4 4 4 3 1 0 0 0 0 3 3 2 0 0 0 0 0 0 0 0 0 0 0 0 0 0 0	0 0 0 0 0 0 0 0 0 0 0 0 0 0 0 0 0 0 1 1 0 0 0 0 0 0 0 4 4 4 1 0 0 0 0 0 4 4 4 4 2 0 0 0 0 4 4 4 4 4 0 0 0 0 4 4 4 4 4 1 0 0 0 3 4 4 4 4 2 0 0 0 0 3 4 4 4 1 0 0 0 3 4 4 4 4 0 0 0 0 4 4 4 4 2 0 0 0 0 4 4 4 2 0 0 0 0 0 2 1 0 0 0 0 0 0 0 0 0 0 0 0 0 0 0 0
Heliostat Number	38,991	43,074

Table 1.5f.3 Field Coefficients for Tower Height Study

Tower Height in Meters	211.2	237.6	264.0	290.4	330.0
Coefficient					
Tower Height	211.2	237.6	264.0	290.4	330.0
First Radial	62.6196	63.6253	63.8487	66.6897	64.0265
Second Radial	- 0.6843	-0.7030	- 0.7279	- 0.8586	- 0.5896
Third Radial	0.02514	0.02500	0.02548	0.02692	0.02067
First Shape	1.4005	1.6557	1.8291	1.8186	4.1012
Second Shape	2.1461	2.1279	2.1162	2.1184	1.9127
Third Shape	-0.02286	0.02255	- 0.02236	- 0.02240	- 0.01814

1.5g The System Size Study

Table 1.5g.1 shows the effect on the baseline system of variations in the input figure of merit relative to the fully converged and optimal baseline figure of merit. In this context, the cell matching parameter for the optimization is proportional to heliostat cost/input figure of merit. Thus, decreasing the input figure of merit has about the same effect as increasing the heliostat cost leading, as intuition would suggest, to a smaller field of less densely packed heliostats which are used more efficiently to collect sunlight.

Use of the input figure of merit to adjust the system size in this manner results, of course, in non-optimal systems in contrast to all previous results of this study. We notice, however, that the output figure of merit varies by only 3.5% while the input figure of merit varies by 50% and the power by 100%. This method of varying system size is more convenient than a proper adjustment of tower height, which requires a new interception calculation. For adjustments of $\leq$ 20 percent in output power, the resulting figure of merit is within one or two percent of the optimum value, which is close enough for most trade studies.

Reference to table 1.5g.1 shows that the output figure of merit does not have its minimum value at the point of convergence in apparent contradiction to the theory of the optimization. The reason for this disparity can be seen in the cost model used in this study. In order to represent the added receiver cost associated with higher power levels, receiver and plumbing costs are scaled with the thermal power level. In this study, we have not taken the added iterative step of using these scaled costs in computing the Lagrangian parameter which provides the optimum cell matching parameter. Consequently, the results are skewed with a slope of about 0.1 at the converged figure of merit. To show the actual performance of the optimizer,

Table 1.5g.1 Performance Comparison for System Size Study

Figure of Merit Input in $/MWH	80.0	90.0	101.8 baseline	110.0	120.0
Equinox Noon Power (MW for 950 W/m^2)	399.26	572.12	722.04	810.76	890.58
Concentration	308.5	442.2	558.0	626.6	688.3
Annual Power (MMWH/yr)	0.953	1.390	1.775	2.005	2.211
(MWH/m^2/yr)	1.422	1.382	1.324	1.285	1.246
Fixed Cost (M$)	4.970	4.970	4.970	4.970	4.970
Tower Cost (M$)	9.480	9.480	9.480	9.480	9.480
Receiver Cost (M$)	12.91	16.38	19.070	20.560	21.850
Land Cost (M$)	2.667	4.319	6.153	7.466	8.821
Wiring Cost (M$)	2.346	3.520	4.695	5.459	6.208
Heliostat Cost (M$)	67.87	101.84	135.82	157.91	179.58
Total Cost (M$)	100.24	140.50	180.19	205.84	230.90
($/$m^2$)	149.54	139.66	134.37	131.95	130.16
Number of Heliostats	18006	27018	36035	41895	47643
Area of Glass $(km)^2$	0.670	1.006	1.341	1.560	1.774
Ground Coverage	.271	.252	.235	.226	.217
Figure of Merit($/MWH)	105.19	101.08	101.52	102.66	104.42
Corrected FOM($/MWH)	107.77	100.07	99.04	99.65	101.05
	+ 8.81%	+ 1.04%	baseline	+ 0.62%	+ 2.03%

we have recomputed the cost model to remove the receiver cost scaling effects. The result, labeled "corrected FOM," is also shown in figure 1.5g.1 and in the bottom line of table 1.5g.1. As expected, the optimizer shows a minimum FOM at the point of convergence. This lower FOM is, in fact, actually unrealistic, for receiver and plumbing costs will increase with power as our model shows. Iterating with a corrected receiver cost would correct the apparent discrepancy.

The wide variation in system size due to a change of the input figure of merit by ± 20% is striking. The output power (figure 1.5g.2) varies by a factor of 2.6, the ground area by a factor of 3.3, and the glass area by a factor of 2.64. In contrast to these gross variations, the system adjusts so that the annual power/m^2 (figure 1.5g.3) changes by only 12%, the system cost/m^2 (figure 1.5g.4) changes by 15%, and the output figure of merit by 3.5% (figure 1.5g.1). The 20 percent change in ground coverage is associated with the inclusion of more distant land (represented by the increase in land cost). In this distant land, blockage is a severe problem leading to a wide radial separation of heliostats. Consequently, as the input Figure of Merit increases, the ground coverage in each specific cell actually increases at the same time the average value decreases. The rim angle to the east changes from 17° to 9.4°.

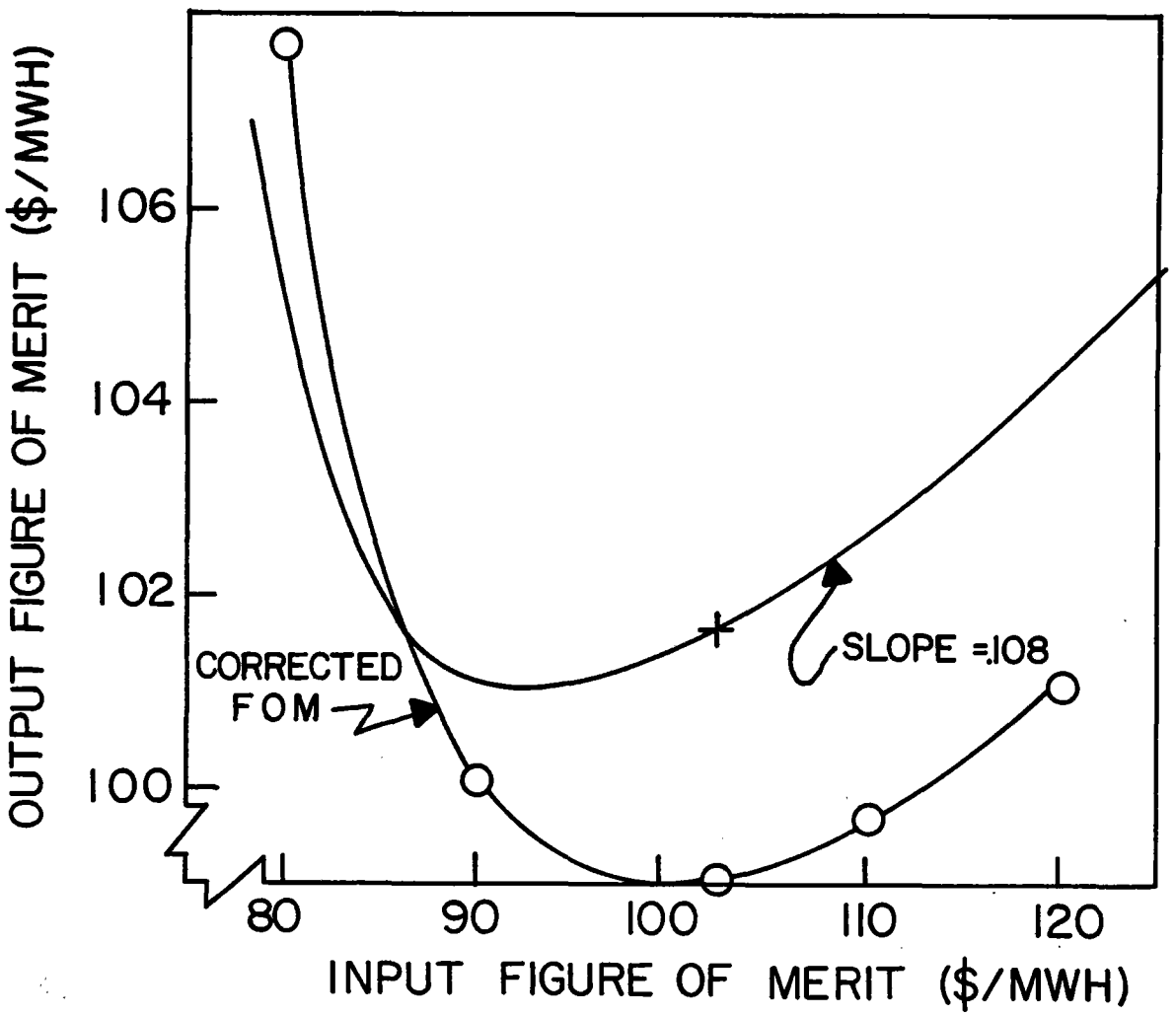

Figure 1.5g.1 Output Figure of Merit Versus Input Figure of Merit.

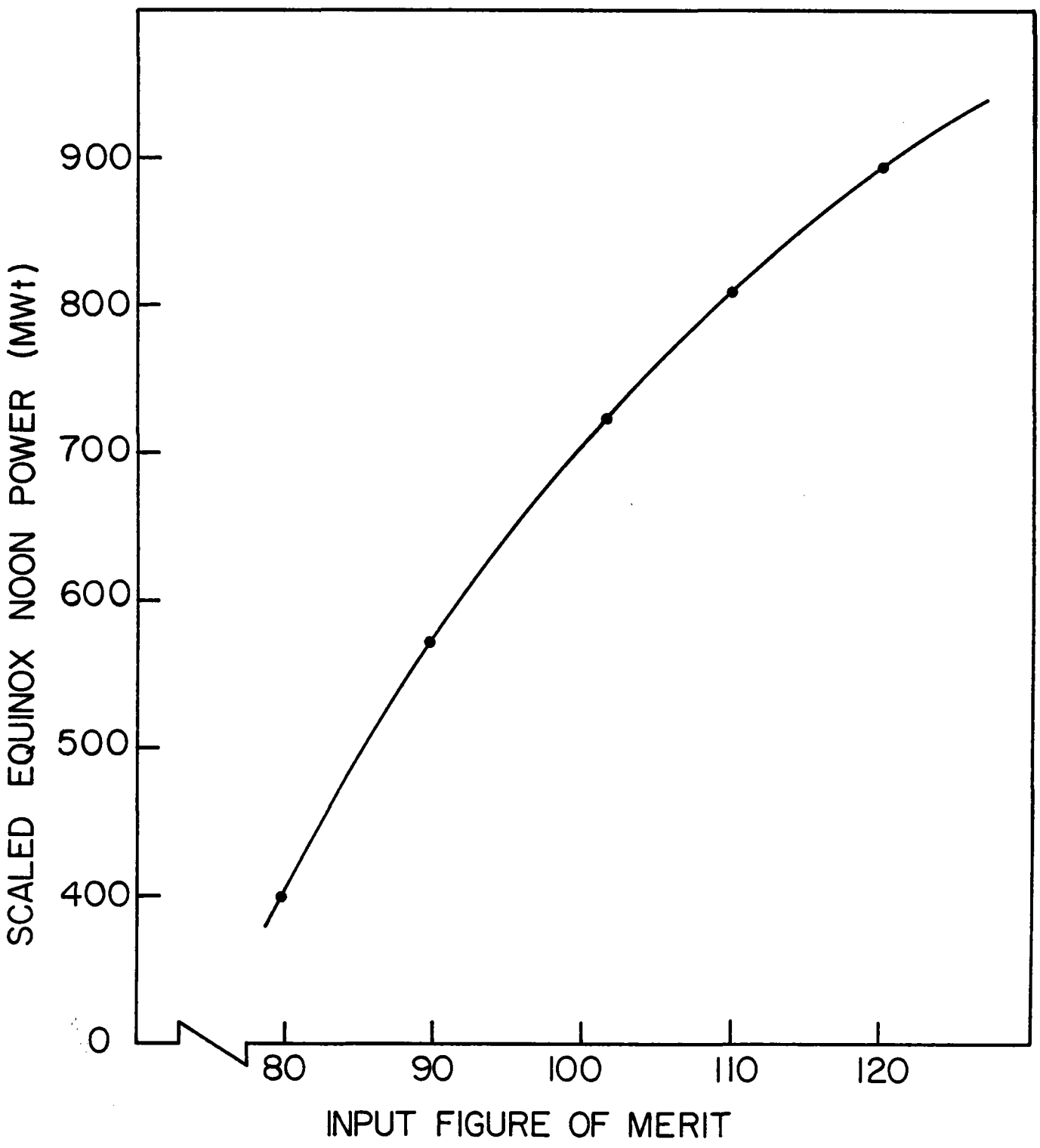

Figure 1.5g.2 Scaled Equinox Noon Power Versus Input Figure of Merit.

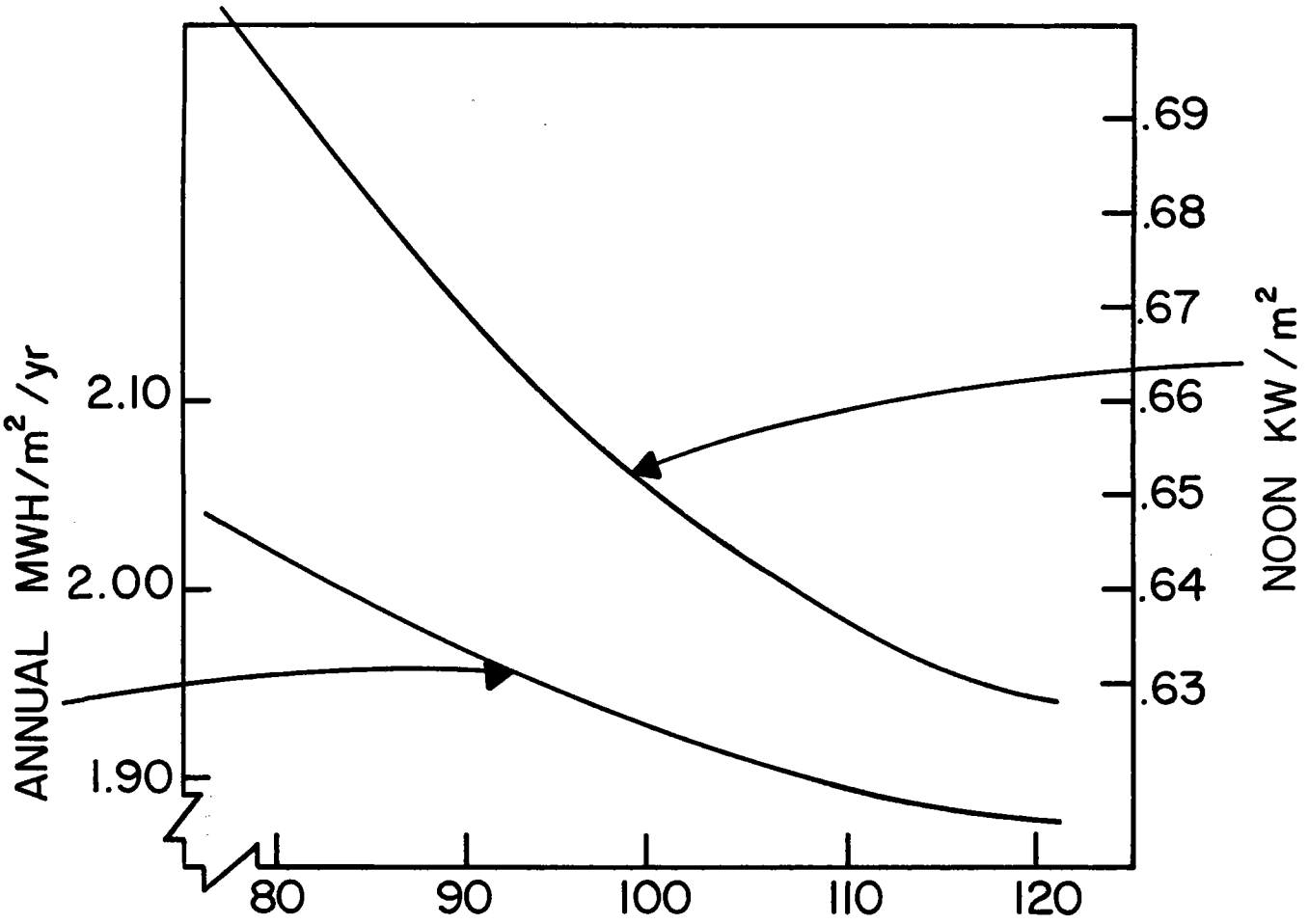

Figure 1.5g.3 Annual and Equinoom Power/m^2 Versus Input Figure of Merit.

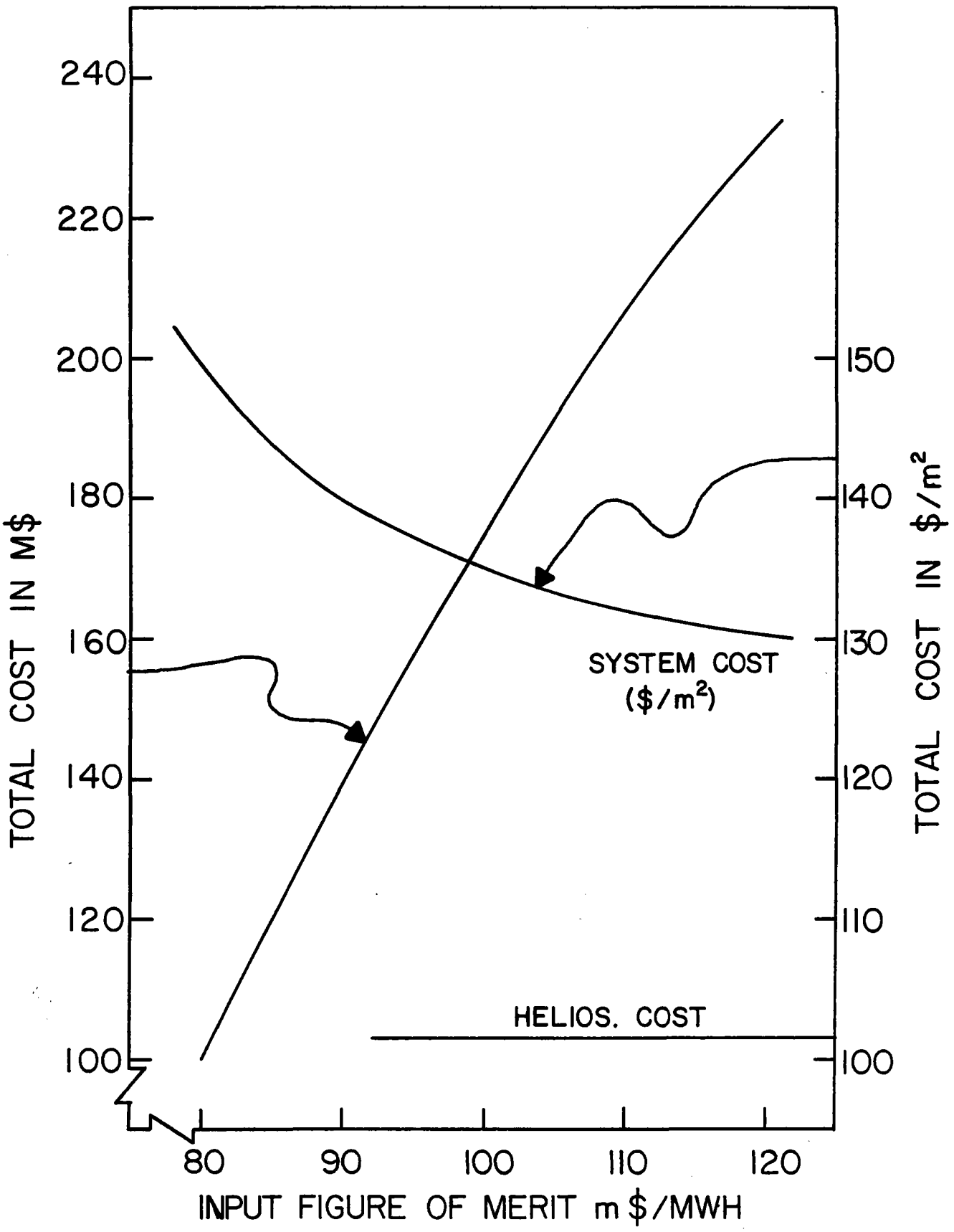

Figure 1.5g.4 Total Cost Versus Input Figure of Merit.

Changes in the field boundary are shown in table 1.5g.2. The enhancement of the southern field for higher input figures of merit is noteworthy. This occurs because the interception of distant heliostats to the north decreases rapidly with distance beyond the nominal boundary. In addition, because of blocking there are very few heliostats in these distant cells. In contrast, the performance of the southern field drops slowly due to increasing cosine effects.

Spacing coefficients for all five fields are shown in table 1.5g.3. Note that it is not safe to use these coefficients to extrapotate beyond the boundary of the defining field.

Table 1.5g.2 Trim Comparison for System Size Study

Input Figure of Merit	80.0	90.0	101.8
$/MWH	0 0 0 0 0 0 0 0 0	0 0 0 0 0 0 0 0 0	3 2 1 0 0 0 0 0
	0 0 0 0 0 0 0 0 0	3 3 1 0 0 0 0 0	4 4 4 3 1 0 0 0
	3 3 1 0 0 0 0 0	4 4 4 3 0 0 0 0	4 4 4 4 4 1 0 0
	4 4 4 2 0 0 0 0	4 4 4 4 3 0 0 0	4 4 4 4 4 3 0 0
Trim Matrix	4 4 4 4 1 0 0 0	4 4 4 4 4 1 0 0	4 4 4 4 4 4 1 0
	4 4 4 4 2 0 0 0	4 4 4 4 4 2 0 0	4 4 4 4 4 4 2 0
	3 4 4 4 2 0 0 0	3 4 4 4 4 2 0 0	3 4 4 4 4 4 2 0
	0 3 4 4 1 0 0 0	0 3 4 4 4 2 0 0	0 3 4 4 4 4 1 0
	3 4 4 2 0 0 0 0	3 4 4 4 4 0 0 0	3 4 4 4 4 4 0 0
	4 3 2 0 0 0 0 0	4 4 4 4 1 0 0 0	4 4 4 4 4 2 0 0
	0 0 0 0 0 0 0 0	4 4 2 1 0 0 0 0	4 4 4 4 3 0 0 0
	0 0 0 0 0 0 0 0	1 0 0 0 0 0 0 0	4 4 3 1 0 0 0 0
	0 0 0 0 0 0 0 0	0 0 0 0 0 0 0 0	1 0 0 0 0 0 0 0
Heliostat Number	18,006	27,018	36,035

Input Figure of Merit	110.0	120.0
$/MWH	0 0 0 0 0 0 0 0 0	3 3 1 0 0 0 0 0
	4 4 4 2 0 0 0 0	4 4 4 4 2 0 0 0
	4 4 4 4 3 0 0 0	4 4 4 4 4 3 0 0
	4 4 4 4 4 3 0 0	4 4 4 4 4 4 2 0
	4 4 4 4 4 4 2 0	4 4 4 4 4 4 4 0
	4 4 4 4 4 4 4 0	4 4 4 4 4 4 4 2
TRIM MATRIX	4 4 4 4 4 4 4 0	4 4 4 4 4 4 4 3
	3 4 4 4 4 4 4 0	3 4 4 4 4 4 4 3
	0 3 4 4 4 4 4 0	0 3 4 4 4 4 4 2
	3 4 4 4 4 4 3 0	3 4 4 4 4 4 4 1
	4 4 4 4 4 4 1 0	4 4 4 4 4 4 4 0
	4 4 4 4 4 2 0 0	4 4 4 4 4 4 1 0
	4 4 4 4 2 0 0 0	4 4 4 4 4 2 0 0
	3 3 2 0 0 0 0 0	4 4 4 3 1 0 0 0
HELIOSTAT NUMBER	41895	47643

Table 1.5g.3 Field Coefficients for System Size Study

Figure of Merit	80.0	90.0	101.8	110.0	120.0
Input in $/MWH					
Coefficient					
First Radial	60.7663	60.7329	63.8487	63.3199	62.5100
Second Radial	- 0.1303	- 0.2265	- 0.7279	- 0.7653	- 0.7794
Third Radial	0.01040	0.01311	0.02548	0.02684	0.02799
First Shape	3.2195	2.9079	1.8291	2.3155	2.5648
Second Shape	1.9509	1.997179	2.1162	2.0676	2.0351
Third Shape	- 0.01643	- 0.01873	- 0.02236	- 0.02171	- 0.02139

1.6 SUMMARY AND CONCLUSIONS

The RCELL computer program provides a cellwise method for the optimization of large central receiver systems on an annual basis. This program contains an adequate model of the solar central receiver system including, the optical behavior, the economic model, and a model for losses; the power conversion system is not modeled. The optimization determines the best deployment of glass in the collector field assuming fixed geometry for the individual heliostat, tower, and receiver. A cell matching condition ensures that all heliostats are working optimally. The collector field utilizes radial-stagger neighborhoods (which have the peak-through feature), and the optimization adjusts the radial and azimuthal spacing coordinates in each cell. A nearly complete set of performance outputs is available for the optimized system.

This report contains six comparative studies corresponding to parametric variations of field slope, site latitude, heliostat cost, land cost, tower height, and system size.

The slope study shows a 1.5 percent improvement in figure of merit for 10° slopes at 35° latitude compared to the level baseline system. For surround fields of the type considered here, the optimum slope is roughly 10° and the optimum is due to changes in the available energy rather than cost. This result assumes that the cost model is independent of slope. A differential cost of $\$2.6 \times 10^6$ would cancel the advantage of the 10° slope. This would correspond to an additional cost of $1700/acre for the sloping system. Clearly, a small northern slope is acceptable, but for surround fields it is not as desirable as originally thought. The sloping system looks somewhat like an unsloped system with a shorter tower (figure 1.5b.2).

The latitude study compares optimized systems at latitudes 25°, 35°, and 45° including weather models for appropriate parts of northern Mexico and western USA. The insolation is based on Allen's clear air model plus a monthly weather model shown in table 1.5c.3. After including site specific factors such as elevation of site, visual range, mean turbidity factor, mean precipitable water, and mean percent of possible sun hours, we do not expect to obtain the same dependance of insolation on latitude that we would find if the sky were always clear. Consequently, the annual insolation at 25° is less than at 35°, mostly because of the increased precipitable water and turbidity factor. The 45° insolation is greatly reduced by the effect of low percent possible sun, caused mainly by high winter time cloud cover. For longitudes corresponding to northern Mexico and western USA, figure 1.5c.1 shows a 50 percent variation in figure of merit with latitudes. Most of this variation is due to the availability of insolation. The efficiency of the optimized collector varies only a few percent.

The heliostat cost study compares optimized systems using heliostat costs of \$81.00/m^2, \$101.25/m^2, and \$121.50/m^2, which correspond to the baseline ±20 percent. The resulting figures of merit are 86.49 \$/$aMWH_t$, 101.45 \$/$aMWH_t$, and 116.19 \$/$aMWH_t$, increasing with heliostat cost. The lower figure of merit is 14.7% below baseline and the higher figure of merit is 12.7% above baseline, which shows that the optimization is fighting rather effectively against the increased heliostat cost, even though the baseline system cost is only 32% more than that of the heliostats alone.

The land cost study compares optimized systems using land costs of 1.08 \$/m^2 (baseline), 3.00 \$/m^2, and 10.00 \$/m^2. A ten-fold increase in land cost makes a 23% increase in the figure of merit, a 25% increase in average ground coverage, and a 27% increase in the $aMWH_t/m^2$(land). By deleting the

land cost, this study also shows the effect on the figure of merit of compressed fields. For an available piece of ground of restricted area, this study indicates that one can increase the energy collected per unit land area by 25 percent at a cost per MWH differential of 1.6 percent.

The tower height study compares optimized systems having five different focal heights but unchanged heliostat size and unchanged receiver size. A fit on the results gives the equinox noon power (scaled to 950 W/m^2 insolation, P_{EQ}) in terms of the focal height, H_T.

$$P_{EQ} = 696.9\ (H_T/250m)^{.736} \text{ in } MW_t.$$

In contrast, if we assume that receiver and heliostat dimensions scale with the focal height and that costs scale generally with power collected, then

$$P_{EQ} = 696.9\ (H_T/250)^2.$$

Under baseline assumptions, using an optimum Hi-Lo aiming strategy suitable for the water/steam receiver and assuming a specific fixed receiver size as mentioned, we find an optimum tower height of roughly 250 m corresponding to an Equinox noon power level of 670 MW_t, but the minimum in the figure of merit is very broad.

The system size study utilized the influence of the input figure of merit. Figure 1.5g.2 shows that system cost is roughly a linear function of the input figure of merit over the range of the study. This is the result of adjustments in the area of the field and in the area of glass in the field. This method of varying system size is more convenient than a proper adjustment of tower height, which requires a new interception calculation. For adjustments of $\leq$ 20 percent in output power, the resulting figure of merit is within one or two percent of the optimum value, close enough for many trade studies. Figure 1.5g.1 shows that the adjusted figure of merit (FOM) is a minimum when the input and output figures of merit are equal. This result confirms

the theoretical concept of the RCELL program.

In conclusion, we find that RCELL is a useful approach to optimization, and we expect to use its optimized results in future studies of the Central Receiver System. Although several important parameters were overlooked in these studies, we feel it is important to report results using a consistent set of costs in order to show the effects of self consistent variations in both the field boundary and the local heliostat spacings within that boundary in response to a reasonable set of variations about a common baseline. This baseline is representative of the commercial design of which the Barstow 10 MW_e pilot plant (Solar One) is a scaled representative. Advanced systems employing the surround field concept vary from the Solar One design primarily in the working fluid, the receiver peak flux limitation, and in the efficiency of the thermodynamic conversion cycle. None of these variations will strongly affect the design of the systems considered here, so reasonably straightforward application of these results to continuing studies is possible.

Appendix I

1.7 THEORY OF OPTIMIZATION PROCEDURE

For purposes of optimization, we assume that the objective of the Central Receiver System is to deliver to the ground solar energy in the form of a heated working fluid. The effect of the temperature required to generate a salable product is reflected in increased component costs for materials at elevated temperatures and in increased receiver losses to radiation, conduction and convection. Subject to specific system constraints such as peak flux limits and net heat gain from all areas of the receiver, a preliminary receiver design is generated, in the case considered in the body of the report, as a cylinder 17 m in diameter and 25 m tall designed to handle about 500 MW_t. Detailed cost and performance models for the major subsystems are assumed to be available.

The objective of the optimization procedure is to define that system which will deliver energy to the ground at the lowest cost per joule (or Megawatt hour), subject to the specified constraints. One can readily calculate the true cost of the delivered energy using any desired economic model for interest, taxes, discount rates, etc., if provided the total capital cost of the installation, the total energy produced in an average year, and the annual operation and maintenance costs. Standard routines exist for computing energy cost from these data. Ideally, one would wish to include O&M costs in the optimization procedures. This can readily be done by converting them to a present value, again using standard economic methods, and including the present value of O ε M with the capital costs for each subsystem.

In either case, the objective function for the optimization can be taken to be the Total System Cost (with or without PV of O&M) divided by the annual energy delivered.

In the discussion which follows it may be convenient to refer to the nomenclature in section 1.11, Glossary of Terms, pp. 155-6.

1.7.1 System Performance Model and Figure of Merit

The figure of merit F is defined as the ratio of the total system cost C_s to the total energy E_T, which is output by the receiver during a suitable period of time. F may also be thought of as a cost-benefit ratio. Let

$$F = C_s/E_T = F^*/\lambda_T,$$

where

$$F^* = C_s/S_o A_T \qquad \text{in } (\$/MWH_t),$$

$$S_o = \int d\tau\, \sigma_o(\tau) \qquad \text{in } (MWH_t/m^2),$$

$$A_T = \sum_c A_c \text{ in } (m^2),$$

and

$$\lambda_T = E_T/S_o A_T = F^*/F,$$

which is the net system efficiency and is dimensionless. A_c is the total area of glass in the c^{th} cell, and A_T is the total area of glass in the whole system. S_o is the total direct beam solar energy/m^2 at normal incidence over the given time period. For the present purposes, this period will be the sunlight portion of a year for which the solar elevation exceeds 10^o. F* represents the figure of merit for an ideal system with no losses and, therefore,

$$\lambda_T < 1,$$

for real systems.

The total energy E_T can be expressed as a sum over cells; for this purpose, we write,

$$E_T = \sum_c E_c \eta_c,$$

where η_c is the receiver interception fraction for the c^{th} cell and E_c is the total energy which is redirected towards the receiver by the c^{th} cell. λ_T is a measure of the efficiency for collecting and transfering sunlight to the working fluid. We assume for simplicity that η_c is time independent and that E_c can be adequately approximated by the behavior of a representative heliostat at the center of the cell. The time independence of η_c is well verified for flat heliostats but is only approximately valid for focusing or canted heliostats. Let the energy avaialable from a single cell be

$$E_c = \lambda_c S_o A_c,$$

and, as previously,

$$E_T = \lambda_T S_o A_T,$$

so that

$$\lambda_T = \sum_c \lambda_c \eta_c z_c,$$

where z_c is the fraction of the glass which is in the c^{th} cell. Clearly,

$$z_c = A_c/A_T, \text{ and}$$

$$1 = \sum_c z_c.$$

The two computer programs, NCELL and RCELL, output the quantity

$$g_c = E_c/A_c = \lambda_c S_o,$$

which represents the aMWH/m^2 of redirected energy from each cell, versus parameters which represent various arrangements of heliostats in the cell. The CYLN program outputs the interception fraction η_c, for an external receiver. Actually, the interceptions of vertical columns of nodes are summed to generate panel interception fractions so that η_c can be formulated for various choices of panels

$$\eta_c(P) = \sum_{p \varepsilon P} \eta_{cp},$$

where P is a set of panels and η_{cp} is the interception fraction for panel p illuminated by the reflected energy from the c^{th} cell.

The parametrization of the cell is not the same in the NCELL and the RCELL programs. For NCELL, we introduce the parameters

$$\rho_x = D_M/D_X \text{ such that } 0 \leq \rho_x \leq 1,$$

$$\rho_y = D_M/D_y \text{ such that } 0 \leq \rho_y \leq 1,$$

where D_M is the heliostat width. D_x and D_y are the heliostat spacings in an assumed north-south cornfield. In this approach, we can not afford the CPU-time required to average over a whole year because we require 121 samples of (ρ_x, ρ_y) covering their entire range, producing shading and blocking "footprints". See reference 2. For RCELL we consider staggers as well as cornfields, and we are prepared to deal with arbitrary orientations of the cell. For the current 100 MW_e study we are interested only in north-south or radial orientations. However, in RCELL we get an average over the whole year at the expense of restricting our output sample to a fraction of the range of the parameters. In this case, the parameters are

$$x = D_x/D_M = 1/\rho_x$$

and

$$y = D_y/D_M = 1/\rho_y.$$

Typically, we will output λ_c and other quantities as 4 x 4 matrices. In reality, g_c and hence λ_c depend on the heliostat location coordinates for all of the heliostats in cell c; however, by assuming a cell model, we have reduced the number of independent parameters to $2N_B$, where N_B is the relevant number of neighbors surrounding the representative heliostat. For the 100 MW_e study, we further restrict the number of independent parameters by limiting the arrangements of neighbors to the four options:

1 Radial Oriented Cornfields,

2 Radial Oriented Staggers,

3 North-South Oriented Cornfields, and

4 North-South Oriented Staggers.

For each of these options there are two independent parameters x_c and y_c, which represent the separation in heliostat widths between neighbors in the two independent directions for the c^{th} cell. Consequently, the area of glass in the c^{th} cell is given by

$$A_c = A_L f_c,$$

where

$$f_c = A_H \, (\gamma_c x_c y_c D_M^2)^{-1}$$

is the ground coverage factor and A_L is the area of the cell itself. A_H is

the area of the heliostat, and $\gamma_c x_c y_c D_M^2$ is the area of land required by each heliostat.

$$\gamma_c = \begin{cases} 1/2 \text{ for staggered cells, and} \\ 1 \text{ for cornfield cells.} \end{cases}$$

A "Standard uniform cell" array is defined by $A_L = D_c^2$ with

$$D_c = \sqrt{N/4}\ H,$$

where H is the focal height of the tower, i.e., the vertical distance from the heliostat center to the receiver center, and N is a small integer called the order. Using our current model we find a need for cells of order 3, hence

$$D_c = \sqrt{3/4}\ H = .866\ H$$

for shorter towers or lower cost heliostats 5th order cells may be required, while for a high resolution study many cells of order 2 or even 1 may be used. In general,

$$f_c = a_c / x_c y_c,$$

where

$$a_c = A_H / D_M^2 \gamma_c = R_H / \gamma_c.$$

It is convenient to introduce the dimensionless parameter $R_H = A_H / D_M^2$ which corrects the ground coverage factor f_c for the shape of the heliostat. For an ideal square heliostat $R_H = 1.0$. In the present case, we have a square heliostat with a central slot and six segments, such that $R_H = .8972$. We may also consider an octagonal heliostat for which $R_H = .8284$.

1.7.2 The Optimization

We now have expressions for λ_c or equivalently g_c as functions of (x_c, y_c). However, in order to proceed with the optimization we will need an alternative parameterization in terms f_c and t_c which form an orthogonal system of hyperbolas. Let

$$f_c = a_c / x_c y_c$$

and

$$t_c = 1/2\ (x_c^2 - y_c^2),$$

so that

$$\lambda_c(x_c, y_c) = \lambda_c(f_c, t_c).$$

We can prove that the curves of constant f_c intersect the curves of constant t_c perpendicularly by considering the variations of f_c and t_c. Let

$$\delta t_c = 0 = x_c \delta x_c - y_c \delta y_c = \vec{u}_t \cdot \vec{\delta}_t,$$

and

$$\delta f_c = 0 = \delta(x_c y_c) = y_c \delta x_c + x_c \delta y_c = \vec{u}_f \cdot \vec{\delta}_f,$$

where $\vec{\delta}_t$ is tangent to the $\delta t_c = 0$ curve and $\vec{\delta}_f$ is tangent to the $\delta f_c = 0$ curve. Clearly

$$\vec{u}_t = (x_c, -y_c)(x_c^2 + y_c^2)^{-\frac{1}{2}}$$

and

$$\vec{u}_f = (y_c, x_c)\ (x_c^2 + y_c^2)^{-\frac{1}{2}}$$

represent unit vectors perpendicular to $\vec{\delta}_t$ and $\vec{\delta}_f$ respectively. A direct

calculation gives

$$\vec{u}_t \cdot \vec{u}_f = 0,$$

and, consequently,

$$\vec{\delta}_t \cdot \vec{\delta}_f = 0,$$

which proves the orthogonality of t and f. We will soon use the direction derivatives

$$\partial_t g = \vec{u}_t \cdot \vec{\nabla}_g$$

and

$$\partial_f g = \vec{u}_f \cdot \vec{\nabla}_g$$

in order to solve for the optimization.

The optimization of the collector field is conveniently divided into two steps. First, we will find the conditions for an optimum having a given amount of glass A_T, and then we will vary A_T to determine its optimum value.

Assuming that C_s is a function of A_T only, for a fixed amount of glass, $\delta C_s = 0$, and

$$\delta_F = - \delta E_T C_s / E_T^2 = 0,$$

which implies that

$$\delta E_T = 0.$$

A variation of E_T, gives

$$\delta E_T = \sum_c (\lambda_c \delta A_c + A_c \delta \lambda_c) \eta_c S_o,$$

where

$$\delta\lambda_c = \delta f_c \, \partial_F \lambda_c + \delta t_c \, \partial_t \lambda_c$$

and

$$0 = \sum_c \lambda f_c$$

because the total amount of glass is fixed. Each δt_c is an independent variation, so that the coefficient of δt_c in the expression for δE_T must vanish at the maximum total energy point $\{(f_c^*, t_c^*)\}$. Consequently, we have

$$\partial_t \lambda_c \, (f_c^*, t_c^*) = 0$$

for all cells. We now see that

$$\delta\lambda_c = \delta f_c \partial_f \lambda_c,$$

and, remembering that $A_c = A_L f_c$,

$$\delta E_T = \sum_c (\lambda_c + f_c \partial_f \lambda_c) \, \eta_c \delta f_c A_L S_o.$$

The set of δf_c variables has a constraint, which must be eliminated before the corresponding optimum condition can be determined. We can solve the constraint condition for any δf_N by writing

$$\delta f_N = - \sum_c^{N-1} \delta f_c.$$

For simplicity, we define

$$\mu_c = (\lambda_c + f_c \partial_f \lambda_c)\eta_c,$$

so that

$$\delta E_T / S_o A_L = \sum_c \mu_c \, \delta f_c = \sum_c^{N-1} \mu_c \delta f_c + \mu_N \delta f_N .$$

After substituting for δf_N, and making use of the fact that $\delta E_T = 0$, we have

$$0 = \sum_c^{N-1} (\mu_c - \mu_N) \, \delta f_c ,$$

where the N-1 variables δf_c are independent, so that

$$\tilde{\mu} = \mu_N = \mu_c$$

for all cells.

Since part of the total system cost is independent of A_T, the total glass area, and the other part is dependent on A_T, we expect to find an optimum value for A_T by considering those variations which change A_T without violating the previously established conditions for the optimum. Thus, at the maximum total energy point f_c^*, t_c^*, we have

$$\tilde{\mu} = \mu_c (f_c^*, t_c^*),$$

and

$$\partial_t \lambda_c (f_c^*, t_c^*) = 0.$$

A variation of the figure of merit gives

$$\delta F = 0 = \delta C_s / E_T - \delta E_T C_s / E_T^2 .$$

Consequently,

$$\delta E_T / \delta A_T = (\delta C_s / \delta A_T) \, (E_T / C_s) = (\partial_A C_s)/F .$$

A variation of the total energy gives

$$\delta E_T = (\sum_c \mu_c \delta f_c)\ A_L S_o = \tilde{\mu} \delta A_T S_o,$$

so that

$$\delta E_T / \delta A_T = \tilde{\mu} S_o = (\partial_A C_s)/F,$$

and, finally,

$$\tilde{\mu} = (\partial_A C_s)(FS_o)^{-1}.$$

Assuming a linear cost model, we can write,

$$C_s = C_o + C_H A_T$$

and consequently

$$\tilde{\mu} = C_H (FS)_o)^{-1}.$$

As shown in the Data Flow Schematic, table 1.4.2, page 1-36, the optimum value of the figure of merit F is output by the MODEL subroutine. Consequently, we are able to calculate the quantity

$$\tilde{E}_L = \tilde{\mu} S_o / \eta_c = C_H / (F \eta_c),$$

which we call the Lagrangian parameter in aMWH/m^2 for cell c. Similarly, we can define the functions

$$E_L(x_c y_c) = S_o \mu_c / \eta_c = S_o (\lambda_c + f_c \partial_f \lambda_c),$$

and

$$E_T(x_c y_c) = S_o \partial_t \lambda_c,$$

which are output by the RCELL program for a 3 x 3 sample of the parameter space $(x_c y_c)$. The optimum point satisfies the equations

$$\tilde{E}_L = E_L(x_c y_c) \text{ and } E_T(x_c y_c) = 0.$$

Each of these equations represents a curve in the (x_c, y_c) plane. The intersection is determined by an interpolation procedure in RCELL.

1.7.3 The Effect of Land and Wiring Costs

To this point, we have assumed that the system cost is a function of A_T, which is the total area of glass. However, the cost of land and the cost of control wiring for the heliostats are not directly related to A_T. The following cost model is typical of the data required, although alternative wiring schemes can equally well be modeled.

Input Data

C_H = 66.0 \$/m^2 for cost of heliostats and guidance devices.

C_L = 1.08 \$/m^2 for cost of land and site preparation.

C_W = 3.30 \$/m for cost of wiring.

D_M = 6.502 m for width of heliostats.

N_o = 25 = number of heliostats/field controller.

Output Requirements

$A_H = D_M^2$ = area of glass/heliostat.

$A_L = D_c^2$ = area of land/cell.

$N_H = f_c A_L / A_H$ = Number of Heliostats/Cell.

$N_F = N_H / N_O$ = Number of Field Controllers/Cell.

$D_H = C_H f_c A_L$ = Cost of Heliostats/Cell.

$D_L = C_L A_L$ = Cost of Land/Cell.

$D_W = C_W W_c$ = Cost of Wiring/Cell,

where W_c is the length of wiring required for the cell. Each field controller serves N_o heliostats. These heliostats may be considered to be on a single arc of the field in which case the effective wire length per heliostat is just $y \cdot D_M$. This approach leads to somewhat different results but essentially the same analysis as that given here. Here we assume the heliostats fed by a single field controller are grouped in a land area A_F, which is given by

$$A_F = N_o A_H / f_c.$$

The mean radius of this area is given by

$$R_F = 2/3 \ (A_F/\pi)^{\frac{1}{2}},$$

and then W_c is given by

$$W_c = N_F N_o R_F = N_H R_F.$$

After substituting for N_F and R_F, we have

$$W_c = (f_c A_L / A_H) \cdot 2/3 \ (N_o A_H / \pi f_c)^{\frac{1}{2}}$$

$$= 2/3 (N_o f_c / \pi)^{\frac{1}{2}} A_L / D_M$$

$$= B A_L f_c^{\frac{1}{2}},$$

where the given input data result in

$$B = 2/3 \ (N_o/\pi)^{\frac{1}{2}} / D_M = .289 \text{ meters}^{-1}.$$

Land costs and wiring costs both tend to increase the effective cost of heliostats in distant cells that must have a low density of glass because of

shading and blocking requirements. Consequently, these costs can play an important role in determining the outer boundary of the collector field (i.e., the trim). Let ϕ_c be the fraction of the c^{th} cell covered by the array of heliostats. The covered portion of the cell has the density of coverage given by f_c, as previously. The area of glass in cell c is now given by

$$A_c = \phi_c f_c A_L = A_L a_c \phi_c / x_c y_c,$$

and ϕ_c becomes an additional parameter that must be determined by the optimization. The total system cost becomes

$$C_s = C_o + C_H A_T + C_+,$$

where

$$C_+ = C_L A_L \sum_c \phi_c + C_W B A_L \sum_c \phi_c f_c^{\frac{1}{2}}.$$

A variation of the cost gives

$$\delta C_s = C_H A_L \sum_c \delta(\phi_c f_c) + C_L A_L \sum_c \delta\phi_c + C_W B A_L \sum_c \delta(\phi_c f_c^{\frac{1}{2}}).$$

Consequently, $\delta C_s = 0$ implies that

$$0 = \Sigma\, [\delta f_c \phi_c (1 + \tfrac{1}{2}\beta\, f_c^{-\frac{1}{2}}) + \delta\phi_c (f_c + \alpha + \beta f_c^{\frac{1}{2}})],$$

where

$$\alpha = C_L/C_H = .0164,$$

and

$$\beta = C_W B/C_H = .0145.$$

A variation of the total energy gives

$$\delta E_T = \delta(\sum_c \lambda_c A_c \eta_c) S_o,$$

where

$$A_c = \phi_c f_c A_L,$$

so that

$$\delta E_T = \sum_c (\delta\lambda_c \phi_c f_c + \lambda_c \delta\phi_c f_c + \lambda_c \phi_c \delta f_c)\, \eta_c A_L S_o,$$

where

$$\delta\lambda_c = \delta f_c \partial_f \lambda_c + \delta t_c \partial_t \lambda_c = \delta f_c \partial_f \lambda_c,$$

as previously stated. We can immediately ignore the term containing δt_c, for this is the only term containing δt_c and, therefore, $\partial_t \lambda_c = 0$ is a condition for the optimization, as before.

The first step in the optimization requires $\delta E_T = 0$ and $\delta C_s = 0$. The δE_T equation can be simplified by introducing μ_c as before. Consequently, after cancelling the factors $A_L S_o$, the $\delta E_T = 0$ equation can be written as

$$0 = \sum_c (\mu_c \phi_c \delta f_c + \lambda_c f_c \eta_c\, \delta\phi_c),$$

which gives

$$\mu_N \phi_N \delta f_N = -\left[\sum_c^{N-1} \mu_c \phi_c \delta f_c + \sum_c^{N} \lambda_c f_c \eta_c \delta\phi_c\right].$$

After substituting the above expression for $\mu_N \phi_N \delta f_N$ into the $\delta C_s = 0$ equation, we have

$$0 = \sum_c^{N-1} [\mu_N \phi_N \phi_c (1 + \tfrac{1}{2}\beta f_c^{-\frac{1}{2}}) - \mu_c \phi_c \phi_N (1 + \tfrac{1}{2}\beta f_N^{-\frac{1}{2}})]\, \delta f_c$$

$$+ \sum_c^{N} [\mu_N \phi_N (f_c + \alpha + \beta f_c^{\frac{1}{2}}) - \lambda_c f_c \eta_c \phi_N (1 + \tfrac{1}{2}\beta f_N^{-\frac{1}{2}})]\, \delta\phi_c.$$

Each of the variations of δf_c and $\delta\phi_c$ which occur in the above equation are independent and, consequently, their coefficients must vanish. Let

$$\tilde{v} = \mu_N(1 + \tfrac{1}{2}\beta f_N^{-\frac{1}{2}})^{-1} \qquad \text{and}$$

$$v_c = \mu_c\ (1 + \tfrac{1}{2}\beta f_c^{-\frac{1}{2}})^{-1}.$$

The coefficient of δf_c gives

$$v_c = \tilde{v}, \qquad \text{if } \phi_c \neq 0 \neq \phi_N$$

and the coefficient of $\delta\phi_c$ gives

$$\lambda_c f_c \eta_c = \tilde{v}\ (f_c + \alpha + \beta f_c^{\frac{1}{2}}), \qquad \text{if } \phi_N \neq 0.$$

At first sight, these equations appear to represent conflicting requirements for the ground coverage factor f_c. However, we realize that $\phi_c \equiv 1$ for the interior cells, so that the coefficient of $\delta\phi_c$ does not occur for these cells. Hence, for interior cells, the one optimum requirement can be written as

$$\tilde{v} = \mu_N\ (1 + \tfrac{1}{2}\beta/f_n^{\frac{1}{2}})^{-1} = \mu_c\ (1 + \tfrac{1}{2}\beta/f_c^{\frac{1}{2}})^{-1},$$

where we have assumed that the N^{th} cell is interior, so that $\phi_N = 1$.

For an exterior cell $\phi_c \equiv 0$; again the coefficient of $\delta\phi_c$ does not occur. A true boundary cell might have some intermediate value of ϕ_c; however, this would imply a conflicting requirement for f_c, which will suffice to determine the boundary. To see how this works, let

$$v_c(f_c^*, t_c^*) = \tilde{v},$$

and let

$$\lambda_c \hat{f}_c \eta_c = \tilde{v}\ (\alpha + \beta \hat{f}_c^{\frac{1}{2}} + \hat{f}_c),$$

where f* and $\hat{f}$ will be equal for a boundary cell and not otherwise.

Figure 1.7.1 indicates a method of solution. Notice that $\partial_f \lambda_c \leq 0$; $\partial_f \lambda_c = 0$ implies no shading or blocking, so that the f_o shown in figure 1.7.1 is the maximum ground coverage possible for zero shading and blocking. f_c^* is the optimum value for cell c if $\alpha = \beta = 0$. Consequently, $f_c^* \leq \hat{f}_c$, and $f_c^* = \hat{f}_c$, only if

$$f_c = \hat{f}_c = f_c^* = f_o,$$

which is the zero shading and blocking solution. In the general case, (figure 1.7.2) $\alpha \neq 0 \neq \beta$, $\hat{f}_c$ is determined by

$$\lambda_c' = \lambda_c/(\alpha \hat{f}_c^{-1} + \beta \hat{f}_c^{-\frac{1}{2}} + 1) = \tilde{\mu}/\eta_c,$$

and f_c^* is determined by

$$\mu_c' \equiv (\lambda_c + f_c^* \partial_f \lambda_c)/(1 + \tfrac{1}{2}\beta f_c^{*-\frac{1}{2}}) = \tilde{\mu}/\eta_c.$$

Notice that $\lambda_c' \leq \mu_c'$ for $f_c \leq f_c^*$, if α and β are positive. Consequently, $\lambda_c'(f_c)$ and $\mu_c'(f_c)$ intersect at some point $f_b \geq f_o$ such that $f_b = f_c^* = \hat{f}_c$, which will correspond to some shading and blocking if $\alpha \neq 0 \neq \beta$.

Proceeding to the final step of the optimization procedure, we again form δE_T and eliminate $\partial_t \lambda_c$:

$$\delta E_T = \sum_c (\mu_c \phi_c \delta f_c + \lambda_c f_c \eta_c \delta \phi_c) A_L S_o .$$

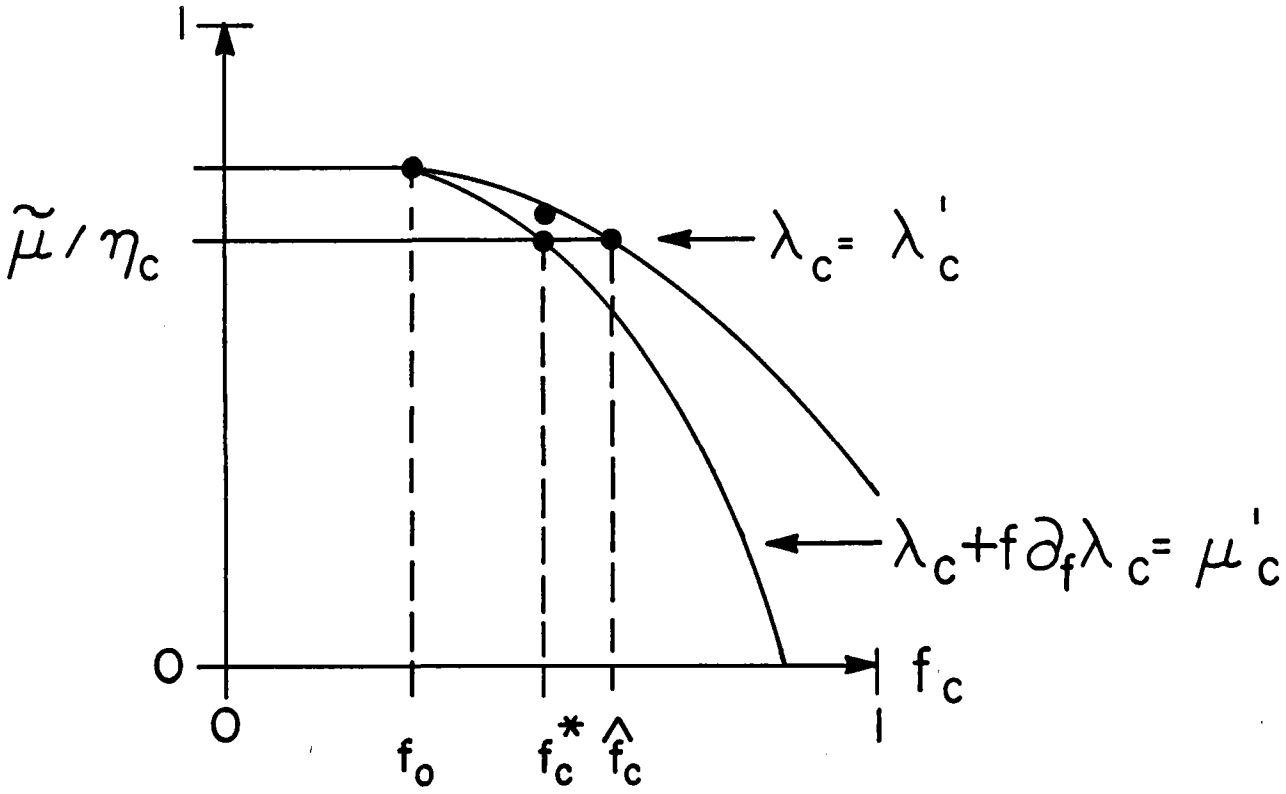

Figure 1.7.1 Determining the Boundary of the Collector Field Assuming Zero Cost Land and Wiring. λ' intersects μ'_c at f_o, which is the zero shading and blocking ground coverage fraction. If the actual interception fraction η_c equals the approximate value η_b, then cell c is a boundary cell and the shading and blocking loss is zero. That is, the allowable losses are all absorbed in cosine effects and in interception losses.

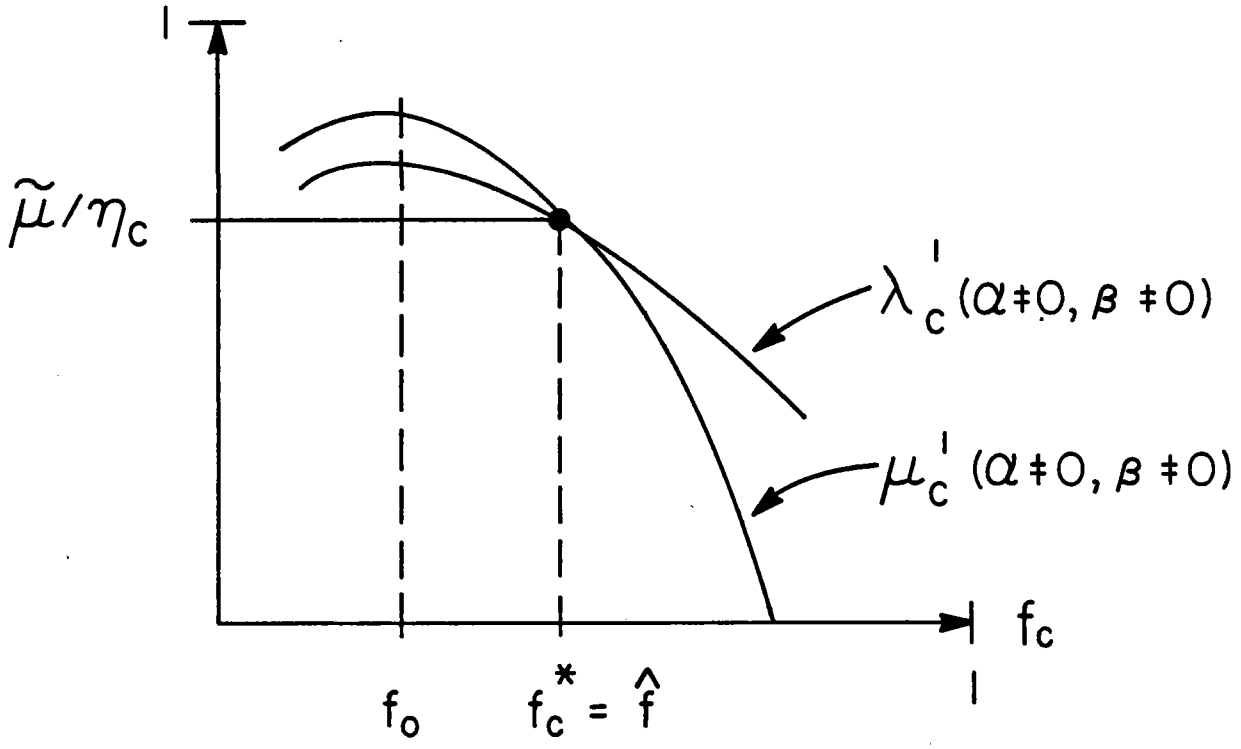

Figure 1.7.2 If land and wiring costs are not zero the curves of Figure 1.7.1 are modified somewhat, as indicated here, particularly at low ground coverage (small f_c) where the heliostats are far apart. The local increase in the effective heliostat cost reduces the allowable losses so that even on the boundary $f_c^* = \hat{f}$ at $f_c > f_o$ and some shading and blocking loss is accepted.

Using the above solutions, we have

$$\delta E_T = \tilde{\nu}\, \Sigma[\phi_c(1 + \tfrac{1}{2}\beta f_c^{-\frac{1}{2}})\, \delta f_c + (\alpha + \beta f_c + f_c^{\frac{1}{2}})\, \delta\phi_c]\, A_L S_o$$

$$= \tilde{\nu}\, (\delta C_s / C_H A_L)\, A_L S_o,$$

so that

$$\delta E_T / \delta C_s = \tilde{\nu}\, S_o / C_H.$$

A variation of the figure of merit gives

$$\delta F = 0 = \delta C_s / E_T - C_s \delta E_T / E_T^2,$$

so that

$$\delta E_T / \delta C_s = E_T / C_s = \tilde{\nu} S_o / C_H = 1/F,$$

and, therefore,

$$\tilde{\nu} = C_H\, (S_o F)^{-1},$$

which is the same as the result previously obtained in section 1.7.2 with $\tilde{\mu} \rightarrow \tilde{\nu}$. Consequently, exactly the same solution procedure can be used.

1.7.4 The Effect of Receiver Losses

To this point, we have ignored losses due to reflectivity, absorptivity, convection, and reradiation. These losses can be included by expressing the total receiver output energy E_o in terms of the previously defined total energy E_T. We can write

$$E_o = \hat{\alpha}\hat{\rho}\, E_T - E_A,$$

where typically $\hat{\alpha} = 0.95$ for the absorptivity of the receiver surface painted with a commercial high temperature black such as PYROMARK®. A typical value for the net reflectivity of a low-iron back-silvered glass heliostat is $\hat{\rho} = 0.91$; however, a better operational value might be 10 percent less due to dust. The estimated annual losses due to convection and reradiation for a 24 panel cylindrical receiver such as was considered in the baseline study may be written as

$$E_A = H_A P_L$$
$$= 3376 \text{ (HRS/YR)} \times 36.89 \text{ (MW)} = 124{,}536 \text{ (MWH}_t\text{/YR)}.$$

The LOSS estimate depends on an assumed mean wind, the operating temperature, the sunlit (i.e. operational) hours and the receiver area.

The figure of merit must be redefined in terms of the delivered energy E_o as

$$F = C_s/E_o,$$

so that

$$\delta F = \delta C_s/E_o - \delta E_o C_s/E_o^2,$$

where

$$\delta E_o = \hat{\alpha}\hat{\rho}\, \delta E_T.$$

Consequently, the first step in the optimization procedure is unchanged (i.e., $\delta F = 0 = \delta C_s$ implies $\delta E_T = 0$, as previously shown). However, in the second step of the optimization, $\delta F = 0$ now gives

$$\delta E_T/\delta C_s = (\hat{\alpha}\hat{\rho})^{-1}\, \delta E_o/\delta C_s = (\hat{\alpha}\hat{\rho})^{-1} E_o/C_s$$
$$= (\hat{\alpha}\hat{\rho}\, F)^{-1} = \tilde{v}\, S_o/C_H,$$

and, therefore,

$$\tilde{v} = C_H(\hat{\alpha}\hat{\rho}\ S_o F)^{-1} = C_H\ (\hat{S}_o F)^{-1},$$

so that

$$\hat{S}_o = \hat{\alpha}\ \hat{\rho}\ S_o$$

is the effective annual insolation for the Central Receiver System in MWH/m^2. $\hat{S}_o$ might also include factors for the expected percent of possible insolation and percent of annual usage.

It is also worth noticing that $\tilde{v}$ is almost independent of $\hat{\alpha}\hat{\rho}$. Substituting the definition of F into the expression for $\tilde{v}$ gives

$$\tilde{v} = C_H[\hat{\alpha}\hat{\rho}\ S_o C_s/(\hat{\alpha}\hat{\rho}E_T - E_A)]^{-1}$$

$$= (E_T - E_A/\hat{\alpha}\hat{\rho})\ C_H(S_o C_s),$$

which becomes independent of $\hat{\alpha}\hat{\rho}$ as the convection and radiation loss $E_A \to 0$.

Appendix II

1.8 The Optimum Trim

1.8.1 Introduction

This appendix should bridge the gap between the theory of the optimization procedure and the RCELL code itself. See appendix I or, for a more complete discussion, the memorandum of November 4, 1976, entitled "A Cellwise Method for the Optimization of Large Central Receiver Systems." (Reference 4)

In the most general case of costs and losses, the optimum coordinates in a given cell are determined by the requirements

$$\partial_t \lambda_c(f^*,t^*) = 0$$

and

$$v_c(f^*,t^*) = \tilde{v} = \tilde{\mu} = C_H/F\hat{S}_o,$$

where

$$\lambda_c = E_c/A_c S_o,$$

and $v_c = \eta_c\ (\lambda_c + f_c \partial_f \lambda_c)\ /\ (1+\tfrac{1}{2}\beta f_c^{-\frac{1}{2}})$.

At the boundary, a variation of the cell fraction ϕ_c leads to an additional requirement, which can be written as

$$\lambda' \equiv \lambda_c(\hat{f},t^*)\ (1+\alpha/\hat{f}_c + \beta/\hat{f}_c^{\frac{1}{2}})^{-1} = \tilde{\mu}/\eta_c.$$

This equation holds at the boundary and not elsewhere. However, the cell matching condition, which holds for all optimized cells, can be rewritten as

$$\mu'_c \equiv (\lambda_c + f^*_c \partial_c \lambda_c)/(1 + \tfrac{1}{2}\beta/\sqrt{f^*_c}) = \tilde{\mu}/\eta_c$$

A glance at figure 1.7.1 (Appendix I) shows that

$$\lambda'(\hat{f}_c) = \mu'(f^*_c) = \tilde{\mu}/\eta_c$$

for a boundary cell. Consequently, we can test for the boundary by defining a Fortran variable

$$\text{RGRND} = \lambda'_c/(\mu'_c),$$

which will be greater than 1 inside the boundary and less than 1 outside of the boundary.

1.8.2. Summary of Fortran Variables

For convenience, we list a few of the most important Fortran variables that occur in the RCELL program.

ATSOL = S_o is the total annual direct beam insolation at ground level.

FINTC = η_c is the interception fraction for cell c.

C(IOPT) = C_H is the cost of heliostats in $\$/m^2$

FMI = F is the input value of the figure of merit in \$/aMWH.

FRLOS = $\alpha\rho$ includes all multiplicative losses, such as mirror reflectivity or receiver absorptivity.

OPSOL = C(IOPT)/(FMI*FRLOS)

ELPS = ELPR = OPSOL/FINTC is called the Lagrangian cell matching parameter.

$\hat{S}_o$ = FRLOS*ATSOL

$\tilde{\mu}$ = OPSOL/ATSOL

$\tilde{\mu}/\eta_c$ = ELPS/ATSOL

$\lambda(f_c^*, t_c^*)$ = ER1/ATSOL

$\partial_t \lambda(f_c^*, t_c^*)$ = ET1 = 0

$(\lambda + f_c^* \partial_f \lambda)/(1 + \frac{1}{2}/\sqrt{f_c^*})$ = EL1/ATSOL = μ_c'

$(1 + \frac{1}{2}\beta/\sqrt{f_c^*})^{-1}$ = GC1

$(1 + \alpha/f_c^* + \beta/\sqrt{f_c^*})^{-1}$ = HC1

λ_c' = ER1*HC1/ATSOL

RGRND = (ER1*HC1)/ELPS

3. The Fractional Cells in RCELL

The RGRND variable is used to trim the field and establish the fractional cells at the boundary of the field, figure 1.81.

ϕ_c = BGRND = IGRND*1/4 = 0, 1/4, 1/2, 3/4, 1

The use of fractional cells allows a better approximation to the smooth boundary which would result from a more detailed model and reduces the arbitrariness of assigning cells to be "in" or "out" of the field. Depending upon various factors in the model, the variable RGRND will vary more or less sharply at the boundary. In extreme cases there may either be vary few fractional cells, in which case DTRIM should be increased; or fractional cells defined over a band several cells wide near the boundary, in which case DTRIM should be decreased.

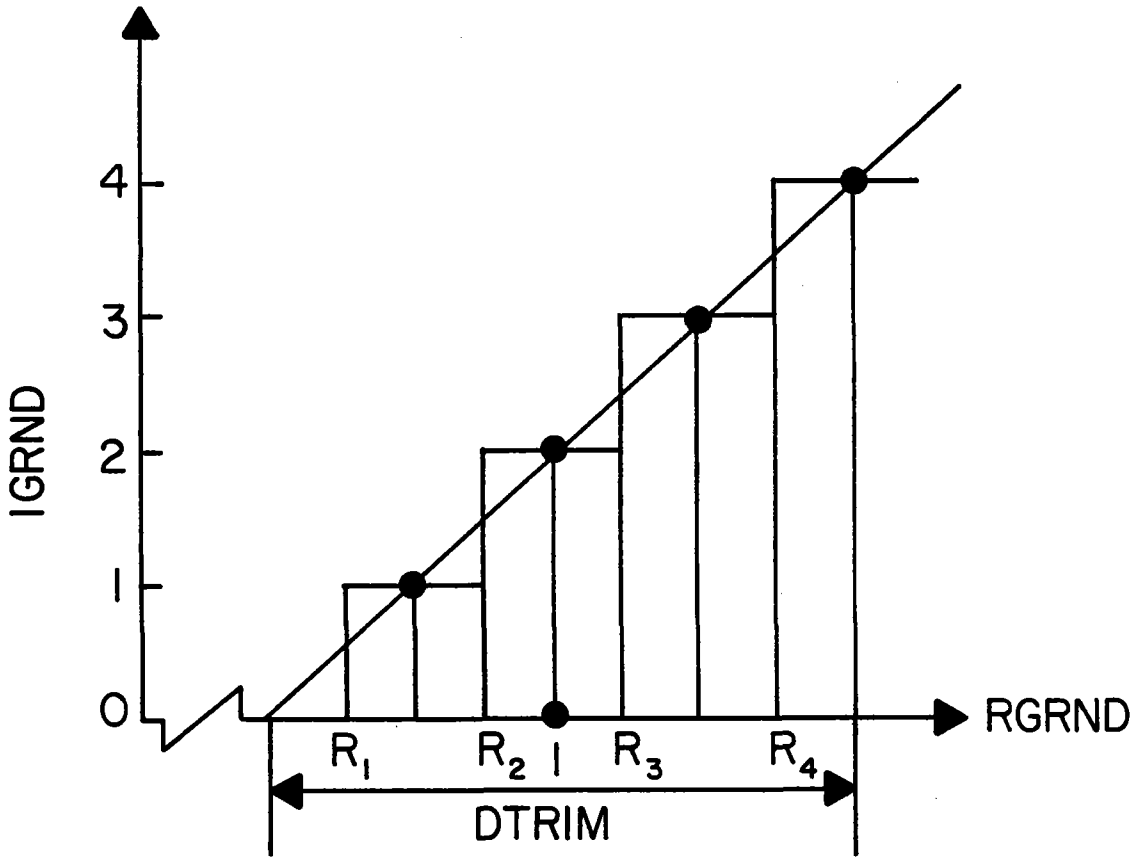

$$R_1 = 1-(3/8)DTRIM$$
$$R_2 = 1-(1/8)\ DTRIM$$
$$R_3 = 1+(1/8)\ DTRIM$$
$$R_4 = 1+(3/8)DTRIM$$

Figure 1.8.1 IGRND Versus RGRND. The chart shows the stair-step relation between IGRND and RGRND. Notice that the segregation of cells into various quartiles depends on the input value of DTRIM, which is adjusted to represent the mean decrement of RGRND in the vicinity of the field boundary. Experience shows that this works satisfactorily and is much better than not using fractional cells at the outer boundary.

1.9 APPENDIX III THE ANALYTIC INSOLATION MODEL

The following summary illustrates the versatility of the analytic insolation model in its present state of development. We can easily input to the model site latitude and elevation, mean monthly values for the precipitable water, turbidity factor, and percent of possible sunlight. Seasonal solar distance is computed within the astronomical model. The model is based on:

1) The spherical earth air mass

2) Allen's clear air extinction data; see C. W. Allen, Astrophysical Quantities, 2nd ed. (The Athlone Press, 1946).

3) The ICAN atmosphere model, See Berry, Bollay, and Beers, Handbook of Meterorology N.Y.: MCGraw-Hill, 1945).

INPUTS

PATMI = 760. mm of Hg = 1013.25 mbars = 1 Atmosphere

REARTH = 6370. Radius of Earth in Kilometers

HATMOS = 8.430 Height of "Uniform Atmosphere" in Kilometers

CMWATR = 1.440 Mean Atmospheric Water Vapor in Centimeters

SOLARØ = 1353. Extraterrestrial Insolation in W/m^2

EARTH 1.000 Solar Distance in Astronomical Units (AU)

ZGRND = .000 Altitude of Site above Sea Level in Meters

$\hat{s}_o$ = (USUNX, USUNY, USUNZ) is a unit vector pointing toward the center of the sun in local topocentric coordinates. The z axis is vertical and positive upward. The x axis is positive southward.

OUTPUTS

AIR = Air Mass

SOLARA = Terrestrial Insolation in W/m^2

PATMOS = Atmospheric Pressure at Site in Atmospheres

CODE

```
PATMOS  =   (1. -0065*ZGRND/288.)**5.2568
PSITE   =   PATMI *PATMOS
RH      =   REARTH/(HATMOS *PATMOS)
AIR     =   SQRT (1. + 2.*RH + (RH*USUNZ)**2) - RH*USUNZ
AIR     =   AIR *PATMOS
EXPT    =   .367 + .134/(.788 + CMWATR)
ABSOR   =   (.263 - .060/(.500 + CMWATR))*AIR**EXPT
TURBY   =   EXP(-ATF * AIR)
SOLO    =   TURBY*SOLARϕ(1-ABSOR)/EARTH**2
SOLARA  =   SOLO *PPS
IF(SOLARA LT.100.) SOLARA = 100.
```

1.10 REFERENCES

1. L. L. Vant-Hull and A. F. Hildebrandt, "Solar Thermal Power System Based on Optical Transmission," Solar Energy 18, 31 (1976).

2. M. S. Abdel-Monem, A. F. Hildebrandt, F. W. Lipps, and L. L. Vant-Hull, "A New Method for Collector Field Optimization, "Heliotechnique and Development 1, 372 (1976), and also Proceedings of the COMPLES International Conference, Dhahran, Saudi Arabia, Nov. 2-6, 1975.

3. J. D. Hankins, "Cost-Optimal Deployment of Mirrors Associated with a High-Temperature Solar Energy System," ISES paper at U. S. Section Annual Meeting, Aug. 19-23, 1974, at Colorado State University, Ft. Collins, Colorado.

4. F. W. Lipps and L. L. Vant-Hull, "A Cellwise Method for the Optimization of Large Central Receiver Systems," Solar Energy 20, 505-516 (1978).

5. C. W. Allen, "Astrophysical Quantities," (The Athlone Press, 1964), 2nd ed., p. 169.

6. J. E. Selby and R. A. McClalche, LOWTRAN II, NTIS Accession No. AFCRL72-0745(A72).

7. E. C. Flowers, R. A. McCormick, and K. Kurtis; "Atmospheric Turbidity over the United States, 1961 1966" Jr. Appl. Meteorology, 8, 955-962 (1969).

8. "Generalized Shading and Blocking Programs," Technical Addendum 11, "Solar Thermal Power Systems Based on Optical Transmission," Final Report NSF/RANN/SE/GI-39456/FR/75/3.

9. M. D. Walzel, F. W. Lipps, and L. L. Vant-Hull, "A Solar Flux Density Calculation For A Solar Tower Concentrator Using A Two-Dimensional Hermite Function Expansion," Solar Energy, 19, 239-253 (1977).

10. F.W. Lipps, The Receiver Programs, in Proceedings of the ERDA Solar Workshop on Methods for Optical Analysis of Central Receiver Systems. August 10-11, 1977, ERDA AT (29-1) 789 (October 1977) NTIS Conf 770-850.

1.11 GLOSSARY OF TERMS

a_c is the maximum ground coverage factor.

A_c is the area of glass in cell in m^2.

A_H is the area of glass/heliostat in m^2.

A_L is the area of land in a cell in m^2.

A_T is the total area of glass in the collector in m^2.

B is a wiring geometry parameter in m^{-1}.

C_H is the cost of heliostats in $\$/m^2$.

C_L is the cost of land in $\$/m^2$.

C_o is fixed cost in the expression for total system cost.

C_s is the total system cost in \$.

C_W is the cost of wiring in \$/m.

C_+ is the additional cost due to land and wiring.

D_c is the width of a cell in the collector model in m.

D_M is the width of the heliostat in m.

D_x is North-South heliostat spacing in m.

D_y is East-West heliostat spacing in m.

E_A is the total annual energy loss in MWH_t (due to convection and reradiation).

E_c is the total energy directed towards the receiver by cell c in the collector field, in MWH_t.

$\tilde{E}_L$ is the Lagrangian energy function for cell c in MWH/m^2.

$E_L(x_c y_c)$ is the Lagrangian energy function for cell c in MWH/m^2.

$E_T(x_c y_c)$ is the transverse energy function for cell c in MWH/m^2.

E_o is the total receiver output energy in MWH_t.

E_T is the total energy in MWH_t before losses.

f_c is the dimensionless ground coverage fraction in cell c.

f_c^* is the optimum value of f_c.

$\hat{f}_c$ is the alternative value of f_c defined by the coefficient $\delta\phi_c$.

F is the figure of merit in $\$/aMWH_t$.

F* is the figure of merit in $\$/aMWH_t$ for an ideal system having no losses.

H_T is the focal height in m.

N is the total number of cells.

N_o is the number of heliostats/field controller.

R_H is the dimensionless heliostat geometry factor occurring in the expression for ground coverage.

S_o is the total direct beam solar energy at normal incidence over the given time period in MWH_t/m^2.

t_c is a dimensionless parameter for the set of hyperbolae orthogonal to f_c.

$\vec{u}_f$, ($\vec{u}_t$) is a unit vector normal to curves of constant f (or t).

W_c is length of wire required by cell c in m.

x_c is first spacing parameter for cell c in heliostat units.

y_c is second spacing parameter for cell c in heliostat units.

z_c is the dimensionless fraction of glass in cell c.

$\hat{\alpha}$ is the dimensionless absorptivity of the "black" receiver.

α is the dimensionless relative cost of land.

β is the dimensionless relative cost of wiring.

γ_c is the dimensionless cell geometry factor for cell c occurring in the expression for ground coverage.

$\vec{\delta}_f$, $(\vec{\delta}_t)$ is the differential vector tangent to the curves of constant f (or t).

η_c is the receiver interception factor for energy coming from cell c.

η_{cp} is the interception fraction for receiver panel p illuminated by the reflected sunlight from cell c.

λ_c is collector efficiency for cell c.

λ_T is a dimensionless measure of total energy, or equivalently, a net system efficiency.

μ_c, (ν_c) is net efficiency function for cell c (same, with land and wiring effects included).

$\tilde{\mu}$, $(\tilde{\nu})$ is the dimensionless Lagrange parameter (same, with land and wiring effects included).

$\hat{\rho}$ is the net reflectivity of the heliostat.

ρ_x is the North-South heliostat density.

ρ_x is the East-West heliostat density.

σ_o is the incident solar flux density in MW/m^2.

τ is the time variable in hours.

ϕ_c is the fraction of cell c which is covered by the heliostat array.

∂ is the math symbol for partial derivative.

ε is the math symbol denoting set membership.

π is the math symbol for 3.14159.

∇ is the math symbol for gradient operator.

$\rightarrow$ is the math symbol for a vector quantity.

SECTION 2

NET ENERGY ANALYSIS

For a Solar Central Receiver System

A. C. Meyers III and L. L. Vant-Hull

Abstract

In this chapter we consider the net energy analysis for the construction of a 100MW$_e$ commercial solar central receiver facility. Using the systems design studies for the 100MW$_e$ unit, a detailed net energy analysis is done on capital energy required to build the thermal collection component, including 6 hours of storage. The Energy Amplification Factor (EAF) for this system was determined. EAF provides a measure of the number of times the energy incorporated in the plant can be replicated during its lifetime. EAF also determines the time required after electricity production begins before the total energy necessary to manufacture and transport materials, assemble components, and construct the 100MW$_e$ plant on site is replicated by the power generated.

Definitions are developed and the thermal collection system with storage is analyzed to determine the materials required to produce the various components. For each material, the process energy consumption per unit of production is determined. To this is added the fabrication, manufacturing, transportation and construction energies expended to produce a completed plant site in Southern California. Due to decomposition, 14.3% of the Caloria HT43 thermal oil must be replaced annually. If the breakdown fraction is recovered and burned as boiler fuel, there will be a loss of 0.15% in the energy production.

Net energy analysis gives a total capital energy cost of 659,000 MWH$_t$. Assuming a net mean conversion efficiency for electric production of 1/3 with the facility producing 446,000 MWH$_e$/yr, on the 540th day of electric power generation the energy expended to produce the 100 MW$_e$ plant will have been replaced. All additional energy production over the facility's 30 year lifetime is essentially "profit". Thus, for the design lifetime cycle of 30 years, the EAF is 20.3. At the end of the 30 years, we estimate that 41.6% of the capital energy can be recovered readily if the system is torn down and recycled.

TABLE OF CONTENTS

LIST OF FIGURES

LIST OF TABLES

2.0 INTRODUCTION

In this chapter we will perform a net energy analysis for the 100 MW_e Solar Tower System commercial baseline design. This specific design incorporating an external receiver, developed by the MDAC team, is based on the use of water/steam as the heat transfer fluid. The specific details of the design used for this analysis have been published elsewhere. [17] We will discuss the net energy problem, the definitions used and the assumptions made in this analysis for basic materials, manufacturing and transportation. The output and configuration of the 100 MW_e plant will be considered, and the weight and specific energy costs for each component will be determined. Total energy required to build the 100 MW_e plant will be calculated for two specific cases, with and without thermal storage. From these results, the energy amplification factor and the reproduction time will be determined. Preliminary results from this net energy analysis have been published previously.[8-12] The references provide a bibliographic listing of the net energy literature applicable to this report.

Solar Towers or central receivers with heliostat concentrator fields have been proposed for commercial electric power production. The commercial units would range in size from 30-300 MW_e. In this study, we are considering a 100 MW_e commercial baseline power plant facility. Currently, the only sited solar tower central receiver for electric power production is the 10 MW_e pilot plant which is to be located at Barstow, California. While no site has been specified for the 100 MW_e demonstration or first commercial facility, we will assume it is also placed near or at Barstow. Net energy analysis is mandated for all new solar facilities; however, only limited work has been done in the net

energy field. Consideration of the feasibility of a power plant, has been traditionally limited to the primary technical considerations of engineering complexity, construction and lead times, the dollar cost of the facility, and the rate of return strictly from a dollar viewpoint. Energy considerations have thus been limited mainly to conversion efficiencies; the primary concern has been cost effectiveness, not conservation.

For the convenience of the reader, the basic concepts and characteristics of the Solar Tower System will be reviewed. The central receiver or boiler is located at the top of the concrete tower placed near the middle of a field of heliostats, as shown in Figure 2.1. The sun's radiant energy is reflected by the heliostats and intercepted and absorbed by the receiver. This heat converts to steam the high-pressure water circulating through the tubes in the external surface of the receiver. This central receiver baseline concept is shown in Figure 2.2. The steam from the receiver subsystem is piped to ground level where it may be used to power a 100 MW_e steam turbine generator complex or charge a thermal storage system for deferred operation.

Interest in energy analysis is not new. The present effort in this area is mainly the result of the mandate contained in PL 93-577 the "Federal Nonnuclear Energy Research and Development Act of 1974."[13] The pertinent section with respect to energy analysis reads:

> "Sec. 5. (2) The Congress authorizes and directs that the comprehensive program in research, development, and demonstration required by this Act shall be designed and executed according to the following principles:
>
> (1) Energy conservation shall be a primary consideration in the design and implementation of the Federal nonnuclear

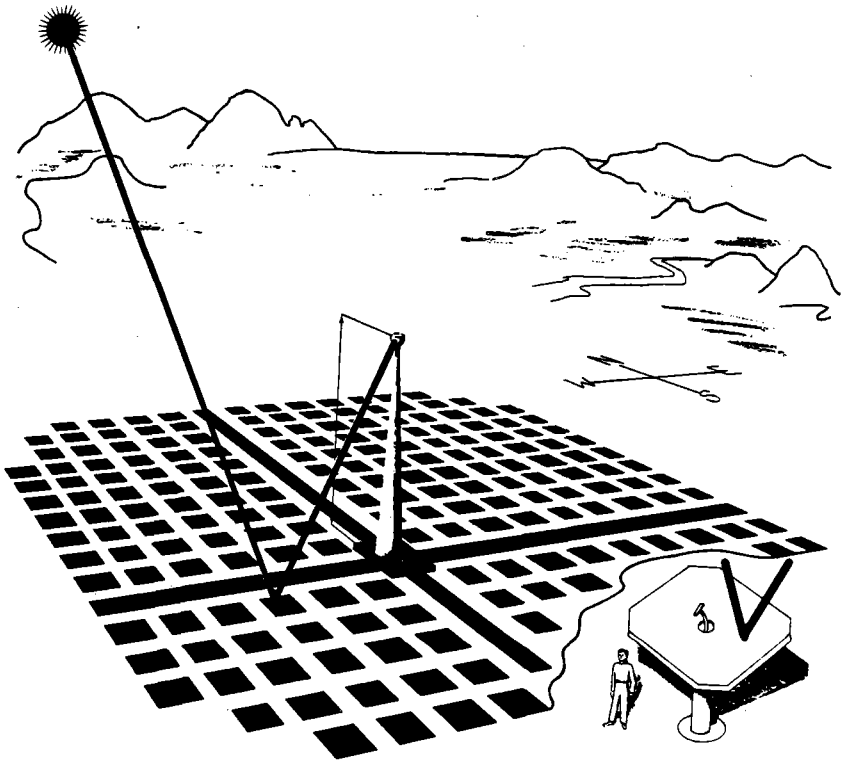

Figure 2.1 Schematic of the Basic Configuration of the Central Receiver Concept. Each of the black squares typically contains several hundred heliostats.

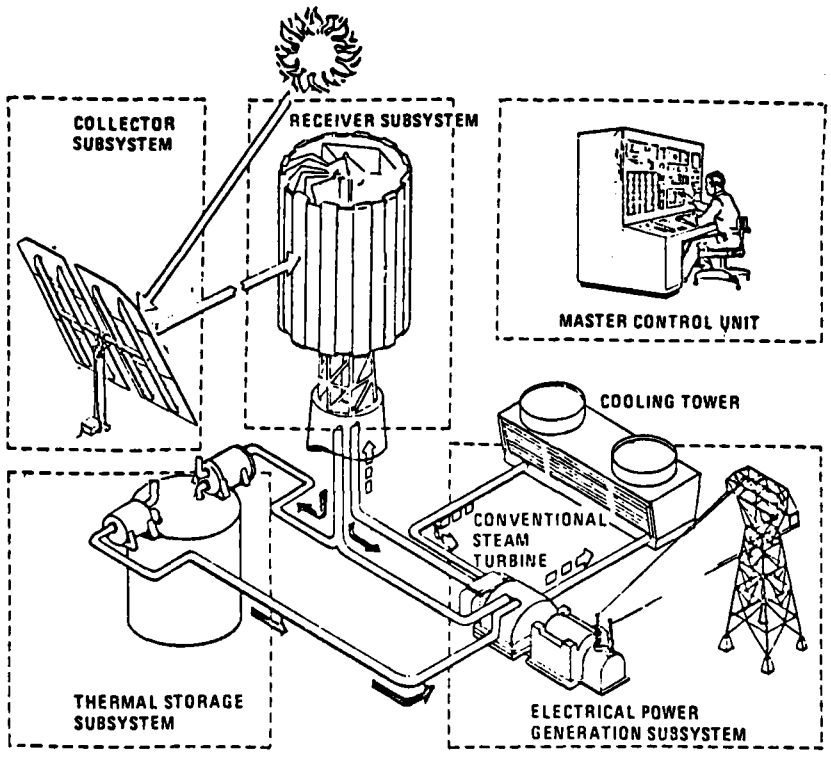

Figure 2.2 Central Receiver Baseline Concept. The 100MW$_e$ Commercial Plant divided into its five main subsystems.

energy program. For the Purposes of this Act, energy conservation means both improvement in efficiency of energy production and use, and reduction in energy waste.

(2) The environmental and social consequences of a proposed program shall be analyzed and considered in evaluating its potential.

(3) Any program for the development of a technology which may require the significant consumptive use of water after the technology has reached the stage of commercial application shall include thorough consideration of the impacts of such technology and use on water resources pursuant to the provisons of section 13.

(4) Heavy emphasis shall be given to those technologies which utilize renewable or essentially inexhaustible energy sources.

(5) The potential for production of net energy by the proposed technology at the stage of commercial application shall be analyzed and considered in evaluating proposals."

While all of section 5 is applicable to solar energy, the current work is directed primarily to the last item. The need for information on the potential for production of net energy has sparked interest in this fairly new field of research. The wording of PL 93-577, Sec. 5 (2) Item (5), can be considered as a directive on the preparation of energy impact statements for new power sources.

2.1 THE NET ENERGY PROBLEM

Net energy analysis is not a new concept, but the impetus of PL 93-577 has caused extensive re-evaluation of the concept and a critical examination of the current status of this field. This review has shown a definite need for guidelines in the inter-disciplinary fields that utilize the concept of net energy. Because of this need, a series of workshops have been held to consider both the basic methodology and the approach used to apply the concepts. The most recent workshop was held at Stanford University in 1975.[14]

To understand problems with net energy analysis, one must consider the background of the field. The energy aspects of man's environment have become a recognized area of serious study only in the last 15 to 20 years, with the greatest interest being in late 1960's and 1970's. The OPEC oil embargo made the energy aspects of the question paramount in the minds of many people for the first time. However, environmental aspects of the problem have been considered since the latter part of the nineteenth century. Because of this interest, a large number of books exist which discuss the basics of energy and the environment.[15-23] Also, there are books on model or systems approaches [24-31] and those which consider an integrated systems energy approach.[32-34] Works listed in the references provide a representative sampling of some of the better materials. Many papers and reports are referenced and discussed in these books. While all the books listed are related to the environmental and energy problem, only the last three [32-34] provide a quantitative modeling technique applicable to net energy analysis for Solar Tower central receiver systems. Pioneering work by H.T. Odum provides an analysis and modeling of energy systems to determine the net energy.

[32,33,35-39]

If one considers the present developmental and conceptual state in the field of net energy analysis, certain basic characteristics or problems become evident. These have been discussed in detail in the workshops.[14] Conclusions drawn from studying the proceedings are summarized in the following comments:

1. Net energy analysis is at an early stage of its development. Persons currently active in the field and responsible for its present stage of development come from various disciplines. Each discipline has its own base line concepts out of which the net energy aspects grew. As a consequence, the several groups have developed and used different variations in rules, definitions, and methodologies.

2. While the field of energy analysis is, in general, directed to the measurement and computation of energy flows for a whole society, net energy analysis is a much more restrictive concept. It is directed primarily toward determining the energy required to deliver a specific energy related product at a predetermined point or stage of use.

3. The essential additional dimension that net energy analysis seeks to add to traditional process energy balances is the actual operating energy, including all losses, required to carry out a specific process.

4. Considering the present state of the art with respect to net energy analysis, it is better to do a number of separate analyses or to consider each component in its optimum analysis format, and then to integrate these results, rather than to calculate and combine all segments analytically.

5. The use of consistent units, preferably a thermal energy unit, will provide a common denominator which will permit the comparison of performance in various systems.

6. It is highly desirable to understand why and how a system works, to analyze the physics and engineering of the process, so that known performance data for existing systems can be used to predict the performance of future systems.

7. Net energy analysis is an important decision making tool only if it is used in conjunction with socio-economic data and/or analyses.

8. There is no single definition or methodology for the field of net energy analysis which is applicable to all systems.

In practice, the analysis method, the boundaries of the system, and the relevant data are dependent upon both the specific questions being asked and the system being considered. Accuracy, comprehensiveness, and usefulness are considerations in the development of a methodology.

With respect to methodology, one can consider the work of the Odums.[33] In their attempt to be both comprehensive and analytic within the framework of a fixed basic methodology, in their case one based on transient signals in analog computer circuits-they have introduced two major problems into their pioneering work in net energy analysis: (1) by insisting on considering all possible energy sources and sinks in a system, they end up considering quantities which differ on the energy or time scale by orders of magnitude as large as 10^6; (2) by always including an energy unit for the dollars spent, energy units and money are made equivalent regardless of the application. They stress the qualitative value of energy but do not consider monetary purchases by the same criteria. This means that their systems are overly complex and, in many cases, questions of double counting need be raised with respect to their energy accounting.

Thus for net energy analysis, the current status can be summarized as follows:

1) Net energy analysis is a fairly new field.

2) Methodology is not explicit.

3) The consequences of system size and scaling, including interfacing, are not completely understood.

4) Information on the various efficiencies for processes involving energy conversion are not always available either in fact or in readily usable units. With regard to the last point most cost figures on energy use are given with respect to some vaguely defined monetary cost/unit dimension (time, length, weight, etc.) for a specified year. Temporal translation of data in this format requires a fairly complex multivariable economic analysis which is dependent on much more than changes in the value of the gross national product, cost of living index, and inflation rates.

For net energy analysis to be viable, energy production and use must be determined and quantified primarily with respect to energy units. Expressing these BTU's, kilowatt hours or joules as having a current monetary value is done only as a secondary designation to provide current cost information.

Net energy analysis, as a field of research, is in a fairly primitive state. After considering current methodologies, we decided that a specific set of definitions and assumptions beyond the use of energy units had to be developed to ensure a meaningful net energy analysis for the 100 MW_e commercial Solar Tower central receiver plant. Definitions and assumptions developed and used for this study are discussed in the following two sections.

2.2 DEFINITIONS

Net energy analysis is a rapidly developing field with broad interdisciplinary input; therefore, it is necessary to define explicitly the terms and concepts used. The basic philosophy in developing the working vocabulary meant defining energy based terms in a manner as closely parallel to relevant non-energy concepts as possible. The terms which need to be defined with respect to net energy analysis of the 100 MW_e plant are:

GROSS ENERGY PRODUCTION of a system is all the energy produced by the primary conversion process for any designated time interval. Gross energy production provides a measure of how close to optimal are the various primary conversion processes with respect to the initial utilization of an available resource. For the ideal optimum utilization of a resource, the gross energy production should be the maximum amount of energy the system is capable of extracting from the resource. Gross energy is a measure of the maximum amount of energy a system or process is able to extract from a resource assuming no losses. Energy expended by the system or process must be subtracted from the gross energy to determine either the net or available energy. To a varying extent, both the end use for the energy and the characteristics of the resource help determine the choice of a particular system. However, within these limits, gross energy production can be used to rank the available primary conversion options.

TOTAL ( ) ENERGY PRODUCTION is the total amount of energy produced over the useful lifetime of the device. Various terms can be placed in the parenthesis, such as gross, net, thermal, and electrical, to designate the type of energy production under consideration.

PROCESS ENERGY PRODUCTION is defined as the actual energy produced by the designated process in converting the resource. This process energy production is determined by the product of the efficiencies for the various components of the system and corresponds to integration of the metered power production data over the chosen time interval.

ENERGY EXPENSES are defined as those costs in energy necessary for the acquisition of fuel, environmentally required clean up systems beyond those normally used in the process, disposal of spent fuel, and operation and maintenance of the plant. Fuel acquisition includes extraction, processing, and transportation to the power plant site. The energy expenses, which in each case must be designated, should include both materials and labor.

NET ( ) ENERGY PRODUCTION is defined as the useful energy produced for any designated time interval. Again various terms may be put in the parenthesis to designate the type of energy.

Net energy production is calculated by subtracting the energy expenses from the process energy production. It is not necessary or always desirable for all systems to have a positive value for net energy production. An example of this would be an energy storage system used to shift power produced with baseline capacity to the load following mode.

TOTAL NET ( ) ENERGY PRODUCTION is defined as the useful energy produced over the useful lifetime of the device. Again, one has the parenthesis option.

CAPITAL ENERGY is the energy required to create the device.

ENERGY AMPLIFICATION FACTOR (EAF) is defined as the total net energy production divided by the capital energy.

2.3 ASSUMPTIONS

Using the definitions of energy concepts, one can understand the explicit methodology to be used. There are two basic approaches to the problem: (1) to consider the actual energy used to carry out a particular process or sequence of processes; (2) to determine the engineering thermodynamic values for the net energy needed in each specific reaction and sum these.[14] There are advantages and disadvantages with each approach.

Using engineering thermodynamic values gives one precise answers, which, however, do not describe the actual amount of energy utilized in a production process. These data have the advantage of providing a measure for determining the maximum theoretical production efficiencies and thus give a reference for developing energy conservation programs.

Actual energy utilization values provide a more accurate and realistic measure of the impact of a particular system on the total energy system of the United States. Since the purchases of materials and services for projects such as the 100 MW_e plant are determined by monetary bids, actual energy values provide a more realistic estimate of the energy impact for specific resources and/or system approaches. Problems develop in determining the actual energy use for a particular process and the time frame reference for the data. The time frame reference is most important and should be included and referenced in all net energy analyses because increased energy costs have accelerated efforts in energy conservation. We decided to use actual energy utilization figures, where possible, because of the inherent advantages in this approach with respect to

determining realistic estimates of the potential impact from solar energy. The first and primary consideration for net energy analysis is the capital energy for any particular system. The capital energy impacts that must be considered can be broken down into the categories of materials, fabrication, construction, and transportation.

2.4 NET ENERGY ANALYSES - MATERIALS

In this section, a net energy analysis will be done to determine the process energy consumption for each major material used in the building of the 100 MW_e solar thermal plant. In each case, using reasonable assumptions, a mean energy/unit mass (KWH_t/Kg or MWH_t/Kg) will be determined for the material. The analysis for the production of each raw material will be summarized in the respective subsection.

Aluminum

The process energy consumption analysis on aluminum is done for the production of aluminum ingot. This analysis restricts itself to primary aluminum as opposed to an analysis that would also include secondary or recycled aluminum. No good figures exist in the public domain on the percentage of the aluminum ingot production from recycled material in 1970. In 1974, however, secondary aluminum represented approximately 20 percent of the total aluminum supply.[40]

The production of aluminum ingot from raw materials involves three principal operations. These are mining the bauxite, refining the bauxite into aluminia, and smelting of this aluminia into aluminum. Bauxite is the ore exclusively used in the United States for the production of aluminum. All but four percent of domestic primary aluminum production is from imported ores. Therefore the available data used for this energy analysis does not include ore mining. Because it was previously

noted that 20 percent of the ingot production in 1974 was from recycled aluminum, we will assume that the energy cost of mining and transporting is comparable to the recycling energy savings for aluminum. As will be seen later, these costs are most likely lower than original production. The problem one encounters when trying to calculate the total process energy for aluminum is the lack of specific energy costs per ton-mile or per metric ton-kilometer for moving materials by ocean going vessels. Both geopolitics and weather make it hard to come up with a meaningful value.

In the United States, all the aluminia is produced from bauxite using the Bayer process. In this process, finely ground bauxite is digested at a high temperature and under pressure by use of a caustic soda solution to produce sodium aluminate. The non-aluminum solids do not dissolve and are separated out while the sodium aluminate is cooled and precipitated as alumina hydrate which is then calcined in rotory kilns at 1200°C to produce alumina. This alumina is then reduced to metallic aluminium by the Hull-Heroult electrolytic process.

The process energy consumption for the production of aluminum ingot is shown in Table 2.1. A breakdown of the primary energy consumed during the production of aluminum ingot from bauxite in terms of resource type used follows:

	% of Energy Supplied [42]
Coal	0.5
Refined Oil Products	15.1
Natural Gas	9.0
Derivative Fuel Products	3.2
Primary Fuel for Purchased Electricity	72.2
	100.0

Table 2.1

PROCESS ENERGY CONSUMPTION FOR THE
PRODUCTION OF ALUMINUM INGOT (1970) [42]

OPERATION	%	KWH_t/Kg
Smelting Alumina to Aluminum*	70.3	39.33
Coke Calcining **	15.4	8.62
Refining Imported Bauxite to Alumina	9.8	5.48
Production of Pitch	3.3	1.85
Caustic Production	1.0	0.56
Production of Synthetic Soda Ash	0.1	0.06
Miscellaneous Other Steps	0.1	0.06
Total	100.0	55.96

5.60×10^{-2} MWH_t/Kg

* 50% from hydroelectric, efficiencies for various energy sources given in text.

** The coke calcining produces carbon (which is used in the anodes) from the "green coke" obtained from coking operations in petroleum refineries. Aluminum production is the single largest user of petroleum coke.

The primary fuel required for generation of the electricity used would be higher except for the fact that about 50% of the electric energy used in the smelting of the alumina was generated by hydroelectric power dams.[42] Since aluminum smelting has such high electrical consumption per unit of material produced, we show here the assumed electrical energy generation efficiencies.

Type of Fuel/Energy	Electrical Energy Production: Generation Efficiency in % [42]
Coal	33.37
Fuel Oil	30.57
Natural Gas	31.77
Nuclear Fuel	32.00
Hydro-Energy	100.00

For transmission, 91% efficiency is assumed for all electrical power produced. Figures used in the quoted reference are slightly high for fuel oil, nuclear, and hydro power, but will be used in this study because they are the values used in development of the national energy data base figures.

Concrete and Sand

The process energy consumption for the production of concrete (1970 energy use base) is given in Table 2.2

The cement data are developed from numbers for the production of cement in either the wet process or the dry process. In general, the raw material process for the production of cement requires two crushing stages before the grinding stage. In the first crushing stage, rocks are reduced to pieces of about 6" diameter; in the second crushing stage, they are reduced to approximately 3/4" diameter pieces. After crushing, the material is stored and then subsequently ground to make a small particle feed. The wet process, used most normally when the raw

Table 2.2

PROCESS ENERGY CONSUMPTION FOR THE

PRODUCTION OF CONCRETE (1970)

Cement	% of Production	KWH_t/Kg [42]
Wet Process	60.4	2.597
Dry Process	39.6	2.342
	100.0	
	Average	2.496

Concrete [43]	% of Weight		% of Energy	KWH_t/Kg of Concrete
Cement	11.52		88.8	.2875
Water	5.53		--	--
Aggregate				
Fine (sand)	18.32			
3/4" - 3/16"	17.27	82.95	11.2	.0362
1 1/2" - 3/4"	47.36		____	____
Total	100.00		100.0	.3237

(.3237 KWH_t/Kg)

materials themselves are very wet, produces a slurry after grinding, which contains over 30% water. This provides the feed for processing in the kiln. In the dry process the materials are also reduced and ground to produce fine particles. However, the material itself is not wet or very moist and is dried, usually with the grinding process or before the grinding process, using hot kiln waste gasses. This crushed material is then stored and, upon mixing and blending, fed into the kilns. If a wet process feed is used, however, the cement plant has to pass the slurry through pre-heaters before it is fed into the kiln to drive down the moisture levels.

The design criteria for the concrete tower is similar to that for other commercial construction using reinforced concrete slab or shell building techniques. A concrete mixture with a minimum compressive strength of 4,200 lbs/in^2 at 28 days is required for use in road slabs. This mix uses ordinary Portland cement and irregular aggregate. The mix has a mean strength of 5,000 lbs/in^2 and a water/cement ratio of 0.48. [43] An average value of the energy needed to produce a kilogram of cement was determined using the national percentage of production figures for the wet and dry process. Depending on the actual percentage of either process cement available, there can be a local variation of up to ±6% in the energy of production. Obviously, dry process cement is the most energy economic with respect to the KWH_t needed, but the fuel used in the cement production process at a particular plant can range from natural gas or oil to coal. Because of the high energy requirements, the industry is rapidly implementing conservation measures. Therefore, an average value seems both reasonable and realistic.

Energy figures for sand and gravel mining in Table 2.2 include no transportation-to-site costs. Manufacturing and transportation costs will be considered separately. These energy figures are based on statistics for glass sand mining and include only the energy derived from refined oil products. We believe this would be the energy necessary to dig the material out of the sand and gravel pit for use in concrete. The rationale for this choice is that glass sand mining is much more stringent and thus should require more energy for separation and grading, etc., than digging sand and gravel out of the earth. Therefore, the glass sand mining energy figure was used in this study to provide an upper bound on the energy necessary for extraction of sand and gravel.[42] For general mining cost information, see the subsection on steel.

Copper

The major copper deposits are found in the form of sulfide ores. Except for the rich ores from central Africa, which can contain up to 5 percent copper, most mined ores have a copper content of around 1 percent or less. By the use of ore benefication techniques, low grade ores with around 0.4 percent copper are currently being economically processed. In 1970, open pit mining produced 89 percent of domestic production. Also in 1970 the United States was a net copper exporter. Thus the process energy consumption values for copper will be based on domestic production.

Copper ore is drilled, blasted, crushed, and ground, so that it can be beneficiated using a froth flotation technique. This froth concentrate contains between 15 and 35 percent copper. Smelting removes remaining impurities in the form of iron, sulphur, and gangue through the use of a two step process that consists of roasting in a reverberatory furnace to produce copper matte which is then converted to blister copper, 98.5 to

99.8 percent coper and approximately 0.3 percent sulphur. Molten blister copper is transferred to a fuel fired furnace to undergo further oxidation which can include putting green wood logs in the copper to scavenge the last of the excess available oxygen. The resulting copper, which is 99 percent pure, is cast into anodes. These are electrolytically refined, with the impurities going into a sludge at the bottom of the tank. Impurities consisting mainly of gold, selenium, silver, and tellurium are further refined and recovered because of their value. In 1970, 41.4 percent of the copper production was from secondary copper which only needed refining. The process energy consumption for the production of copper is shown in Table 2.3. High energy costs of mining and ore preparation and smelting are a direct result of the fact that only low grade copper sulfide ores are available.

Table 2.3

PROCESS ENERGY CONSUMPTION FOR THE PRODUCTION OF COPPER (1970) [44]

Operation	% of Energy	KWH_t/Kg
Mining and Ore Preparation	54.3	19.61
Smelting	40.8	14.73
Refining	4.9	1.77
	100.0	36.11

Copper Production (1970)	% of Total	KWH_t/Kg
New Refined Copper	58.6	36.11
Secondary Copper	41.4	1.77
	100.0	
	Average	21.89

A breakdown of the energy equivalent for the ultimate fuels used shows a strong dependence on natural gas (for smelting) and electricity (for ore benefication). The fuel energy distribution for copper can be listed in tabular form

Type of Fuel/Energy	% of Energy Supplied
Coal	27.7
Oil Products	20.5
Natural Gas	48.6
Nuclear	1.0
Hydro	2.2
	100.0

As lower grade copper ores are mined, the amount of energy needed for benefication will increase.[44]

Glass

The largest tonnage of glass production in this country is for the manufacture of glass containers, consequently most of the energy analysis for glass has been done on the container manufacturing process. This glass is basically a soda-lime glass; 20 percent of the glass removed from the furnaces starts out as cullet. For glass production, energy consumed in terms of ultimate fuel resources as a percentage of the total used is:

Type of Fuel/Energy	% of Energy Supplied [45]
Coal	42.9
Crude Oil	8.8
Natural Gas	53.4
Nuclear Energy	0.4
Hydro-Energy	0.9
Derivative Fuel Product Credit	(6.4)
	100.0

The glass container production itself uses 64.4 percent of the total energy consumed. Glass containers require, a process energy consumption value of 5.87 KWH_t/Kg.[45] Since the glass being used in the heliostats is float process sheet glass, however we will use the process energy consumption value of 3.23 KWH_t/Kg [46] for all glass in this net energy analysis.

Plastic

Four major thermoplastic resins are produced in the United States. These are low density polyethylene, high density polyethylene, polystyrene, and polyvinyl chloride. These thermoplastic resins represent approximately 83 percent of the total thermoplastic and approximately 64 percent of the total plastic production during the period of 1970 to 1972. All four resins depend on ethylene as a primary raw product. The ethylene is produced by the pyrolysis of hydrocarbon feedstock. The feedstocks and the percentage of the ethylene market they provide are:

Pyrolysis Feedstock	% of Total Ethylene Production [47]
Ethane	51
Propane	34
N - Butane	3
Naptha	6
Gas Oil	6
	100

The actual production energy process mix is in many cases proprietary information, but mean values can be determined from the gross energy data. An analysis of production data for polyurethane gives a value of 2.85 KWH_t/Kg for the process energy consumption for production in 1970.[47]

Silver

In the case of silver, it is hard to derive an exact process energy consumption for production value since most commercial silver production is from base metals either as a by-product or a co-product as shown in Table 2.4 [48]

Table 2.4

DOMESTIC SILVER BY-PRODUCT AND CO-PRODUCT PRODUCTION 1973 [48]

Ore Source	% of Total Output
Silver	28.7
Copper	43.2
Lead	16.6
Zinc	10.3
Gold	1.1

Thus we see that only in a few cases are silver ores treated for their own metalic value, but three-fourths of the world's silver is produced mainly as the by-product of base metal production, the major metals being copper, lead, and zinc. In 1968, for example, twice the amount of the United States production of newly mined silver was recovered from secondary sources, excluding demonitized coinage. With respect to the reprocessing of silver waste to recover the silver, one should assume the material goes through the entire recovery or process production sequence because of the low grade state of most silver material, such as photographic salts, collected for secondary recovery. [49]

Therefore, in order to determine the upper limit for the process energy consumption for the production of silver, the data for copper will be used directly for the mining and ore preparation and smelting parts of the operation.

This is done because primary recovery of silver from the ore uses processing methods that are quite similar to the current methods used in the case of copper ores. Thus, this assumption seems to be the most reasonable considering no direct energy process data exists for the silver industry. In refining, the only differences are due to the individual atomic and electrical characteristics of copper and silver. The unit for plating or electrodepositing is the Faraday which equals 26.81 amp hours. One Faraday of charge deposits 3.4 times as much silver as it does copper on a cathode in the electrolytic refining stage, or the process energy for refining silver is 29 percent of that necessary for copper. It should also be noted that a minimum driving anode voltage is necessary to drive the plating process. A similar effect is observed in batteries. Variations in the driving voltage have been ignored in the above considerations. Therefore, the process energy consumption is calculated to be 34.85 KWH_t/Kg for primary silver production. Because of the energy requirements for recovery and reprocessing of secondary silver, this value will be assumed as representative of all silver production where the major interest is the production of silver. Insufficient data exist to determine a reduction factor for this figure where silver is produced is a by-product or co-product since additional refining and processing are still required in order to separate silver from the rest of the residue. Additional comments on silver production will be made when zinc is analyzed.

Since silver is a commodity which suffers from scarcity, another issue to be considered is the impact the use of silver for coating the heliostat mirrors will have on the market. To determine this, silver consumption data will be considered 1974, the most recent year available. This data is listed in Table 2.5.[50]

Steel

When one considers the process energy consumption needed for the production of steel, designation of the type of steel being produced must be the first consideration. The material analysis for the types used in the $100MW_e$ solar thermal central receiver power plant must include carbon steel and Incoloy 800 steel.

The production of raw steel involves three principal operations. These are mining the iron ore, smelting this iron ore into pig iron and the refining the pig iron and scrap into steel. In the United States in 1970, 94% of the iron ore was mined from open pits. The average iron content of the domestically mined crude ore in 1970 was 34%. The original sources of iron ore mined in 1976 are shown in Table 2.6. In that year, the United States produced 64% of its domestic needs. Of all the ore produced, approximately 76% of it went, in general, to feed the northeastern United States complex of iron and steel industries. This is seen in the statistics for pig iron and steel production. The three states producing the largest amount of pig iron in 1976, Pennsylvania, Indiana and Ohio, produced 59% of the total, while in the same year, in the western United States, Colorado, Utah and California together, produced only 5% of the pig iron. In the case of raw steel production Pennsylvania, Ohio, Indiana, Illinois and Michigan produced 72% of the total, while California produced only 3% of the total.[51] These figures reflect the fact that

Table 2.5

SILVER CONSUMPTION IN 1974 [50]

Use	% of Consumption
Electroplated Ware	7.46
Photographic Materials	28.02
Coins, Medallions (commemorative)	12.60
Sterlingware	12.49
Other and Miscellaneous	11.19
Brazing Alloys and Solders	8.19
Electrical and Electronic	20.05
Total	100.00

Total consumption in 1974 was 5.51×10^6 Kg.

Table 2.6

SOURCE OF IRON ORE - 1976 [51]

Original Source	% of Total
United States	
Great Lakes	54.23
Northeastern	1.49
Southern	2.79
Western	5.58
Canada	
Great Lakes	3.83
Eastern	16.23
All other foreign Countries*	15.85
Total	100.00

* 85% (13.47% of total) of all the iron ore imported from all other foreign countries comes from Brazil, Liberia, and Venezuela.

the iron and steel industry is still basically a great lakes region industry and all energy and material analysis for steel must consider this concentration of facilities. This is most important with respect to sources for determining transportation patterns.

We will first consider the analysis for primary energy consumption of the production of raw carbon steel on the 1970 energy use base. These results are given in Table 2.7. Comments with respect to Table 2.7 can be summarized as follows:

1. All data is in kilowatt hours thermal/kilogram. Electrical energy has been given in terms of the primary energy necessary to produce the electricity.
2. Pig iron production from the blast furnace is a mean value. The three major types of furnaces in which the pig iron is refined into steel, after having been smelted in an oxygen enriched blast furnace are (a) the open hearth furnace, (b) the basic oxygen furnace, and (c) the electric furnace.
3. The basic oxygen furnace and the electric furnace are being used increasingly instead of open hearth processes. In 1970, the electric furnace provided 15% of the raw steel production, and in 1971, it provided 17% of the raw steel production.
4. The percentage breakdown of the type of total energy consumed for the production of raw steel is:

	% of Total Energy Consumed [52]
Coal	81.1
Refined oil products	6.6
Natural Gas	13.5
Derivative fuel product credits	(9.6)
Primary fuels for purchased electric energy	8.4
Total	100.0

Table 2.7

PROCESS ENERGY CONSUMPTION FOR PRODUCTION OF RAW STEEL (1970)[52]

Operation	%	KWH_t/Kg
Pig Iron Production (Blast Furnace)	26.7	1.6668
General Utilities (for mills)*	26.5	1.6543
Coke Production	18.3	1.1424
Molten Steel Production (furnaces)	10.1	.6305
Soaking Pits	7.0	.4370
Mining & Benefication (iron ore)	7.0	.4370
Iron Ore Agglomeration	1.6	.0999
Merchant Oxygen Production	1.5	.0936
Lime Production & Mining	1.3	.0812
Total	100.0	6.2427

$6.243 KWH_t/Kg$

* Includes primary energy for electric power produced.

The derivative fuel credit refers to coke oven gas which is exported and burned elsewhere. In terms of the ultimate fuel use, coal represents 85% of the total energy used. This says that 4.9% of the electric energy used comes from coal.

5. The following figures for lime production and mining give totals presented in Table 2.7.[52]

Operation	%	KWH (thermal)/Kg
Lime Production	1.1	6.88
Mining-Limestone & Dolomite	0.1	0.62
Mining-Feldspar	0.1	0.62

Consideration of Incoloy 800 steel is much more complex. Incoloy 800 is a nickel chromium steel alloy which has a composition of 48% iron, 20% chromium and 32% nickel by weight. An estimation of the process energy content of the Incoloy requires a consideration of the final alloy.

A search of the literature discloses that there exists almost no data on nickel and chromium directly applicable to determining their process energy factors. In order to analyze Incoloy, we had to consider the mineral industries in general, the question of chromiums and chromite ore, and the metallurgy of nickel which are all related to Incoloy 800 steel process energy consumption considerations. The results of this work will be discussed in the following paragraphs.

The problem of net energy analysis with respect to the mineral industries generally breaks down into two areas of consideration. The first of these concerns the overall general characteristics of all mineral industries. The second considers the unique characteristics of special mineral industries such as iron, copper, other ferrous metal

alloys, and the various nonmetallic fields. These include fuel extraction (such as oil, gas, and coal) or the general area of mineral production such as would be included in of sand and gravel/mining, cement production, and the quarrying of building stone.

A short definition of the mineral industry would, in most cases include two outstanding characteristics. These are applicable to most mineral industries. First, mineral deposits are not equally distributed over the earth, but have been localized by natural geophysical processes. Second the mineral industries are based on the concept of depleting these natural resources. In an economic sense, they are developed for the wasting of their capital assets. An energy analysis for these types of industries must be based on these fundamental ideas and the economics unique to the field. The geological availability of the material, both in the percentage of the earth's crust and in the percentage of local concentration in a particular ore body will influence the exploration and exploitation of any particular ore body, while the geographical availability will determine the socio-economic control of the distribution and availability of a particular mineral resource.[53]

The mineral industries consider raw materials to be specifically and absolutely essential to the industrial prosperity and military strength of the country. Therefore, they must be available in substantial quantities regardless of cost. Any variation in the cost of procuring a particular mineral compared to the cost of any competing mineral added to the respective production costs will determine which particular mineral is likely to be used in the marketplace. Because of economics and pricing, it has been true to the present time that the cost of extracting a mineral from the ground is in most cases only a small

fraction of the value of the end use product or service to which the mineral or its by-products are applied.

The energy used by a mining operation begins with the construction and systematic development of the mineral deposit. Additional energy is necessary to extract the ore, while the mechanical and metallurgical processing required to eliminate worthless or harmful impurities consumes additional amounts of energy and power. The preferable disposal method for the waste or the end products is one which allows for the contingency of recovery of some fraction of production energy costs. To compare relative cost factors for energy in the entire mineral industry, the following tables should be considered. These tables were derived from U. S. Census data and Bureau of Mines statistics for the specific years mentioned. An additional set of data for the year 1963 is available from the Census Bureau, but it has not been reduced into the format of the following figures. Table 2.8 shows the general trend of decreasing relative cost factors for energy in the entire mineral industry as a percentage of the total value of the products for the years from 1909 through 1958.

Table 2.9 shows the relative costs factors for energy in the form of fuel and power in the various mineral industries for the year 1958. The data is given as a percentage of the total value of the products. For all mineral industries, the percentage of the total value of the products expended on energy is 2.9. This percentage is a result of the low energy cost factors for the oil and gas well industry, with a value of 1.7. If relative energy cost factor values for oil and gas wells are ignored, the average value for the relative cost factors for energy consumption for the rest of the mineral industry is 4.85 as a percentage

Table 2.8

RELATIVE COST FACTORS FOR ENERGY (FUEL AND ELECTRICITY) IN THE ENTIRE MINERAL INDUSTRY 1541

Year	% of Total Value of Production
1909	4.1
1919	4.5
1929	4.9
1939	3.8
1954	2.6
1958	2.9

Table 2.9

RELATIVE COST FACTORS FOR ENERGY (FUEL AND POWER) IN VARIOUS MINERAL INDUSTRIES FOR THE YEAR 1958 [54]

Industry	% of Total Value of Products
All Mineral Industries	2.9
Coal Mines:	
Anthracite	4.9
Bituminous	3.8
Oil and Gas Wells	1.7
Mines	
Metal	4.8
Other Non-metal	5.9

of the total value of products.

In order to determine the dependence of a particular mining industry with respect to the total value of the product expended for energy in the form of fuel and power, the metal mining and nonmetal mining industries were considered separately. In Table 2.10, data on the relative cost factors for energy for the years 1939 and 1958 are compared for a number of the metal industries. This data shows that, with rare exceptions, the cost of the energy expended on the mining of products remains a fairly constant percentage of the value of the final product. This is true for both the data based on the year 1939 and the data based on the year 1958. An analysis of the nonmetal mining industry, is shown in Table 2.11 where data for the years 1939 and 1958 for representative nonmetal mining industries are compared with respect to the relative cost factors for energy expenditures.[54] Recent higher energy costs will tend to increase the relative cost factor, but this will eventually act to reduce the actual amount of energy expended.

From a preliminary analysis of the data shown in the series of figures discussed previously, certain general characteristics are identified with respect to energy expenditures in the mineral industries. If we know the value of the particular product being produced, either mineral or nonmineral, an estimate of the value of energy consumption can be made. Obviously, this is a crude analysis of the energy needs and does not address itself to any particular energy source or to the net energy question with respect to the production of a specific metal or non-metalic mineral. We now proceed to compare Tables 2.10 and 2.11 for the metal and nonmetal mining industries and select the metal mining industries which are of importance to us in this analysis. These selected metal

Table 2.10

METAL MINING INDUSTRIES: COMPARISON OF THE RELATIVE COST FACTORS FOR ENERGY (FUEL AND POWER) FOR THE YEARS 1939 AND 1958 [54]

Industry	% of Total Value of Products	
	1939	1958
All Metal Mines	5.6	4.8
Iron Ore	4.3	5.0
Copper Ore	5.7	5.1
Lead-Zinc Ore	7.0	6.7
Gold-lode	5.6	5.2
Gold-placer	7.7	11.9
Silver Ore	3.5	4.3
Manganese Ore	8.2	5.2
Tungsten Ore	6.4	1.6
Mercury Ore	9.5	5.7
Titanium Ore	11.0	---
Uranium-Radium-Vanadium Ore	---	3.1

Table 2.11

NON-METAL MINING INDUSTRIES: COMPARISON OF THE RELATIVE COST FACTORS FOR ENERGY (FUEL AND POWER) FOR THE YEARS 1939 AND 1958 [54]

Industry	% of Total Value of Products	
	1939	1958
Dimension Stone (Quarries Only)	7.9	5.3
Crushed Stone	9.0	6.2
Common Sand and Gravel	10.7	7.0
Glass Sand	11.2	8.3
Foundry Sand	7.7	9.4
Fireclay	3.4	7.3
Fuller's Earth	12.3	15.0
Kaolin, Ball Clay	10.7	7.9
Phosphate Rock	14.3	10.4
Rock Salt	4.4	1.8
Potash, Etc.*	9.6	7.2
Sulphur	3.6	6.1
Feldspar	---	8.2
Flourspan	5.3	7.0
Barite	7.1	6.2
Talc	6.1	5.6

*Potash, Sodium Salts and Borates

mining industries are shown in Table 2.12. Results show that in general between 1939 and 1958, for a wide range of metals mined, the relative cost factors for the fuel and power required were approximately five percent of the final price. In order to determine the mining cost factor for chromium and nickel, more information is needed on their abundance, occurrance, and metallurgy.

The chemical element chromium (Cr) is not normally encountered in nature in its pure state. Chromite is the only important ore mineral of chromium. The major producing countries for chromite are Turkey, the Union of South Africa, the Soviet Union, the Philippines, and Rhodesia. High grade chromites contain up to 65 percent chromium oxide (Cr_2O_3), but these are quite rare in nature. The usual high grade ore from which chromium is produced or which is used to feed furnaces for chromate-type steel is an ore which contains 48 percent Cr_2O_3 with a chromium to iron ratio of approximately three to one. The iron content can vary over a wide range of values. In addition to the major producing countries, chromate is produced in the United States, Canada, Cuba, Guatemala and Brazil.

Chromium is produced most usually in the form of a ferro-chromium by the reduction of chromate ores with carbon or silicon in an electric furnace. Chromium metal can also be produced on a commercial scale by electrolysis processes. For our work, the use of chromium alloys is of particular importance. We are specifically interested in Incoloy 800 steel. Chromium is used quite extensively for alloying iron or stainless steel. Special high strength steels and electrical resistance wire are also uses for which chromium is required. In steel, chromium is used to prevent corrosion by atmospheric conditions, water, acids, or high

Table 2.12

SELECTED METAL MINING INDUSTRIES: COMPARISON OF THE RELATIVE COST FACTORS FOR ENERGY (FUEL AND POWER) FOR THE YEARS 1939 AND 1958 [54]

Industry	% of Total Value of Products	
	1939	1958
All Metal Mines	5.6	4.8
Iron Ore	4.3	5.0
Copper Ore	5.7	5.1
Lead-Zinc Ore	7.0	6.7
Gold-lode	5.6	5.2
Silver Ore	3.5	4.3
Manganese Ore	8.2	5.2
Mercury Ore	9.5	5.7

Average cost factor for all metal mines (1939, 1958) = 5.2%

temperature fluid flow conditions. If one desires a heat resistant alloy, chromium is usually alloyed with nickel where the composition of the alloys is such that the chromium value lies between 15 and 28 percent while the nickel value lies between 5 and 78 percent. Basic characteristics of nickel-based alloys, where chromium is added, are their high strength and unique resistance to deformation and degradation conditions induced by high temperatures.[55]

Nickel as an element ranks 24th in order of abundance for the elements found in the surface of the crust of the earth. Also, nickel averages approximately one-hundredth of one percent of the content of igneous rock. However, there are very few nickel deposits of commercial importance. The nickel ores that are mined and from which nickel is extracted fall into two specific generic types. These are sulfides and laterites. In the case of sulfides, nickel is present as a nickel iron sulfide usually in association with other iron pyrite complexes. The most important known deposits are in Sudbury, Canada, and have provided the major portion of the world's supply of nickel since the year 1905. Other substantial deposits have been discovered and developed in northern Manitoba in Canada, and western Australia. Other deposits are found in the Soviet Union, South Africa, and Finland. Lateritic nickel ores occur mainly in the form of oxides or silicates. The lateritic ores are widely distributed throughout the world's surface, with their major concentration in the tropics. These lateritic ores constitute the major percentage of the world's known reserves of nickel. In the United States, nickel ore of the lateritic variety is mined in Oregon. Additional deposits are found in New Caladonia, Cuba, the Dominican Republic, Greece, the Philippines, Australia, Indonesia and Guatemala.

Nickel is marketed in many forms and used for many particular products. The commercial world market price of nickel is based on the cost of electrolitic nickel. A late 1975 price for this material would be about $5 per kilogram ($2.20 U.S. per pound).

If one wishes to determine net energy aspects for nickel, certain characteristics of the smelting process must be considered for sulfide ores and for lateritic ores. Both processes are used to produce commercial nickel and nickel alloys. According to the American Bureau of Metal statistic data for the year 1973, 40.5 percent of the total nickel consumed in the United States was used for stainless and other steel products. It should also be noted that where the lateritic process is used, it is commercially competitive with the process for sulfide ores.

Sulfide ores that are mined for the production of nickel usually contain from one to three percent nickel and various amounts of copper. The ore is crushed and ground and the metals are concentrated by a froth flotation process. Magnetic separation and differential flotation techniques may also be used to separate and concentrate the iron, nickel, or copper constituents in the ore. Fairly standard smelting techniques are used to reduce and separate the various constituents to produce the final metallic pigs.

In the case of lateritic ore, the bulk of the metal produced is marketed as a ferro-nickel alloy. In this case, the process is fairly simple. The ore is dried and pre-heated under a reducing atmosphere and then reduced and melted in an electric arc furnace to be cast into ferro-nickel pigs. Two other processes involving a nickel sulfide mat technique or ammonia leeching are slightly more complicated but are cost competitive with the relatively simple smelting process used for the production of

ferro-nickel alloys.[56]

Combining the mining industry analysis with the information base developed for chromium and nickel, the following assumptions can be justified to estimate the process energy consumption for the production of Incoloy 800 steel. Since chromate ores are 48 percent to 65 percent chromium oxide with a general iron to chromium ratio of 1:3, it is reasonable to assume that the energy costs for the production of chromium are the same as iron. For the case of nickel, it is reasonable to assume that energy costs for mining are comparable to those for iron, while the smelting costs are comparable to those for copper, since many of the same techniques are used. Because concentrated ore, not completely refined metal, in many cases is used for the steel and ferro-nickel alloy production, these figures represent but an educated estimate of the energy content of the Incoloy 800. The estimated process energy consumption analysis for the production of Incoloy 800 is summarized in Table 2.13.

Zinc

Zinc is third in non-ferrous metal consumption in the world, being surpassed only by copper and aluminum. The major user is the automobile industry which used one-third of the United States slab zinc consumption. In the United States, demand has steadily increased, while domestic metal producing capacity has declined by almost 50 percent between 1968 and 1975. There are two major production resources. Primary zinc is produced from newely mined ores. Secondary, redistilled, or resmelt zinc, depending on the recovery process, is produced from zinc scrap or residues. At the present time five companies account for 89 percent of the slab zinc production and also for 77 percent of the domestic mine output.

Table 2.13

ESTIMATED PROCESS ENERGY CONSUMPTION FOR PRODUCTION OF INCOLOY 800 STEEL

Incoloy:	Energy Content in KWH_t/Kg
Iron (Fe) - 48%	3.00
Cromium (Cr) - 20%	1.25
Chromate ore is 48% Plus Cr Fe:Cr ratio in ore is 1:3 Assume same energy costs as Fe	
Nickel (Ni) - 32%	
Mining - Assume Fe energy costs	0.16
Smelting - Assume Cu energy costs	4.71
Total	9.12

The ratio of process energy consumption for the production of Incoloy 800 steel to that of regular steel is estimated to be 1.46.

Most zinc is found in the form of zinc sulfide ores which contain 3 percent to 10 percent zinc with the average being around 5 percent. In 1974 mine production of zinc was carried out in 54 countries. The ranking zinc mining countries are:

	Metal Content of Mine Production ($\times 10^5$ tons)
Canada	12.8
USSR	7.5
Australia	5.0
United States	5.0
Peru	4.4

The ranking metal producing countries are:

	Metal Produced ($\times 10^5$ tons)
Japan	9.37
USSR	7.5
United States	5.55
Canada	4.7

The major zinc sources in the world for primary zinc, in percentage of total production, are zinc ores 59 percent, zinc-lead ores 15 percent, lead ores 19 percent, and all other ores 7 percent. Zinc and zinc ore production figures for the United States in 1973 are given in Table 2.14. As shown in Table 2.14, the determination of the process energy consumption for zinc is fairly complex.[57]

With respect to domestic mine production, five states account for the major share of the primary zinc which is produced from both zinc and lead zinc ores. These are:

Table 2.14

ZINC AND ZINC ORE PRODUCTION IN THE UNITED STATES (1973) [57]

Ore	Metal	% of U.S. Production
Zinc*	Cadmium	100.0
	Germanium	100.0
	Indium	100.0
	Thallium	100.0
	Lead	11.9
	Silver	10.3
	Gold	5.3
	Zinc	74.9
Lead*	Zinc	21.7
Copper*	Zinc	2.7
Silver*	Zinc	0.5

*These four ores (primary production) account for 99.8% of the domestic zinc production.

Table 2.15

PROCESS ENERGY CONSUMPTION FOR PRODUCTION OF ZINC [57]

Process	Energy Content m KWH_t/Kg
Electrolytic	19.43
Vertical Retort	21.01
Electrothermic	23.44
Weighted Average for Industry	20.99

	% of U. S. Production of Zinc	
	Zinc Ore	Lead-Zinc Ore
New York	19%	0
Missouri	18%	8.2%
Tennessee	17%	4.5-5.0%
Colorado	10%	4.1-9.4%
Maine	0	4.31-6.4%

These five states account for 86 percent to 93 percent of the total domestic primary zinc ore, depending on the magnitude of lead demand.[58]

Since commercial grade zinc ores are sulfide in nature, of relatively low grade, and contain many valuable co-products or by-products, the processing is basically classified into three major steps. In the first step the ore is concentrated or beneficiated by grinding and froth seperation. The resulting concentration is then 50% to 69% zinc. The second step consists of preparation for smelting which involves roasting and sintering. H_2SO_4 is a commercial by-product produced by the roasting of zinc ores. The third and final step is the smelting process. There are basically five smelting processes used: the horizontal retort, the vertical retort, electric thermal, blast furnace and electrolytic.[59] Because of the complex mixture of process techniques involved in the metallury of zinc, we will use the industrial mean average value for process energy consumption for the production of zinc. These data are summarized in Table 2.15.

The results are summarized in Table 2.16 for the separate analyses of the process energy consumption values of the various materials needed to perform the net energy analysis of the 100 MW_e Solar Tower collector system, including the thermal collection component.

Table 2.16

PROCESS ENERGY CONSUMPTION FOR THE PRODUCTION OF VARIOUS MATERIALS (1970 BASE)

Material	KWH_t/Kg
Aluminum	55.96
Cement	0.3237
Copper	21.89
Glass	3.23
Plastic-Polyurethane	2.85
Sand	0.0362
Silver	34.85
Steel-Carbon	6.24
Steel-Incoloy 800	9.12
Zinc	20.99

2.5 MANUFACTURING

The next problem is to determine the fraction of the total energy used in a specified industry that is consumed directly by the typical manufacturer. Because of the wide variation in manufacturing methods, plant locations, plant age, production tooling costs, and the cost savings due to the variation in the size of production runs for a specific product, the only reasonable method is to use average values for particular industries. For general assembly line manufacturing, energy costs, except for exotic products, tend to be only mildly dependent on the specific differences in various forms of the same products. The differences in most instances are cosmetic-trim, paint, and component placement, and not in the basic design. This fact has made our current mass production society possible. The energy fractions consumed directly by manufacturers for a large number of industries are listed in Table 2.17. These figures are distributed by the Office of Energy Programs of the United States Department of Commerce. For those industries of interest in this study, the percentages of total energy used in an industry and consumed directly by the manufacturer are summarized in Table 2.18. From an analysis of the existing manufacturers energy consumption data, we decided that different manufacturing and construction percentage cost figures need be used for different industries. The specific manufacturing and construction energy costs for the various components are specifically identified for each separate net energy analysis on the appropriate table.

2.6 TRANSPORTATION

Very little data exists on transportation energy costs. Even less information is available about comparative transportation energy costs. Data listed in Table 2.19 were developed from the most reasonable available source.

Table 2.17

ENERGY FRACTION CONSUMED DIRECTLY BY MANUFACTURER [60]

Manufacturer	Energy Fraction Consumed Directly by Manufacturer
Motor Vehicles and Equipment	.1049
Aircraft and Parts	.1218
Transport Equipment	.0806
Construction & Mining Equipment	.1181
Materials Handling Equipment	.0662
Metal Working Equipment	.1000
Special Industry Machinery	.0875
General Industry Machinery	.1042
Heating and Plumbing	.0819
Screw Machine Products	.0846
Electrical Apparatus	.1103
Household Appliances	.1110
Electric Lighting and Wiring Equipment	.1093
Radio and TV Equipment	.0851
Electronics Components	.1129
Misc. Electrical Equipment	.1083
New Construction	.1892
Plastics	.3514
Fabricated Metal	.1198
Engines and Turbines	.1168
Farm Machinery	.1133

Table 2.18

PERCENTAGE OF TOTAL ENERGY USED IN AN INDUSTRY CONSUMED DIRECTLY BY MANUFACTURER [60]

Industry	Percentage
Motor Vehicles and Equipment	10.5
Aircraft and Parts	12.2
Transportation Equipment	8.1
Metal Working Equipment	10.0
General Industry Machinery	10.4
Electrical Apparatus	11.0
New Construction	18.9
Plastics	35.1

Table 2.19

TRANSPORTATION ENERGY COST-BASED

ON UNITED STATES NATIONAL AVERAGES [61]

Mode	KWH_t/Metric Ton Km (net)
Rail (line haul)	.1365
Barge	.1566
Highway Truck	.5621
Cargo Plane	5.4198

Table 2.20

SUMMARY OF TRANSPORTATION FACTORS

Material	Assumed Source	Transportation Method Assumed (See text)	Mileage (Km)	Transportation Multiplier*
Glass	Pittsburgh	Rail	4,957.0	2.0
Steel	Gary	Rail	4,237.0	1.0
Motors	New York	Rail	5,549.0	1.3
Cement	300 Mi.	Truck	482.7	1.0
Aggregate	100 Mi.	Truck	160.9	1.0
Polyurethane	500 Mi.	Truck	804.5	1.0

* The extra weight that must be shipped in the form of packing and crating that increases the weight transported by this multiplier.

In developing Table 2.19, the following assumptions were made with respect to transportation.

1) All mileage was taken from highway road maps. The route used was from the assumed sources in Table 2.20 through Chicago to Los Angeles by way of Houston unless otherwise specified. This routing was chosen since most East-West railroad lines in the Northeastern United States pass through Chicago.
2) The assumed sources are the result of the materials analyses done in Section 2.4 with respect to sources of supply and industrial concentrations.
3) The transportation factors are summarized in Table 2.20. The transportation method listed in column three is based on an assumption of transportation routes and the methods of shipment.
4) Analyses decisions were made in order to give reasonable limits on the transportation energy costs.

2.7 CAPITAL ENERGY COSTS

The net energy analysis of the 100 MW_e plant is being limited to the thermal collection component. This component can be classified into the following subsystems; heliostat array, receiver, riser and downcomer piping, the tower, and the thermal storage system. This net energy analysis is based on the inverted heliostat configuration, in Figure 2.3, which used 22,940 heliostats. The inverted heliostat design is shown in Figure 2.4. The heliostat systems are to be designed for operation in an open loop mode. The differences in the two system modes - open loop and closed loop - will not be considered with respect to energy requirements. The closed loop option would add the sensor post subassembly, the dashed outline

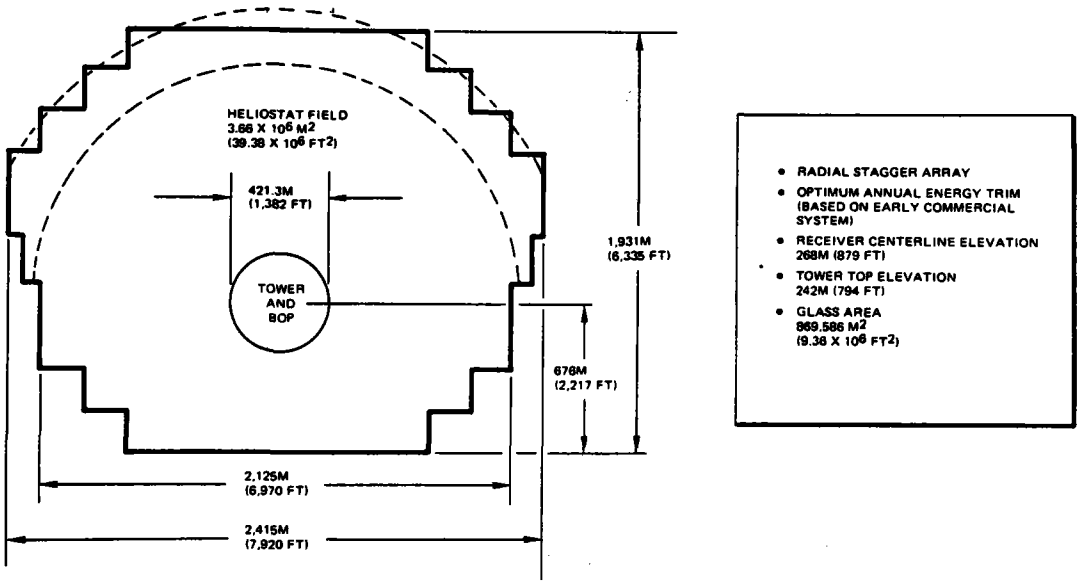

Figure 2.3 Schematic of Heliostat Field Layout for the Commercial System. Source: [2], p. 1-2.

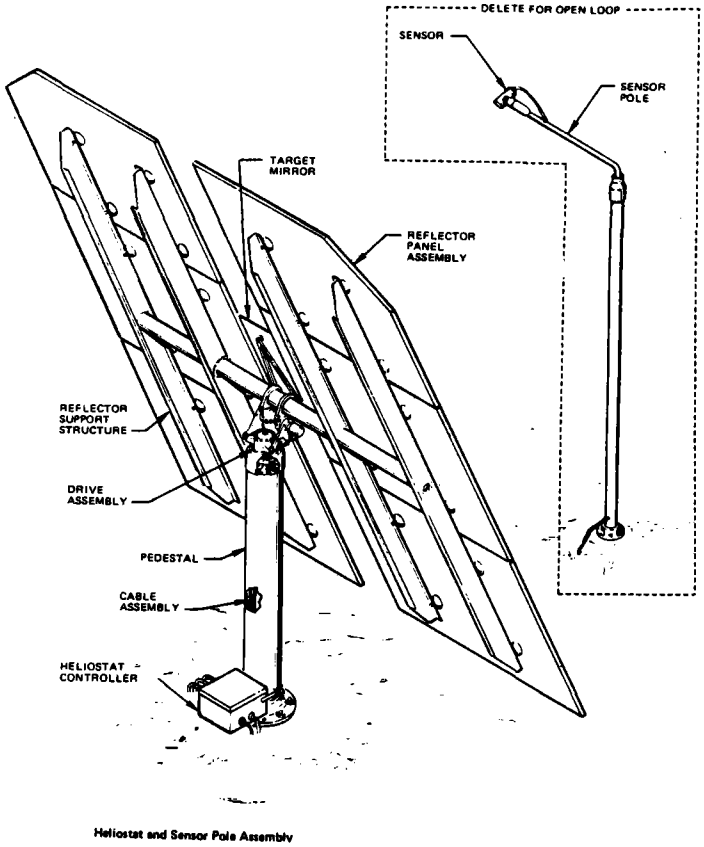

Figure 2.4 Heliostat and Sensor Pole Assembly. One inverted heliostat is shown with the sensor post that would be included if the system worked in a closed loop mode. The net energy analyis considers only the open loop system, the most economic of the two systems. Source: [4], p. 5-2.

in Figure 2.4, to each heliostat position. Previous analyses have assumed use of a closed loop mode in the case of the heliostat system, but improved electronic control and reduction in the cost of microchips make the open loop mode more attractive and feasible. The open loop mode has lower material requirements per unit and thus corresponding energy savings, guidance of the open loop system is not, however quite as accurate. Other suggested central receiver proposals have generally considered the use of the open loop mode. Thus this design change makes this system comparable with other proposals.

Using the report on central receiver solar thermal power system [3], a material and weight listing for the inverted heliostat can be generated from the information provided. This listing is given in Table 2.21. However, this listing is too fragmented to be used in the net energy analysis, except for information it provides on the weight of zinc used to galvanize the steel. The zinc information is added to other inverted heliostat materials usage data on the system, the best compilation of existing data for one inverted heliostat is given in Table 2.22.[62]

Each heliostat in the collector field array is positionally oriented by the motor drive mechanism. These motors are supplied with power from the electrical generator system for the power plant through a branching network of step down transformers and power feeders. In addition, the open loop computer control operating mode requires a bus and signal cable hook up between the heliostat and the computer that controls orientation. Thus the 100 MW_e power plant will require cabling and transformers to control and power the heliostats. The net energy equivalent for these control and power elements (cable and transformers) are therefore prorated for each heliostat.

Table 2.21

INVERTED HELIOSTAT-MATERIALS AND WEIGHT BREAKDOWN

Component	Material	Weight lbs	Weight Kg	Reference
Reflector Panel (1)*	1/8 in glass	110.3	50.3	[3] 4-38
	Foam	22.4	10.2	[3] 4-38
	Galvanized Steel Sheet			
	Steel	52.5	23.8	[3] 4-38
	Zinc	8.5	3.9	[3] 4-42
	Attachment Cups (Steel)	5.7	2.6	[3] 4-38
Tracking Mirror**	(Completer Assembly)	38.9	17.6	[3] 4-38
Structural Support	Torque Tube			
	Steel	552.5	250.6	[3] 4-45
	Zinc	33.0	15.0	[3] 4-45
	Crossbeams			
	Steel	509.8	231.2	[3] 4-45
	Zinc	13.0	5.9	[3] 4-45
Pedestal	Steel	472.5	214.3	[3] 4-75
	Zinc	36.0	16.3	[3] 4-75
Foundation	Precast Concrete	9,750.0	4,422.5	[3] 4-75

(CONTINUED ON 2-58)

Continuation of Table 2.21

Summary of Weight Breakdown

	Weight Breakdown		Reference
Reflector panels: (1/8 in. glass)	Pounds	Killograms	
485 in x 114 in	798	362	[3] 4-228
2 clipped	390	177	[3] 4-228
Tracking mirror **	39	18	[3] 4-228
Structural support	1,108	503	[3] 4-228
Drive unit	670	304	[3] 4-228
Pedestal	509	231	[3] 4-228
Total (without foundation)	3,514	1,595	
Foundation	9,750	4,422	[3] 4-228
Total (with foundation)	13,264	6,017	

* Six reflector panels needed/heliostat.

** Needed for closed loop operation only.

Table 2.22

INVERTED HELIOSTAT MATERIALS USAGE [62]

Collector Element	Material	Weight	
Reflector	Silver	33 gm	
	Glass	611.0 kg	(1,345 lbs)
	Polyurethane Foam	61.98 kg	(136.3 lbs)
	Polyurethane Bond	6.3 kg	(13.8 lbs)
	Low Carbon Steel	725.8 kg	(1,600 lbs)
	Zinc	44.3 kg	(98 lbs)
Heliostat Drive	Low Carbon Steel	22.7 kg	(50 lbs)
	Bearings and Actuators	122.7 kg	(270 lbs)
	Motors (2)	9.1 kg	(20 lbs)
	Meehanite Ductliron	150.0 kg	(380 lbs)
Heliostat Pedestal	Low Carbon Steel	172.7 kg	(380 lbs)
	Zinc	16.3 kg	(36 lbs)
Heliostat Foundation	Concrete	2.84 m^3	(3.7 yd^3)
	Rebar and Anchor Bolts	185.5 kg	(408 lbs)
Reflector Area		38.1 m^2	(409.9 ft^2)

A substantial effort was made to survey the market place in order to make a cost effective choice of cabling. An attempt was made to locate both a best cable type and a marginally satisfactory type on which to run cost comparisons. The best cable type for the use proved to be (see Figure 2.5) continous corrugated aluminum sheath armored cable. For comparison, a spiral type shield cable without armor was chosen as the bare minimum case. However, this cable was only 13 percent less expensive. The next best cable from a functional viewpoint was corrugated tape shielded cable, but this cable, even though it was still less satisfactory, cost 20 percent more than the continous sheath cable. The major dollar cost figures are in the manufacturing processes. Therefore a 4 Conductor AWG#4 Aluminum Sheath Cable was chosen for the power cable. This decision was made using information restricted to price and application. The net energy analysis for this cable per kilometer is shown in Table 2.23. We assumed that the cable was made in the general Chicago area and shipped to southern California by rail in coiled rolls. In addition to the power cable, each heliostat has an unshielded signal cable. An approximate net energy was calculated for representative signal cabling without shielding.

The proposed power and data distribution array for the collector field network, Figure 2.6; the branch collector field network, Figure 2.7; and network layout, Figure 2.8 were analyzed to determine the average amount of wire per heliostat and the number of transformers needed. The analysis showed that an average of 28 m of cabling are needed per heliostat. A study of the required transformers showed that two types were needed. These results can be summarized as follows:

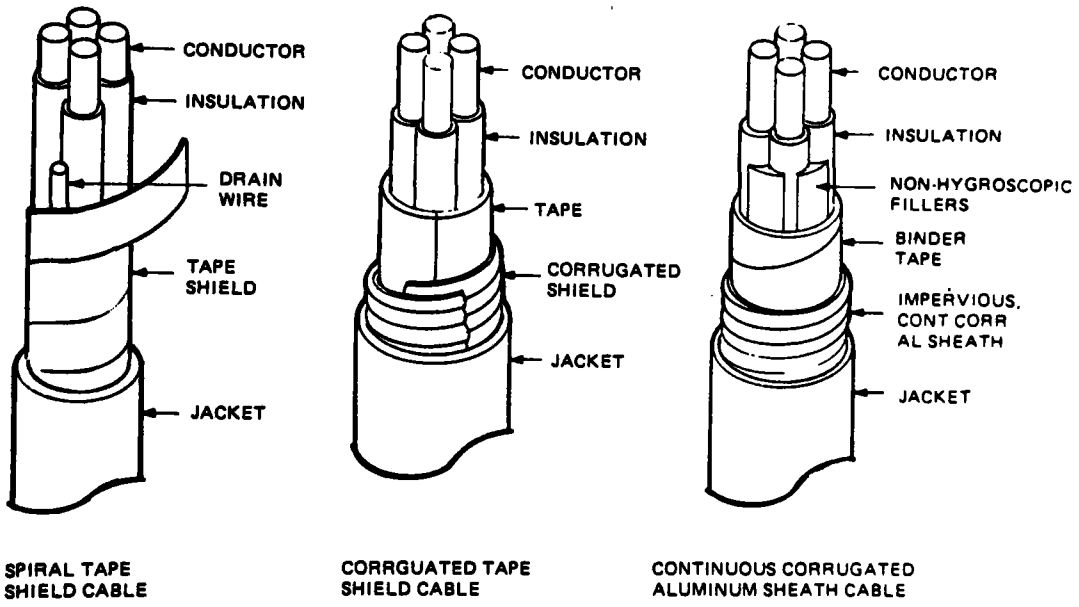

Figure 2.5 Cable Construction. Source: [3], p. 4-173.

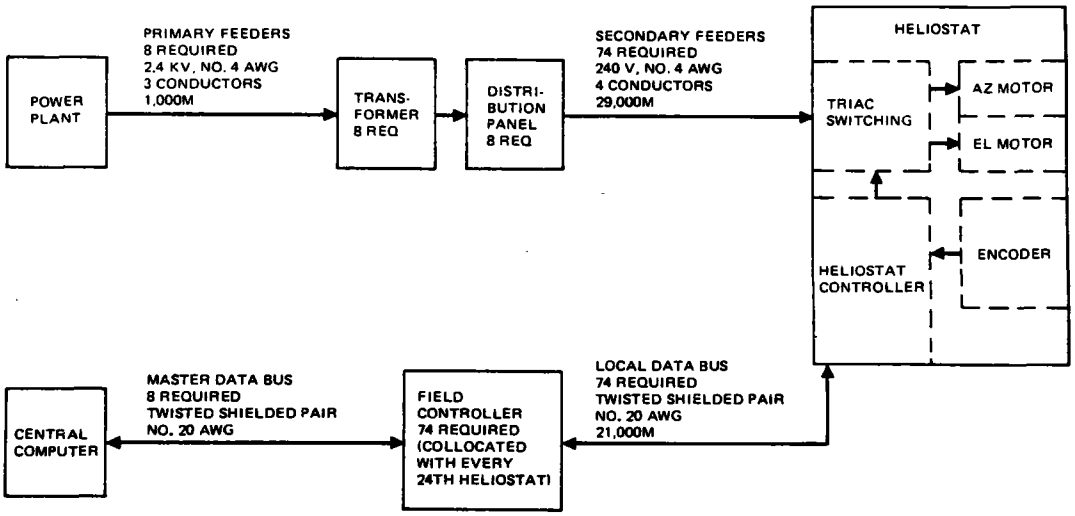

Figure 2.6 Pilot Plant Power and Data Distribution-Collector Field Network. This network was scaled up in transformer number and feeder wire lengths for use in the 100MW$_e$ Commercial System. Source: [3], p. 4-178.

Table 2.23

NET ENERGY ANALYSIS OF CABLE FOR HELIOSTAT CONTROLS

4C AWG#4 ALUMINUM SHEATH CABLE

Material	Weight (Kg/Km)	Energy (MWH_t/Km)	
Copper	752	16.46	
Insulation (Conductors)	495	1.41	
Sheaths (Plastic)	344	0.98	
Sheath (Aluminum)	260	14.55	
Total	1,851	33.40	33.40
Transportation (Nominal Distance-Chicago to Los Angeles; Mode-Rail; Transportation Multiplier = 1)			1.07
Manufacturing			3.77
		TOTAL	38.24

Net Energy in Power Cable = 38.24 MWH_t/km

Net Energy in Signal Cable ~18.26 MWH_t/km

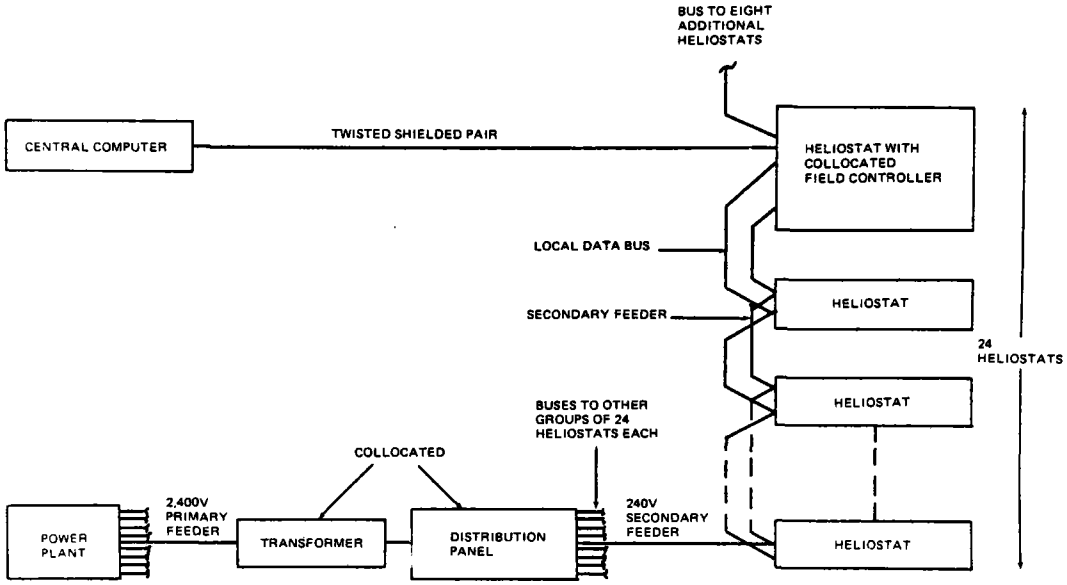

Figure 2.7 Branch-Collector Field Network. This Network was scaled with respect to transformer number and feeder and signal cable lengths for the 100MW$_e$ commercial heliostat field array. Source: [3], p. 4-179.

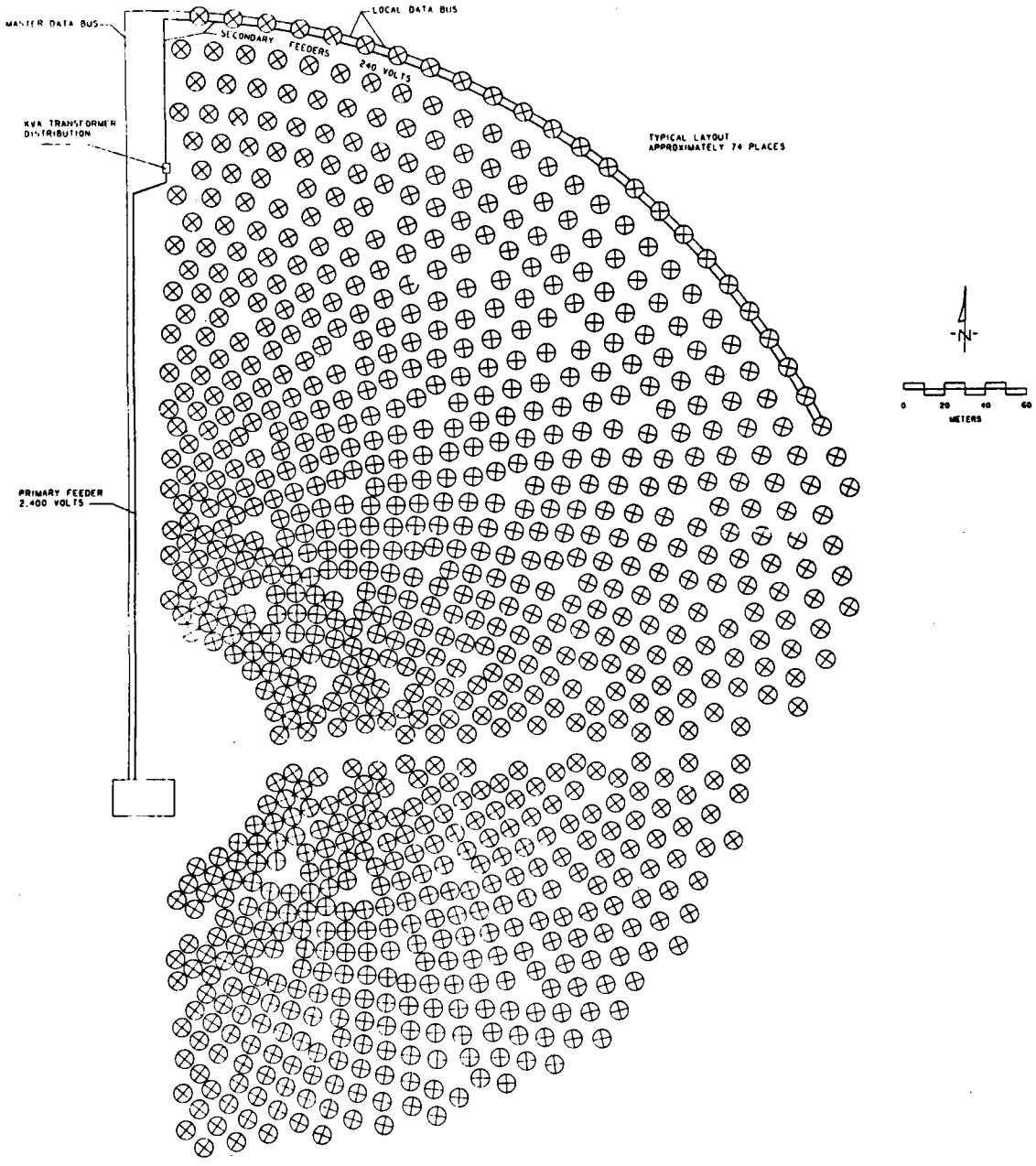

Figure 2.8 Network Layout. This figure shows the layout for a single branch in circle number 32 of the pilot plant heliostat array. A similar scaled up version of this layout is used for the 100MW$_e$ commercial facility. Source: [3], p. 4-180.

Transformer Type	Number of Heliostats Served
4160 Volts-2300 Volts 225 KVA	432
2300 Volts-240 Volts 15-20 KVA	24

These transformers are off the shelf items. The net energy analysis of the transformers is shown in Table 2.24. Cabling and transformer net energy data are combined with the net energy determination for one heliostat using the materials usage information in Table 2.22 and the transformer data from Tables 2.19 and 2.20 to give, in Table 2.25, the total net energy required to produce all materials, transport them to southern California, build, and assemble one complete inverted heliostat,and place it in its final position on the site. With respect to the results summarized in Table 2.25, energy content represented by the silver plating is too small to show up for a calculation of this sensitivity except in the last decimal place. The zinc was assumed to be plated on the steel at the mill, and this galvanized steel is then transported to the site. Since the weight of the silver is very small compared to the weight of the glass and the glass already has a transportation multiple of 2, additional transportation energy required by the weight of the silver on the glass can be ignored. Next it is necessary to determine the materials and net energy requirements for the other segments of the total thermal component for the 100 MWH_e commercial plant. These components are the receiver, the riser and downcomer, and the concrete tower.

The weights of the components in the commercial receiver are summarized in Table 2.26. A cross sectional drawing of the commercial receiver

Table 2.24

NET ENERGY ANALYSIS OF TRANSFORMERS (OFF THE SHELF ITEMS)

Materials	4160 V -- 2300 V 225 KVA Weight (kg)[63]	4160 V -- 2300 V 225 KVA Energy Required (MWH_t)	2300 V -- 240 V 15 - 20 KVA Weight (kg)[63]	2300 V -- 240 V 15 - 20 KVA Energy Required (MWH_t)
Copper Coils	363	7.95	45	0.98
Iron Core	544	3.39	91	0.57
Busings & Terminal Bases (Fe)	91	0.57	23	0.14
Steel Can	907	5.66	45	0.28
Oil	680	9.99	68	1.00
Glass (Insulation)	136	0.44	23	0.07
TOTALS	2,721	28.00	295	3.04
Transportation		1.84		.20
(Nominal Distance-Pittsburgh to Los Angeles; Mode-Rail; Transportation Multiplier = 1)				
Manufacturing		3.28		.36
TOTAL NET ENERGY		33.12 MWH_t		3.60 MWH_t
HELIOSTATS SERVED	432		24	

Table 2.25

NET ENERGY REQUIRED FOR ONE INVERTED HELIOSTAT

Material	Weight (Metric Tons)	Energy Required in MWH_t	
Steel	1.379	8.605	
Glass	0.611	1.970	
Concrete	6.733	2.180	
Polyurethane	0.078	0.194	
Motors	0.009	0.197	
Zinc	0.061	1.280	
Silver	(3.3×10^{-5})	0.001	
TOTAL		14.427	14.43
Transportation			
Steel		0.798	
Glass		0.827	
Cement		0.076	
Aggregate		0.505	
Polyurethane		0.031	
Motors (Copper)		0.009	
Zinc		0.035	
TOTAL		2.281	2.28
Cabling (28 m Heliostat)			1.58
Transformers (Net Energy/Heliostat)			0.23
Manufacturing & Construction (15%)			2.78
	TOTAL NET ENERGY		21.30

Table 2.26

COMMERCIAL RECEIVER WEIGHT SUMMARY

Item	Weight Kilograms x 10^3 (kips)	Reference
Carbon Steel (Structural)	653 (1437)	[5] 2-25
24 Panel Assemblies	155 (340)	[5] 2-25
Piping	307 (675)	[5] 2-25
Crane	42 (92)	[5] 2-25
Other Components	73 (160)	[5] 2-25
Total Weight	1,229 (2704)	

is shown in Figure 2.9; the information for the commercial system user and downcomer piping was taken from the data in Figure 2.10. The commercial system tower design information was taken from the data in Figure 2.11 The receiver, riser and downcomer, and tower data were analyzed to determine their total net energy content including manufacturing and transportation. The results of this analysis are shown in Table 2.27 as the net energy required to build the thermal collection component of the 100 MW_e commercial plant without considering the net energy equivalent due to the storage subsystem. The thermal storage subsystem will be analyzed shortly.

In order to determine the number of days that it is necessary for the 100 MW_e plant to operate in order to provide the amount of energy equivalent to that consumed in the building of the facility, average energy calculations must be done for the site under consideration. Annual energy calculations for several different insolation models were carried out for the 100 MW_e system. The simplest model assumed a constant insolation level of 950 W/m^2 for the whole year. The system assumptions were:

1) The system has solar multiple of 1.7 with six hour storage capacity.
2) The collector field is activated at a 10° sun elevation angle.
3) At a 15° sun elevation angle, the receiver has reached the derated steam condition.
4) All the energy could be diverted to storage if there is no electric power demand.
5) The threshold for rated steam operation from the receiver was 50% of maximum design flow, subject to the condition that the turbine has completed the starting and loading phase.
6) The net cycle efficiency is 33.7% including parasitic plant loads.
7) The system is down 35 days/year for cloudiness and maintenance.

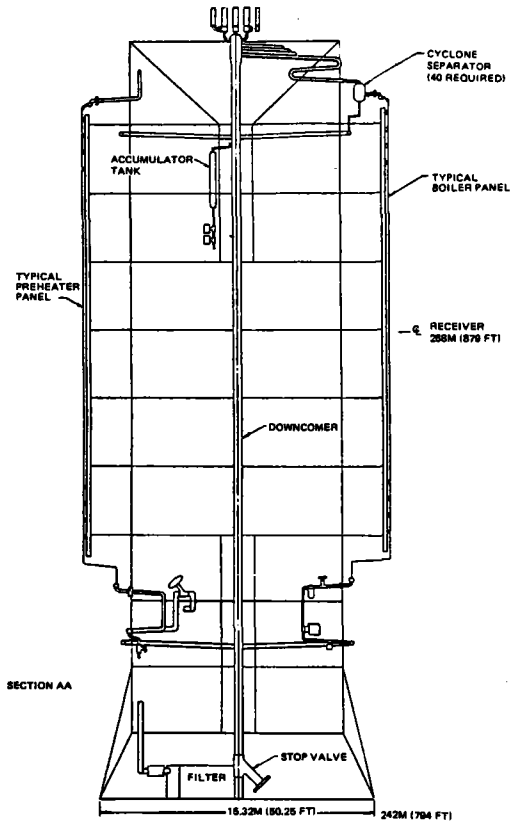

Figure 2.9 Commercial Receiver, Plane View. Source: [64], p. 95.

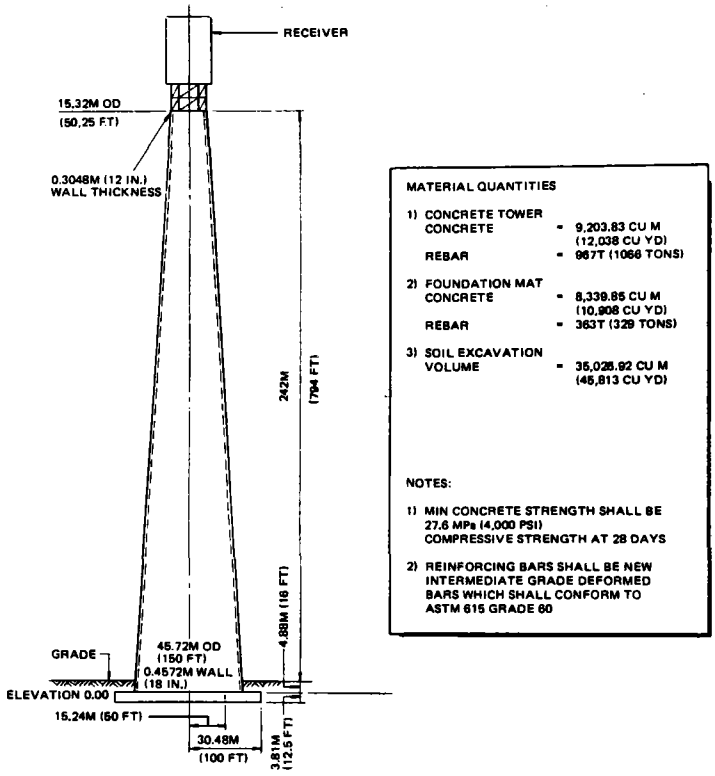

Figure 2.11 Commercial System Tower Design. Source: [64], p. 144.

Figure 2.10
COMMERCIAL SYSTEM RISER/DOWNCOMER

RISER

- 30.5 CM (12 IN.) SCHEDULE 160 CARBON STEEL, ASTM A106, GRADE C
- 8.9 (3.5 IN.) CALCIUM SILICATE WITH ALUMINUM JACKET
- DESIGN TEMPERATURE = 260°C (500°F)
- DESIGN PRESSURE = 21.65 MPa (3,140 PSIA)

DOWNCOMER

- 34.3 CM (13.5 IN.) MIN. I.D. X 4.5 CM (1.773 IN) NOM. WALL
- LOW ALLOY STEEL ASTM A335, GRADE P22
- 14.0 CM (5.5 IN.) CALCIUM SILICATE WITH ALUMINUM JACKET
- DESIGN TEMPERATURE = 537.8°C (1,000°F)
- DESIGN PRESSURE = 12.24 MPa (1,775 PSIA)

Source: [64] p. 147

Table 2.27

NET ENERGY REQUIRED FOR 100 MW_e COMMERCIAL PLANT
(THERMAL COMPONENT WITHOUT STORAGE)

Part	Item	Weight (Metric Tons)	Energy Required - MWH_t Unit	Total
One Heliostat	Steel	1.38	8.60	
	Glass	.61	1.97	
	Concrete	6.73	2.18	
	Other	.15	1.67	
	Transportation		2.28	
	Wiring		1.81	
	Manufacturing & Construction		2.78	
			21.3	
Heliostats	(22,940 Complete)			488,622
Receiver				
	Incoloy 800 Steel	154.2	1,406	
	Structural Steel	1,072.3	6,695	
	Transportation		718	
	Manufacturing & Construction (26%)		2,279	
	Total			11,098
Riser & Downcomer				
	Steel	182	1,135	
	Transportation		105	
	Manufacturing & Construction (10%)		124	
	Total			1,364
Tower				
	Concrete	41,757	13,517	
	Steel	1,266	7,899	
	Transportation		5,170	
	Manufacturing & Construction (10%)		2,659	
	Total			29,245
Total Net Energy Required to Build Plant (Without Storage)				530,329

Number of Days Needed to Provide Equivalent Energy: Thermal 145

(Production Rate 446,000 MWH/yr) Electric 435

Under these assumptions, the calculations give a net anticipated annual electrical production of 446,000 MWH_e.[65]

The remaining component that must be considered is the thermal storage system. The value for the annual electrical production of 446K MWH_e was based on the $100MW_e$ commercial plant having both a solar multiple of 1.7 and a six hour thermal storage capacity. The thermal storage system consists of a 4 field assembled cylindrical insulated steel tanks each with dimensions of 27.6 m (90.5 ft.) in diameter and 18.3 m (60 ft.) in height. A single tank is shown in Figure 2.12. These tanks will be filled with a mixture of granite rock, silica sand, and a thermal oil known as Caloria HT43. The rock and sand serve two purposes. (1) to reduce the total volume of oil needed (2) to reduce thermal convection in the tank and thus help to stratify the temperature in the tank.

The quantitative description of the design for the $100MW_e$ commercial plant thermal storage system is given in Table 2.28. The heat exchanger components for the thermal storage system are listed in Table 2.29.

A limited net energy analysis was derived from information for the thermal storage. Combining published data with personal communications and conversations with various representatives in the storage tank and related industries, we were able to complete a representative net energy analysis for the thermal storage system.

The materials used to build the four tanks, including heat exchangers, which constitute the $100MW_e$ six hour thermal storage system, are itemized in Table 2.30, including the energy required to produce said materials.

SHELL COURSE SCHEDULE (ASTM A537 CLASS 2 STEEL)				
COURSE	HEIGHT, m (FT)		PLATE THICKNESS, mm (IN.)	
1 (BOTTOM)	1.83	(6)	44.4	(1.75)
2	1.83	(6)	39.6	(1.56)
3	1.83	(6)	35.0	(1.38)
4	1.83	(6)	30.2	(1.19)
5	1.83	(6)	25.4	(1.00)
6	1.83	(6)	20.6	(0.81)
7	1.83	(6)	16.0	(0.63)
8	1.83	(6)	11.2	(0.44)
9	1.83	(6)	6.35	(0.25)
10 (TOP)	1.83	(6)	6.35	(0.25)

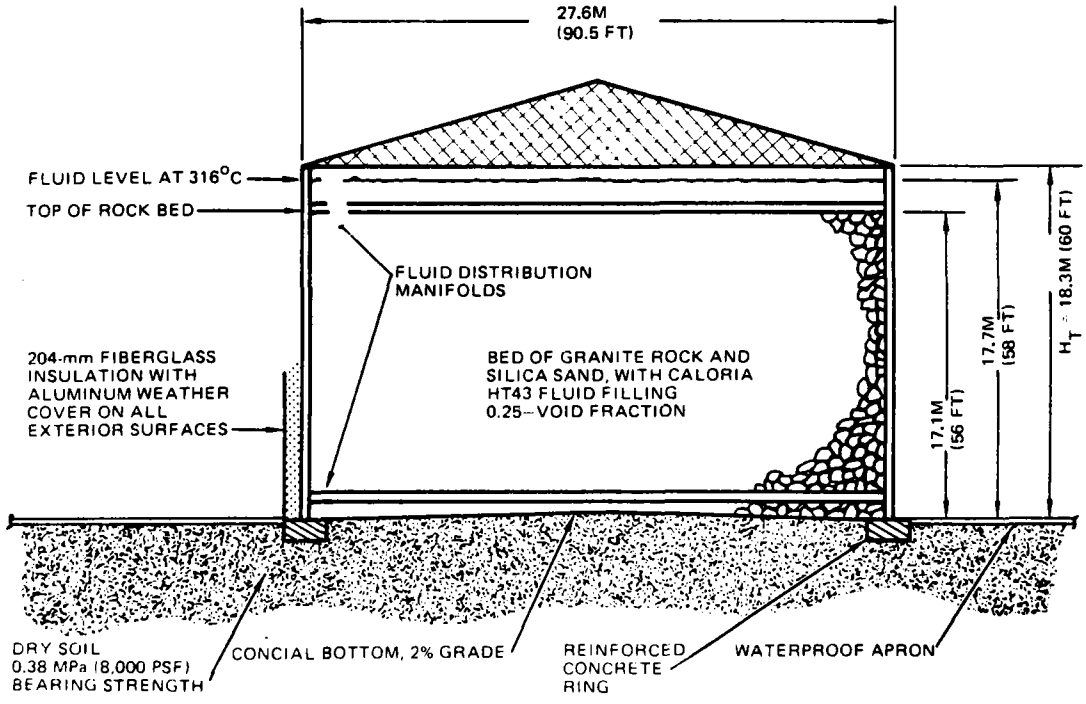

Figure 2.12 Design for the 100MW$_e$ Commercial Plant Storage Unit. This figure shows one of the four tanks which are used for the six hours of thermal storage. Source: [6], p. 3-17.

Table 2.28

DESCRIPTION OF DESIGN FOR 100MW_e COMMERCIAL PLANT THERMAL STORAGE UNIT

TSU Configuration

Four cylindrical tanks, axis vertical, installed above ground, supported on dry soil of 0.383 MPa (8000 psf) bearing strength by excavation to 2.44 (8 ft) below grade

Tank Dimensions (heights measured at circumference)

Inside diameter	27.6 m (90.5 ft)
Overall height	18.3 m (60 ft)
Packed bed height	17.1 m (56 ft)
Free fluid surface height at 318°C (600°F)	17.7 m (58 ft)
Effective height of top manifold	17.0 m (55.6 ft)
Effective height of bottom manifold	.305 m (1.0 ft)
Tank cross-sectional area	598m^2 (6432 ft^2)

Thermal Performance (all tanks):

Extractable capacity after 20 hour hold time:		1857 MWH_t
Design storage temperatures:	maximum	318°C (600°F)
	minimum extraction	310°C (585°F)
	minimum	232°C (450°F)

Thermal rates: maximum charge 255 MW_t, maximum extraction 285 MW_t

minimum charge 12.5 MW_t, minimum extraction 31.1 MW_t

Heat losses during 24-hour hold: less than 2% of extractable capacity

(CONTINUED 2-76)

Table 2.28 (continued)

Solid Storage Medium

25 mm (1 in.) river gravel and 1.5 mm (1/16 in.) No. 6 silica sand in 2:1 ratio, with 0.25 bed void fraction

Superficial bed volume per tank	10,200 m^3 (360,225 ft^3)
Weight of solids per tank	20,270 Mg (22,325 tons)
Total weight of solids (all tanks)	81,000 Mg (89,300 tons)

Liquid Storage Medium

Caloria HT43 heat transfer fluid

2208 m^3 (0.58×10^6 gal.) at 21.1°C (70°F) in one tank

8830 m^3 (2.33×10^6 gal.) at 21.1°C (70°F) in all tanks

Two manifolds, each with 19,300 holes of 3.1 mm (0.125 in.) diameter uniformly spaced over cross section

One seal steam manifold

Tank Structural Details

Fabricated of A537 Class 2 structural steel with field welded construction

Upward conical bottom plate 6.35 mm (0.25 in.) thick, 2 percent slope

Plate thickness for 1.83 m (6 ft) high shell courses varies from 44.5mm (1.75) in. at bottom to 6.36 mm (0.25 in.) at the top

Roof is single skin with trusses, 1-in-12 pitch conical

Roof and sides covered with 204 mm (8 in.) fiberglass blanket insulation with corrugated aluminum weather cover

Interfaces (Flow penetrations)

1. Caloria HT43 piping per tank for primary thermal charging and extraction: top and bottom manifold, each 14 in. pipe.
2. Caloria HT43 for night-time seal steam, 2 in. sidewall at 1.2 m (4 ft) height of each tank.
3. Nitrogen gas for ullage gas blanket 10 in. pipe into roof of each tank.

Source: [6] p. 3-15

Table 2.29

THERMAL STORAGE SYSTEM-HEAT EXCHANGER COMPONENTS

Item	Material	Quantity	Reference
Heat Exchangers			
Heaters (5)	Steel	502.5 klbs	[66]
Preheaters(5)	Steel	105 klbs	[66]
Boilers (5)	Steel	338 klbs	[66]
Superheaters (5)	Steel	135 klbs	[66]
Charging Loop			
Pumps		5-Dean Brothers Model # R484-8"x10" x15½" (Item 1)	[6] 3-49
Motors		5-Single Speed, Induction Motor, 260Hp, 4160 Volt 3 Phase (Item 2)	[6] 3-49
Pipe	Steel	61 m (200 ft) 26 in, Schedule 40	[6] 3-49
		122 m (400 ft) 14 in, Schedule 40	[6] 3-49
Extraction Loop			
Pumps		5 - (Item 1)	[6] 3-63
Motors		5 - (Item 2)	[6] 3-63
Pipe	Steel	61 m (200 ft) 26 in, Schedule 40	[6] 3-63
		91 m (300 ft) 14 in, Schedule 40	[6] 3-63

Table 2.30

NET ENERGY REQUIRED FOR THERMAL STORAGE SYSTEM
FOR 100 MW_e COMMERCIAL PLANT
(FOUR TANKS) - MATERIALS

Part	Item	Weight (Metric Tons)	Energy Required MWH_t
Tank			
Tank Walls, Bottoms and manifolds †	Steel	1528.6	9538
Roof and Truss Structure[67]	Steel	143.34	894.4
Concrete Ring			
Concrete		76.80	24.9
Rebar		1.14	7.1
Insulation			
Fiberglass [68]	Glass	106.56	344.2
Weather cover [69]	Aluminum	19.24	1076.7
Storage Medium			
Gravel & sand †		81,100	2,936
Thermal Fluid †	Oil	8,211.90	103,610 [70]**
Heat Exchangers	Steel	490.1	3,058
Pumps (10) [71]	Iron & Steel	9.12	56.9
Motors (10) [72]*		9.41	179.1
Pipe	Steel	55.70	347.6
	TOTAL		122,073

* Total energy content, materials, manufacturing and transportation; delivered to site (Southern California)

† Explicitly described in Figure 2.12 or Table 2.28

** > 90% of this energy value recoverable at end of 30 year life

The concrete support was estimated to have a cross sectional area of one foot squared with a fairly standard ratio of rebar mass to concrete volume. The standard weight of fiberglass insulation for thermal insulating this type of tank is 3 lbs/ft^3. The aluminum weather covering used was 1-1/4 in. corregated .024 in. thick material which is fairly standard for petroleum tanks.

In the case of the thermal oil, here specified to be Caloria HT43, the net energy content had to be estimated. This oil is refined and manufactured as a co-product from the heavy aromatic streams in the larger refineries. The American Petroleum Institute classifies refineries from A (the simplest) to E (the most complex). Class A type refineries are those in the rural parts of the midwest prairie which produce mainly automobile gasoline, heating oil, and related incidental products for local consumption. Class E type refineries are the highly integrated petrochemical complexes which produce hundreds of petrochemical products. Each of these refinery classes has a general specific energy consumption per unit of product production. These can be summarized in tabular form:

Refinery Class	Specific Energy/Ton of Product
A	1.0 MBTU
B	1.5 MBTU
C	3.0 MBTU
D	4.5 MBTU
E	5.0 MBTU

The thermal oil would come from the production of Class D or E refineries. We will use the specific energy for Class E refineries. For the co-product stream, this means each oil product produced has a process energy cost of 1.615 KWH_t/Kg assigned to it as the manufacturing energy

cost.[70] We assume that the thermal oil has an energy content equal to crude which would be reasonable if it were burned as boiler fuel. Therefore, the energy content of the thermal oil Caloria HT43, assuming 5.92×10^9 joules of energy per barrel of oil, is 12.617 KWH_t/Kg.

For the heat exchanger module of the thermal storage system, materials and weights of the exact specified pumps listed in Table 2.29 were ascertained from the local Dean Brothers, factory outlet [71] who specified the electric motor criteria and their source. Using data supplied by the source [72] specifically the composition, weights and manufacturing location, we determined the estimated net energy for the 300 hp pump motor. The results are outlined in Table 2.31, giving the net energy content for one motor delivered on site in southern California. All information was combined for the materials in the thermal storage system of 122,000 MWH_t.

The net energy from the material was combined with that for transportation, manufacturing and construction to give the total net energy required to build the complete 6-hour thermal storage system for the $100MW_e$ power plant. These results are summarized in Table 2.32. The transportation energies were taken from Table 2.19. Locations of sources, transportation modes and transportation multipliers were taken from Table 2.20 unless otherwise noted. The four tanks used for the thermal storage subsystem are field assembled tanks. Considering that the center of this business is in southeastern Texas and Louisiana, we assumed that the tanks parts were made in Houston and assembled on site. The thermal oil would probably be shipped from the production site at a southern California petrochemical complex near Los Angeles. Because extensive manufacturing was done offsite and also much construction had to be done on site energy costs for manufacturing of 10 percent and construction of 10 percent were added sequentially.

Table 2.31

ESTIMATED NET ENERGY CONTENT

FOR THE PUMP MOTORS

Motors - 300 hp weight 941.2Kg (2075 lbs) [71,72]

Composition by Motor Weight

Material	%of Weight[71]	Weight(Kg)	Energy Required MWH_t	
Aluminum	20%	188.24	10.53	
Copper	5%	47.06	1.03	
Iron	60%	564.72	3.52	
Steel	15%	141.18	0.88	
TOTAL	100%	941.20	15.96	15.96

Transportation of Materials (motors made in Prescott, Arizona)

Material	Mode	Distance (km)	Energy Required MWH_t	
Aluminum	Rail	1978	0.05	
Copper	-	local product	-	
Iron & steel	Rail	650	0.06	
			0.11	0.11

Manufacturing Energy Cost (11%)	1.76
Transportation of Motors from Prescott, Arizona, to Los Angeles	0.08
Net Energy Content of one motor delivered to the site	17.91 MWH_t

Table 2.32

NET ENERGY REQUIRED FOR THERMAL STORAGE SYSTEM FOR 100 MW_e COMMERCIAL PLANT - COMPLETE SYSTEM

Energy Equivalent		Energy Required MWH_e
Materials (from Table 2.30)		122,073
Transportation:		
Tank Steel Parts (Indiana to Houston and on to Los Angeles)	968	
Cement	8	
Insulation (Pittsburgh)(Trans. Mult.=1)	49	
Aluminum Shield (Portland)	5.2	
Gravel and Sand	733	
Heat Exchangers, Pumps & Pipe (Gary, Indiana region as source)	321	
Caloria HT43 Thermal oil (Los Angeles source-Tank Car)	728.6	
TOTAL	2812.8	2,813
Manufacturing (10% of Materials exclusive of thermal oil, sand and gravel, and motors)		1,535
Construction and Misc Parts (10% of materials exclusive of thermal oil)		1,846
TOTAL		128,267

With respect to site preparation and materials movement and assembly, a conservative figure of 10 percent of materials was made for the energy cost of each of these tanks. Considering that the elbows, fittings and valves are not included in the listing of components for the heat exchanger modules, nor associated concrete pads, these figures are reasonable considering the uncertainties. Because of the extraordinarily high energy content of the oil plus the fact that all one had to do with it was put it in the tanks before final systems testing, the energy content of the oil was not included in determining the construction costs. The net energy needed to construct the entire thermal storage system thus comes to 128,000 MWH_t. However, there is one additional loss factor that must be considered before we can determine the energy amplification factor (EAF).

The design yearly electric power production of 446K MWH_e was produced with a solar multiplier of 1.7 and six hours of thermal storage. The Caloria HT43 thermal oil breaks down under use and there must be continual fluid make-up to the system and removal of the degraded thermal oil. This fluid make-up amounts to 14.3 percent of the total thermal oil per year. [73] Because of the high energy content of the oil, a correction factor must be added to reflect this continuous energy drain on the operating system. A spent oil recovery system collects the volatiles and residues. However, these are no longer useful as a thermal storage medium.

Since the processed fresh Caloria HT43 thermal oil has an assumed total energy content of 12.71 KWH_t/Kg for raw crude equivalent, processing and transportation, etc., and the spent oil will still have the energy content of crude as boiler fuel, energy loss designated due to Caloria HT43 breakdown will be limited to the process and transportation energies. We will assume that the thermal content of the oil is recovered by use as

boiler fuel or some other appropriate use. The net energy of 12.71 KWH_t/Kg for the Caloria HT43 considers both production in the Los Angeles area and railroad tank car transportation. Even with these assumptions, transportation and processing represent 13.5 percent of the net energy equivalent for the thermal oil. The most resonable method of handling this constant and continuous loss is first to determine the thermal equivalent of the loss and then to subtract this from the average yearly power production of 446K MWH_e to give an adjusted energy production figure that can be used to determine the payback time in days needed to provide the equivalent energy and the energy amplification factor.

Table 2.30 considers the MWH_t equivalent of the thermal oil. The 8,212 metric tons of oil have an energy equivalent value of 103,610 MWH_t. However, only the process and transportation energy is lost. Therefore, 14.3% replacement per year, amounts to a total of 1,174.3 metric tons of oil, which have a total energy equivalent value for the crude oil processing and transportation of 14,925 MWH_t. The crude oil energy equivalent amounts to 12,920 MWH_t. Thus, the yearly energy loss due to the breakdown of the thermal oil is 2,005 MWH_t, or a conversion efficiency of 1/3, 668.8 MWH_e which is 0.55 days. If the thermal content equivalent to the crude was not recovered, the replacement of the breakdown fraction of Caloria HT43 would amount to 4.07 days, or 1.11% of the yearly energy production, rather than the actual energy cost of 0.15% of the yearly energy production. Assuming that recovery of the crude oil energy equivalent for the thermal oil gives a corrected figure for the net average yearly electric production of 445.3K MWH_e, the electric production value is reduced by only 0.15% due to the effect of thermal oil replacement and energy recovery as crude boiler fuel compared to the original electric power production value. Using the corrected

electric power production figure of 445K MWH_e/yr to include the energy equivalent for thermal oil losses, we can determine the net energy required for the complete system as a function of the number of days of operation needed to provide the equivalent energy. These results are shown in Table 2.33. The use of day equivalents allows us to identify the greatest energy cost. Obviously, the heliostats and the Caloria HT43 thermal oil are the high energy equivalent components, the heliostats because of the number and the oil because of both the large volume and the high energy density per unit volume. The actual percent of the total capital energy required as a function of component is shown in Table 2.34. Here we see that 89.9% of the total capital energy requirements are represented by the heliostats (74.2%) and the thermal oil (15.7%.) The central concrete tower (4.44%), brings the capital energy requirement to 94.3 percent of the total. The rest of the system requires only 5.6 percent of the capital energy.

For the complete solar energy thermal collection component, including six hours of thermal storage, of the 100 MW_e Commercial Solar Tower central receiver power plant, the energy amplification factor (EAF) for a 30 year lifetime with respect to capital energy cost is 20.3.

Because this is based on average actual production energy costs which are both effective and realistic; materials, transportation, manufacturing, and construction costs quoted in this chapter are fairly hard and conservative numbers. The EAF for the solar thermal collection component of the current design for a 100 MW_e commercial Solar Tower central receiver power plant can be safely quoted as 20. Design refinements are already under way which will decrease the weight and number of heliostats and improve this number: 30 is not an unreasonable goal.

Table 2.33

NET ENERGY REQUIRED FOR COMPLETE COLLECTION SYSTEM
FOR 100 MW_e COMMERCIAL PLANT

Annual Electric Production = 445K MW_e/yr

Part	Energy Required MWH_t	Number of Days Needed to Provide Equivalent Energy	
		Thermal	Electric
Collection System			
Heliostat	488,622	133.6	400.8
Receiver	11,098	3.0	9.1
Riser & Downcomer	1,364	.4	1.1
Tower	29,245	8.0	24.0
Subtotal	530,329	145.0	435.0
Thermal Storage System			
Caloria HT43	103,610	28.3	85.0
Rest of System (Materials, Manufacturing, Transportation, and Construction)	24,657	6.7	20.2
Subtotal	128,267	35.0	105.2
NUMBER OF DAYS NEEDED TO PROVIDE EQUIVALENT ENERGY FOR COMPLETE SYSTEM (Total 658,596 MWH_t)		180.0	540.2
Days After Start-Up System Completely Paid For - Capital Energy Cost		180	540.2
Energy Amplification Factor (30 year lifetime)			20.3

Table 2.34

PERCENT OF THE TOTAL CAPITAL ENERGY REQUIRED

AS A FUNCTION OF COMPONENT

Total Capital Energy = 658,596 MWH_t

Part		% of Total Capital Energy
Collector System		
Heliostats		74.20
Receiver		1.69
Riser & Downcomer		0.21
Tower		4.44
	Total	80.54
Thermal Storage System		
Caloria HT43		15.70
Rest of System		3.74
	Total	19.44

2.8 RECOVERY AND RECYCLING

In addition to the net energy analysis for the 100 MW_e commercial facility discussed in the previous section, the effect of both recovery and recycling of materials is a consideration.

With respect to energy recovery, we are interested in the collection of the broken down thermal oil, Caloria HT43, and extraction of the energy equivalent from this material. This is the only significant recovery possibility. The breakdown corresponds to 14.3% of the thermal oil or energy content equivalent per year. If this material is not recovered, 4.07 days or 1.11% of the yearly energy production would be lost. This corresponds to lowering the EAF from 20.3 to 20.16 for a 1% change in the EAF value.

With respect to recycling, some estimate can be made on the amount of the materials used to build the system that would be easily salvageable and economically recoverable at the end of one estimated life cycle for the facility, 30 years. The basic assumptions are that a reasonable maintenance and reliability schedule will be sustained throughout the lifetime of the plant and that the utility will consider the option of refurbishing and reconditioning for further use as a power generation facility beyond thirty years. These are reasonable assumptions from a utility viewpoint. Therefore, the materials in the solar thermal collection component, of the 100 MW_e commercial plant were analyzed with respect to recyclability, including storage.

The general assumptions were that the recyclable material must be easily separated from the other materials and that the separated material is compatible with the normal resource recovery market. With these criteria in mind, we can study the material in a single heliostat first. Table 2.22

and Figure 2.4 note that the back silvered glass heliostat mirrors are part of reflector panel assemblies. These consist of glass epoxied onto polyurethane foam which is itself bonded onto 20 mill galvanized steel sheet metal. There is no simple method for separating these panels, and they will be considered as a complete loss with respect to recycling. The rebar in the concrete base will also be non-recyclable. All steel in the support structure, drive assembly, and pedestal will be recoverable. Therefore, 76 percent of the steel in the heliostat system is recoverable. The energy content for recycling heliostat motors will be assumed as the amount of energy equivalent which would be recovered if the motors were made from steel. These are fairly small motors, and the only economic way to recover materials is to melt them down and separate the metals. For resmelting and separation, the steel scrap energy figure is more realistic than that for copper scrap. In the case of the cabling, the copper conductor wire and the aluminum sheath material are completely recoverable and recyclable. Both of these metals require large amounts of energy for ore benefication and primary reduction to crude metal. In fact, these two steps are the major energy consumers in the production of aluminum and copper from virgin ore. Therefore, secondary copper and recycled aluminum have both a high energy credit and high market price. The assumption was made that transformers would be rebuilt and the oil replaced since they have no moving parts to wear out. Results of the analysis for recyclable materials for the single heliostat are given in Table 2.35. The zinc is assumed to be vaporized and lost in the melting furnace which is unhappily true in many cases where galvanized steel scrap is recycled. The steel scrap energy value was developed from considerations in reference [74] and the process energy consumption data for the production of raw steel given in Table 2.7.

If we compare Tables 2.25 and 2.35, we can see that only 33 percent of the net energy required to produce a heliostat is recoverable if the materials in the 100 MW_e plant are recycled. All transportation and manufacturing energies are lost for recycled materials.

Table 2.27, the net energy for the thermal collection component with no storage, shows that all materials in the receivers and the riser and downcomer piping are recoverable. However, the reinforced concrete tower itself, the first 242 m (794 ft) of the commercial system tower shown in Figure 2.11 is not recyclable with respect to recovery of materials. Either another use would have to be found for it, or it would have to be leveled because its height might prove a safety hazard.

In the case of the thermal storage system, Figure 2.12, the steel in the tanks, pipes and heat exchangers is completely recoverable. A conservative figure has 90 percent of the thermal oil recoverable. The rest of the oil would coat the walls, pipes,works and be mixed with the silica sand. The 300 hp motors are massive enough to be disassembled and recycled for the individual materials. Recyclable materials in one motor can be summarized as follows:

Material	Weight(kg)	Energy Value	Energy Equivalent Recovered in MWH_t
Aluminum	188.24	Recycled	7.4
Copper	47.06	Secondary	1.0
Iron & Steel	705.90	Scrap	3.9
		Total (one 300 hp motor)	12.3

The aluminum weather shields on the four storage tanks would be recovered and recycled, but the fiberglass insulation would not be recyclable.

Table 2.35

RECYCLABLE MATERIALS IN THE 100 MW_e COMMERCIAL PLANT

Part	Material	% of Total	Weight (Metric Tons)	Energy Value	Energy Equivalent Recovered MWH_t	
Heliostat						
	Steel	76	1.042	Scrap	5.73	
Motors	(as steel)	100	0.009	Scrap	0.05	
Cabling	Copper	100	--	Secondary	0.063	
	Aluminum	100	--	Recycled	0.042	
Transformers-see Table 2.24		(100% minus oil)	--	Rebuilt	0.13	
				ONE HELIOSTAT	6.96	
				22,940 HELIOSTATS		159,662
Receiver	Steel	100	1,225	Scrap	6,743	
Riser and Downcomer	Steel	100	183	Scrap	1,001	
				TOTAL	7,744	7,744
Thermal Storage System						
Tanks Piping & Steel		~100	2,226.9	Scrap	12,248	
Heat Exchangers						
Thermal Oil Caloria HT43		90	7,390.7	Thermal Oil	93,249	
Motors (10) see text					123	
Weather Shield (Aluminum)		100	19.24	Recycled	757	
				TOTAL	106,377	106,377
				TOTAL RECYCLABLE ENERGY (41.6%)		273.783

A summary of these results in Table 2.35, indicates that even though both manufacturing and transportation energies are lost, the recycling of the materials in the 100 MW_e commercial plant will recover 41.6 percent of the entire initial capital energy at the site. One should note, however, that the transportation costs necessary to move the recycled materials from the site to the reprocessing facility have not been included in this analysis. These energy costs must be subtracted from the stated energy recovery values.

From an economic viewpoint there is a second problem. Freight rates are monetary ton mileage amounts set by politically controlled regulatory agencies. Virgin or raw materials have preferential freight rates. The higher rates experienced for salvaged material may make recycling economically unattractive even though it is energy effective. At the end of the 30 year design lifetime, the plant should be analyzed to determine the monetary and energy costs for refurbishing and renovating the facility for an additional 30 years of service. Preliminary rough quantitative analysis leads one to expect that renovation and modernization would require less energy expenditure than recycling, leveling and building a similar updated or modernized facility. This decision would depend on the status of the plant after 30 years and on current technology at that time.

REFERENCES

1. Raymon W. Hallet, Jr. and Robert L. Gervais, et al., Central Receiver Solar Thermal Power System, Phase 1, CDRL Item 2, Pilot Plant, Preliminary Design Report, Vol. I: Executive Overview, SAN/1108-8 (Huntington Beach, CA.: McDonnell Douglas Astronautics Co., Oct. 1977).

2. Raymon W. Hallet, Jr. and Robert L. Gervais, et al., Central Receiver Solar Thermal Power System, Phase 1, CDRL Item 2, Pilot Plant, Preliminary Design Report, Vol. II: System Description and System Analysis SAN/1108-8/1, (Huntington Beach, CA.: McDonnell Douglas Astronautics Co., Oct. 1977).

3. Raymon W. Hallet, Jr. and Robert L. Gervais, et al., Central Receiver Solar Thermal Power System, Phase 1, CDRL Item 2, Pilot Plant, Preliminary Design Report, Vol. III, Book 1: Collector Subsystem, SAN/1108-8/2, (Huntington Beach, CA.: McDonnell Douglas Astronautics Co., Oct. 1977)

4. Raymon W. Hallet, Jr. and Robert L. Gervais, et al., Central Receiver Solar Thermal Power System, Phase 1, CDRL Item 2, Pilot Plant Preliminary Design Report, Vol. III; Book 2: Collector Subsystem, SAN/1108-8/3. (Huntington Beach, CA.: McDonnell Douglas Astronautics Co., Oct. 1977).

5. Raymon W. Hallet, Jr. and Robert L. Gervais, et al., Central Receiver Solar Thermal Power System, Phase 1, CDRL Item 2, Pilot Plant, Preliminary Design Report, Vol. IV: Receiver Subsystem, SAN/1108-8/4 (Huntington Beach, CA.: McDonnell Douglas Astronautics Co., Oct. 1977).

6. Raymon W. Hallet, Jr. and Robert L. Gervais, et al., Central Receiver Solar Thermal Power System, Phase 1, CDRL Item 2, Pilot Plant, Preliminary Design Report, Vol. V: Thermal Storage Subsystem, SAN/1108-8/5 (Huntington Beach, CA,: McDonnell Douglas Astronautics Co., Oct. 1977).

7. Raymon W. Hallet, Jr. and Robert L. Gervais, et al., Central Receiver Solar Thermal Power System, Phase 1, CDRL Item 2, Pilot Plant, Preliminary Design Report, Vol. VI: Electrical Power Generation/Master Control Subsystems and Balance of Plant, SAN/1108-8/6 (Huntington Beach, CA.: McDonnel Douglas Astronautics Co., Oct. 1977).

8. L. Vant-Hull, G. C. Coleman, T. Springer, et al., Liquid Metal Cooled Solar Central Receiver Feasibility Study and Heliostat Field Analysis, ORO 5178-77-1 (Solar Energy Laboratory, University of Houston, 5 May, 1977)

9. A. C. Meyers III and A. F. Hildebrandt, "Solar Tower-Thermal Collection Component-10MW Pilot Plant." Proceedings of the 1977 Annual Meeting American Section of the International Solar Energy Society, Volume 1, ed. C. Beach and E. Fordyce (Cape Canaveral, Florida: Am. Sec. of ISES, 1977) pp. 20-11 to 20-15.

10. A. C. Meyers III and A. F. Hildebrandt, "Solar Tower - Net Energy Analysis of the Thermal Collection Component - 100 MW_e Commercial Plant" (a paper presented at A Solar World, American Section ISES, Orlando, Florida, June 6, 1977).

11. A. C. Meyers III and A. F. Hildebrandt, " A Report on the Net Energy Analysis of the 100 MW_e Solar Tower Collector." Report No. UH/SEL 770620-1 (Houston, Texas: Solar Energy Laboratory, University of Houston, 1977).

12. A.F. Hildebrandt and L.L. Vant-Hull, "Power with Heliostats," Science, 197 (1977), 1139-1146.

13. Federal Nonnuclear Energy Research and Development Act of 1974, Public Law 93-577, 42 USC 5901-5915.

14. T.J. Connolly and J.R. Sprual, eds. "Report of the NSF-Stanford Workshop on Net Energy Analysis," NTIS Report #27976-6001-RU-000 (December 1975).

15. G. Tyler Miller, Living in the Environment (Belmont, CA.: Wadsworth, 1975).

16. John M. Fowler, Energy and Environment (New York: McGraw-Hill, 1975)

17. Edward H. Thorndike, Energy and Environment (Reading Mass.: Addison-Wesley, 1976).

18. "Energy and Power" Scientific American, 224 (Sept. 1971).

19. Theodore C. Foin, Ecological Systems and the Environment (Boston, MA.: Houghton Mifflin, Co. 1976).

20. Gerard M. Crawley, Energy (New York: Macmillan Pub. Co., 1975).

21. Andrew L. Simon, Energy Resources (New York: Pergamon Press, Inc., 1975).

22. S. S. Penner, and L. Icerman, Energy (Reading, Mass: Addison-Wesley 1974).

23. J. T. McMullan, R. Morgan, and R. B. Murray, Energy Resources and Supply (London: J. Wiley & Sons, 1976).

24. Bernard Patten, Systems Analysis and Simulation in Ecology, 4 Vols. (New York: Academic Press, 1976).

25. Donella, Meadows, et al., The Limits to Growth (New York: Universe Books, 1972).

26. Robert M. May, Theoretical Ecology (Philadelphia, PA.: Saunders Co., 1976).

27. Michael Batty, Urban Modeling (Cambridge University Press, 1976).

28. Brian J.L. Berry, et al., The Geography of Economic Systems (Englewood Cliffs, N. J.: Prentice-Hall, 1976).

29. J. Maynard Smith, Models in Ecology (Cambridge University Press, 1974).

30. John H. Milsum, Biological Control Systems Analysis (New York: McGraw-Hill, 1966).

31. Kenneth E. F. Watt, Ecology and Resource Management (New York: McGraw-Hill, 1968).

32. H. T. Odum, Environment, Power and Society (New York: John Wiley, 1971).

33. H. T. Odum, and E. C. Odum, Energy Basis for Man and Nature (New York: McGraw-Hill, 1976).

34. Charles A. S. Hall, and John W. Day, Jr., Ecosystem Modeling in Theory and Practice (New York: John Wiley, 1977).

35. H. T. Odum, "Energy, Ecology, and Economics." AMBIO, 2 (6) (1973), 220-277.

36. H. T. Odum, "Energy Cost-Benefit Models for Evaluating Thermal Plumes." Thermal Energy, ed. Gibbons and Shoritz (Tech, Info. Center, U.S.A.E.C., 1974), pp. 628-649.

37. S. Bayley and H. T. Odum, "Simulation of Interrelations of the Everglades' Marsh, Peat, Fire, Water, and Phosphorous." Ecological Modelling, 2 (1976) 169-188.

38. H. T. Odum, et al., "Net Energy Analysis of Alternatives for the United States, Middle and Long Term Energy Policies and Alternatives, Part 1," Congressional Record Serial No. 94-63 (March 25-26, 1976), pp. 253-302.

39. H. T. Odum, "Net Benefits to Society from Alternative Energy Investments." Transactions of the 41st North American Wildlife and Natural Resources Conference (Washington, D.C.., Wildlife Management Institute 1976), pp. 327-338.

40. U.S. Dept of Commerce, U.S. Industrial Outlook 1976, 16th Edn. (G.P.O., 1975), p. 65.

41. Federal Energy Administration, The Data Base, Conservation Paper No. 8 (G.P.O. 1975), pp. 295-319.

42. Federal Energy Administration, The Data Base, Conservation Paper No. 11, Vol. 3: Cement (G.P.O., 1975).

43. A. M. Neville, Properties of Concrete (New York: J. Wiley & Sons, 1973), pp. 597-599.

44. Federal Energy Administration, The Data Base, Conservation Paper No. 12, Vol. 4: Copper (G.P.O. 1975).

45. Federal Energy Administration, The Data Base, Conservation Paper No. 15, Vol. 7: Glass (G.P.O., 1975).

46. E. Cszensney and W. Bagley, Guardian Industries, private communication.

47. Federal Energy Administration, The Data Base, Conservation Paper No. 9, Vol. 1: Selected Plastics (G.P.O., 1975).

48. T. G. Clarke, "Silver," Mineral Facts and Problems, 1975 Edition, Bureau of Mines Bulletin 667 (G.P.O., 1976), pp. 1001-1015.

49. R. D. Mushlitz, "Silver Metallurgy," McGraw-Hill Encyclopedia of Science Technology, Vol. 12 (New York: McGraw-Hill, 1977), pp.379-381.

50. T. G. Clarke, "Silver," Minerals Year Book 1974, Metals, Minerals, and Fuels, Bureau of Mines (G.P.O., 1976), pp. 1181-1200.

51. Annual Statistical Report American Iron and Steel Institute 1976 (Washington D.C.: AISI, 1977).

52. Federal Energy Administration, The Data Base, Conservation Paper No. 14, Vol. 6: Steel (G.P.O. 1975).

53. C. H. Behre, Jr. and N. Arbiter, "Distinctive Features of the Minerals Industries," ed. E. H. Robie, Economics and the Minerals Industries. 2nd Ed. (New York: American Institute of Mining, Metallurgical and Petroleum Engineering, Inc., 1964), pp 167-223.

54. P. M. Tyler, "Cost of Acquiring and Operating Mineral Properties; Part 1. Metal, Nonmetalic, and Coal," ed. E. H. Robie, Economics of the Minerals Industries (New York: American Institute of Mining, Metallurgical and Petroleum Engineers, Inc., 1964), pp. 167-223.

55. W. D. Wilkinson, "Chromium," McGraw-Hill Encylopedia of Science and Technology, Vol. 3 (New York: McGraw-Hill Book Co., 1977), pp. 114-115B.

56. A. Illis, "Nickel Metallurgy," McGraw-Hill Encyclopedia of Science and Technology, Vol. 9 (New York: McGraw-Hill Book Co., 1977), pp. 114-115.

57. V. A. Cammortara, Jr., H. R. Babitzke, and J. M. Hague, "Zinc," Mineral Facts and Problems, 1975 Edition, Bureau of Mines Bulletin 667 (G.P.O., 1976), pp. 704A-706.

58. V. A. Cammortara Jr., and H. R. Babitzke, "Zinc," Minerals Year Book 1974, Vol, 1: Metals, Minerals and Fuels, Bureau of Mines (G.P.O., 1976), pp. 1363 -1396.

59. C. H. Cotterill, "Zinc Metallurgy," McGraw-Hill Encyclopedia of Science and Technology, Vol. 14 (New York: McGraw-Hill Book Co., 1977), pp. 704A-706.

60. C. Bullard III, B. Hannon, and R. Herendeen, Energy Flow Through the United States Economy (Washington, D.C.: Office of Energy Programs, U.S. Department of Commerce, 1975).

61. A. N. Addie, "Rail Power Systems," Energy Technology Handbook, ed. D.M. Considine (New York: McGraw-Hill, 1977), pp. 9-228.

62. C. R. Applebaugh, McDonnell Douglas Astronautics Co., Huntington Beach, California, and L.L. Vant-Hull, University of Houston, Houston, Texas, personal communication.

63. John Norwood, Gulf Electroquip, Houston, Texas, personal communication.

64. Central Receiver Solar Thermal Power System, Phase I, Preliminary Design Review, Book 2, Collector and Receiver Subsystem, MDG G6775 (Huntington Beach, CA.: McDonnell Douglas Astronautics Co., May 1977).

65. Reference [2], p. 47.

66. L. L. Vant-Hull, University of Houston, Houston, Texas, personal communication.

67. Stephen Hall, Graver Tank and Manufacturing Co., Houston, Texas personal communication.

68. Richard Sorenson, J. T. Thorpe Co., Houston, Texas, personal communication.

69. Robert Chavanec, Childress Products, Houston, Texas, personal communication.

70. H. W. Prengle, Jr. et al., Potential for Energy Conservation in Industrial Operations in Texas. Final Report, Project No. S/D-10 (Austin, TX.: Texas Energy Advisory Council, November 1974), and personal communication.

71. Guy Hanes, Dean Brothers Pumps, Regional Sales Office, Houston, Texas, personal communication.

72. Thomas Cook, U. S. Electric Motors Division of Emerson Electric Co., Bellaire, Texas, personal communication.

73. Central Receiver Solar Thermal Power System, Phase I, Fifth Project Review, Book I-Systems, Receiver and Thermal Storage Subsystems, MDC G6737 (Huntington Beach, CA.: McDonnell Douglas Astronautics Co., March 1977), p. 144.

74. E. Hirst, "Pollution-Control Energy Costs." Mechanical Engineering, 96 (9) (September 1974), 28-35.

SECTION 3

LOCATING THE SUN

Charles L Pitman and Lorin L. Vant-Hull

Abstract

In many solar energy applications, there is a need for an accurate method of locating the sun. However, the methods used to fix the sun's position vary significantly in accuracy. The design of flat-plate systems probably is not very susceptible to errors in the sun's position. However, the computer tracking of concentrating systems or the comparison of model predictions of direct normal solar intensity with experimental normal incidence pyrheliometer (NIP) readings demands a higher precision computer sun tracker.

In this chapter, a means for calculating the sun's position as a function of time is presented. The fundamental reference frames for observing celestial objects are defined, and the basic notions of orbits and time reckoning are explained. Series solutions for the equation of time and for the equation of the center are given. Table 3.3 summarizes the phenomena affecting the sun's position and the errors which result when one disregards their effects.

A computer program to accurately locate the sun was written, using the concepts contained in this chapter. This program enabled the calculation of the ephemerides of the sun for the years 1962, 1887, and 1978. A comparison of these results with the Astronomical Ephemeris indicated a maximum difference in the ecliptic longitude of only 32", compared to differences as large as two degrees from a simpler model.

Finally, a comparison of the effects that two different sun tracker programs (with different accuracies) have on insolation prediction shows a maximum difference (for 30° north latitude) of about 1.5% between the

daily integrals of the predicted direct normal intensity. The insolation model used in this comparison was Allen's clear air model because it assumes a cloudless atmosphere. Further, the study indicates that the differences between the daily integrals increase with increasing north latitude.

TABLE OF CONTENTS

CONTENTS

LIST OF FIGURES

LIST OF TABLES

3.0 INTRODUCTION

Models for the attenuation of sunlight by the atmosphere require an accurate knowledge of the sun's position. In the central receiver system for solar power generation, there has been much debate over the guidance system for the heliostats. The questions which have arisen concern the expense of a computer system that could orient the thousands of mirrors in the field without the aid of light sensors on each heliostat. The search for solutions to these types of problems begins with an investigation of the apparent motion of the sun. One must decide which aspects of the sun's complex movements can be disregarded and how much error occurs when one ignores them.

In this section we propose a means for calculating the position of the sun as a function of time. Subsection 3.1 describes basic concepts, such as the many different frames of reference which one employs when tracking the sun. The reader may find much familiar material here, and he should skip those subsections with which he is well acquainted. Subsection 3.2 is concerned with the mathematical description of a planetary orbit, and, in subsection 3.3, we define the various time systems encountered while studying the sun's motion. In subsection 3.4, the summary of the phenomena affecting the sun's position (Table 3.3), the brief description of the new computer program to track the sun, and the discussion of the effects of errors in locating the sun on insolation predictions are the end results of this investigation.

This section is an abbreviated version of a master's thesis, Locating the Sun, by Charles L Pitman. Many aspects of this section

are covered in greater detail in this thesis. The complete thesis is available from the Energy Laboratory, University of Houston.

Throughout the text, the abbreviation A.E. is used to stand for the Astronomical Ephemeris. The Explanatory Supplement to the Astronomical Ephemeris and the American Ephemeris and Nautical Almanac is referred to as the Explanatory Supplement. We have tried to adhere to the astronomical symbols and sign conventions recommended by the International Astronomical Union (I.A.U.), and we highly recommend that the I.A.U. system of astronomical symbols and sign conventions should be followed in all reports which use standard astronomical terms.

3.1 SYSTEMS OF COORDINATES

3.1.1 Altitude and Azimuth

• Definitions

To an observer standing on its surface, the earth (appearing to be planar) and the vertical (pointing directly overhead) constitute the most familiar and obvious reference frame for viewing the sky. This reference system is most often referred to as the horizontal or horizon or altazimuth system. The stars appear to be on the surface of a vast sphere - the celestial sphere - of which the individual observer is the center. In Figure 3.1 [1], O is the observer on the earth's surface and Z (the astronomic zenith) is the point vertically overhead on the celestial sphere. The line OZ also cuts the celestial sphere at a point (the nadir) which is vertically below O and hidden by the ground. (For an important clarification of the definition of the zenith, see the subsection entitled Variation of the Local Vertical.)

The plane through O at right angles to OZ is the plane of the horizon and cuts the celestial sphere in the great circle NAS, called the celestial or astronomical horizon. Clearly, the celestial horizon might not coincide with an observer's visible horizon because of local terrain. All small circles (on the celestial sphere) which are parallel to the horizon are called parallels of altitude. LXM in Figure 3.1 is a parallel of altitude through X. The angle AOX (also the great circle arc AX) is the altitude or elevation of the star X; the angle ZOX (also the great circle arc ZX) is the zenith distance of X and clearly $ZX = 90° - AX$. z will denote zenith distance and h will denote altitude.

Choose OP parallel to the earth's axis of rotation (Figure 3.1). The position P on the celestial sphere is called the north celestial pole (assuming that the observer is in the northern hemisphere). Any great circle containing Z is called a vertical circle. The vertical circle NZS, containing the zenith and both celestial poles, is called the principal vertical or the celestial, local, or observer's meridian. The points N and S in which the observer's meridian intersects the horizon are called the north point and the south point of the horizon, respectively. The vertical circle at right angles to the observer's meridian is the prime vertical, which cuts the horizon in the west(W) and east(E) points. (E is not shown in Figure 3.1) The positions of W and E relative to N and S are obtained in this manner: if the observer faces north, W is to his left and E is to his right. The points N, E, S, and W are called the cardinal points.

In Figure 3.1 the azimuth A of the star X is defined to be the angle between the planes ZOA and ZOS. Azimuth angle is measured from the south point S through west, north, and east, and it can assume values from 0° to 360°. Various conventions exist for measuring azimuth, but the one above is recommended by the I.A.U. [2]

Coordinate axes for the horizontal system are established as follows: the x'-axis is directed toward the south point S, the y'-axis toward the east point E, and the z'-axis toward the zenith Z. However, note again that the azimuth angle A is measured through west, north, and east; this is opposite to the direction in which A would normally be measured for the right-handed axes chosen. One derives the following

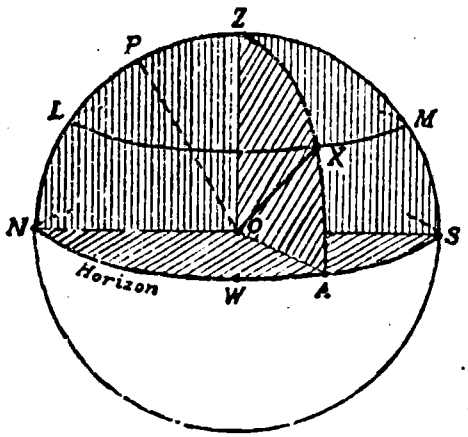

Figure 3.1

Altitude and Azimuth [1]

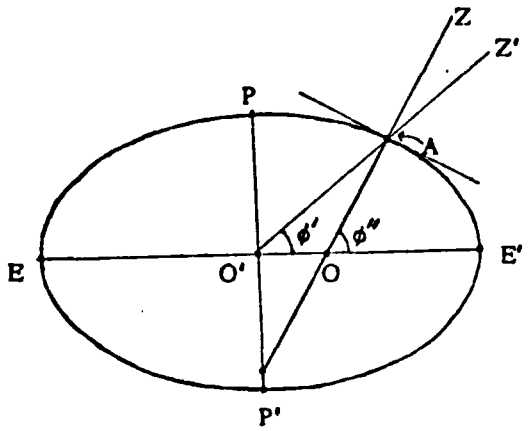

Figure 3.2

Variation of the Local Vertical

formulas which connect the spherical and rectangular horizon coordinates:

$$(3\text{-}1)\quad \frac{x'}{\Delta} = \sin z \cos A = \cos h \cos A$$

$$(3\text{-}2)\quad \frac{y'}{\Delta} = -\sin z \sin A = -\cos h \sin A$$

$$(3\text{-}3)\quad \frac{z'}{\Delta} = \cos z = \sin h$$

Here Δ is the distance from the center of the earth to the celestial body.

· Variation of the Local Vertical

If we wish to predict the positions of celestial objects, we must refine our basic ideas of the horizontal system of coordinates. This is because we have not yet precisely identified the astronomic zenith, which is the point on the celestial sphere directly overhead of the observer. Consequently, we must consider what is meant by the term "directly overhead".

The earth is not a perfect sphere. Instead, the earth is very nearly an oblate spheroid - i.e. an ellipsoid of revolution, generated by revolving an ellipse about its minor axis. For the earth, the minor axis of the generating ellipse is the polar diameter, and the major axis is the equatorial diameter.

Figure 3.2 shows an elliptical cross-section of the earth, assuming the earth to be a perfect oblate spheroid. PP' is the axis of rotation, the polar diameter. O' is the earth's center and A is the position of an observer on the surface of the spheroid. EE' is the equatorial diameter. O'Z' is the continuation of the line joining the earth's center

to the observer A, and, since the earth is not spherical, it is not perpendicular to the earth's surface. Z' is the geocentric zenith. Let OZ be the line which is normal to the spheroid at A; Z would be directly overhead of the observer at A if the earth were a perfect oblate spheroid. Z is the geodetic zenith. The angle Z'O'E' is the geocentric latitude ϕ', and the angle ZOE' is the geodetic latitude ϕ''.

When attempting to locate the sun to an accuracy of 1', the importance of the concepts discussed in this subsection should not be underestimated. If an observer makes an error in determining his terrestrial position or the time, this error has a primary effect on the prediction of the sun's position. For example, suppose an observer has inaccurately fixed his latitude by x seconds of arc. This will cause an error of x seconds of arc in the position predicted for the sun. Thus, since there are at least three different sorts of terrestrial latitude in use, one must determine the correct type of latitude to use in the formulas of this chapter.

We know that the surface of the earth has mountains, valleys, and other landforms on the continents. These landforms constitute the terrain, and studies of the physical features of the earth are investigations of the earth's topography. In this chapter, however, we are not concerned with the topography of the earth. Rather, we are interested in the shape of the mean sea level surface of the earth; this surface is called the geoid. On the oceans, the geoid is the surface which these huge bodies of water would assume if they were undisturbed by winds or tides. Conceptually, we can extend this sea level surface un-

derneath the continents to complete the geoid, which is a closed surface. (A portion of the geoid lying underneath a continent can be pictured as the undisturbed, watery surface of a very narrow, very deep canal cut through the entire length or breadth of the continent.)

The geoid is an equipotential surface of the earth's gravitational attraction and the centrifugal force of the earth's rotation. As a first approximation to the geoid, we see that the sea level surface is very closely that of an oblate spheroid; the flattening is due to the centrifugal force resulting from the earth's rotation. In fact, the geoid would be a perfect oblate spheroid if the earth's density was uniform throughout the planet. However, since there are both lateral and vertical density variations in the earth, the geoid is not a perfect oblate spheroid. In recent years, much attention has been given to finding the "best" reference ellipsoid to approximate the earth's shape. Indeed, the"best" reference oblate spheroid for one region of the earth may not be the "best" one for another region. Today, there are many reference spheroids in use on different continents. A brief description of the constants of each can be found in the American Practical Navigator. [3]

We define the flattening f by the formula 1-f = b/a, where a is the equatorial radius and b is the polar radius. [4] For example, values for f of 1/298.25 and for a of 6378.16 kilometers were adopted by the A.E. in 1968 [5] and recommended by the International Astronomical Union (I.A.U.). These values seem to result from observations of artificial satellites. [6] In 1924 and 1930, the International Union of

Geodesy and Geophysics adopted the value of 1/297 for f.

Regardless of the particular reference spheroid chosen, the geocentric latitude ϕ' and the geodetic latitude ϕ'' are related by the formula: [7]

$$\tan \phi' = \frac{b^2}{a^2} \tan \phi'' = (1-f)^2 \tan \phi''$$

Expanding in a series in f and ϕ'' yields:

$$\phi'' - \phi' = (f + \tfrac{1}{2}f^2) \sin 2\phi'' - (\tfrac{1}{2}f^2 + \tfrac{1}{2}f^3) \sin 4\phi''$$

And substituting f=1/298.25, we find:

$$(3\text{-}4) \quad \phi'' - \phi' = 692.''74 \sin 2\phi'' - 1.''16 \sin 4\phi''$$

The maximum difference is about 12'.

The direction of the plumb line is very important; buildings are aligned by the plumb bob, and some astronomical measurements are made with respect to this direction. If we extend the plumb line in both directions, the point directly overhead where this extended plumb line intersects the celestial sphere is the <u>astronomic zenith</u>. We also refer to the extended plumb line as the <u>astronomic vertical</u>, because it is normal to the surface of the geoid. The <u>astronomic latitude</u> ϕ is the angle between the extended plumb line and the plane containing the celestial equator.

Note that we are referring to the actual direction indicated when one drops a plumb line, with no "corrections" being applied to this direction for effects such as "centrifugal force deflection". Such"corrections" would render invalid the ideas and definitions of astronomic zenith which are discussed here.

What is the difference between the geodetic and the astronomic zeniths ? Recall that line OZ in Figure 3.2 is the normal to the reference oblate spheroid; we term OZ the geodetic vertical of the observer at A. On the other hand, the plumb line (i.e. the astronomic vertical) is normal to the geoid. Thus, any differences between the geoid and the reference oblate spheroid would mean that the geodetic and astronomic zeniths are different. It is a fact that the earth is not a perfect oblate spheroid. There are local gravitational anomalies which are due to the lateral and vertical variations of the earth's density. For example, massive mountains cause the geoid to bulge upward from the reference spheroid. Because the density of water is less than that of rock, the geoid (the sea level surface) over the oceans is depressed below the surface of the reference oblate spheroid. These deviations, or undulations, in the geoid with respect to the reference oblate spheroid necessitate the distinction between the geodetic and astronomic verticals. The angle between the geodetic and astronomic verticals is termed station error. There is no closed mathematical expression which gives the station error as a function of latitude and longitude. The station error may commonly be between 4" and 6", and at some places in the United States can be 25". [8]

Note that we can associate a separate horizon coordinate system with each of the three different zeniths. The most convenient one for observations is that one which uses the astronomic zenith, because this point is defined with respect to the plumb line. Once we have chosen this particular horizon coordinate system, we relate it to the other astronomical coordinate systems described in subsection 3.1 by specifying the

astronomic latitude ϕ. This is because we are neglecting parallax errors. If parallax errors are considered significant, the more exact relationships (as given in the Explanatory Supplement) between the reference oblate spheroid, geocentric coordinates, and topocentric coordinates will have to be used. [9]

Neglecting parallax errors, we see that, to refer observations to the astronomic zenith, the correct latitude to use in the formulas of this chapter is the astronomic latitude ϕ. Most maps, however, give the geodetic latitude ϕ".[10] In general then, if use is made of a map, there will be a small error in the latitude and longitude of the observer due to station error. Also, a correction for the projection on which the map is based may be necessary. Thus, if one fixes his terrestrial coordinates by using a map, care must be taken to determine the accuracy of such a procedure. [11] Alternatively, there are established methods, to be found in the literature [12], for the precise determination of the astronomic latitude and longitude. These methods usually involve the precise measurement of the altitude of a star(s) as it(they) transits the local meridian. If one knows the time(s) of transit and the declination(s), then the astronomic latitude ϕ can be determined using the formulas in Table 3.1 . (These formulas are derived in section 3.1.4 .) In practice, one of these methods may have to be used if the station error is large enough to force the total error in the sun's position to an unacceptably high value (e.g., over 1').

In conclusion, it should be noted that an error of x degrees in the latitude of the observer will cause an error of x degrees in the

altitude of the sun. For example, since 1' is about 1 nautical mile along a great circle on the earth's surface and since the heliostat field for a 100 megawatt electric power plant is around 1 mile by 1 mile, the latitude varies by about 1' from the southern to the northern boundary of the field, due to the curvature of the earth.

This simple example illustrates that there is a variety of "observational errors" associated with locating the sun's position to an accuracy of 1'. These include instrumental errors such as backlash, clock errors, latitude and longitude errors, etc. All of these types of"observational errors" are not treated in this chapter. Indeed, it is assumed that they are eliminated by the observer, either mathematically, statistically, or otherwise.

3.1.2 Equatorial and Ecliptic Coordinates

Three other fundamental astronomical coordinate systems are based on the celestial equator (coplanar with the earth's equator) and the plane of the ecliptic (the plane of the earth's orbit around the sun). The first of these coordinate systems - the equatorial coordinates - is defined with respect to the earth's axis of rotation and the plane containing the celestial equator. Any small circle parallel to the equator is called a parallel of declination. Due to the earth's daily rotation, a star appears to describe a parallel of declination on the celestial sphere. (Figure 3.3) The declination δ of a celestial object is the angle between the plane containing the celestial equator and the line joining the observer to the object. δ ranges from 0° to 90°; north declinations (those parallels between the north pole and the celestial

equator) are designated positive, while south declinations are taken to be negative. The angle between the line joining the observer to the north celestial pole and the line joining the observer to the celestial object is the north polar distance (N.P.D.). We see that:

$$N.P.D. = 90° - \delta$$

This formula holds for points with either northern or southern declinations.

Any semi-great circle terminated by the north and south poles is called a meridian. In particular, the meridian which contains the zenith Z is called the local or observer's or celestial meridian. The observer's meridian is shown in Figure 3.3. (Note the restriction that a meridian be a semi-great circle. In the case of the local meridian, the whole great circle containing the zenith and both celestial poles is often called the local meridian. No confusion generally arises from this ambiguity because this is the only exception to the rule that a meridian is a semi-great circle.)

The angle between the local meridian and the meridian containing a celestial object is the hour angle H of the body. It is measured westward from the local meridian and either $0° \leqq H < 360°$ or $0^h \leqq H < 24^h$. The correspondence between time and degrees is $1^h = 15°$, $1^m = 15'$, and $1^s = 15''$.

It is easy to establish the following connection between the horizon and equatorial coordinate systems:

(continued on next page)

If a star's azimuth is west (i.e. between 0° and 180°), its hour angle is between 0^h and 12^h; if the star's azimuth is east (i.e. between 180° and 360°), its hour angle is between 12^h and 24^h.

The equatorial coordinates (H,δ) uniquely define the position of a celestial body at any instant, but δ is the only one of the two coordinates which remains constant for a point fixed on the celestial sphere. The relative positions of the stars remain more or less fixed due to their large distances from us. Thus, it is desirable to denote the positions of points on the celestial sphere with respect to the sphere itself rather than with reference to the local meridian. Then, knowing the relationship between the local meridian and some chosen point on the celestial sphere, one can relate this new equatorial system to the coordinates (H,δ).

The reference point chosen is the vernal equinox or the first point of Aries (Υ). The reference meridian is thus the meridian containing the vernal equinox; it defines a plane which moves with the celestial sphere. The vernal equinox is the ascending node of the ecliptic on the equator; the ascending node is the point at which the sun, in its annual (not diurnal) apparent path around the earth, crosses the equator from the south to the north. (Figure 3.4)

We replace the hour angle H of a celestial point S by its right ascension α, which is the angle between the plane containing the reference meridian and the plane containing the meridian on which S lies. Right ascension is measured eastwards from the vernal equinox (Figure 3.4) and $0^h \leq \alpha < 24^h$. (Here, eastward denotes the sun's apparent yearly

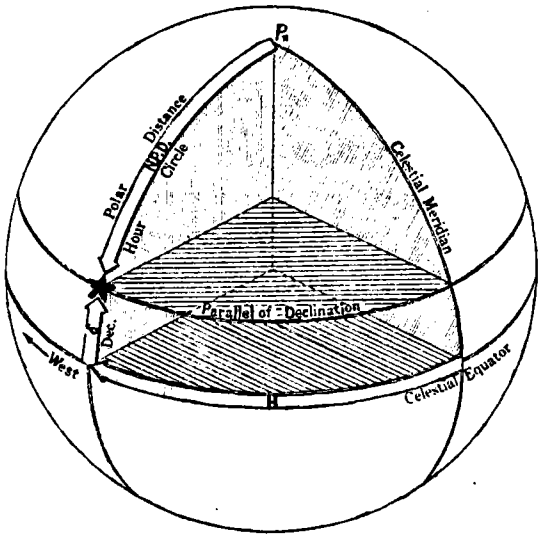

Figure 3.3

The Equatorial Coordinates (H,δ)

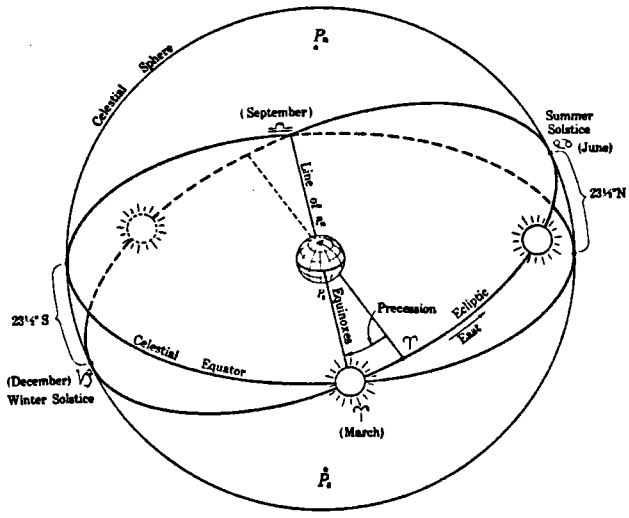

Figure 3.4

The Apparent Motion of the Sun in the Ecliptic

motion with respect to the stars.)

With this system of spherical equatorial coordinates (α,δ) , one defines a rectangular reference frame which, neglecting small effects that will be considered in subsection 3.4, is fixed with respect to the celestial sphere and not with respect to the observer. The ξ-axis points toward the vernal equinox Υ, the η-axis to a point that is 90° to the east along the celestial equator. The ζ-axis points toward the north celestial pole. Equatorial rectangular coordinates and distance are conventionally denoted by X, Y, Z, and R for the sun and by ξ, η, ζ, and Δ for the planets. A familiar set of relations exist between spherical and rectangular equatorial coordinates:

$$(3\text{-}5)\quad \frac{X}{R} \text{ or } \frac{\xi}{\Delta} = \cos\delta\cos\alpha$$

$$(3\text{-}6)\quad \frac{Y}{R} \text{ or } \frac{\eta}{\Delta} = \cos\delta\sin\alpha$$

$$(3\text{-}7)\quad \frac{Z}{R} \text{ or } \frac{\zeta}{\Delta} = \sin\delta$$

To relate the two sets of spherical coordinates (α,δ) and (H,δ), it is necessary to specify the hour angle of Υ. This angle is called the local sidereal time and denoted θ. Suppose S is a celestial object with hour angle H at local sidereal time θ and with right ascension α. We have the fundamental formula connecting the two equatorial reference systems (α,δ) and (H,δ):

$$(3\text{-}8)\quad \theta = H + \alpha$$

With this formula, the system of equatorial coordinates is complete.

One further system of coordinates is important to terrestrial observers, and it is called ecliptic coordinates. The rectangular axes

$(\bar{\xi}, \bar{\eta}, \bar{\zeta})$ of this system are shown in Figure 3.5. [13] Also pictured are the $\xi\eta\zeta$-axes of the equatorial system (α,δ). Identical are the $\bar{\xi}$ and ξ axes, but the $\bar{\zeta}$-axis points to the north pole of the ecliptic,K. Hence, the $\bar{\eta}$-axis lies in the plane of the ecliptic and is directed toward a point 90° to the east of T. East, in the sense used here, denotes the direction indicated by the small arrow next to the sun in Figure 3.5.

For a point S, we define the ecliptic or celestial longitude λ as the angle which the plane containing S and both poles of the ecliptic makes with the plane containing T and both poles of the ecliptic. Celestial longitude is measured eastwards from 0° to 360°. The ecliptic or celestial latitude β of S is the angle which the line joining the observer to S makes with the ecliptic plane. β, like terrestrial latitude, is measured from 0° through 90°; it is positive for all points north of the ecliptic and negative for all points south. In the case of the sun, the geocentric ecliptic longitude and latitude are denoted by L and B, respectively. [14]

The relationships between the rectangular axes of Figure 3.5 and (λ,β) are:

$$\begin{aligned} \frac{\bar{\xi}}{\Delta} &= \cos\beta\cos\lambda \\ \frac{\bar{\eta}}{\Delta} &= \cos\beta\sin\lambda \\ \frac{\bar{\zeta}}{\Delta} &= \sin\beta \end{aligned} \qquad (3\text{-}9)$$

In practice, ecliptic coordinates are used mainly in problems re-

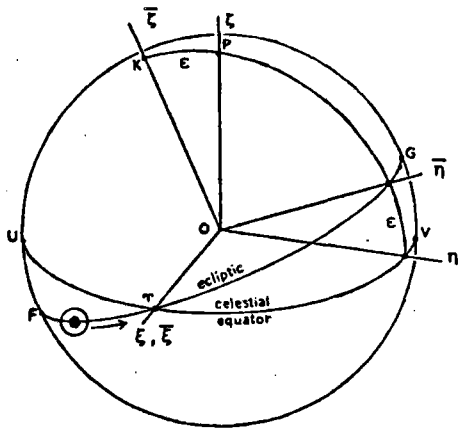

Figure 3.5

Rectangular Equatorial and Rectangular Ecliptic Coordinates [13]

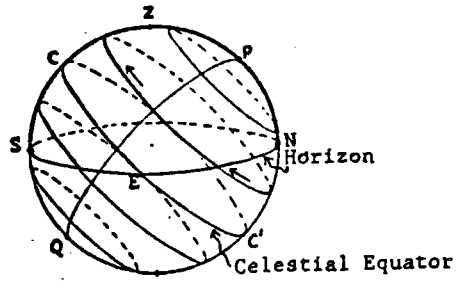

Figure 3.6

The Paths of Stars Across the Sky When the Observer is at a Latitude Between the Equator and the North Pole [15]

lated to planetary motion. Indeed, geocentric ecliptic coordinates are used only for the sun. Heliocentric ecliptic coordinates are used for the planets.

3.1.3 Transformations Between Coordinate Systems

Once the ecliptic longitude of the sun is known, a sequence of three coordinate rotations (and an angular coordinate inversion) is required to fix the sun's position in the horizon system of coordinates.

It is clear (Figure 3.5) that equatorial coordinates are obtained from ecliptic coordinates by a rotation through an angle ε about the $\bar{\xi}$-axis. The sense of this rotation may be obtained by the right-hand rule with the thumb pointing along the $-\bar{\xi}$ direction, i.e. toward the autumnal equinox. ε is called the obliquity of the ecliptic and is the angle at which the earth's axis is inclined with respect to the ecliptic plane.

We write the formulas for a rotation through the angle ε:

$$\frac{\xi}{\Delta} = \frac{\bar{\xi}}{\Delta}$$

$$\frac{\eta}{\Delta} = \left(\frac{\bar{\eta}}{\Delta}\right)\cos\varepsilon - \left(\frac{\bar{\zeta}}{\Delta}\right)\sin\varepsilon \tag{3-10}$$

$$\frac{\zeta}{\Delta} = \left(\frac{\bar{\eta}}{\Delta}\right)\sin\varepsilon + \left(\frac{\bar{\zeta}}{\Delta}\right)\cos\varepsilon$$

or, in terms of the spherical coordinates:

$$\frac{\xi}{\Delta} = \cos\delta\cos\alpha = \cos\beta\cos\lambda$$

$$\frac{\eta}{\Delta} = \cos\delta\sin\alpha = \cos\varepsilon\cos\beta\sin\lambda - \sin\varepsilon\sin\beta \tag{3-11}$$

$$\frac{\zeta}{\Delta} = \sin\delta = \sin\varepsilon\cos\beta\sin\lambda + \cos\varepsilon\sin\beta$$

Knowing the coordinates (α,δ), the coordinates (H,δ) are obtained by means of equation (3-8). This requires a knowledge of the sidereal time θ. We define the rectangular axes associated with the spherical coordinates (H,δ) as follows. The x"-axis points toward the intersection of the local meridian with the celestial equator. (As these curves meet in two places, the intersection closest to the zenith is used and not the crossing point below the horizon.) The y"-axis is directed toward the east point E, while the z"-axis is directed toward the north celestial pole. Thus we have the relations:

$$\begin{aligned} \frac{x''}{\Delta} &= \cos\delta\cos H \\ \frac{y''}{\Delta} &= -\cos\delta\sin H \\ \frac{z''}{\Delta} &= \sin\delta \end{aligned} \tag{3-12}$$

We see that equation (3-8) is equivalent to a coordinate rotation (through the time angle θ) of the $\xi\eta\zeta$-axes about the ζ-axis. This rotation yields the x"y"z"-axes from the $\xi\eta\zeta$-axes. (However, the rotation alone does not quite produce the equatorial coordinates (H,δ) from the coordinates (α,δ) because α and H are measured in opposite directions around the celestial equator. Thus, an angular coordinate inversion is also required.)

The third coordinate transformation produces the horizon coordinates (x'y'z'-frame) from the equatorial coordinates (x"y"z"-frame). Suppose that ϕ is the terrestrial latitude of the observer. Since the y"-axis points toward the east point E, a rotation (through the angle $\psi = 90° - \phi$) of the x"y"z"-frame about the y"-axis (i.e. in the plane

of the local meridian) would superimpose the z"-axis over the z'-axis. The sense of this rotation is given by the right-hand rule with the thumb pointing along the y"-axis.

The transformation equations between the x"y"z"-axes and the x'y'z'-axes can be written:

$$(3\text{-}13)\quad \begin{aligned} \frac{x'}{\Delta} &= (x''/\Delta)\cos\psi \;-\; (z''/\Delta)\sin\psi \\ \frac{y'}{\Delta} &= \frac{y''}{\Delta} \\ \frac{z'}{\Delta} &= (x''/\Delta)\sin\psi \;+\; (z''/\Delta)\cos\psi \end{aligned}$$

or, in terms of the spherical coordinates:

$$(3\text{-}14)\quad \begin{aligned} \frac{x'}{\Delta} &= \sin z\cos A = -\sin\delta\cos\phi \;+\; \cos\delta\sin\phi\cos H \\ \frac{y'}{\Delta} &= -\sin z\sin A = -\sin H\cos\delta \\ \frac{z'}{\Delta} &= \cos z \;=\; \sin\delta\sin\phi \;+\; \cos\delta\cos\phi\cos H \end{aligned}$$

To conclude this section, note that we can rewrite equation (3-11c) for the sun:

$$\sin\delta = \sin\varepsilon\cos B\sin L \;+\; \cos\varepsilon\sin B$$

Since the ecliptic latitude B of the sun is very nearly 0, we have:

$$(3\text{-}15)\quad \sin\delta = \sin\varepsilon\sin L$$

Occasionally, some authors approximate this equation with the formula:

$$(3\text{-}16)\quad \delta = \varepsilon\sin L$$

The approximate maximum error incurred by using (3-16) instead of (3-15) is about ¼°.

3.1.4 Transits of the Local Meridian and Hour Angles of Rising and Setting

Due to the diurnal rotation of the earth about an axis through the celestial poles, each star in the sky appears to move along a parallel of declination. If any portion of this parallel dips below the horizon (Figure 3.6 [15]), then the star will rise and set. Some stars, of course, are close enough to the poles that they are always either above or below the horizon. (Figure 3.6) Such stars are called circumpolar stars.

Now suppose that the celestial object is on the local meridian - i.e. that H is either 0° or 180°. When this occurs, the object is said to transit or to be in transit. In general, a celestial body will transit twice a day. The point at which the body reaches its maximum altitude is called upper culmination, and the point where it reaches its minimum altitude is called lower culmination.

Let $h_1[h_2]$ be the altitude of a celestial object at upper[lower] culmination. Let $z_1[z_2]$ be the zenith distance of the celestial object at upper[lower] culmination. h_1 and h_2 can be calculated using (3-14c). Table 3.1 summarizes the results of this calculation.(Note that, by convention,ϕ is positive for northern latitudes and negative for southern latitudes.) Table 3.1 provides the information necessary to determine whether a star is circumpolar. Assume the star's declination is δ and the observer is at latitude ϕ. Because the star descends to its minimum altitude h_2 at lower culmination, the star will be circumpolar - i.e. it will be above the horizon throughout the day - if $h_2>0$. Analogously, if $h_1<0$ then the star will be below the horizon all day because

Table 3.1

Zenith Distances at Upper and Lower Culmination

Observer at Latitude ϕ

	Altitude h; zenith distance z	Hour angle, H	Characteristic Feature
Upper Culmination	$h_1 = 90° - \lvert\phi-\delta_1\rvert$; $z_1 = \lvert\phi-\delta_1\rvert$	H=0°	Maximum altitude point; minimum zenith distance point.
Lower Culmination	$h_2 = -90° + \lvert\phi+\delta_2\rvert$; $z_2 = 180° - \lvert\phi+\delta_2\rvert$	H=180°	Minimum altitude point; maximum zenith distance point.

its maximum altitude h_1 is attained at upper culmination. Finally, the star will appear to rise and set if $h_1>0$ and $h_2<0$.

Suppose the condition for either rising or setting is that the center of the celestial body lies on the horizon. Then, at rising and setting, h=0 and z=90°-h=90°; cos z = 0. Equation (3-14c) yields:

$$0 = \cos z = \sin \phi \sin \delta + \cos \phi \cos \delta \cos H$$

Since we assume that δ and ϕ are known, an expression for the hour angles of rising and setting is found by solving for cos H.

(3-17) $\cos H = - \tan \phi \tan \delta$

(Note that the conditions $h_1>0$ and $h_2<0$ [see Table 3.1] are sufficient to prove that $-1 < - \tan \phi \tan \delta < +1$.) Rewriting equation (3-17) gives:

(3-18) $H = \cos^{-1} (\tan \phi \tan \delta)$

Here we restrict the range of the inverse cosine to its principal values - i.e. 0° through 180°. Since a celestial object sets when its hour angle is between 0° and 180°, equation (3-18) defines the hour angle of setting H_S. The hour angle of rising H_R will be given by H_R=360°-H. If the declination of the celestial object changes over the length of one day, then one must solve equation (3-18) twice, first using the morning value of δ and then using the afternoon value of δ.

The above discussion ignores atmospheric refraction and the apparent finite size of astronomical bodies like the sun and moon. Both of these phenomena delay the setting of a celestial object because they tend to make the object visible even after the central point of the body crosses the horizon. Subsection 3.4 contains a short discussion of at-

mospheric refraction.

Now, suppose we wish to determine the hour angle at which a celestial body sets, not below the horizon, but rather below a parallel of altitude h_0'. For example, one may be interested in the sun's motion through the sky only when its altitude above the horizon is greater than 10°. Therefore, the hour angles at which the sun crosses the parallel of altitude 10° would replace the hour angles of rising and setting as the "times" between which the observer views the sun.

Let $z_0'=90°-h_0'$. Then the hour angles for crossing the parallel of altitude h_0' are given simply by (3-14c):

$$\cos z_0' = \sin \phi \sin \delta + \cos \phi \cos \delta \cos H_0'$$

Solving for $\cos H_0'$ yields:

$$\begin{aligned} \cos H_0' &= (\cos z_0' - \sin \phi \sin \delta)/(\cos \phi \cos \delta) \\ &= - \tan \phi \tan \delta + [\cos z_0'/(\cos \phi \cos \delta)] \end{aligned} \tag{3-19}$$

We limit the range of H_0' to the principal values of the inverse cosine; thus $0° \leqq H_0' \leqq 180°$. As with equation (3-17), two solutions (i.e. $H_S=H_0'$ and $H_R= 360°-H_0'$) are then constructed.

Note that it is possible that equation (3-19) will not have a solution. The criteria $h_1>0$ and $h_2<0$ are no longer sufficient to prove that the inequalities $-1 \leqq \cos H_0' \leqq +1$ hold. However, from the definitions of h_1 and h_2, it is clear that the restrictions $h_1>h_0'$ and $h_2<h_0'$ are sufficient. The only assumptions inherent in this statement are the same as those given earlier, namely, that there is no atmospheric refraction and that the celestial object has no finite size. Hence, we

have the conditions (see Table 3.1):

(3-20) $h_2 = -90° + |\phi+\delta| \geqq h_0'$ Star will always be above the parallel of altitude h_0'

(3-21) $h_1 = 90° - |\phi-\delta| \leqq h_0'$ Star will always be below the parallel of altitude h_0'

We see that the techniques of subsection 3.1 allow us to determine the position of the sun at any time, provided we know:

(1) the ecliptic longitude of the sun at the time t, and
(2) what we mean by the concept of time.

Problem number 1 is considered in subsection 3.2, while subsection 3.3 deals with problem number 2.

3.2 THE APPARENT ORBIT OF THE SUN

3.2.1 The Elements of the Sun's Apparent Orbit

Two differential equations of motion describe the classical problem of two bodies moving under the influence of a mutual central force. For their complete solution, twelve constants of integration must be specified. As the center of mass of the two-body system moves in a straight line with constant speed, six of these twelve constants are associated with the motion of the center of mass. Consequently, the remaining six constants of integration supply information about the movements of the two bodies relative to each other. In classical mechanics these last six constants are usually the three rectangular components of the total angular momentum vector, the two rectangular components of the vector pointing toward the position of closest approach, and the time T of passage through the point of closest approach. However, we need not choose these particular ones since any appropriate set of six independent constants will suffice.

When studying the orbits of the planets, an astronomer generally uses the six constants of integration known as the elements of the orbit. The elements of an orbit are [16] :

Ω = the longitude of the ascending node of the orbit, measured eastwards around the ecliptic from Υ; $0° \leqq \Omega \leqq 360°$;

i = the inclination of the orbital plane to the ecliptic, i.e. the angle between the normal to the orbit of the planet and the $\bar{\zeta}$-axis; $0° \leqq i \leqq 180°$;

ω = the argument of perihelion = the longitude measured along the orbit from the ascending node to perihelion; $0° \leqq \omega \leqq 360°$;

a = the length of the semi-major axis of the orbit;

e = the eccentricity of the orbit;

T = the time of perihelion passage.

The first three elements - Ω, i, and ω - determine the orientation of the plane of the orbit and the direction of perihelion in this plane. The last three elements - a, e, and T - determine the shape of the orbit and give an initial position for the planet's motion. a, e, and T are called the dynamical elements.

The mean anomaly M is often used instead of the time of perihelion passage T. M is defined by the relation $M = n(t-T)$, where (t-T) is the time since perihelion passage. It is clear that M represents the angle that would be described in an interval (t-T) by the planet if it moved around the sun at constant angular velocity n. Furthermore, M=0 if t=T, i.e. at perihelion. Although M is not strictly a constant of integration (it depends on t), it is widely used because of the form which the orbital equations assume when it is introduced.

As viewed from the earth, the sun annually appears to describe an elliptic orbit around us. The earth occupies one focus of the ellipse. Thus, we can speak of the elements of the sun's apparent orbit. The mean orbital elements of the sun may be found in the Astronomical Ephemeris [17] :

Epoch 1900 January 0.5 E.T. = J.D. 241 5020.0

$$\varepsilon = 23^\circ\ 27'\ 08''.26 - 46''.845\ T - 0''.0059\ T^2 + 0''.00181\ T^3 \quad (3\text{-}20)$$

$$= 23^\circ.452294 - 0^\circ.0130125\ T - 0^\circ.00000\ 164\ T^2 + 0^\circ.00000\ 0503\ T^3$$

$$= 23^\circ.452294 - 0^\circ.0035626\ D - 0^\circ.00000\ 0123\ D^2 + 0^\circ.00000\ 00103\ D^3$$

(continued on next page)

(3-20) contd.

$$\omega\ (= \Gamma) = 281^\circ\ 13'\ 15''.00 + 6189''.03\ T + 1''.63\ T^2 + 0''.012\ T^3$$

$$= 281^\circ.220833 + 0^\circ.00004\ 70684\ d + 0^\circ.00003\ 39\ D^2 + 0^\circ.00000\ 007\ D^3$$

$$M\ (= g) = 358^\circ\ 28'\ 33''.04 + 129596579''.10\ T - 0''.54\ T^2 - 0''.012\ T^3$$

$$= 358^\circ.475845 + 0^\circ.98560\ 02670\ d - 0^\circ.00001\ 12\ D^2 - 0^\circ.00000\ 007\ D^3$$

$$e = 0.01675104 - 0.00004\ 180\ T - 0.00000\ 0126\ T^2$$

$$= 0.01675104 - 0.00001\ 1444\ D - 0.00000\ 00094\ D^2$$

$$a = 1.00000\ 023 \text{ astronomical units (A.U.)} \simeq 1 \text{ A.U.}$$

The notation in parentheses is that used by the A.E. The value of the obliquity of the ecliptic is included here as it, in effect, defines the ecliptic plane. Note that $\Omega=0^\circ$ and $i=0^\circ$ for the sun.

"In these formulas, the interval of time since the epoch is denoted by T when measured in Julian centuries of 36525 ephemeris days, by D = 3.6525 T when measured in units of 10000 ephemeris days, and by d = 10000 D = 36525 T when measured in ephemeris days." [18] The epoch is merely a particular point in time, arbitrarily chosen as the reference point for which the initial position of the sun is specified. The epoch chosen here is Julian Day 2415020.0 or, in more familiar terminology, Greenwich mean noon on December 31, 1899. Astronomers also refer to this time as 1900 January 0.5 Ephemeris Time. Note that Julian Days begin at Greenwich mean noon, not at midnight.

The elements given in equations(3-20) are called mean orbital elements. Usually this means that the elements refer to a selected reference orbit, from which the actual orbit is derived using perturbation theory to incorporate the gravitational attraction of the other planets.

However, in the Explanatory Supplement, no attempt is made to explain what is meant by the mean orbital elements of the sun. It is clear that the formulas given take into account the effects of general precession of the equinoxes (see subsection 3.4.1) because their values are in reference to the mean equator, mean ecliptic, and mean equinox of date [19]. However, the discussion in the Explanatory Supplement is not clear as to which astronomical effects were accounted for in the derivations of formulas (3-20); thus, we assume that the elements given in equations (3-20) represent (to a sufficient accuracy) the actual elements of the apparent solar orbit. Furthermore, to this same accuracy, we assume $\Omega=0°$ and $i=0°$ for consistency with the definitions of the ecliptic plane and of Υ. The validity of these assumptions can be judged from the results of subsection 3.4.

To conclude this section, we note the formula for the solar longitude used in the solar tracker program (here at the University of Houston) prior to this paper's composition:

$$(3\text{-}21) \quad L = \frac{360°}{365.25 \text{ days}} N$$

where N is the number of days from the vernal equinox. If we express L in seconds of arc and N in centuries, we have:

$$\frac{360°}{365.25 \text{ days}} = \frac{360°}{365.25 \text{ days}} \times \frac{36525 \text{ days}}{\text{century}} \times \frac{3600''}{1°}$$

$$= (3.6)^2 \times 10^7 = 12.96 \times 10^7 \text{ seconds of arc per century}$$

Inserting this result in equation (3-21) and using the symbol T instead of N, yields:

$$L = 1296\ 00000''.00\ T$$

Comparison of this result with the equation for M in (3-20) leaves no doubt that the formula for M in (3-20) is one in which the sun moves at a constant angular velocity. The fictitious point, moving along the ecliptic with the constant angular velocity $n=\frac{2\pi}{P}$ and coinciding with the real sun at perigee and apogee, is called the dynamic mean sun.

3.2.2 Kepler's Equation and the Equation of the Center

A simple geometrical construction is used to relate the mean and actual motions of the sun. In Figure 3.7 [20], the apparent elliptical orbit of the sun S about the earth E is ASD. The center of the elliptical orbit is C. A circle with center C and radius CA = a is drawn so that the plane of the circle is inclined at an angle i to the plane of the ellipse. This circle is called the eccentric circle, and the angle i is chosen so that if the circle were projected onto the plane of the ellipse, the projection of the circle would be identical with the orbital ellipse.

Defining the eccentric anomaly E to be the angle S'CE, it may be shown that:

(3-22) $M = E - e \sin E$

This is called Kepler's equation. Note that both E and M are expressed in radians. Since M is known from equation (3-20), E may be found by solving equation (3-22). Because (3-22) is a transcendental equation, numerical methods of solution are required [21].

Let υ denote the angle AES in Figure 3.7. υ is called the true anomaly because it is the angle between perigee and the radius vector

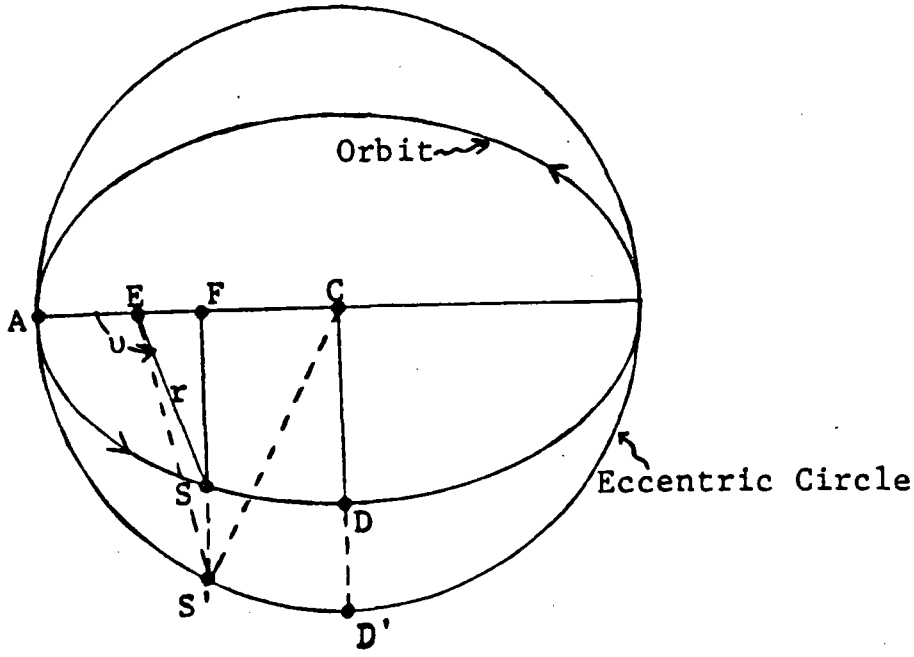

Figure 3.7

The Eccentric Circle and Kepler's Equation [20]

to the sun. Let L denote the ecliptic longitude of the sun. Since ω is the longitude of perigee, we have $L = \omega + \upsilon$. (3-23)

The eccentric anomaly E is related to the position (r,υ) of the sun using Figure 3.7:

$$(3\text{-}24) \quad r = a(1 - e \cos E)$$

$$(3\text{-}25) \quad \cos \upsilon = \frac{\cos E - e}{1 - e \cos E}$$

One may also show that [22]:

$$(3\text{-}26) \quad \tan \frac{\upsilon}{2} = \left(\frac{1+e}{1-e}\right)^{\frac{1}{2}} \tan \frac{E}{2}$$

The following expansions for small e may also be derived from equations (3-22), and (3-24) through (3-26) [23]:

$$(3\text{-}27) \quad \frac{r}{a} = 1 - e \cos M + \tfrac{1}{2}e^2(1-\cos 2M) - \tfrac{1}{8}e^3(3 \cos 3M - 3 \cos M)$$

$$(3\text{-}28) \quad \upsilon - M = 2e \sin M + \tfrac{5}{4}e^2 \sin 2M + \tfrac{1}{12}e^3 (13 \sin 3M - 3 \sin M)$$

Equation (3-28) is called the equation of the center. These formulas are correct to order e^3 and are very useful because they give $\frac{r}{a}$ and υ directly in terms of M. Note that υ and M must be expressed in radians.

3.3 TIME

3.3.1 Systems of Time Measurement

What measure of time is employed in the expressions (3-20) for the elements of the sun's apparent orbit ? The time upon which these formulas are based is ephemeris time (E.T.). Theoretically, ephemeris time is uniform because the length of the ephemeris second is fixed; hence, it is independent of the fluctuations in the rate of rotation of the earth. In practice, ephemeris time is determined through observations of the motion of the moon in its orbit around the earth. A value for ephemeris time is computed from these observations by assuming that ephemeris time is the independent variable in the gravitational theories of the sun, moon, and planets.

The difference between the computations of the elements of the sun using ephemeris time or using universal time (U.T.) is negligible. This convenience will probably apply for the next few centuries, though the random variations in the earth's speed of rotation make it impossible to state this with certainty [24]. In 1960 ephemeris time was greater than universal time by about 35 seconds. The approximate maximum error in the ecliptic longitude of the sun caused by overlooking this difference is about:

$$\frac{35 \text{ sec}}{(60 \times 60 \times 24)\text{sec/day}} \times \frac{1^\circ}{\text{day}} \times \frac{3600''}{1^\circ} = \frac{35''}{24} \approx 1.5''$$

For the end of the twentieth century, this error is less than about 3".

Furthermore, note that the hour angle H of the sun and the sidereal time θ are related to the observed rotation of the earth. Thus, uni-

versal or sidereal time is the correct time to use when applying the coordinate transformations of subsection 3.1.3. True, we must theoretically convert from U.T. to E.T. when evaluating the elements and ecliptic longitude of the sun; however, once we have obtained the ecliptic longitude, we must use U.T. to determine the sun's hour angle.

There are five other familiar systems of time measurement:

(1) Sidereal Time (S.T.) is the hour angle of the vernal equinox Υ. Mean sidereal time is the hour angle of the mean equinox of date, where only precession is considered in the motion of Υ along the ecliptic. Greenwich mean sidereal time (G.M.S.T.) is the hour angle of Υ for an observer at Greenwich (0° longitude).

(2) Greenwich Mean Astronomical Time (G.M.A.T.) is the hour angle of the fictitious mean sun as seen from Greenwich, England. Mean noon at Greenwich is 0^h G.M.A.T. (See below for definition of the fictitious mean sun.)

(3) Universal Time (U.T.) is the G.M.A.T. + 12^h. Mean noon at Greenwich is 12^h U.T. In America there was a brief period when U.T. was referred to as Greenwich Civil Time (G.C.T.).

(4) Apparent Solar Time (A.S.T.) is the hour angle of the sun. Local apparent noon is 0^h A.S.T.

(5) Zone or Standard Time (Z.T.) is the U.T. - Λ_0, where Λ_0 is the longitude of the standard meridian for the zone. Λ_0 is expressed in units of time. Terrestrial longitude, Λ, must lie in the range $-12^h \leqq \Lambda < +12^h$ (i.e. $-180° \leqq \Lambda < +180°$); Λ is positive for west longitudes and negative for east longitudes. Standard time is the most familiar to all of us. The longitude of the standard meridian Λ_0 is usually an integral multiple of 15°.

Apparent solar time has serious disadvantages for general use as a primary standard of time. Its most undesirable feature is that it is not a uniform measure of time. For a moment let us assume that the earth's rate of rotation is constant and let us neglect precession and nutation. This implies that sidereal time θ is a uniform measure of time. However, the sun's annual motion is along the ecliptic and not along the celestial equator. Hence, its right ascension α does not increase uniformly with time. Since $H=\theta-\alpha$, we conclude that H can not increase uniformly either. Furthermore, the apparent orbit of the sun is an ellipse, and its angular velocity is not constant. Consequently, the sun's ecliptic longitude and hour angle do not increase uniformly.

Mean solar time overcomes these difficulties. Suppose there were a celestial object which moved along the celestial equator with the average angular velocity n of the sun. This body would complete one orbit around the equator in one solar year. Since it would move along the equator and since its angular velocity would be constant, the right ascension of this object would increase uniformly, and its motion would yield a uniform measure of time. This fictitious body is called the mean sun when we further specify that its right ascension is 0 at the same time that the right ascension of the dynamic mean sun (subsection 3.2.1) is 0. Indeed, the mean sun is defined so that at any instant its right ascension α is equal to the mean longitude ℓ of the sun. (Note that $\ell = \omega + M$.)

When we consider that the sun has a very small secular acceleration and that the earth's rate of rotation is variable, we find that

both mean time and sidereal time are no longer strictly uniform. Nevertheless, the assumption that mean time and sidereal time are uniform is consistent with the assumption that E.T. = U.T.

Local sidereal time is the hour angle of the vernal equinox measured with respect to the local meridian. Similarly, local mean astronomical time is the hour angle of the mean sun, measured with respect to the local meridian. In both cases, the relationship between local time and Greenwich time is:

(3-29) Greenwich time = local time + longitude of local meridian

where the longitude of the local meridian (Λ) is measured in terms of hours, minutes, and seconds.

The relationship between local mean astronomical time and universal time is:

(3-30) Universal time = local mean astronomical time + 12^h
+ longitude of local meridian
= Greenwich mean astronomical time + 12^h

$$U.T. = L.M.A.T. + 12^h + \Lambda$$

We establish the convention that $-180° \leqq \Lambda < +180°$, i.e. Λ can be $-180°$ but not $+180°$. Universal time - not local time - is required in (3-20) for calculating the elements of the sun's orbit.

3.3.2 The Equation of Time

The difference α_m minus $\alpha_\odot$, as shown in (3-31) below, is known as the equation of time (E). Suppose at sidereal time θ the hour angle and right ascension of the sun are $(H_\odot, \alpha_\odot)$ and the hour angle and right ascension of the mean sun are (H_m, α_m).

(3-31) $E = \alpha_m - \alpha_\odot$

(3-32) $\theta = H_m + \alpha_m = H_\odot + \alpha_\odot$

or

$$E = (\theta - H_m) - (\theta - H_\odot)$$

(3-33) $E = H_\odot - H_m$

Thus E represents the correction which must be added to local mean astronomical time to give apparent solar time.

Let ℓ be the mean longitude of the sun so that $\ell = \omega + M$. By definition, $\alpha_m = \ell$. Thus

(3-34) $E = \ell - \alpha_\odot$

One can obtain a series expansion for E. The following expression is correct to second order in e and $y = \tan^2 \frac{\varepsilon}{2}$: [25]

(3-35) $E = y \sin 2\ell - 2e \sin M + 4ey \sin M \cos 2\ell$
$- \frac{1}{2} y^2 \sin 4\ell - \frac{5}{4} e^2 \sin 2M$

The maximum value of E is about 16 minutes and occurs sometime in November. Since the value of E is always small and since the sun's mean ecliptic longitude changes slowly (<1° per day), the equation of time changes by a very small amount over the course of a day. Since $\ell = \omega + M$, we have from (3-20):

(3-36) $\ell = 279° \; 41' \; 48".04 + 129602768".13 \; T + 1".089 \; T^2$
$= 279°.696678 + 0°.98564 \; 73354 \; d + 0°.00002 \; 267 \; D^2$

where T, D, and d are as defined in (3-20).

3.3.3 Tracking the Sun

Apparent solar time H, while not very useful as a primary standard of time,is very useful in following the motion of the sun through the sky. However, there are two different cases to be considered. First, take the case of computer modeling of a solar energy system. Here, we can assume that we always know the apparent solar time. In the second case, where one actually tries to observe the sun's position in the sky, we can not make this assumption. Instead, we assume that only the local mean time is known (e.g. from radio time signal broadcasts and a knowledge of the observer's terrestrial longitude); the apparent solar time must then be calculated using the equation of time (3-35) [computed for the instant of observation] and equations (3-20) and (3-36).

In the solar tracker computer program, the apparent solar time is assumed known and is one of the inputs. Consequently, if observations are to be made, a separate calculation, independent of the solar tracker program, must first be performed to evaluate the equation of time E.

Suppose we know the apparent solar time H for an observer at latitude ϕ and longitude Λ. We wish to find the position of the sun in its apparent orbit. Denote by JD the Julian Day number of the date. As a first approximation, the G.M.A.T. corresponding to H is given by:

$$\text{G.M.A.T.} = H + \Lambda$$

(Λ is expressed in hours not degrees.) T is then given by:

$$T = \frac{(JD + \text{G.M.A.T.}/24) - 2415020.0}{36525} \tag{3-37}$$

When using (3-37), recall that the Julian Day number increases by one at noon. Values for the Julian Day number can be found in the appropriate annual volume of the A.E. Equations (3-36) and (3-20) are used to calculate ℓ and M, using this approximate value of T. These values of ℓ and M will yield very accurate values for E when used in equation (3-35). Then $H_m = H - E$ from (3-33). This value of H_m is used to evaluate the elements of the sun's orbit, (3-20), with T calculated via the expression G.M.A.T. = $H_m + \Lambda$ and (3-37). Even if E is evaluated only once each day - say at noon - the approximate maximum error in the ecliptic longitude of the sun would be:

$$\frac{20 \text{ sec}}{(60 \times 60 \times 24) \text{ sec/day}} \times \frac{1^\circ}{\text{day}} \times \frac{3600''}{1^\circ} = \frac{20''}{24} < 1''$$

Often we ignore the orbital motion of the sun over one day. The approximate maximum error in the ecliptic longitude arising from this assumption is:

$$\frac{6 \text{ hours}}{24 \text{ hour/day}} \times \frac{1^\circ}{\text{day}} = \tfrac{1}{4}^\circ = 15' \text{ for every 6 hours}$$

The equation of time need not be evaluated before calculating the orbital elements (3-20).

3.4 SUMMARY, RESULTS, AND CONCLUSIONS

3.4.1 Several Small Perturbations in the Sun's Apparent Motion

The apparent motion of the sun is very complex. One reason for this complexity is the fact that small forces acting on the earth produce measurable effects. In the following, we consider some of the small perturbations which affect the sun's apparent motion through the sky.

- Precession and Nutation

The earth is not a perfect sphere as we have assumed. Rather, it is approximately a spheroid of revolution. The moon and sun exert gravitational torques on the earth's equatorial bulge. Since the earth acts like a spinning top, its axis precesses. The orbital plane of the moon is not the ecliptic plane, and, therefore, the precession is not constant and is broken into two components:

(i) luni-solar precession is the smoothed, long period (about 26,000 years) motion of the mean pole of the mean equator about the normal to the ecliptic plane;

(ii) nutation is the relatively short period motion that carries the actual (or true) pole around the mean pole in an irregular curve. The nutation is also divided into two parts:

(a) the nutation in the longitude, $\Delta\psi$, and

(b) the nutation in the obliquity, $\Delta\varepsilon$.

The amplitude of $\Delta\varepsilon$ is about 9", and its main term has a period of about 18.6 years [26]. The amplitude of $\Delta\psi$ is about 18" [27]. $\Delta\psi$ and $\Delta\varepsilon$ are often referred to as astronomical nutation to distinguish their origin from the smaller nutation which would be present even if the torques were constant [28].

There is one further type of precession - planetary precession. This is due to the gravitational forces exerted on the earth by the other planets and consists of a slow rotation of the mean ecliptic plane about a slowly rotating chord of the earth's orbit.

Both luni-solar and planetary precession are very slow and their combined effect is called general precession. The mean equinox is defined as the intersection of the mean equator with the mean ecliptic. This point of intersection moves with time, but of main importance to us is the mean equinox of date, in other words, the mean equinox for the day on which an observation is made.

As explained in subsection 3.2.1, the assumption appears to be justified that (3-20) incorporate corrections for general precession as a function of time. However, the effects of nutation are not considered.

- The Motion of the Earth's Center About the Center of Mass of the Earth and Moon

The earth moves in an elliptic orbit around the center of mass of the earth and moon. Now, the center of mass of the earth-moon system (sometimes called the barycenter) is approximately 3000 miles from the earth's center, or about 1000 miles below the surface. At full moon the earth's center is 3000 miles closer to the sun than the barycenter, and at new moon the earth's center is 3000 miles further from the sun than the barycenter. The apparent displacement of the sun caused by this effect is approximately the angle subtended by a line 3000 miles long when viewed from 93 x 10^6 miles away [29]; specifically:

$$(3\text{-}38)\quad \frac{3000}{93 \times 10^6} \times \frac{180^\circ}{\pi \text{ rad}} \times \frac{3600''}{1^\circ} \approx 6.7''$$

We neglect this effect. Note, however, that the A.E. takes this effect into consideration when determining the ecliptic longitude of the sun.

· Parallax

The phenomenon of parallax occurs because the sun appears to be in a slightly different position in the sky if viewed by an observer at the earth's center instead of an observer on the earth's surface 4000 miles away. The maximum apparent displacement is calculated in the same way as in (3-38):

$$(3\text{-}39)\quad \frac{4000}{93 \times 10^6} \times \frac{180^\circ}{\pi \text{ rad}} \times \frac{3600''}{1^\circ} \simeq 8.8''$$

We neglect parallax errors.

· Aberration

Aberration is caused by the fact that the velocity of light is finite. Thus, at any instant, the position of a moving object as seen by a moving observer differs from the position which he would observe for that object, if he could see it instantaneously [30].

When discussing aberration, the following terms which describe the position of a celestial object are frequently encountered. The geometric position of a body is its actual position at the time of observation; the apparent position of the body at the same instant is the place in which an observer would see the object [31].

There are various types of aberration, but we are concerned only with planetary aberration. Suppose τ is the length of time that it takes light to travel from the sun to the earth. For 1 A.U., $\tau = 499^s.012$ [32].

The effect of planetary aberration on the position of the sun is as follows [33]:

> If we assume that the motion of the earth during the light-time τ is rectilinear and uniform, the apparent position at time t is the same as the geometric position that the sun occupied at time $t-\tau$.

The phenomenon of planetary aberration is in no way connected with the diurnal motion of the earth. Instead, it is connected with the orbital motion of the earth around the sun and with the finite velocity of light. Consequently, the approximate maximum error which would arise from neglecting planetary aberration would be:

$$(3\text{-}40) \quad \frac{499 \text{ sec}}{(60 \times 60 \times 24) \text{ sec/day}} \times \frac{1^\circ}{\text{day}} \times \frac{3600''}{1^\circ} \simeq 21''$$

We do not neglect planetary aberration.

· Atmospheric Refraction

When a ray of light from a celestial object enters the atmosphere its path is bent, causing the apparent position of the object to differ from its actual position at the same instant. Since the optical density of the atmosphere increases as the ray of light traverses its path, Snell's law of refraction implies that the ray will be continually refracted toward the instantaneous normal to the earth's surface at each point of its path. Therefore, the apparent position of a celestial body will always lie closer to the zenith than its geometric position. Atmospheric refraction only affects the zenith distance of a celestial object; its azimuth angle is unaffected.

Various formulas may be obtained for the amount of refraction R [34].

Table 3.2 lists some data on refraction [35]. R is less than 5' for altitudes greater than 10°. R is less than about 4' for altitudes greater than 15°. When dealing with the central receiver system, we are interested in the sun's position only if its altitude exceeds 10°. For this reason, we will ignore atmospheric refraction. Indeed, one must use a more precise formula for calculating optical air masses if the effect of atmospheric refraction is considered.

3.4.2 Summary of Phenomena Affecting the Sun's Apparent Motion

Table 3.3 lists the phenomena affecting the sun's position and the errors which result when one disregards their effects. A few remarks about those phenomena which have not been incorporated into the new computer tracking program are appropriate. (Keep in mind that the "approximate maximum error" is not a least upper bound. Indeed, it may not be an upper bound but only close to one.)

The errors which have not been incorporated into the new program can be grouped into three sets. The largest error results from neglecting the earth's orbital motion during one day. Thus, there is an option in our tracking program to evaluate the solar declination, δ, at each instant instead of only at noon of each day. The approximate maximum error from computing the orbital position of the sun only at noon is ±30' in ±12 hours, or ±15' in ±6 hours. In contrast, the error should not exceed 2.5' if δ is evaluated at the beginning of each hour.

The second largest error is due to atmospheric refraction; it becomes significant only when the sun is low in the sky. The remaining errors can be grouped together. Their total effect is at most:

(continued on next page)

Table 3.2

Refraction versus Elevation [35]

Elevation (Degrees)	Refraction (Min. & Sec.)	(Mrads)
0°	34' 50"	10.132
1	24 22	7.088
2	18 06	5.265
3	14 13	4.135
4	11 37	3.379
5	9 45	2.836
10	5 16	1.532
20	2 37	.761
30	1 40	.484
50	0 48	.233
70	0 21	.102
90	0 0	.000

1° = 17.453 milLiradians (mrads)

Table 3.3

Phenomenon	Approx. Maximum Error if Neglected [in Quantity stated]	Phenomenon Incorporated in Computer Tracker	Sections Discussing Phenomenon
General Precession	5025".64 per tropical century [in ecliptic longitude of sun]	Yes	3.2.1 & 3.4.1
Change in Obliquity due to Planetary Precession	47" per tropical century [in obliquity]	Yes	3.2.1 & 3.4.1
Nutation	18 " [in ecliptic longitude of sun]	No	3.2.1 & 3.4.1
Difference Between Ephemeris Time and Universal Time	3" [in ecliptic longitude of sun]	No	3.3.1
Motion of Earth's Center Around Earth - Moon Center of Mass	7" [in ecliptic longitude of sun]	No	3.4.1
Parallax	9" [in ecliptic longitude of sun]	No	3.4.1
Planetary Aberration	21" [in ecliptic longitude of sun]	Yes	3.4.1
Change in equation of time, E , over 1 day	1" [in ecliptic longitude of sun]	No	3.3.3
Atmospheric Refraction	5' for altitudes above 10°; 4' for altitudes above 15° [zenith distance of sun is affected.]	No	3.4.1
Change in orbital position of sun over 1 day	15' every 6 hours [in ecliptic longitude of sun]	No (for one option) Yes (for other option)	3.3.3 & 3.4.2
Eccentricty of Earth's Orbit	2° [in ecliptic longitude when sun is near equinoxes]	Yes	3.2.2
Variation of Local Vertical	12' [in zenith distance of sun]	N/A : Observer must use correct astronomic latitude	3.1.1
"Observational errors": Instrumental backlash, incorrect time or latitude or longitude, etc.		Must be eliminated by observer	3.1.1

(3-41) 18" + 3" + 7" + 9" + 1" = 38"

Should future attempts be made to improve the computer tracking program, Table 3.3 will prove helpful in identifying those errors which will no longer be small enough to ignore.

3.4.3 SUNLOC - A Computer Program to Locate the Sun

The appendix contains a listing of the computer program which was developed to calculate the sun's position at any given time. Also included in the appendix is a table which provides brief definitions of each of the variables used in the program.

Written as a FORTRAN subroutine, the program has four entry points: SUNLOC, DAYLIT, MIDST, and AST. SUNLOC locates the sun's position, in its apparent orbit, at apparent solar noon of the day with Julian Day number JD. The longitude, XLONG, of the observer must be known. (For input to SUNLOC, the value of JD must be computed without considering the longitude of the observer. SUNLOC makes this correction automatically.)

SUNLOC also determines, for an observer situated at the latitude XLAT, the times at which the sun rises above and sets below the parallel of altitude HO. A switch variable,HIPREC, allows the user some control over the precision to be used in calculating these rise and set times. If HIPREC is .FALSE., no allowance will be made for the sun's motion in its apparent orbit, over the length of the day JD. If HIPREC is .TRUE., a refinement on the rise and set times is computed. However, no guarantee is made as to the precision of the solutions. (In general,

it should be noted that, for XLAT close to ±90°, the solutions for the rise and set times are less precise than for lower latitudes.)

DAYLIT is an alternative entry point for the rise and set times calculations; its purpose is to allow the user to change XLAT and/or HO, while keeping JD and XLONG fixed.

AST may be called only after reference has been made to SUNLOC (and also DAYLIT, if necessary). Beginning with the supplied apparent solar time, TIME2, AST computes the solar altitude, h, at TIME2. Since days begin at noon when one uses apparent solar time, an alternate entry point, MIDST, is provided as a convenience for the user of the program. MIDST performs the same calculations as AST, but the user supplies the solar time, TIME1. TIME1 is the solar time reckoned with midnight as the hour 0, while TIME2 is the solar time reckoned with noon as the hour 0. (See the appendix and subsection 3.3.3.)

LOPREC and ID are two other switch variables. If LOPREC is .FALSE., then both AST and MIDST recalculate the sun's orbital position for the instant of observation. If LOPREC is .TRUE., then the position of the sun in its apparent orbit is taken to be that which was last computed. On the first reference to AST or MIDST (when LOPREC is .TRUE.),the position of the sun in its apparent orbit is taken to be that of noon on the day JD. If ID is 1, then the sun's azimuth, right ascension, and mean longitude are also calculated, as well as the local sidereal time.

The input and output parameters of this FORTRAN subroutine are passed to the calling program via the common region SLC. The input var-

iables are JD, TIME1 (or TIME2), XLONG, XLAT, HO, ID, LOPREC, and HIPREC. Default values for the input parameters are provided in a BLOCK DATA subroutine. For this reason, the input parameters may not be initialized in DATA statements within the calling program. If the user wishes to change the default value of a particular input variable, he need only change the appropriate number in the BLOCK DATA subprogram.

A listing of a program to generate an ephemeris of the sun is included in the appendix. Brief descriptions of the input parameters are provided. This program not only serves as an example of the use of the SUNLOC subprogram, but the output of the program may be compared with the Astronomical Ephemeris. We made such a comparison, using the ephemerides of the sun for the years 1962, 1887, and 1978. While this analysis is not meant to be comprehensive, our search for the maximum deviations between the A.E. and our computations led to the results indicated in Table 3.4. Because the differences had to be calculated "by hand", we grouped the days of each year into 73 sets of five days each. For the years 1887 and 1978, one day was picked at random from each of the 73 sets and the differences computed. However, each day of the year 1962 was used in the study.

3.4.4 The Effects of Errors in Locating the Sun on Insolation Predictions

- Errors in the Ecliptic Longitude and the Declination of the Sun

We compared values of the ecliptic longitude L and the declination δ of the sun, as predicted by SUNLOC, with their values, L' and δ', as predicted by a tracking method which assumes a constant orbital angular

Table 3.4

Maximum Deviations in the Ephemerides of the Sun *

	1962	1887	1978
Ecliptic Longitude	20"	22"	32"
Right Ascension	3 sec	2.3 sec	2.2 sec
Declination	12"	14"	15"
Radius Vector	7×10^{-5} A.U.	***	7×10^{-5} A.U.
Equation of Time	17 sec	4 sec	**

* The deviations given here are the differences between the values listed in the Astronomical Ephemeris and the values computed by the "ephemeris generator" computer program in the appendix of this report. Only the largest differences for each year are shown. All results are rounded.

** The A. E. stopped publishing the equation of time in 1965. It now publishes values for the "ephemeris time of ephemeris transit."

*** Only values of the logarithm of the radius vector are given in the 1887 edition of the American Ephemeris and Nautical Almanac.

velocity for the sun. Use the term sun(Kepler)to describe the point on the celestial sphere which SUNLOC locates. (We do not imply, however, that the correction for the eccentricity of the sun's orbit is the only difference between the computer program SUNLOC and a tracking method which assumes a constant orbital angular velocity for the sun. Indeed, in the following studies we have used HIPREC = .TRUE. and LOPREC = .FALSE. in SUNLOC. See subsection 3.4.3.)

Two different formulas were used to describe the ecliptic longitude L' of a "sun" which appears to move with constant orbital angular velocity:

(3-42a) $L' = \ell = 279°.696678 + 36000.76892\ T + 3.025\times10^{-4}\ T^2$

(3-42b) $L' = 360°N/365.25$

T, d, and D are as defined in (3-20). N is the number of days from March 21; e.g. N=0 on March 21.

Use the term sun(mean) to describe the point on the celestial sphere which is located by a tracking method that uses one of formulas (3-42a) or (3-42b) to calculate the sun's ecliptic longitude. Additionally, we refer to the tracker which uses (3-42a) as model a; similarly, we use the name model b with respect to (3-42b).

Equation (3-42a) is the formula for the ecliptic longitude of the dynamic mean sun. (See subsection 3.2.1.) Figure 3.8 is a plot of the difference ΔL between the sun(Kepler) and the sun(mean). Because $\Delta L = L - L' = L - \ell = (\omega + \upsilon) - (\omega + M) = \upsilon - M$, Figure 3.8 is a plot of the equation of the center (see (3-28)).

In this graph, the length of time between successive points is

seven days. The first day is day 7, or March 28, 1976; the last day plotted is day 364, or March 20, 1977. Thus, the total number of points shown for each model is 52. Each symbol used to plot the data is centered about the location of a data point. On each day, the difference between the ecliptic longitudes is that corresponding to local solar noon for an observer on the Greenwich meridian.

The minimum differences ΔL between the two models occur at about apogee (about day 105, or July 4, 1976) and at about perigee (about day 287, or January 2, 1977). The maximum differences occur on about day 14 (April 4, 1976) and day 196 (October 3, 1976). On these two days, M is approximately 90° and 270°, respectively, and (3-28) gives a difference of 1.9° and -1.9° for these values of M, a result in agreement with Figure 3.8. Furthermore, note the symmetries of Figure 3.8. This curve is very nearly symmetric about perigee and apogee. Also, the heights of the two peaks are about the same, namely, 1.9°.

Figure 3.9 shows the differences $\Delta\delta$ between the values of the solar declination predicted by the two models. The number of points and spacing between points is the same as in Figure 3.8, except that $\Delta\delta$ for day 0 is also plotted. The declination of the sun is zero at the vernal equinox (about day 0, or March 21) and at the autumnal equinox (about day 186, or September 23). At the summer solstice (about day 92, or June 21) and at the winter solstice (about day 276, or December 22), the solar declinations are 23° 27' and -23° 27', respectively. Because the solar declination varies more rapidly around the equinoxes than around the solstices, a given error in the ecliptic longitude will cause

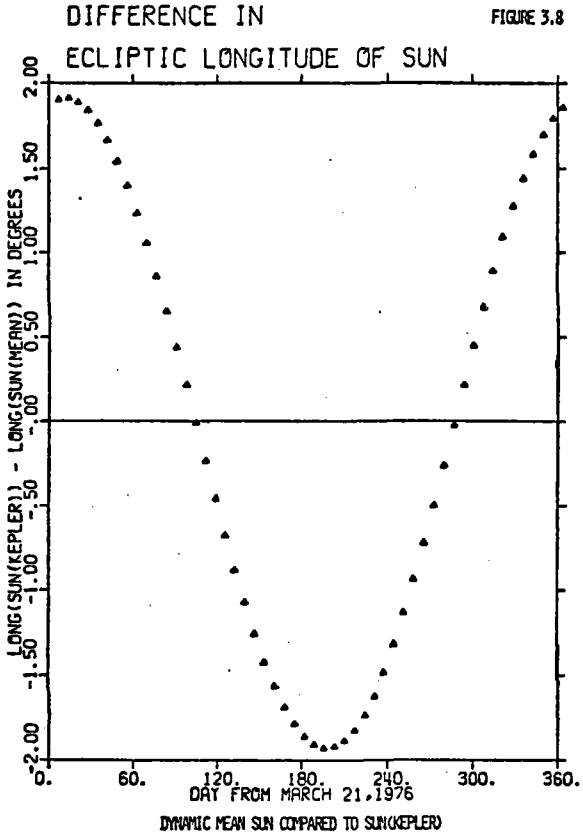

FIGURE 3.8

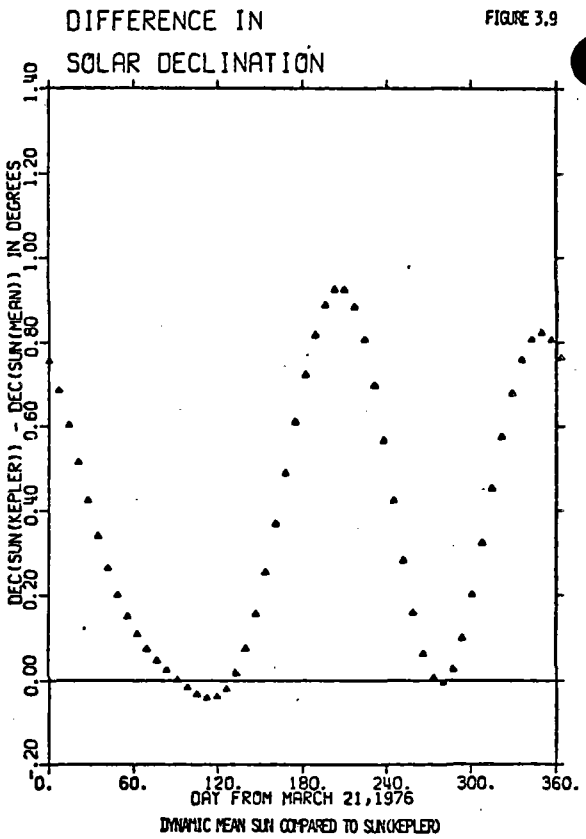

FIGURE 3.9

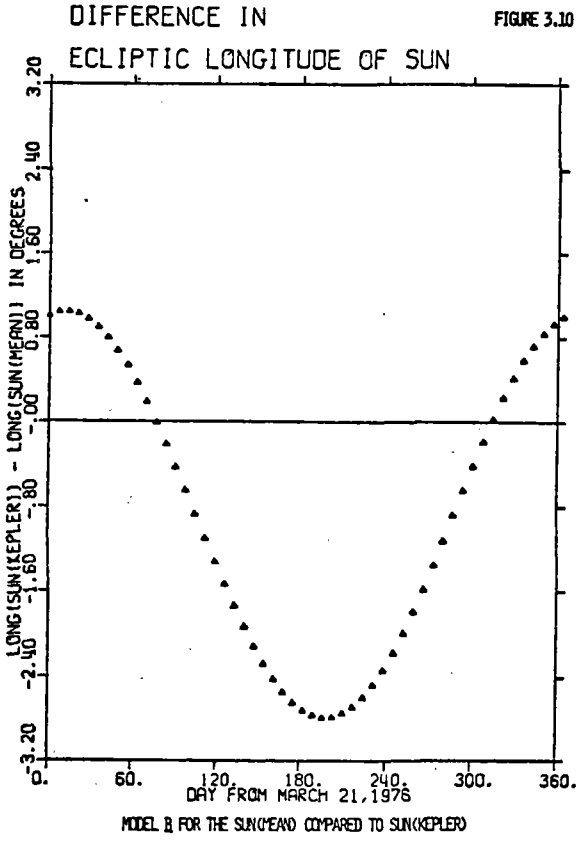

FIGURE 3.10

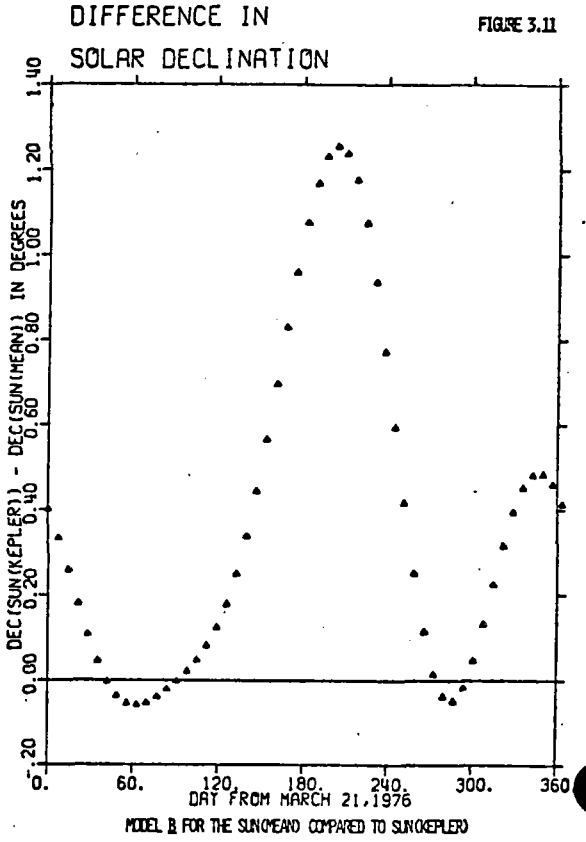

FIGURE 3.11

a larger error in the solar declination around the equinoxes than around the solstices. This effect and the fact that the longitude errors are larger near the equinoxes than near the solstices (Figure 3.8) explain the prominent features of Figure 3.9. The two peaks(of about equal height) occur about at the equinoxes, and the curve passes through zero around the solstices. The maximum differences $\Delta\delta$ are about .93° near day 205 (or October 12, 1976) and .82° near day 350 (or March 6, 1977).

(3-42b) is the formula for the solar longitude that was used here at the University of Houston, prior to this paper's composition, in some of the computer programs for modeling central receiver systems. Note that the vernal equinox (i.e. L' = 0°) always occurs at noon on March 21, regardless of the year or the terrestrial longitude of the observer. Figures 3.10 and 3.11 exhibit the differences between model b and the sun(Kepler). On March 21, 1976 the difference in the values of the ecliptic longitude predicted by the two models is about 1.0°. The first peak of Figure 3.10 occurs on about day 14 and has a height of 1.0°; there is another peak on about day 196 which has a height of -2.8°. The main peak in Figure 3.11 occurs on about day 204 and has a height of 1.25°; there is a peak on about day 347 which has a height of .49°.

Comparing Figures 3.8 and 3.10, one concludes that a change in the date on which the sun(mean) and sun(Kepler) coincide translates the graph of ΔL a distance down the vertical axis. To see this, note that, since each of models a and b describe a "sun" with constant orbital angular velocity, we must have $L' = \ell + c$, where c is a constant for each model. For example, c=0° for model a. Hence,

(continued on next page)

$$\Delta L = L - L' = L - \ell - c$$
$$= (\omega+\upsilon) - (\omega+M) - c$$

$$(3\text{-}43) \quad \Delta L = (\upsilon - M) - c$$
$$\simeq 2e \sin M - c$$

where the last step follows from (3-28).

Therefore, ΔL is approximately a periodic function of M. A change in the time of coincidence of the sun(mean) and sun(Kepler) translates the graph of this periodic function along the vertical axis. Consequently, the difference between the two peaks of the graph will be about 3.8°.

Throughout the remainder of subsection 3.4.4, discussion will be limited to a comparison of model b with the SUNLOC program. Hence, we will only use the term sun(mean) to designate the point on the celestial sphere which is located by a tracking method that uses formula (3-42b) to calculate the sun's ecliptic longitude L'. We will find that the graphs of the difference in the insolation predicted by the two sun models versus day of the year will resemble Figure 3.11. If, instead, one wished to use model a for the sun(mean), then the graphs of the difference in the predicted insolation versus day of the year would resemble Figure 3.9.

· Changes in the Solar Intensity versus Time of Day

Figures 3.12 and 3.13 illustrate the effect of different tracking methods on the intensity of sunlight reaching the earth's surface. Figure 3.12 is a plot of the direct normal intensity I_{Dn} received at sea level on day 224 from March 21, 1976 - i.e. on October 31, 1976. The

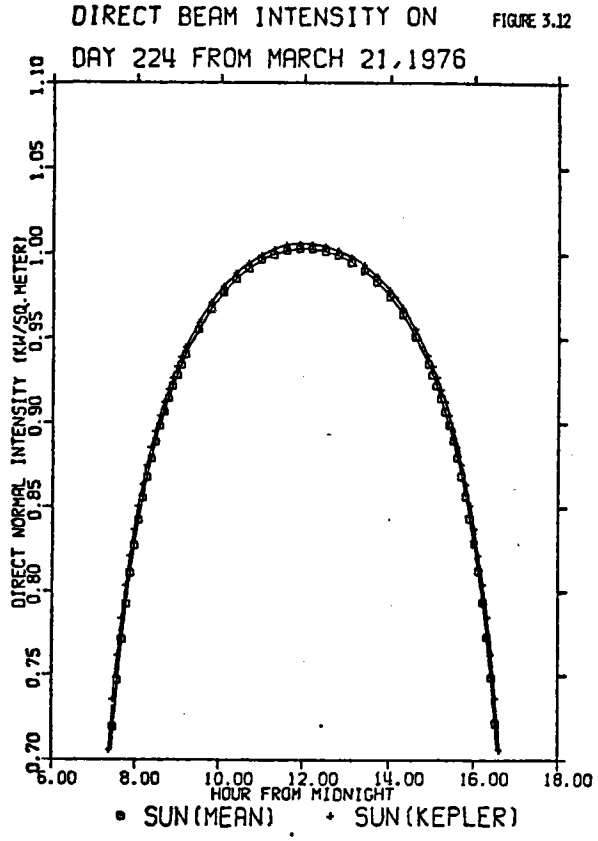

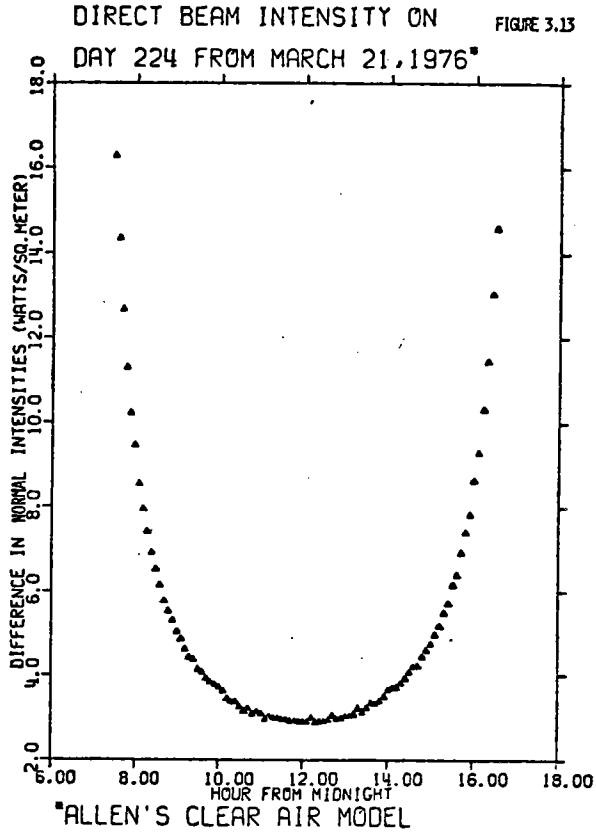

Figure 3.14 *

The Relative Air Mass m_r is a Function of the Solar Altitude h

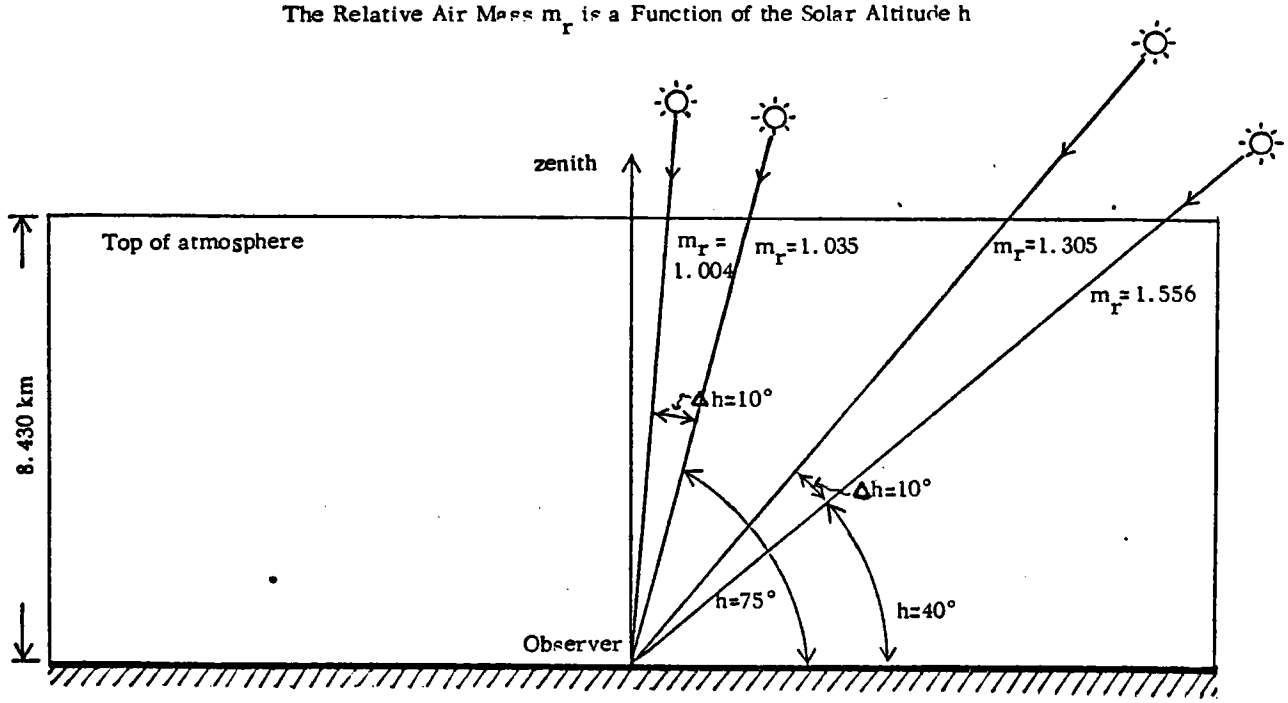

* For a given altitude h, let m(h) be the mass of air through which sunlight must pass to reach the earth's surface. Then $m_r(h)=m(h)/m(90°)$. For a plane, homogeneous atmosphere, $m_r(h)=\csc h=\sec z$.

latitude of the observer is 30° north. The direct normal solar intensity is the intensity of direct solar radiation incident upon a surface which is normal to the incoming radiation. (This implies that an instrument to measure direct normal radiation at the earth's surface would have to track the sun during a day.) Allen's clear air model is the solar intensity model used to generate both curves [36]. These curves only show the intensity for solar altitudes greater than 10°. Figure 3.13 shows the difference ΔI_{Dn} between the values of direct normal intensity predicted using the sun(Kepler) and the sun(mean). Note that the "roughness" of the curve in Figure 3.13 is due to numerical round-off error. In reality, the curve is smooth.

From Figure 3.12, observe that the length of day 224 increases when the sun(Kepler) is used. From Figure 3.13, note that the largest differences in intensity occur near sunrise and sunset. When the sun is low in the sky, the air mass through which sunlight passes is much greater than when the sun is in the zenith. Thus, small changes (or errors) in the sun's altitude have a greater effect on I_{Dn} when the sun is low in the sky because these errors have a greater effect on the relative air mass through which the sunlight must pass. (See Figure 3.14 for an illustration of this effect for a planar atmosphere.)

Table 3.5 gives the percentage errors at selected times during the day. Note that the errors in the solar altitude angle are smaller when the sun is low in the sky, but the differences in the intensity are greater. At hours 8 and 16, the percentage difference is about 1%. At hours 7.5 and 16.5, the difference is about 2%.

TABLE 3.5 *

TIME	ALTITUDE OF SUN(KEPLER)	SUN(MEAN)	Δ	DIRECT NORMAL INTENSITY SUN(KEPLER)	SUN(MEAN)	Δ	Δ
HOURS	DEGREES			KW/M²		W/M²	%
7.5	11°29′	10°50′	39′	.7419	.7266	15.3	2.1
8.0	17°18′	16°36′	42′	.8397	.8306	9.1	1.1
10.0	37°11′	36°15′	56′	.9784	.9747	3.7	.4
12.0	45°46′	44°41′	1°05′	1.0060	1.0031	2.9	.3
14.0	37°08′	36°15′	53′	.9783	.9747	3.6	.4
16.0	17°14′	16°36′	38′	.8390	.8306	8.4	1.0
16.5	11°24′	10°50′	34′	.7405	.7266	13.9	1.9

* THIS INFORMATION IS FOR DAY 224 FROM MARCH 21,1976 - I.E. FOR OCTOBER 31,1976. MIDNIGHT IS THE HOUR 0.

TABLE 3.6 *

TIME	DIFFERENCE IN INTENSITIES	ΔT	AREA
HOURS	WATTS/M²	HOURS	WATT-HRS/M²
11.00	3.06		
		1.0	½(3.06 + 2.90)(1.0) = 2.98
12.00	2.90		
		1.0	½(2.90 + 3.06)(1.0) = 2.98
13.00	3.06		
			5.96
15.51	6.20		
		.1	½(6.20 + 6.40)(.1) = .63
15.61	6.40		
		.3	½(6.40 + 7.80)(.3) = 2.13
15.91	7.80		
		.3	½(7.80 + 10.26)(.3) = 2.71
16.22	10.26		
		.3	½(10.26 + 14.58)(.3) = 3.73
16.52	14.58		
			9.20
7.377	706.0		
		.054	½(706.0+722.2)(.054)=38.6
7.431	722.2		
		9.138	46.5
16.569	720.7		
		.049	½(720.7+706.1)(.049)=35.0
16.618	706.1		

38.6 + 46.5 + 35.0 = 120.1

32% + 39% + 29% = 100%

*DAY IS OCTOBER 31, 1976. HORIZON IS 10° ABOVE ASTRONOMICAL HORIZON.

Similarly, the differences in the amount of energy per meter^2 predicted by the two models is larger around sunrise and sunset than around noon. Table 3.6 shows trapezoidal rule integrals for various time intervals during day 224. The horizon is 10° above the astronomical horizon. From Figure 3.12, we again note that day 224 is about .1 hour longer when the sun(Kepler) is used. During this .1 hour, we agree that no energy is received from the sun(mean), but that 38.6 + 35.0 = 73.6 watt-hrs per meter^2 of energy is received from the sun(Kepler). Hence, we have introduced an important convention here - namely, when the sun is below the given cut-off elevation (10° in the above case), we receive no energy from it. This represents a generalized definition of sunrise and sunset. For a 10° horizon, we observe from Table 3.6 that 32 + 29 = 61% of all the extra energy received from the sun(Kepler) on day 224 results from the increased length of daylight. Of course, for a 0° horizon, the percentage of extra energy received during the period of extra daylight is much less. (Furthermore, note that the difference in predicted daily energy is about the same [about 118 watt-hrs/m^2] for both the 0° and 10° horizons.)

How are the preceding results altered for a latitude other than 30° north ? As we have found, small changes (or errors) in the sun's position affect the direct normal radiation more when the sun is low in the sky. We know that the sun is closer to the horizon for latitudes greater than 30° north. Thus, for more northerly latitudes, the differences between the two sun models increase. At latitudes where the sun is higher in the sky, the difference in the predicted daily direct nor-

mal energy densities (ΔE_{Dn}) is less.

Up to this point, we have discussed only direct normal solar radiation. Direct horizontal intensity is the intensity of direct radiation incident upon a horizontal surface. What effects does an improved tracker have on direct horizontal solar intensity predictions ?

Figure 3.15 displays the answer for 30° north latitude on October 31, 1976. The curves in Figure 3.15 only show the differences in intensity for solar altitudes greater than 10°. Note that the "roughness" of the curve in Figure 3.15 is due to numerical round-off error. In reality, the curve is smooth.

Direct horizontal intensity I_{Dh} is related to the direct normal intensity I_{Dn} by the formula:

$$(3\text{-}44) \quad I_{Dh} = I_{Dn} \cos z = I_{Dn} \sin h$$

where z is the zenith distance of the sun and $h = 90° - z$ is the solar altitude. We are distinguishing between the direct horizontal solar intensity I_{Dh} and the total horizontal solar intensity I_{Th}. These are related by the formula:

$$(3\text{-}45) \quad I_{Th} = I_{Dh} + I_{dh}$$

where I_{dh} is the intensity of diffuse solar radiation incident on a horizontal surface [37]. In general, I_{Dn} is not a linear function of sin h and varies much less rapidly with sin h than would a linear function. Hence, we expect small errors in h to affect I_{Dh} more than I_{Dn}. This is exactly what we observe in Figure 3.15. Throughout the course of day 224, the difference $\Delta I_{Dh} = I^k_{Dh} - I^m_{Dh}$ is larger than 9.6 watts/m^2. (The

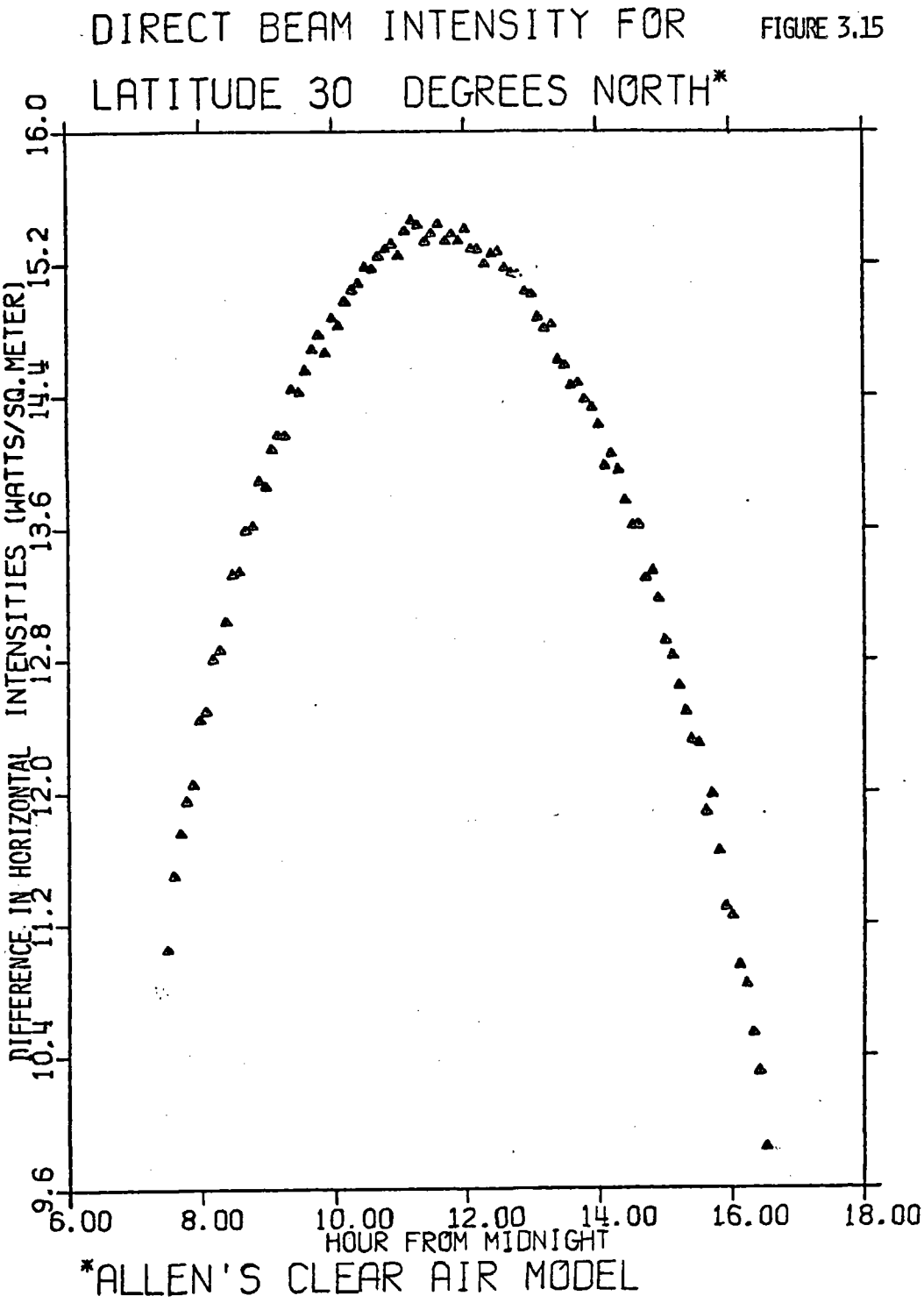
DIRECT BEAM INTENSITY FOR
LATITUDE 30 DEGREES NORTH*
DIFFERENCE IN HORIZONTAL INTENSITIES (WATTS/SQ.METER)
16.0
15.2
14.4
13.6
12.8
12.0
11.2
10.4
9.6
6.00
8.00
10.00
12.00
14.00
16.00
18.00
HOUR FROM MIDNIGHT
*ALLEN'S CLEAR AIR MODEL

FIGURE 3.15

superscript k indicates the sun(Kepler), while the superscript m refers to the sun(mean).) In contrast, the difference ΔI_{Dn} is less than 4.0 watts/m^2 during a significant length of time around noon. At noon, the the percentage difference in the predicted horizontal intensities is about 15.4/720 = 2.1%, whereas at sunrise the percentage difference is about 11.0/130 = 8.5%. The differences ΔE_{Dh} between the integrals of the direct horizontal solar radiation are 139 watt-hrs/m^2 , or 2.9%, for a 0° horizon and 139 watt-hrs/m^2, or 3.0%, for a 10° cut-off elevation.

From Figure 3.15, we observe that the largest difference ΔI_{Dh} occurs at noon instead of near sunrise and sunset. (Compare Figure 3.13.) Again, the reason for this behavior is that the direct horizontal is affected more by errors in the solar altitude h than is the direct normal.

To conclude this section, we note an important implication of the preceding analysis. Often, one wishes to determine the diffuse intensity I_{dh} from (3-44) and (3-45), where I_{Th} and I_{Dn} are measured quantities and h is calculated.

$$(3\text{-}46) \quad I_{dh} = I_{Th} - I_{Dh} = I_{Th} - I_{Dn} \sin h$$

Since $I_{Th}$and I_{Dn} are measured quantities, an error Δh in the sun's calculated position produces an error $\Delta I_{Dh} = I_{Dn}[\Delta(\sin h)]$ in the value for I_{dh}. We can use Table 3.5 to estimate the magnitude of ΔI_{Dh}. Thus, Allen's clear air model predicts that, at noon, ΔI_{Dh} = 13.3 watts/m^2. Now, on a fairly clear day, typical values of I_{dh} can range from 0 to about 200 watts/m^2. Consequently, even at noon, the error in I_{dh} can

be 13.3/200 = 7%, or greater. Thus, a given error in locating the sun's position affects values of I_{dh} more than I_{Dn} or I_{Dh}.

· Changes in the Energy Density versus Day of the Year

Figure 3.16 shows the difference in the direct normal insolation predicted by the two sun models versus day of the year. This plot is for 30° north latitude and for a 10° cut-off elevation. Note the similarities between Figure 3.16 and Figure 3.11. The maximum differences ΔE_{Dn} between the energy densities predicted by the sun(mean) tracker and SUNLOC occur around day 214 and day 340. On day 214, the difference in predicted energy is 126 watt-hrs/m^2, and the energy density received(E^k_{Dn}) is about 9.0 KWH/m^2. Thus, the percentage difference is 126/9000 = 1.4%. On day 340, ΔE_{Dn} is 48 watt-hrs/m^2, and E^k_{Dn} is about 9.2 KWH/m^2.(The superscript k refers to the sun(Kepler).) Thus, the percentage difference is 48/9200 = .5%. Furthermore, for a period of about 60 days (from day 176 to day 240), the difference in predicted energy is greater than 80 watt-hrs/m^2. During this time, the percentage difference is greater than .8%.

A graph of the difference in the direct horizontal insolation versus day of the year was also made. Again, this plot was for 30° north latitude and for a 10° cut-off elevation. The maximum differences ΔE_{Dh} between the daily horizontal energy densities predicted by the sun(mean) tracker and SUNLOC were found to occur around day 210 and day 343. On day 210, we discovered that the difference in predicted energy is 155 watt-hrs/m^2 and that the value E^k_{Dh} of the horizontal energy density is about 5.2 KWH/m^2. Thus, the percentage difference is 155/5200 = 3.0%.

FIGURE 3.16

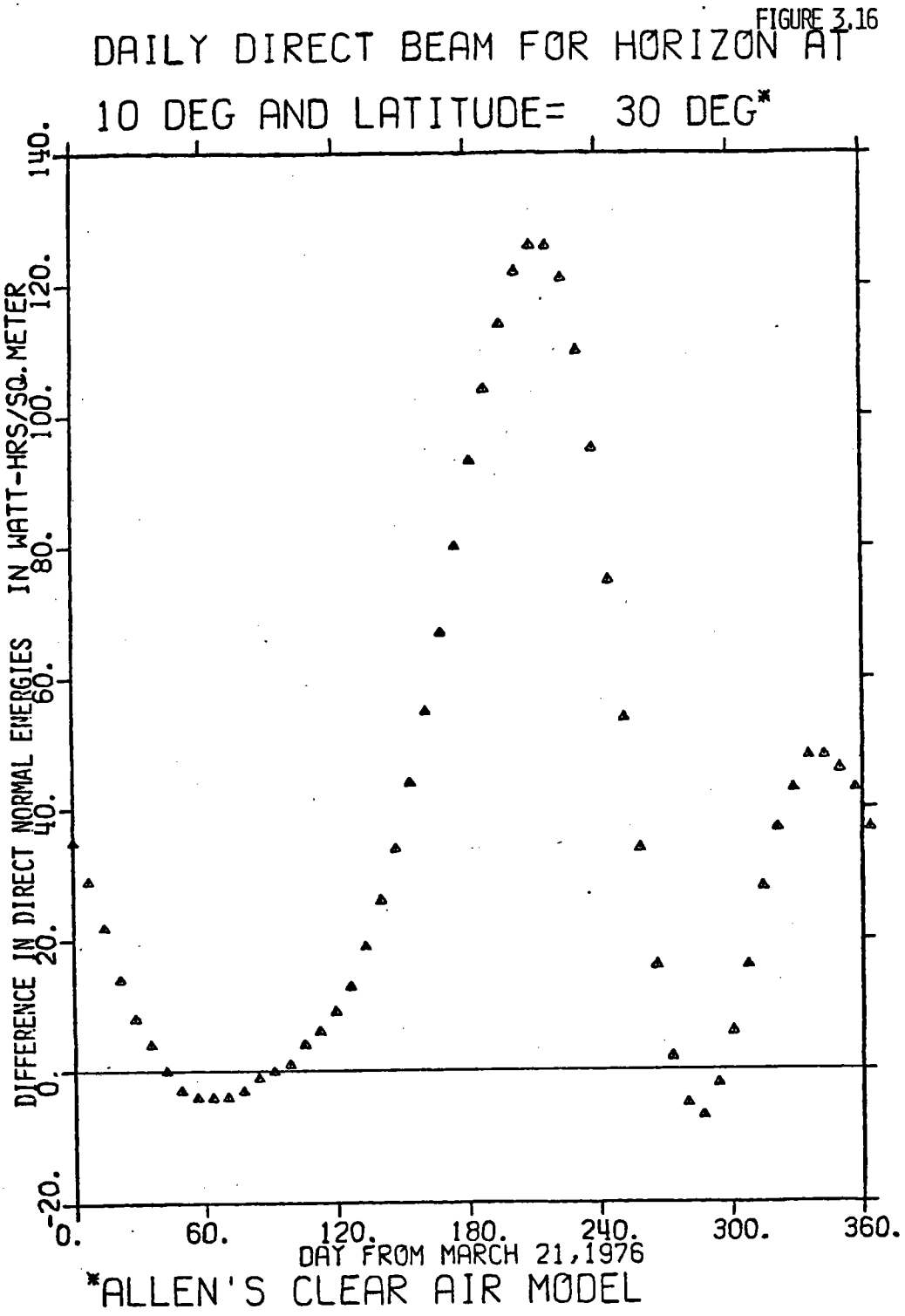
DAILY DIRECT BEAM FOR HORIZON AT
10 DEG AND LATITUDE= 30 DEG*
DIFFERENCE IN DIRECT NORMAL ENERGIES IN WATT-HRS/SQ.METER
140.
120.
100.
80.
60.
40.
20.
0.
-20.
0.
60.
120.
180.
240.
300.
360.
DAY FROM MARCH 21,1976
*ALLEN'S CLEAR AIR MODEL

For day 343, we found that ΔE_{Dh} is 60 watt-hrs/m^2, and E^k_{Dh} is 5.4 KWH/m^2. Thus, the percentage difference is 60/5400 = 1.1%. Additionally, the difference ΔE_{Dh} is greater than 80 watt-hrs/m^2 for about three months, and, during this time, the percentage difference is greater than 1%.

Note that, as discussed in previous sections, all of these results are affected by the particular formula chosen for the ecliptic longitude of the sun(mean), the latitude and longitude of the observer, the cut-off elevation, and the year.

· Predictions of the Annual Insolation

One obtains the annual insolation by integrating the daily energy density over one year. Recall that we have not included weather effects in any of the solar radiation predictions. All predictions represent upper bounds; all quantities have been calculated assuming clear weather for the entire year.

Table 3.7 shows annual statistics (of the direct normal energy received at sea level) as predicted by the SUNLOC computer program. Table 3.8 gives similar annual statistics as predicted by the sun(mean) tracker. In these tables, we show averages of the years 1976, 1977, 1978, and 1979. Thus, the annual statistics are for a year having 365.25 days. The results are presented as a function of north latitude and cut-off elevation. For each model, two similar tables were also prepared giving the annual number of hours of sunlight and the annual direct horizontal energy density versus north latitude and cut-off elevation. For 30° north latitude and for two cut-off elevations, 0° and 10°, let us consider the results indicated by these six tables.

TABLE 3.7 Annual Statistics : SUNLOC Tracker & Allen's Clear Air Model

TABLE OF ANNUAL DIRECT NORMAL INSOLATION IN MWH/M2 **** ROW ENTRIES FOR GIVEN LATITUDE **** COLUMN ENTRIES FOR GIVEN CUT-OFF ELEVATION

	0	5	10	15	20	25	30	35	40	45	50	55	60	65	70	75
0	3.955	3.882	3.727	3.537	3.324	3.099	2.863	2.619	2.367	2.107	1.837	1.557	1.257	0.913	0.498	0.266
5	3.952	3.879	3.723	3.532	3.319	3.092	2.855	2.609	2.354	2.092	1.818	1.530	1.211	0.843	0.552	0.277
10	3.943	3.869	3.711	3.516	3.301	3.071	2.829	2.578	2.317	2.044	1.756	1.435	1.064	0.790	0.555	0.337
15	3.927	3.852	3.691	3.491	3.271	3.034	2.785	2.524	2.250	1.958	1.629	1.246	0.966	0.728	0.521	0.338
20	3.905	3.827	3.662	3.456	3.226	2.980	2.719	2.442	2.145	1.808	1.410	1.119	0.871	0.654	0.465	0.304
25	3.875	3.794	3.621	3.406	3.166	2.905	2.626	2.323	1.977	1.564	1.260	0.999	0.770	0.567	0.394	0.245
30	3.836	3.753	3.570	3.342	3.086	2.805	2.497	2.141	1.713	1.395	1.121	0.878	0.660	0.471	0.307	0.170
35	3.788	3.699	3.505	3.259	2.981	2.669	2.305	1.861	1.529	1.240	0.982	0.749	0.544	0.362	0.207	0.076
40	3.729	3.634	3.421	3.153	2.841	2.469	2.011	1.664	1.360	1.086	0.837	0.615	0.415	0.242	0.091	0.
45	3.655	3.551	3.317	3.013	2.637	2.167	1.805	1.485	1.193	0.927	0.687	0.469	0.276	0.106	0.	0.
50	3.565	3.449	3.179	2.810	2.332	1.955	1.618	1.308	1.022	0.762	0.524	0.312	0.121	0.	0.	0.
55	3.451	3.317	2.984	2.510	2.122	1.765	1.435	1.126	0.845	0.584	0.350	0.137	0.	0.	0.	0.
60	3.310	3.138	2.707	2.311	1.936	1.580	1.246	0.938	0.652	0.392	0.154	0.	0.	0.	0.	0.
65	3.142	2.920	2.539	2.143	1.757	1.391	1.051	0.733	0.442	0.175	0.	0.	0.	0.	0.	0.
70	3.096	2.847	2.425	1.995	1.582	1.196	0.836	0.505	0.200	0.	0.	0.	0.	0.	0.	0.
75	3.126	2.934	2.394	1.875	1.411	0.983	0.593	0.235	0.	0.	0.	0.	0.	0.	0.	0.
80	3.150	2.973	2.542	1.840	1.243	0.740	0.291	0.	0.	0.	0.	0.	0.	0.	0.	0.
85	3.163	2.989	2.588	2.028	1.132	0.418	0.	0.	0.	0.	0.	0.	0.	0.	0.	0.
90	3.171	2.979	2.562	2.062	1.335	0.	0.	0.	0.	0.	0.	0.	0.	0.	0.	0.

TABLE 3.8 Annual Statistics : Sun(mean) Tracker & Allen's Clear Air Model

TABLE OF ANNUAL DIRECT NORMAL INSOLATION IN MWH/M2 **** ROW ENTRIES FOR GIVEN LATITUDE **** COLUMN ENTRIES FOR GIVEN CUT-OFF ELEVATION

	0	5	10	15	20	25	30	35	40	45	50	55	60	65	70	75
0	3.955	3.882	3.727	3.535	3.324	3.098	2.862	2.618	2.365	2.104	1.835	1.554	1.253	0.907	0.491	0.260
5	3.950	3.877	3.721	3.528	3.316	3.089	2.851	2.605	2.350	2.087	1.812	1.523	1.201	0.830	0.541	0.270
10	3.938	3.864	3.707	3.512	3.296	3.065	2.823	2.572	2.310	2.036	1.746	1.422	1.047	0.775	0.543	0.329
15	3.921	3.845	3.685	3.484	3.263	3.026	2.776	2.515	2.239	1.946	1.614	1.227	0.948	0.714	0.510	0.332
20	3.896	3.819	3.653	3.447	3.216	2.970	2.708	2.430	2.131	1.791	1.388	1.098	0.854	0.641	0.456	0.300
25	3.864	3.783	3.611	3.394	3.153	2.892	2.612	2.307	1.958	1.540	1.236	0.980	0.755	0.557	0.389	0.243
30	3.823	3.739	3.556	3.328	3.071	2.789	2.479	2.120	1.686	1.369	1.099	0.860	0.648	0.465	0.304	0.168
35	3.772	3.683	3.488	3.242	2.963	2.649	2.280	1.831	1.500	1.216	0.963	0.735	0.537	0.359	0.205	0.076
40	3.709	3.614	3.402	3.132	2.818	2.442	1.979	1.633	1.334	1.065	0.822	0.607	0.412	0.240	0.091	0.
45	3.632	3.530	3.293	2.987	2.608	2.132	1.771	1.456	1.171	0.910	0.678	0.465	0.274	0.106	0.	0.
50	3.537	3.422	3.151	2.778	2.294	1.919	1.587	1.283	1.004	0.753	0.520	0.310	0.121	0.	0.	0.
55	3.419	3.285	2.949	2.470	2.083	1.732	1.407	1.106	0.834	0.579	0.347	0.136	0.	0.	0.	0.
60	3.271	3.098	2.663	2.269	1.899	1.550	1.224	0.927	0.646	0.390	0.154	0.	0.	0.	0.	0.
65	3.094	2.871	2.493	2.103	1.724	1.367	1.038	0.726	0.439	0.174	0.	0.	0.	0.	0.	0.
70	3.042	2.795	2.380	1.958	1.554	1.182	0.828	0.502	0.200	0.	0.	0.	0.	0.	0.	0.
75	3.070	2.882	2.351	1.843	1.393	0.974	0.589	0.234	0.	0.	0.	0.	0.	0.	0.	0.
80	3.090	2.920	2.500	1.818	1.232	0.735	0.290	0.	0.	0.	0.	0.	0.	0.	0.	0.
85	3.104	2.935	2.555	2.009	1.125	0.417	0.	0.	0.	0.	0.	0.	0.	0.	0.	0.
90	3.121	2.962	2.557	2.060	1.335	0.	0.	0.	0.	0.	0.	0.	0.	0.	0.	0.

The difference in the annual number of hours of sunlight is 4394 - 4383 = 11, or 11/4394 = .2%, for a 0° horizon; similarly, 3797 - 3785 = 12, or .3%, for a 10° horizon. The difference in the annual direct normal energy density is 3.836 - 3.823 = .013 MWH/m^2, or .3%, for a 0° horizon; similarly, 3.570 - 3.556 = .014 MWH/m^2, or .4%, for a 10° horizon. The difference in the annual direct horizontal energy density is 2.266 - 2.250 = .016 MWH/m^2, or .7%, for a 0° horizon; similarly, for a 10° horizon, the difference is 2.237 - 2.221 = .016 MWH/m^2, or .7%.

In the above cases, a more accurate solar tracker has a small effect on predictions of the annual direct normal energy density. As we have seen, though, the main effect of a more accurate tracker is to add significant extra energy during two or three months of the year.(Figure 3.16) Indeed, if one is interested in predicting the direct normal intensity as a function of time of day, then the effects of a more precise sun tracker are not negligible around sunrise and sunset. (Table 3.5) The effects on predictions of the direct horizontal and diffuse intensities as a function of time of day are greater.

3.4.5 Conclusions and Recommendations

- The I.A.U. system of astronomical symbols and sign conventions should be followed in all reports which use standard astronomical terms. In the computer programs for the central receiver, for example, the positive direction for the azimuth angle of the sun should be changed so as to agree with the I.A.U. convention. (See subsection 3.1.1.)

- Alterations were made on some of the computer programs which are used here at the University of Houston to model central receiver systems. These alterations take into account the eccentricity of the sun's orbit. These corrections are based on methods described in this report.

- Apparent solar time (modified so that midnight is the hour 0) is the most convenient time system to use when predicting the position of the sun as a function of time. (Of course, apparent solar time must first be calculated from the mean time if observations are to be made.) However, the computer programs, which are used in modeling central receiver systems, do not have incorporated in them a clear distinction between solar time and mean time. Further, no allowance is made for the difference between local time and Universal time when calculating the sun's position in its apparent orbit. On the other hand, these problems are dealt with correctly in the subprogram SUNLOC.

- The maximum difference between the values of the solar declination predicted by SUNLOC and those given in the A.E. is 15", for the years 1962, 1887, and 1978. Using SUNLOC (with LOPREC = .FALSE.), the approximate maximum error in predicting the sun's position should be 24", disregarding atmospheric refraction. Similarly, the approximate maximum error in the ecliptic longitude should be about 41".

- Further improvements on the solar tracker are possible. Methods for eliminating some of the errors

listed in Table 3.3 might be found in the more advanced literature of spherical astronomy and celestial mechanics [38,39]. However, one pays a price for improved accuracy. In this case, the price is longer computer programs and greater execution times.

- A more precise sun tracker such as SUNLOC has a significant effect on predictions of the daily amounts of solar energy received at the earth's surface. For 30° north latitude, between 1 and 1.5% extra direct normal solar energy per day is predicted for a period of two months during autumn. These figures result from a comparison of the SUNLOC program with a sun(mean) tracker (namely, with model b of subsection 3.4.4). Most of this extra energy is received near the hours of sunrise and sunset, when the sun is low in the sky. This effect is greater for more northerly latitudes. In comparison, recall that the distance between the earth and sun varies from a(1-e) to a(1+e), or ±1.7%. This causes a variation in the solar intensity of ±3.4%.

- One may ask whether a program such as SUNLOC, which calculates the sun's position at any instant, is more useful than a table of sun locations, from which one interpolates the sun's position for a given time. For the guidance of heliostats in a central receiver system, a tabular approach might be the most useful. Each morning, the master computer could calculate the solar altitudes and azimuths for the day, storing the rectangular horizon coordinates on a disk or tape. To demonstrate, this would only require storing

some 129,600 numbers for a twelve-hour day, with a one second time interval between consecutive entries in the table. However, for research and modeling purposes, where the times used are subject to frequent changes, direct recourse to a tracking program is probably more useful. Of course, these are generalizations, and, in practice, such conclusions depend heavily on the methods chosen to solve the complex programming problems encountered in modeling central receiver systems.

Definitions of Variables for the Subroutine Sunloc *

Variable Name	Symbol in Report	Description
C(1 to 3)	C_1, C_2, C_3	3 intermediate coefficients, depending only on the day of the year
MNANOM	M	Mean anomaly of the sun
MLONG	λ	Mean ecliptic longitude of the sun
PLONG	ω	Ecliptic longitude of perigee of the sun
SLONG	L	True ecliptic longitude of the sun
PIMATH	π	3.14159265358979
PIMATT	2π	-
PIMAT2	$\pi/2$	-
RAD	$180/\pi$	Conversion factor from radians to degrees
MNANO4	M_4	Mean anomaly(auxillary variable)
SLONG4	L_4	True ecliptic longitude(auxillary variable)
ABERR	-	Planetary aberration in sun's ecliptic longitude
LOPREC	-	If .TRUE.,the elements of the sun's orbit are assumed unchanged. Usually this means that they are assumed to be those for noon of the day JD.
HIPREC	-	If .FALSE.,no improvements are made on the values for the times of rising and setting of the sun
T(1 to 4)	T_1,T_2,T_3,T_4	4 intermediate time variables
JD	J_D or J.D.	Julian Day number for noon of civil day on which sun position is to be computed. (Default is 2442859 which is March 21,1976)
TIME1	t_1	Apparent solar time with midnight reckoned as the hour 0.For lack of an accepted name,this will be called midnight(cont'd.)

Variable Name	Symbol in Report	Description
		solar time (MIDST). Default is noon, i.e. 12. TIME1 is the input time variable for entry point MIDST. Also, 0. ≦ TIME1 < 24.
TIME2	t_2	Apparent solar time. Noon is the hour 0. TIME2 is the input time variable for entry point AST. The default value for TIME2 is 0, i.e. noon. Also, 0. ≦ TIME2 < 24.
TIME3	t_3	Same as TIME1 except that TIME3 is an auxillary variable which is only used in the calculation of the times of rising and setting.
XLONG	Λ°	Longitude of observer in degrees. This is an input variable for entry point SUNLOC. The default value for XLONG is +105°.
XLONGT	Λ^h	Longitude of observer in hours. 1 hour= 1^h=15°
XLAT	ϕ°	Latitude of obsever in degrees. XLAT is an input variable for entry points SUNLOC and DAYLIT. 35° is the default value for XLAT.
XL	ϕ	Latitude of observer in radians.
HO	h_0'	Cut-off altitude of sun in degrees. The times of rising and setting are those times at which the sun crosses the parallel of altitude HO. By definition, HO>0. The default value of HO is 10°. HO is an input variable for entry points SUNLOC and DAYLIT.
H1	h_1'	Cut-off altitude of sun in radians.
ID	-	=1 to determine all sun coordinates =0 to determine only those sun coordinates necessary to calculate USUNZ and ESUN. This is an input variable for the entry points MIDST and AST. The default value of ID is 0.
GMAT	G.M.A.T.	Greenwich mean astronomical time. This is mean solar time for 0° longitude. Noon is reckoned as the hour 0.

Variable Name	Symbol in Report	Description
TCENT	T	Julian date for the instant at which the sun's position is to be determined. The Julian date is the Julian Day number plus the fraction of a day that has elapsed since noon.
TCENT4	T_{c4}	Same as TCENT except that TCENT4 is used in the rise and set times calculation.
OBLIQ	ε	Obliquity of the ecliptic
ECENT	e	Eccentricity of the earth's orbit
TIME	t	Apparent solar time. Same as TIME2 except that TIME is the local variable which is actually used in the calculations in MIDST and AST.
TIME4	t_4	Same as TIME except that TIME4 is used in the rise and set times calculation.
ET	E	Equation of time
EC	E_c	Equation of the center: $E_c=\upsilon-M$
EC4	E_{c4}	Equation of the center(auxillary variable used in the rise and set times calculation)
SDEC	δ	Solar declination angle
SDEC1	δ_1	Solar declination at apparent solar noon
SDEC4	δ_4	Solar declination angle(auxillary variable used in the rise and set times calculation)
ONEPNT	-	ONEPNT is set to -1. normally. However , if the sun intersects the parallel of altitude HO at only one time on the day JD,then ONEPNT is assigned the value of the time at which this intersection occurs. In effect, this time is both the rise and set time for the day JD.
RISTIM	t_R	The time at which the sun rises above the parallel of altitude HO.

Variable Name	Symbol in Report	Description
SETTIM	t_S	The time at which the sun sets below the parallel of altitude HO.
DAY	D	The length of time in hours that the sun is above the parallel of altitude HO.
HAI	H	Hour angle of the sun
HAI4	H_4	Hour angle of the sun(auxillary variable used in the rise and set times calculation)
USUNX,USUNY, USUNZ	x'/R , y'/R , z'/R	Rectangular horizon coordinates of the sun
USUNZ4	z'_4/R	Same as USUNZ except that USUNZ4 is an auxillary variable used only in the rise and set times calculation.
ESUN,ZSUN	h,A	Polar horizon coordinates of the sun. h is the solar altitude(elevation) angle. A is the solar azimuth angle.
ESUN1	h_1	Solar altitude angle at noon
ESUN4	h_4	Solar altitude angle(auxillary variable used only in the rise and set times calculation)
DH1	$\Delta_1 h$	The difference between the solar altitude at time t_R and the solar altitude h'_0.DH1 is in degrees.
DH2	$\Delta_2 h$	The difference between the solar altitude at time t_S and the solar altitude h'_0.DH2 is in degrees.
DT1	$\Delta_1 t$	The difference between the improved value of t_R and its initial approximation. DT1 is in hours.
DT2	$\Delta_2 t$	The difference between the improved value of t_S and its initial approximation.DT2 is in hours.
RASUN	α	Right ascension of the sun
S_1	-	Intermediate test variable

Variable Name	Symbol in Report	Description
Y	y	$y=\tan^2 \varepsilon/2$
SM,SL,CL,CM,SM2	-	Intermediate variables. SM=sin M , SL=sin 2l , CL=cos 2l , CM=cos M , SM2=sin 2M=2*SM*CM
SM4,CM4,SM24	-	Intermediate variables used only in the rise and set times calculation. SM4=sin M_4 , CM4= cos M_4 , SM24=2*SM4*CM4
EARTH	R/a	Distance from the earth to the sun in astronomical units(A.U.)
SD,CD,SD1,CD1	-	Intermediate variables. SD=sin δ, CD=cos δ, SD1=sin δ_1, CD1=cos δ_1
SD4,CD4	-	Intermediate variables used only in the rise and set times calculation. SD4=sin δ_4, CD4=cos δ_4
COPY	-	Intermediate variable for storing copies of a variable.
CHC	-	CHC=cos H_c ,where H_c is the improved approximation to the hour angle of rising. It is also used later for the set time calculation,where H_c is the improved approximation to the hour angle of setting.
IND	-	Intermediate variable used to indicate which of C_1or C_2 and T_1or T_2 to use.
IND4	-	Same as IND except that IND4 is only used in the rise and set times calculations.
CH	-	CH=cos H
CH4	-	CH4=cos H_4
ST	θ	Local sidereal time

* All angles are in radian measure unless the units are specifically given as otherwise.

Intermediate variables are those variables which are used only to store results of a calculation for later reference.

The values of the input variables(JD,TIME1(or TIME2),XLONG,XLAT,HO,ID,LOPREC,and HIPREC) are not changed by this subprogram.

SUNLOC Subprogram

```
      BLOCK DATA
      DOUBLE PRECISION MNANOM,MLONG,PLONG,SLONG,PIMATH,PIMATT,
     C PIMAT2,RAD,ABERR
      LOGICAL LOPREC,HIPREC
      COMMON/SLC/JD,TIME1,TIME2,XLONG,XLAT,HO,ID,LOPREC,HIPREC,PIMATH,
     C PIMATT,PIMAT2,RAD,GMAT,TCENT,MNANOM,MLONG,PLONG,OBLIQ,ECENT,
     C SLONG,ABERR,TIME,ET,EC,SDEC,SDEC1,ONEPNT,RISTIM,SETTIM,DAY,HAI,
     C USUNZ,ESUN,USUNX,USUNY,ZSUN,DH1,DT1,DH2,DT2,RASUN,ST,ESUN1,
     C EARTH
      DATA PIMATH,RAD/3.1415926535897900,57.295779513082380/
      DATA PIMATT,PIMAT2/6.2831853071795800,1.5707963267948950/
      DATA ID,LOPREC,HIPREC/0,.FALSE.,.TRUE./
      DATA XLONG,XLAT,HO/105.,35.,10./
      DATA JD,TIME1,TIME2/2442859,12.,0./
      END
```

SUNLOC Subprogram

```
      SUBROUTINE SUNLOC
C *** PROGRAM INITIALIZATIONS
      DOUBLE PRECISION C(3),MNANOM,MLONG,PLONG,SLONG,PIMATH,PIMATT,
     C PIMAT2,RAD,MNANO4,SLONG4,ABERR,TCENT1
      LOGICAL LOPREC,HIPREC
      DIMENSION T(4)
C *** SUNLOC AND DAYLIT FIND THE TIMES OF RISING AND SETTING OF THE
C      SUN WITH RESPECT TO THE PARALLEL OF ALTITUDE HO. DAYLIT CAN
C      BE USED TO RE-EVALUATE THESE QUANTITIES FOR AN
C      OBSERVER AT ANOTHER LATITUDE OR FOR A DIFFERENT CUT-OFF
C      ALTITUDE HO. SUNLOC MUST ALWAYS BE EXECUTED FIRST WHENEVER
C      A NEW VALUE OF EITHER JD OR XLONG IS SUPPLIED. THEN, MIDST
C      (AST) LOCATES THE SUN'S POSITION AT TIME1 (TIME2) OF DAY JD.
      COMMON/SLC/JD,TIME1,TIME2,XLONG,XLAT,HO,ID,LOPREC,HIPREC,PIMATH,
     C PIMATT,PIMAT2,RAD,GMAT,TCENT,MNANOM,MLONG,PLONG,OBLIQ,ECENT,
     C SLONG,ABERR,TIME,ET,EC,SDEC,SDEC1,ONEPNT,RISTIM,SETTIM,DAY,HAI,
     C USUNZ,ESUN,USUNX,USUNY,ZSUN,DH1,DT1,DH2,DT2,RASUN,ST,ESUN1,
     C EARTH
C *** THE INPUT AND OUPUT PARAMETERS OF THIS SUBROUTINE ARE PASSED
C      VIA THE ABOVE COMMON REGION SLC. THE INPUT VARIABLES FOR
C      THIS ROUTINE ARE JD,TIME1(OR TIME2),XLONG,XLAT,HO,ID,
C      LOPREC,AND HIPREC. IF INPUT VALUES ARE NOT SUPPLIED, THE INPUT
C      PARAMETERS ASSUME DEFAULT VALUES AS GIVEN IN THE BLOCK DATA
C      SUBROUTINE. FURTHER INFORMATION ABOUT SUNLOC MAY BE
C      FOUND IN THE DOCUMENTATION FOR THIS PROGRAM.
      DATA S1/1./
      DATA WRAD,HPIMAT/5.7295779E1,1.5707963E0/
C *** FIND APPROX ELEMENTS OF ORBIT FOR NOON OF DAY JD
      ONEPNT=-1.
      XLONGT=XLONG/15.
      GMAT=XLONGT
      T(1)=(FLOAT(JD-2415020))/36525.
      T(2)=(FLOAT(JD-2415020-1))/36525.
      T(3)=GMAT/8.766E5
      TCENT=T(1)+T(3)
      C(1)=358.475845D0+DMOD(3.599904975D4*DBLE(T(1)),360.D0)
      C(2)=358.475845D0+DMOD(3.599904975D4*DBLE(T(2)),360.D0)
      MNANOM=C(1)+(  3.599904975D4*DBLE(T(3)) - DBLE( (1.5E-4
     C +3.33E-6*TCENT)*(TCENT**2) )  )
      MNANOM=DMOD(MNANOM,360.D0)/RAD
      C(3)=279.696678D0+DMOD(3.600076892D4*DBLE(T(1)),360.D0)
      MLONG=C(3) + (  3.600076892D4*DBLE(T(3))
     C + DBLE( 3.025E-4*(TCENT**2) )  )
      MLONG=DMOD(MLONG,360.D0)/RAD
      OBLIQ=(((5.028E-7*TCENT-1.639E-6)*TCENT-.0130125)*TCENT+23.452294
     C)/WRAD
      ECENT=0.01675104-(1.26E-7*TCENT+4.18E-5)*TCENT
C *** EVALUATE EQUATION OF TIME AT NOON ON DAY JD
      Y=(SIN(OBLIQ/2.)/COS(OBLIQ/2.))**2
      SM=SIN(MNANOM)
      SL=SIN(2.*MLONG)
      CL=COS(2.*MLONG)
```

```
      ET=Y*SL-2.*ECENT*SM+4.*ECENT*Y*SM*CL-(Y**2)*SL*CL-1.25*(ECENT**2)
     C *SNGL( SIN(2.*MNANOM) )
      ET=ET*WRAD/15.
C *** RE-EVALUATE SOME OF THE ORBITAL ELEMENTS
      GMAT=XLONGT-ET
      T(3)=GMAT/8.766E5
      TCENT=T(1)+T(3)
      TCENT1=DBLE(TCENT)
      MNANOM=C(1) + (  3.599904975D4*DBLE(T(3))
     C - DBLE( (1.5E-4+3.33E-6*TCENT)*(TCENT**2) )  )
      MNANOM=DMOD(MNANOM,360.D0)/RAD
      PLONG=(((3.33D-6*TCENT1+4.528D-4)*TCENT1+1.719175D0)*TCENT1+
     C 281.220833D0)/RAD
C *** FIND ECLIPTIC LONGITUDE OF SUN AT NOON ON DAY JD
      SM=SIN(MNANOM)
      CM=COS(MNANOM)
      SM2=2.*SM*CM
      XM=SNGL(MNANOM)
      EARTH=1.+((0.5*(1.-COS(2.*XM))-0.375*(COS(3.*XM)-CM)*
     C ECENT)*ECENT-CM)*ECENT
      ABERR=9.937D-5/DBLE(EARTH)
      EC=(((1.083333*SIN(3.*XM)-0.25*SM)*ECENT+1.25*SM2)*ECENT+
     C 2.*SM)*ECENT
      SLONG=DBLE(EC)+MNANOM+PLONG-ABERR
      SLONG=DMOD(SLONG,PIMATT)
C *** COMPUTE SOLAR DECLINATION AT NOON ON DAY JD
      SD=SIN(OBLIQ)*SNGL( DSIN(SLONG) )
      SDEC=ARSIN(SD)
      CD=COS(SDEC)
      SDEC1=SDEC
      SD1=SD
      CD1=CD
      ENTRY DAYLIT
C *** TEST INITIALIZATIONS
      XL=XLAT/WRAD
      SXL=SIN(XL)
      CXL=COS(XL)
      H1=HO/WRAD
      ESUN1=HPIMAT-ABS(XL-SDEC1)
      ESUN2= -HPIMAT + ABS(XL+SDEC1)
C *** DOES SUN EVER RISE ABOVE PARALLEL OF ALTITUDE HO?
      IF(ESUN1 .GT. H1) GO TO 10
      IF((H1-ESUN1) .LT. 1.E-5) ONEPNT=12.
      RISTIM=-1.
      SETTIM=-1.
      DAY=-1.
      GO TO 1000
C *** DOES SUN EVER SET BELOW PARALLEL OF ALTITUDE HO?
   10 IF(ESUN2 .LT. H1) GO TO 20
      IF((ESUN2-H1) .LT. 1.E-5) ONEPNT=0.
      RISTIM=0.
      SETTIM=24.
```

```
      DAY=24.
      GO TO 1000
C *** FIND TIME OF RISING AND SETTING WITH RESPECT TO ALTITUDE HO
   20 SETTIM=ARCOS((SIN(H1)-SXL*SD1)/(CXL*CD1))
      SETTIM=SETTIM*WRAD/15.
      DAY=2.*SETTIM
      RISTIM=12.-SETTIM
      SETTIM=12.+SETTIM
C *** IS HIGHER PRECISION DESIRED FOR RISTIM AND SETTIM?
      IF(.NOT. HIPREC) GO TO 1000
C *** INITIALIZATIONS
      DH1=0.
      DH2=0.
      DT1=0.
      DT2=0.
      TIME3=RISTIM
      N=1
      GO TO 100
C *** POINT OF RETURN FROM "SUBROUTINE 100"
  120 DH1=ESUN4*WRAD-HO
      COPY=RISTIM
      CHC=(SIN(H1)-SXL*SD4)/(CXL*CD4)
      IF(ABS(CHC) .LE. 1.) GO TO 140
      IF(ESUN4 .LE. H1) GO TO 150
      RISTIM=0.
      DT1=-COPY
      GO TO 150
C *** COMPUTE SECOND APPROXIMATION TO RISE TIME
  140 RISTIM=12.-(WRAD/15.)*ARCOS(CHC)
      DT1=RISTIM-COPY
  150 TIME3=SETTIM
      N=2
      GO TO 100
C *** POINT OF RETURN FROM "SUBROUTINE 100"
  130 DH2=ESUN4*WRAD-HO
      COPY=SETTIM
      CHC=(SIN(H1)-SXL*SD4)/(CXL*CD4)
      IF(ABS(CHC) .LE. 1.) GO TO 160
      IF(ESUN4 .LE. H1) GO TO 500
      SETTIM=24.
      DT2=24.-COPY
      GO TO 500
C *** COMPUTE SECOND APPROXIMATION TO SET TIME
  160 SETTIM=12.+(WRAD/15.)*ARCOS(CHC)
      DT2=SETTIM-COPY
  500 DAY=SETTIM-RISTIM
      GO TO 1000
C *** CONVERT MIDNIGHT SOLAR TIME TO APPARENT SOLAR TIME
  100 IF(TIME3 .GE. 12.) GO TO 300
      TIME4=TIME3 + 12.
      IND4=2
      GO TO 310
```

```
  300 TIME4=TIME3-12.
      IND4=1
C *** COMPUTE ELEMENTS AND ALTITUDE AT TIME4
  310 GMAT4=TIME4 + XLONGT - ET
      T(4)=GMAT4/8.766E5
      TCENT4=T(IND4) + T(4)
      MNANO4=C(IND4) + (  3.599904975D4*DBLE(T(4))
     C - DBLE( (1.5E-4+3.33E-6*TCENT4)*(TCENT4**2) )  )
      MNANO4=DMOD(MNANO4,360.D0)/RAD
      SM4=SIN(MNANO4)
      CM4=COS(MNANO4)
      SM24=2.*SM4*CM4
      EC4=(((1.083333*SIN( 3.*SNGL(MNANO4) )-0.25*SM4)*ECENT
     C +1.25*SM24)*ECENT+2.*SM4)*ECENT
      SLONG4=DBLE(EC4)+MNANO4+PLONG-ABERR
      SLONG4=DMOD(SLONG4,PIMATT)
      SD4=SIN(OBLIQ)*SNGL( DSIN(SLONG4) )
      SDEC4=ARSIN(SD4)
      CD4=COS(SDEC4)
      HAI4=TIME4*15./WRAD
      CH4=COS(HAI4)
      USUNZ4=SXL*SD4 + CXL*CD4*CH4
      IF( ABS( 1.-ABS(USUNZ4) ) .LT. 1.E-6 ) USUNZ4=SIGN(S1,USUNZ4)
      ESUN4=ARSIN(USUNZ4)
C *** GO TO 120 IF N=1. GO TO 130 IF N=2.
      GO TO (120,130) ,N
      ENTRY MIDST
C *** USE THIS ENTRANCE IF USING APPARENT SOLAR TIME WITH
C       MIDNIGHT RECKONED AS 0 HOURS.
      IF(TIME1 .GE. 12.) GO TO 30
      TIME=TIME1+12.
      IND=2
      GO TO 50
   30 TIME=TIME1-12.
      IND=1
      GO TO 50
      ENTRY AST
C *** USE THIS ENTRANCE IF USING APPARENT SOLAR TIME WITH
C       NOON RECKONED AS 0 HOURS.
      TIME=TIME2
C *** SET APPROPRIATE INDICATORS
      IF(TIME .GE. 12.) GO TO 40
      IND=1
      GO TO 50
   40 IND=2
C *** CAN THE SUN'S POSITION AT TIME BE DETERMINED SUFFICIENTLY
C       ACCURATELY BY USING THE SUN'S ELEMENTS FOR ANOTHER TIME?
   50 IF(LOPREC) GO TO 70
C *** FIND ELEMENTS OF SUN'S ORBIT FOR TIME ON DAY JD
      GMAT=TIME+XLONGT-ET
      T(3)=GMAT/8.766E5
      TCENT=T(IND)+T(3)
```

SUNLOC Subprogram

```
      MNANOM=C(IND) + (  3.599904975D4*DBLE(T(3))
     C - DBLE( (1.5E-4+3.33E-6*TCENT)*(TCENT**2) )  )
      MNANOM=DMOD(MNANOM,360.D0)/RAD
      SM=SIN(MNANOM)
      CM=COS(MNANOM)
      SM2=2.*SM*CM
      XM=SNGL(MNANOM)
      EARTH=1.+((0.5*(1.-COS(2.*XM))-0.375*(COS(3.*XM)-CM)
     C *ECENT)*ECENT-CM)*ECENT
      EC=(((1.083333*SIN(3.*XM)-0.25*SM)*ECENT+1.25*SM2)*ECENT
     C +2.*SM)*ECENT
      SLONG=DBLE(EC)+MNANOM+PLONG-ABERR
      SLONG=DMOD(SLONG,PIMATT)
      SD=SIN(OBLIQ)*SNGL( DSIN(SLONG) )
      SDEC=ARSIN(SD)
      CD=COS(SDEC)
   70 HAI=TIME*15./WRAD
      CH=COS(HAI)
      USUNZ=SXL*SD+CXL*CD*CH
      IF(ABS( 1.-ABS(USUNZ) ) .LT. 1.E-6) USUNZ=SIGN(S1,USUNZ)
      ESUN=ARSIN(USUNZ)
C *** IS FINDING ESUN ALL THE INFORMATION NEEDED?
      IF(ID .EQ. 0) GO TO 1000
C *** EVALUATE REMAINING HORIZON COORDINATES
      USUNX=CD*SXL*CH-SD*CXL
      USUNY=-1.*SIN(HAI)*CD
      IF( ABS( HPIMAT-ABS(ESUN) ) .GT. 1.E-6 ) GO TO 60
      ZSUN=0.
      GO TO 200
   60 COPY=USUNX/COS(ESUN)
      IF(ABS( 1.-ABS(COPY) ) .LT. 1.E-6) COPY=SIGN(S1,COPY)
      ZSUN=ARCOS(COPY)
      IF(USUNY .LE. 0.) GO TO 200
      ZSUN=SNGL(PIMATT) - ZSUN
C *** CALCULATE SUN'S RIGHT ASCENSION
  200 IF(ABS(CD) .GT. 1.E-6) GO TO 210
      RASUN=0.
      GO TO 220
  210 COPY=DCOS(SLONG)/DBLE(CD)
      IF(ABS( 1.-ABS(COPY) ) .LT. 1.E-6) COPY=SIGN(S1,COPY)
      RASUN=ARCOS(COPY)
      IF( SNGL(SLONG) .LE. SNGL(PIMATH) ) GO TO 220
      RASUN=SNGL(PIMATT) - RASUN
C *** FIND MEAN ECLIPTIC LONGITUDE AND LOCAL SIDEREAL TIME
  220 MLONG=DMOD(MNANOM+PLONG,PIMATT)
      ST=AMOD(TIME + RASUN*WRAD/15.,24.)
 1000 RETURN
      END
```

Definitions of Variables for Ephemeris Generator Program

Variable Name	Description
IYR	Calendar year for which the ephemerides of the sun are to be calculated. Default is 1962.
ITIM	= 1 to generate ephemerides at local mean midnight = 2 to generate ephemerides at local mean noon Default is 1 .
LEAPYR	= .TRUE. if IYR is a leap year = .FALSE. if IYR is not a leap year Default is .FALSE.
JDM21	Julian Day number for March 21 of year IYR. Default is 2437745, or March 21, 1962 .
XLONG	Longitude of observer of the sun, expressed in degrees. Default is 0°.
XLAT	Latitude of observer in degrees. Default is 35°.
H0	Cut-off altitude of sun in degrees. The times of rising and setting are those times at which the sun crosses the parallel of altitude H0. By definition, H0 > 0. The default value is 10°.
LOPREC	If .TRUE. , the elements of the sun's orbit are calculated only for solar noon of each day.
HIPREC	If .FALSE. , no improvements are made on the values for the times of rising and setting of the sun .

The above variables are the input variables for this routine. Data input is NAMELIST type of input and uses standard READ unit number 5.

Variable Name	Description
PT	The precession of the mean equinox since the beginning of the year IYR.

The following variables are the output variables for this routine.

SLONG3	The ecliptic longitude of the sun, referred either to the mean equinox for Jan 1 of year IYR or to the mean equinox of date. See program listing for information. It is printed in degrees, minutes, and seconds.
RASUN2	The right ascension of the sun. It is printed in hours, minutes, and seconds.
SDEC	The declination of the sun. It is printed in degrees, minutes, and seconds.
ET	The value of the equation of time, E. It is printed in hours, minutes, and seconds.
EARTH	The length of the radius vector from the earth to the sun. It is printed in A. U.

The preceding variables are printed in the first table, and the following variables are printed in the second table.

RISTIM	The time at which the sun rises above the parallel of altitude H0.
SETTIM	The time at which the sun sets below the parallel of altitude H0.
DAY	The length of time that the sun is above the parallel of altitude H0.
ESUN1	Solar elevation angle at noon of each day.
USUNE	$1 - (x'^2 + y'^2 + z'^2)^{1/2}$, where (x', y', z') are the horizon coordinates of the sun.

Variable Name	Description
NDAY	The day number from March 21 of the year IYR. Jan 1 is -79 if IYR is not a leap year. Dec 31 is day number 285. All 365 values of NDAY are output in both tables.

The subroutine HMS is used to convert angles expressed in degree or radian measure into degrees, minutes, and seconds or hours, minutes, and seconds, as required. ISKIP is used to inform HMS as to whether conversion from radians to degrees is necessary first step.

```
      DOUBLE PRECISION MNANOM,MLONG,PLONG,SLONG,PIMATH,PIMATT,
     C PIMAT2,RAD,SLONG2,ABERR
      LOGICAL LOPREC,HIPREC,LEAPYR
      COMMON/SLC/JD,TIME1,TIME2,XLONG,XLAT,HO,ID,LOPREC,HIPREC,PIMATH,
     C PIMATT,PIMAT2,RAD,GMAT,TCENT,MNANOM,MLONG,PLONG,OBLIQ,ECENT,
     C SLONG,ABERR,TIME,ET,EC,SDEC,SDEC1,ONEPNT,RISTIM,SETTIM,DAY,HAI,
     C USUNZ,ESUN,USUNX,USUNY,ZSUN,DH1,DT1,DH2,DT2,RASUN,ST,ESUN1,
     C EARTH
      INTEGER H(8),S(8),DMS(365,16),SN(8),JT(2,2)
      DIMENSION ISKIP(8),M(8),NDAY(365),USUNE(365),REFTIM(2)
      NAMELIST/OBSERV/IYR,ITIM,LEAPYR,JDM21,XLONG,XLAT,HO,
     C LOPREC,HIPREC
      DATA REFTIM/0.,12./
      DATA JDM21/2437745/
      DATA ISKIP/0,0,0,1,1,1,1,0/
      DATA IBLANK/'      '/
      DATA JT(1,1),JT(1,2),JT(2,1),JT(2,2)/'MIDNIG','HT.',
     C 'NOON.',' '/
      DATA IYR,ITIM,LEAPYR/1962,1,.FALSE./
      XLONG=0.
      ID=1
  300 READ(5,OBSERV,END=99)
      WRITE(6,107) IYR,(JT(ITIM,J),J=1,2)
  107 FORMAT(1X,'EPHEMERIDES OF THE SUN FOR THE YEAR ',I4,
     C ' AT LOCAL MEAN ',2A6)
      WRITE(6,106) XLONG,XLAT,HO
  106 FORMAT(1X,'COORDINATES OF OBSERVER:LONG=',F5.0,' DEG,LAT=',
     C F4.0,' DEG.',5X,'CUT-OFF ALTITUDE=',F4.0,' DEG.')
      WRITE(6,102) IBLANK
      WRITE(6,100)
  100 FORMAT(5X,'DAY',6X,'LONGITUDE',4X,'RT ASCENSION',4X,
     C 'DECLINATION',5X,'DISTANCE',5X,'EQN OF TIME')
      WRITE(6,110)
  110 FORMAT(1X,'FROM MAR 21',3X,'DEG',2X,1H',2X,1H",8X,'H',2X,'M',
     C 2X,'S',6X,'DEG',2X,1H',2X,1H",8X,'AU',11X,'H',2X,'M',2X,'S')
      LP=80
      IF(LEAPYR) LP=81
      JJ=0
      J=0
      DO 10 I=1,365
      J=J+1
      JJ=JJ+1
      NDAY(I)=J-LP
      JD=JDM21+NDAY(I)
      CALL SUNLOC
      TIME1=ET+REFTIM(ITIM)
      CALL MIDST
C *** USE THE FOLLOWING 4 STATEMENTS IF VALUES OF THE ECLIPTIC
C      LONGITUDE,REFERRED TO THE MEAN EQUINOX FOR JAN 1 OF YEAR
C      IYR, ARE REQUIRED.
C     P=2.4364990E-4 + 1.07629E-7*TCENT
C     PT=P*FLOAT(J-1)/365.25
```

```
C       SLONG2=SLONG-DBLE(PT)+ABERR
C       SLONG3=SNGL(SLONG2)
C *** USE THE FOLLOWING STATEMENT IF VALUES OF THE ECLIPTIC
C        LONGITUDE,REFERRED TO THE MEAN EQUINOX OF DATE, ARE
C        REQUIRED.
        SLONG3=SNGL(SLONG)
        RASUN2=RASUN/15.
        USUNE(I)=(-.5)*SNGL(   ( DBLE(USUNX) )**2 +
       C ( DBLE(USUNY) )**2 + ( DBLE(USUNZ) )**2
       C - 1.D0  )
        CALL HMS(SLONG3,RASUN2,SDEC,ET,RISTIM,SETTIM,DAY,ESUN1,
       C Z,Z,8,SN,H,M,S,ISKIP)
        WRITE(6,101) NDAY(I),(SN(K),H(K),M(K),S(K),K=1,3),EARTH,
       C SN(4),H(4),M(4),S(4)
  101 FORMAT(5X,I3,3(5X,A1,I3,I3,I3),5X,F8.6,5X,A1,I3,I3,I3)
        IF(JJ .NE. 5) GO TO 70
        WRITE(6,102) IBLANK
  102 FORMAT(1X,A6)
        JJ=0
   70 K=0
        DO 20 II=1,16,4
        K=K+1
        DMS(I,II)=SN(4+K)
        DMS(I,II+1)=H(4+K)
        DMS(I,II+2)=M(4+K)
        DMS(I,II+3)=S(4+K)
   20 CONTINUE
   10 CONTINUE
        WRITE(6,105)
  105 FORMAT(5X,'DAY',5X,'RISE TIME',7X,'SET TIME',6X,'DAY LENGTH',
       C 4X,'NOON ALTITUDE',5X,'USUNE')
        WRITE(6,112)
  112 FORMAT(1X,'FROM MAR 21',5X,'H',2X,'M',2X,'S',8X,'H',
       C 2X,'M',2X,'S',8X,'H',2X,'M',2X,'S',6X,'DEG',2X,1H',2X,1H",6X,
       C 'ERROR')
        JJ=0
        DO 30 I=1,365
        JJ=JJ+1
        WRITE(6,103) NDAY(I),(DMS(I,II),II=1,16),USUNE(I)
  103 FORMAT(5X,I3,4(5X,A1,I3,I3,I3),5X,1P E8.1)
        IF(JJ .NE. 5) GO TO 30
        WRITE(6,102) IBLANK
        JJ=0
   30 CONTINUE
        WRITE(6,108) LOPREC,HIPREC
  108 FORMAT(1X,'MODES OF CALCULATION:LOPREC= ',L1,', HIPREC= ',L1)
        WRITE(6,109)
  109 FORMAT(1H1)
        GO TO 300
   99 STOP
        END
```

```
      SUBROUTINE HMS(A0,A1,A2,A3,A4,A5,A6,A7,A8,A9,N,SN,H,M,S,ISKIP)
      INTEGER H(N),S(N),SN(N),BLNK
      DIMENSION T(10),M(N),ISKIP(N)
      DATA WRAD,J/5.7295779E1,1/
      DATA BLNK,MSN/' ','-'/
      T(1)=A0
      T(2)=A1
      T(3)=A2
      T(4)=A3
      T(5)=A4
      T(6)=A5
      T(7)=A6
      T(8)=A7
      T(9)=A8
      T(10)=A9
      DO 10 I=1,N
      IF(ISKIP(I) .EQ. 1) GO TO 20
      X=T(I)*WRAD
      GO TO 30
   20 X=T(I)
   30 IF(X .GE. 0.) GO TO 40
      SN(I)=MSN
      GO TO 50
   40 SN(I)=BLNK
   50 X=ABS(X)
      H(I)=INT(X)
      X=( X-FLOAT( H(I) ) )*60.
      M(I)=INT(X)
      X= (  X - FLOAT( M(I) )  )*60.
      S(I)=INT(X+.5)
      IF( S(I) .NE. 60 ) GO TO 10
      S(I)=0
      M(I)=M(I)+1
      IF(M(I) .NE. 60) GO TO 10
      M(I)=0
      H(I)=H(I) + 1
   10 CONTINUE
      RETURN
      END
```

REFERENCES

1. W. M. Smart, Text-book on Spherical Astronomy. 5th Ed. (London: Cambridge University Press, 1962), Chap. 2, p. 25. Figure 3.1 is adapted from Figure 10, p. 25.

2. Commission 3 (Notations), "List of Notations." Transactions of the International Astronomical Union, 6 (1938), pp. 345-355.

3. Originally by Nathaniel Bowditch, American Practical Navigator, Volume 1 (Washington, D. C.: Defense Mapping Agency Hydrographic Center, 1977), Appendix D, pp. 1117-1120, Appendix X, pp. 1297, 1302, & 1304-1309.

4. Prepared jointly by the Nautical Almanac Offices of the United Kingdom and the United States of America, Explanatory Supplement to The Astronomical Ephemeris and The American Ephemeris and Nautical Almanac (London: Her Majesty's Stationery Office, 1961), pp. 57-59.

5. Supplement to the Astronomical Ephemeris 1968: The Introduction of the I.A.U. System of Astronomical Constants (United States Government Printing Office, 1968), pp. 1s, 5s-7s, & 21s. This supplement may be found at the back of the 1968 Astronomical Ephemeris and contains information relating to the introduction into the A.E. of the 1964 I.A.U. System of Astronomical Constants.

6. M. Caputo, The Gravity Field of the Earth (New York: Academic Press, 1967), pp. vii-ix, 25-30, & 33-35. See also, G. D. Garland, The Earth's Shape and Gravity (New York: Pergamon Press, 1965), Chap. 3, pp. 37-38 & 44-45. Chapter 3 of Garland contains a short discussion of "The Shape of the Sea-level Surface."

7. Explanatory Supplement, pp. 57-58. For a slightly different treatment, see W. Chauvenet, A Manual of Spherical and Practical Astronomy, Volume 1 (Philadelphia, 5th edition, 1891; reprinted by Dover Publications, Inc., New York, 1960), Chap. 3, pp. 97-98.

8. "Latitude," Van Nostrand's Scientific Encyclopedia, 5th Ed., edited by Douglas M. Considine (New York: Van Nostrand Reinhold Co., 1976), p. 1447. See also, American Practical Navigator, Appendix X, p. 1298.

9. Explanatory Supplement, pp. 60 & 63-64.

10. American Practical Navigator, Appendix X,p. 1299. Also, in Figures 507a & 507b (in between pages 112 & 113) there is a notation (below the title of the charts, in the center of the right-hand side) which gives the particular reference spheroid on which these two charts are based.

11. For points in the United States, the United States Coast and Geodetic Survey may be able to provide assistance in determining the accuracy of one of their maps.

12. For example, Chauvenet, Volume I, Chap. VI, pp. 228-316 gives several methods for determining the latitude, and Chap. VII, pp. 317-424 gives several methods for determining the longitude. Also, Volume II, Chap. VIII, pp. 340-366 contains a discussion of the zenith telescope, an instrument used to determine the astronomic latitude of the observer. See also American Practical Navigator, Part Three, Chaps. XV-XVII & XX-XXI. A reference describing in detail a procedure for determining the astronomic latitude is A. J. Hoskinson and J. A. Duerken, Manual of Geodetic Astronomy: Determination of the Longitude, Latitude, and Azimuth, U. S. Coast and Geodetic Survey Special Publication No. 237 (U. S. Government Printing Office, 1947).

13. D. McNally, Positional Astronomy (New York: John Wiley & Sons, Inc., 1975), Chap. 3, p. 37. Figure 3.5 is adapted from Figure 3.8, p. 37 of McNally.

14. "List of Notations." Transactions of the International Astronomical Union, 6 (1938), p. 348.

15. M. Davidson, Elements of Mathematical Astronomy. 3rd Ed.(London: Hutchinson & Co. LTD, 1962), Chap. 2, pp. 36-37. This book was revised by Cameron Dinwoodie in 1962. Figure 3.6 is adapted from Figure 11, p. 37 of Davidson.

16. For example, see J. M. A. Danby, Fundamentals of Celestial Mechanics (New York: The Macmillan Company, 1962), Chap. 6, pp. 155-157.

17 Explanatory Supplement, Chap. 4, p. 98.

18. Explanatory Supplement, Chap. 4, p. 98.

19. Explanatory Supplement, Chap. 4, p. 98.

20. For a similar derivation of Kepler's Equation, see McNally, Chap. 10, pp. 289-292.

21. Danby, Chap. 6, pp. 148-151. Also, Smart, Chap. 5, pp. 114-116.

22. For example, see Smart, Chap. 5, pp. 111-112.

23. Danby, Chap. 6, pp. 152-154. See also Smart, Chap. 5, pp. 117-120 for a different approach.

24. See the Explanatory Supplement, Chap. 3, p. 88 and pp. 90-91 for the general trend through the past three centuries.

25. Smart, Chap. 6, pp. 146-150.

26. Explanatory Supplement, Chap. 2, p. 28.

27. McNally, Chap. 7, p. 157.

28. H. Goldstein, Classical Mechanics (Menlo Park, California: Addison-Wesley Publishing Co., 1950), Chap. 5, p. 175.

29. Davidson, Chap. 11, pp. 164-166.

30. See Davidson, Chap. 8, pp. 125-130 or the Explanatory Supplement, Chap. 2, pp. 46-54.

31. Explanatory Supplement, Chap. 2, p. 25.

32. Supplement to the A.E. 1968, p. 5s.

33. Explanatory Supplement, Chap. 2, p. 51.

34. For example, see N. Robinson, Solar Radiation (New York: Elsevier Publishing Co., 1966), Chap. 3, pp. 51-52. See also Smart, Chap. 3, pp. 58-73.

35. R. H. Baker, Astronomy (Van Nostrand, 1950), 5th Ed.,p. 97.

36. For a detailed discussion and further references on Allen's Clear Air Model, see L. L. Vant-Hull, "Methods for Estimating Total Flux in the Direct Solar Beam At Any Time," Sharing the Sun in the Seventies: Joint Conference of the American Section, International Solar Energy Society, and Solar Energy Society of Canada, Inc., August 15-20, 1976, Winnipeg, Canada,Volume 1, edited by K. W. Boer (American Technological University, P. O. Box 1416, Killeen, Texas 76541 : American Section of the International Solar Energy Society, Inc., 1976), pp. 369-375.

37. For a more complete explanation of the difference between total and direct horizontal intensities, see A. B. Meinel and M. P. Meinel, Applied Solar Energy (Menlo Park, California: Addison-Wesley Publishing Co., 1976), Chap. 2, pp. 39-40. Note, however, that they use the symbol I_d where we use I_D and that they use I_S where we use I_d.

38. For example, see E. W. Woolard and G. M. Clemence, Spherical Astronomy (Academic Press).

39. See also, D. Brouwer and G. M. Clemence, Methods of Celestial Mechanics (New York: Academic Press, 1961).

SECTION 4

THE SODIUM HEAT ENGINE

Applied to a Solar Central Receiver System

A. K. DETWILER, III.

TABLE OF CONTENTS

LIST OF ILLUSTRATIONS

LIST OF TABLES

4.0 The Sodium Heat Engine

The Sodium Heat Engine (SHE) was invented by Neill Weber and J. T. Kummer. In 1968, the patent was asigned to Ford Motor Company [1]. The heart of the machine is beta''-alumina, a refractory material remarkable for its high conductivity of sodium ions. Beta-Alumina and sodium are also used in the well known experimental Ford Sodium Sulphur Battery.

The SHE is a continuous isothermal expansion engine for sodium vapor (Fig. 4.1). The engine consists of high temperature elements, which include the hot liquid sodium, the membrane composed of the beta''-alumina, and the parts of the vapor just below the membrane, all of which are at temperature T2. The low temperature elements are the condenser at temperature T1 and the cool components of the vapor above the condenser. The condensed sodium is recirculated by an electromagnetic pump. The processes occurring in the membrane and at its interfaces are very nearly equivalent to an isothermal expansion of sodium vapor at temperature T2, from a vapor pressure P2 to a vapor pressure P1.

The E.M.F. across the membrane is derived from the Nernst-Einstein equation for the isothermal expansion of a vapor:

$$V = \frac{R\ T2}{F} \ln \frac{P2}{P1} - i_c R, \text{ where}$$

R = the gas constant

F = the Faraday

R_c = the ceramic (beta"-alumina) resistance to ionic current

i = the ionic current density through the membrane

P2 = the vapor pressures of the hot (T2) liquid sodium

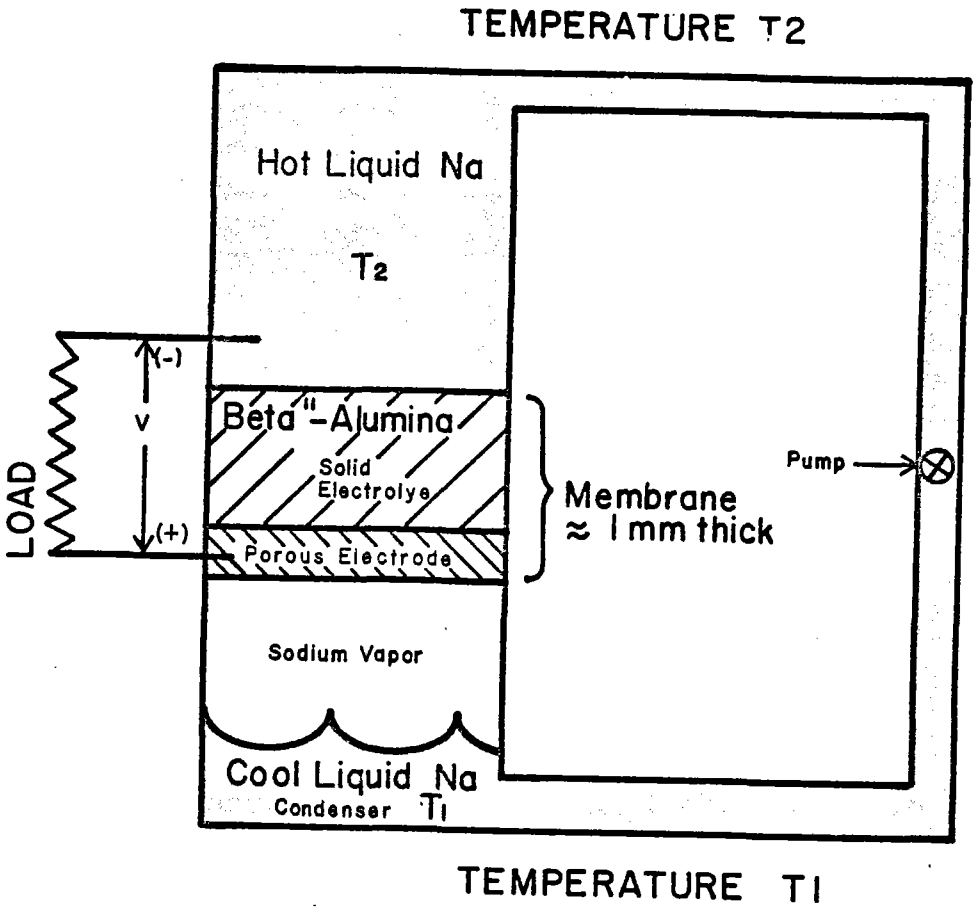

Figure 4.1 Schematic Diagram of a Sodium Heat Engine.

P1 = vapor pressure of the cold (T1) liquid sodium

T = temperature in degrees Kelvin (K)

The electrial power P of the SHE is P = iV. The efficiency η of the SHE is:

$$\eta = \frac{iV - W}{iV + \frac{i}{F}(L + H) + \dot{Q}_r + \dot{Q}_c}, \text{ where}$$

W = the work rate required to recirculate the sodium

L = the heat of vaporization of sodium at T2

H = the enthalpy increase of the liquid sodium brought from T1 to T2

$\dot{Q}_c$ = the thermal power lost from the macine through conduction.

$\dot{Q}_r$ = the radiative power lost from the hot membrane to the cool condenser.

$$\dot{Q}_r = \sigma (T2)^4 / Z$$

σ = 5.67×10^{-12} w/cm^2 is the Stephan Boltzman constant

$Z = \frac{1}{1 - R}$ is the radiation resistance for heat transfer from the hot electrode to the cool condensor

R = reflectivity of the cool condenser surface; essentially a film of condensed liquid sodium. A typical value of R = 0.95 gives a Z of 20

For a small machine iV>>W. The power $\dot{Q}_c$ exits the machine mainly via thermal conduction through the electrical leads. This loss can be made relatively small by series connecting electrically independent membrane sections, thus raising the output voltage. The cross sectional area of the

leads and $\dot{Q}_c$ can then be reduced by V^{-2}. In the calculations for this report, $\dot{Q}_c$ and W have been set equal to zero. This gives:

$$\eta = \frac{iV}{iV + (L + H)\ i/F + \sigma\ (T2)^4/Z}$$

In this paper, a conservative value for Z is chosen: Z = 20.

Thus by choosing T2, T1, R_c, and Z, we can determine V and η for each i; since P = iV, we have established a curve between η and P. Such a curve is displayed in Figure 4.2. The values of V and i are typical of the SHE, a low voltage, high current density device.

In steady state operation, the condenser must maintain a temperature T1 and, therefore, must reject a thermal power of $(L + H)\ i/F + \sigma(T2)^4/Z$. A bottoming cycle has been fit to the condenser. The exit temperature of the bottoming cycle is 303 K (30°C), and the Carnot efficiency η_c is

$$\eta_c = \frac{T1 - 303K}{T1}$$

The condenser is transparent to the power transmitted to it from the membrane. This power is converted into electricity by the bottoming cycle at $0.7\eta_c = \bar{\eta}$; that is, the efficiency of the bottoming cycle is assumed to be 70 percent of the Carnot efficiency.

The power lost between the membrane and the bottoming cycle is $X(P_t)$, i.e., a fraction of the total thermal power into the SHE. Also,

P_t = the total thermal power into the SHE per unit membrane area

P = the electrical power produced by the SHE per unit membrane area

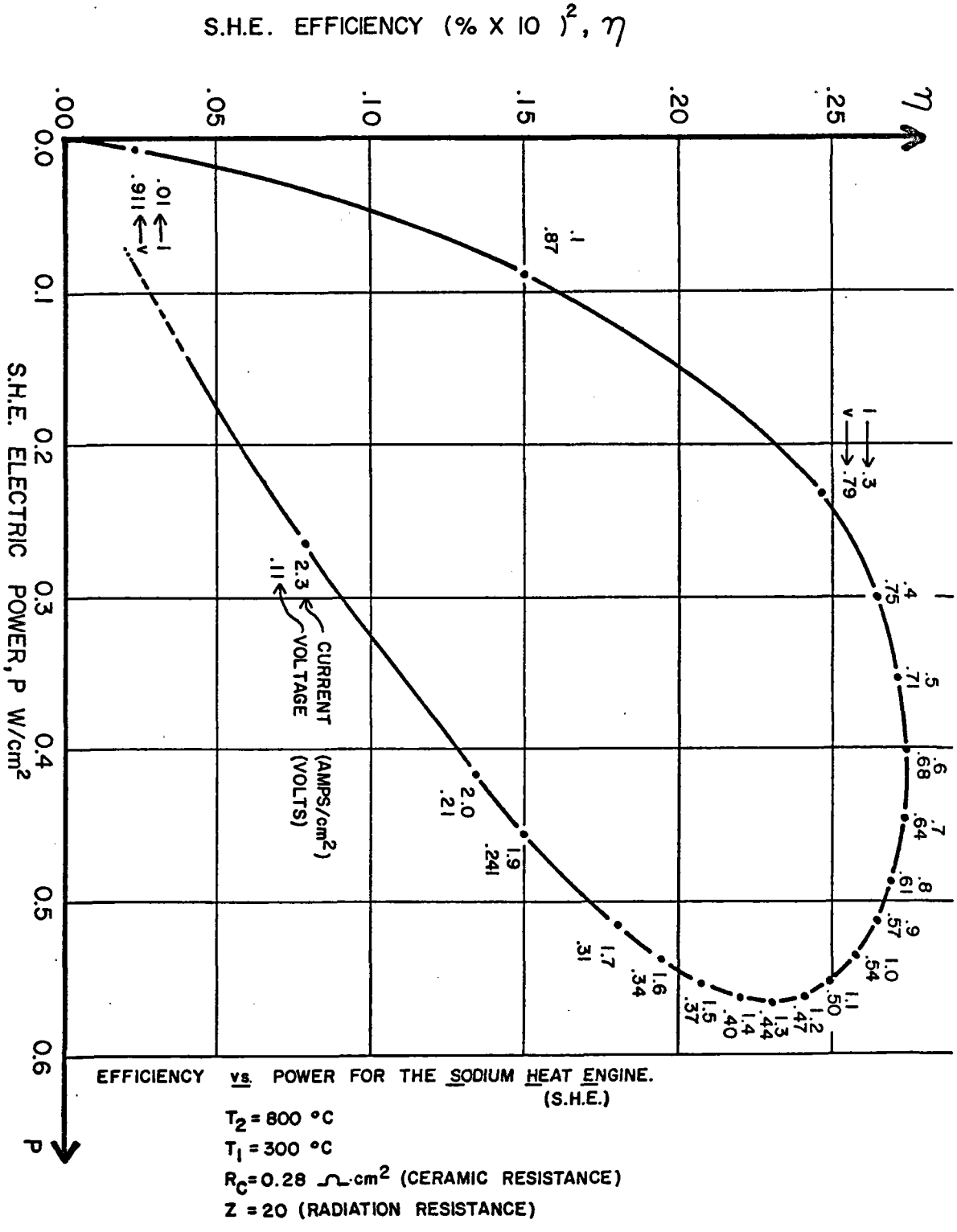

Figure 4.2. SHE Efficiency vs. Output Electric Power for Specific Operating Conditions.

$\bar{P}$ = the electrical power produced by the bottoming cycle per unit membrane area

$\bar{P}$ = $\bar{\eta}\, P_t = 0.7\eta_c[(L + H)\, i/F + \sigma(T2)^4/Z - X\,(P_t)]$

η = the efficiency of the SHE

$$\eta = \frac{iV}{iV + (L + H) + i/F^4 + \sigma(T2)\ /Z}$$

$\bar{\eta}$ = the efficiency of the bottoming cycle.

$$\bar{\eta} = 0.7\eta_c = \frac{T1 - 303\ K}{T1}$$

$\bar{\bar{P}}$ = the total electrical power produced by the SHE and the bottoming cycle per unit membrane area

$\bar{\bar{P}}$ = $\bar{\bar{\eta}}\, P_t$

$\bar{\bar{\eta}}$ = $\eta\,(1 + \bar{\eta}\,(\frac{1}{\eta} - 1))$, the overall thermal to electrical efficiency.

The model is shown schematically in Figure 4.3.

Note that <u>all</u> power densities are per square centimeter of membrane area in the SHE. Therefore, there is an assumption that the area of the condenser is about equal to the area of the membrane.

The points of maximum power and maximum efficiency have been found from curves such as Figure 4.2, by evaluating the power and efficiency for all combinations of

T2 = 973, 1073 K

T1 = 573, 673 K

R_c = 0.28, 0.1 ohm - cm^2.

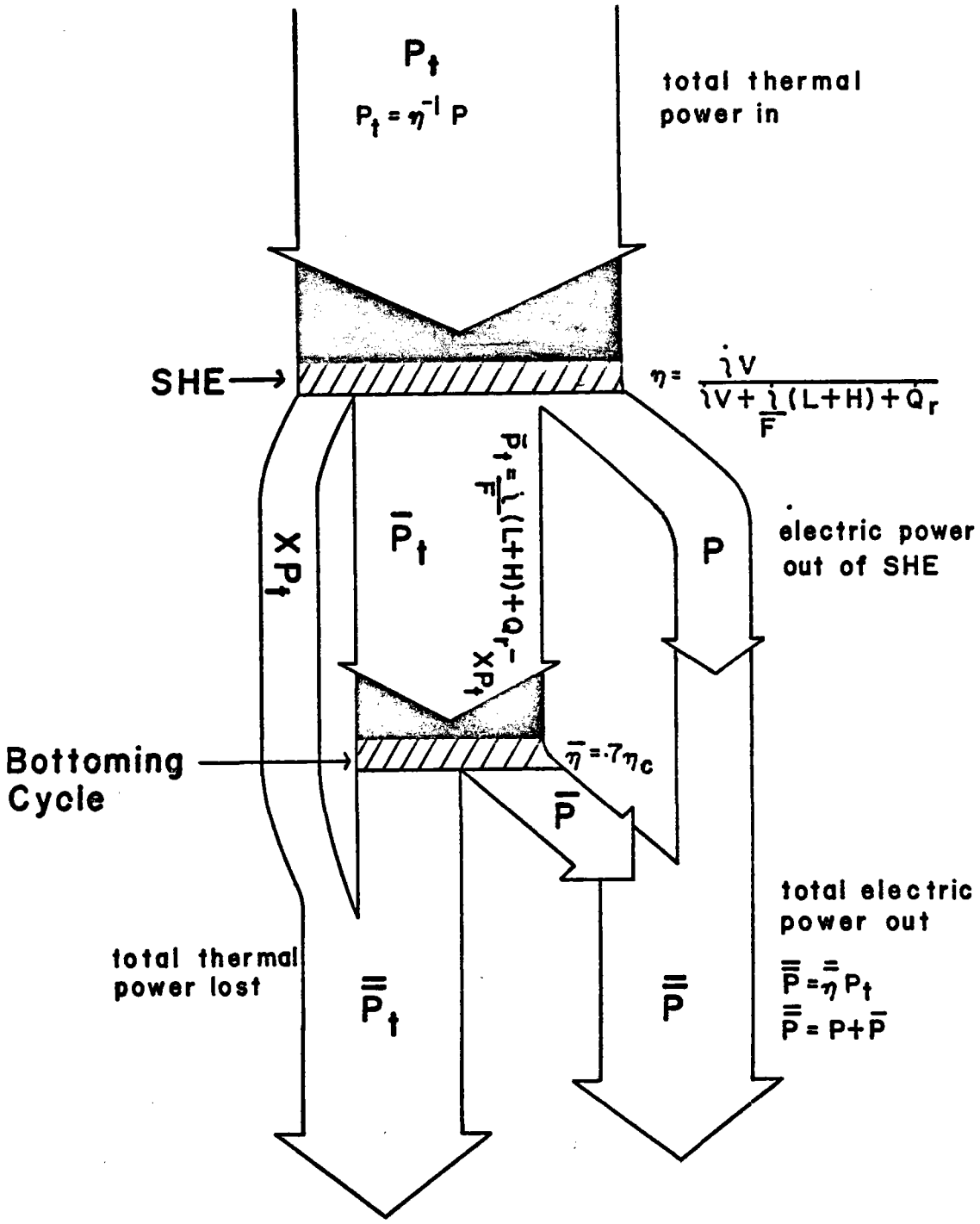

Figure 4.3. Schematic of Thermal Power Flow in a SHE Connected to a Bottoming Cycle.

Also, two choices have been made for the power loss fraction X:

$X = 0$

$X = \sigma(T2)^4/2ZP_t$ i.e., one-half of the power radiated from the membrane to the condenser is routed around the bottoming cycle.

The results for these choices are displayed in Table 4.1 for (a) X = 0 and for (b) $X = \sigma (T2)^4/2ZP_t$. The maximum system efficiency is seen to occur for the higher inlet temperature and the lower ceramic resistance. For case (a) the maximum efficiency is 54.1% independent of bottoming temperature, while in case (b) the lower bottoming temperature of 300°C gives the best efficiency of 51.5%

The power requirement of the SHE <u>at its membrane</u> is

$$H\ i/F + \dot{Q}_c + iV + Li/F + \dot{Q}_r$$

and is much greater, at interesting levels of power, than can be provided by sensible heat exchange. This power requirement suggests a particular design for a SHE at a Liquid-Metal Cooled Solar Central Receiver (LMCSCR), similar to the design schematically rendered in Figure 4.4. A liquid metal, like sodium, is evaporated in the receiver and condensed at a temperature around T2 on the lower portions of the receiver's support tower, thus releasing the power very near where it is needed, at the membrane of the SHE, which is fixed to the outside of the heat transfer pipe. An alternative would be to have a receiver surface composed of multiple directly heated sodium heat pipes, with the condensor end of each one providing heat to a pool of sodium in direct contact with the membrane of an individual SHE.

To begin to study mechanical problems of this scheme, a parabolic dish with a sodium heat pipe inserted through the focus of the dish can be mated

Table 1

OPTIMUM OPERAING PARAMETERS FOR THE SODIUM HEAT ENGINE WITH Z = 20

	Rc	.1	.1	.1	.1	.1	.1	.1	.1	.28	.28	.28	.28	.28	.28	.28	.28	Rc	Ωcm^2
	i	2.2	2.6	2.9	3.2	.8	.8	1.1	1.1	.8	1.1	1.1	1.3	.4	.5	.6	.6	i	amp/cm^2
	V	.233	.327	.311	.413	.381	.578	.502	.700	.237	.334	.304	.435	.352	.539	.447	.676	V	volts
	P	.513	.851	.901	1.321	.305	.463	.552	.770	.190	.367	.334	.565	.141	.270	.267	.406	P	W_e/cm^2
	η	.159	.207	.196	.242	.209	.282	.253	.316	.141	.201	.170	.229	.167	.245	.202	.273	η	% X 10^2
	P_t	3.23	4.11	4.60	5.46	1.46	1.64	2.18	2.44	1.348	1.83	1.96	2.47	.844	1.10	1.32	1.49	P_t	W_t/cm^2
	$\bar{P}_t$	2.71	3.26	3.70	4.40	1.15	1.18	1.63	1.67	1.16	1.46	1.63	1.90	.703	.832	1.05	1.08	$\bar{P}_t$	W_t/cm^2
	x	0	0	0	0	0	0	0	0	0	0	0	0	0	0	0	0	x	---
(a)	η_c	.55	.47	.55	.47	.55	.47	.55	.47	.55	.47	.55	.47	.55	.47	.55	.47	η_c	% x 10^2
	$\bar{\eta}$	.385	.329	.385	.329	.385	.329	.385	.329	.385	.329	.385	.329	.385	.329	.385	.329	$\bar{\eta}$	% x 10^2
	$\bar{P}$	1.043	1.073	1.425	1.362	.443	.388	.628	.549	.447	.480	.628	.625	.271	.274	.404	.355	$\bar{P}$	W_e/cm^2
	$\bar{\bar{P}}$	1.556	1.924	2.326	2.683	.748	.851	1.180	1.319	.637	.847	.962	1.19	.412	.544	.671	.761	$\bar{\bar{P}}$	W_e/cm^2
	$\bar{\bar{\eta}}$	.482	.468	.506	.491	.512	.519	.541	.541	.473	.464	.491	.482	.488	.495	.508	.511	$\bar{\bar{\eta}}$	% x 10^2
(b)	x	.039	.031	.028	.023	.087	.078	.058	.052	.095	.070	.065	.052	.151	.116	.097	.086	x	--
	$\bar{P}_t$	2.58	3.13	3.51	3.95	1.02	1.05	1.44	1.48	1.03	1.33	1.44	1.72	.576	.705	.867	.894	$\bar{P}_t$	W_e/cm^2
	$\bar{P}$	.993	1.03	1.35	1.30	.393	.345	.555	.487	.397	.438	.554	.566	.222	.232	.334	.294	$\bar{P}$	W_t/cm^2
	$\bar{\bar{P}}$	1.506	1.88	2.25	2.62	.698	.808	1.107	1.257	.587	.805	.888	1.131	.363	.502	.601	.700	$\bar{\bar{P}}$	W_e/cm^2
	$\bar{\bar{\eta}}$	.466	.458	.490	.480	.478	.493	.507	.515	.435	.440	.453	.458	.430	.456	.455	.470	$\bar{\bar{\eta}}$	% x 10^2
	AT MAX POWER	✓	✓	✓	✓					✓	✓	✓	✓					AT MAX POWER	
	AT MAX EFFICIENCY					✓	✓	✓	✓					✓	✓	✓	✓	AT MAX EFFICIENCY	
	T2	700	700	800	800	700	700	800	800	700	700	800	800	700	700	800	800	T2	
	T1	400	300	400	300	400	300	400	300	400	300	400	300	400	300	400	300	T1	

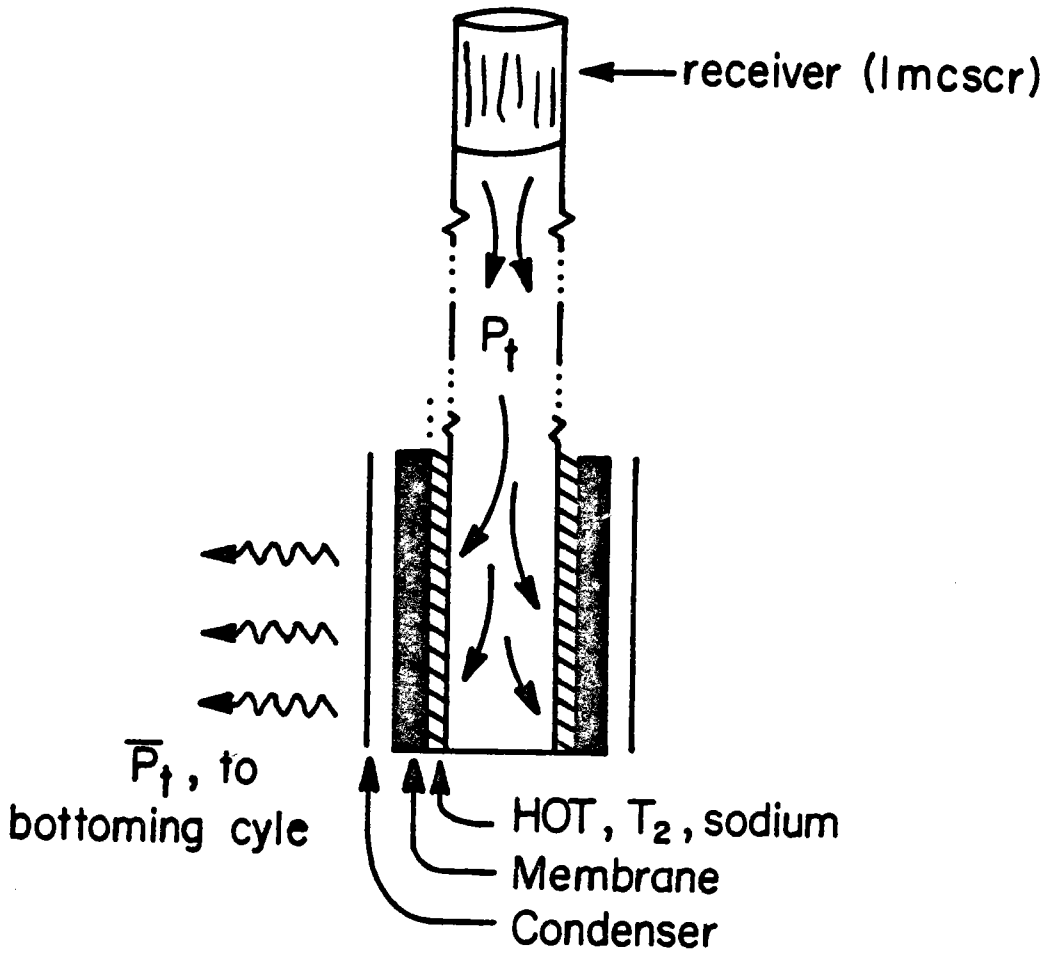

Figure 4.4. A SHE Coupled to a Liquid Metal Cooled Solar Central Receiver.

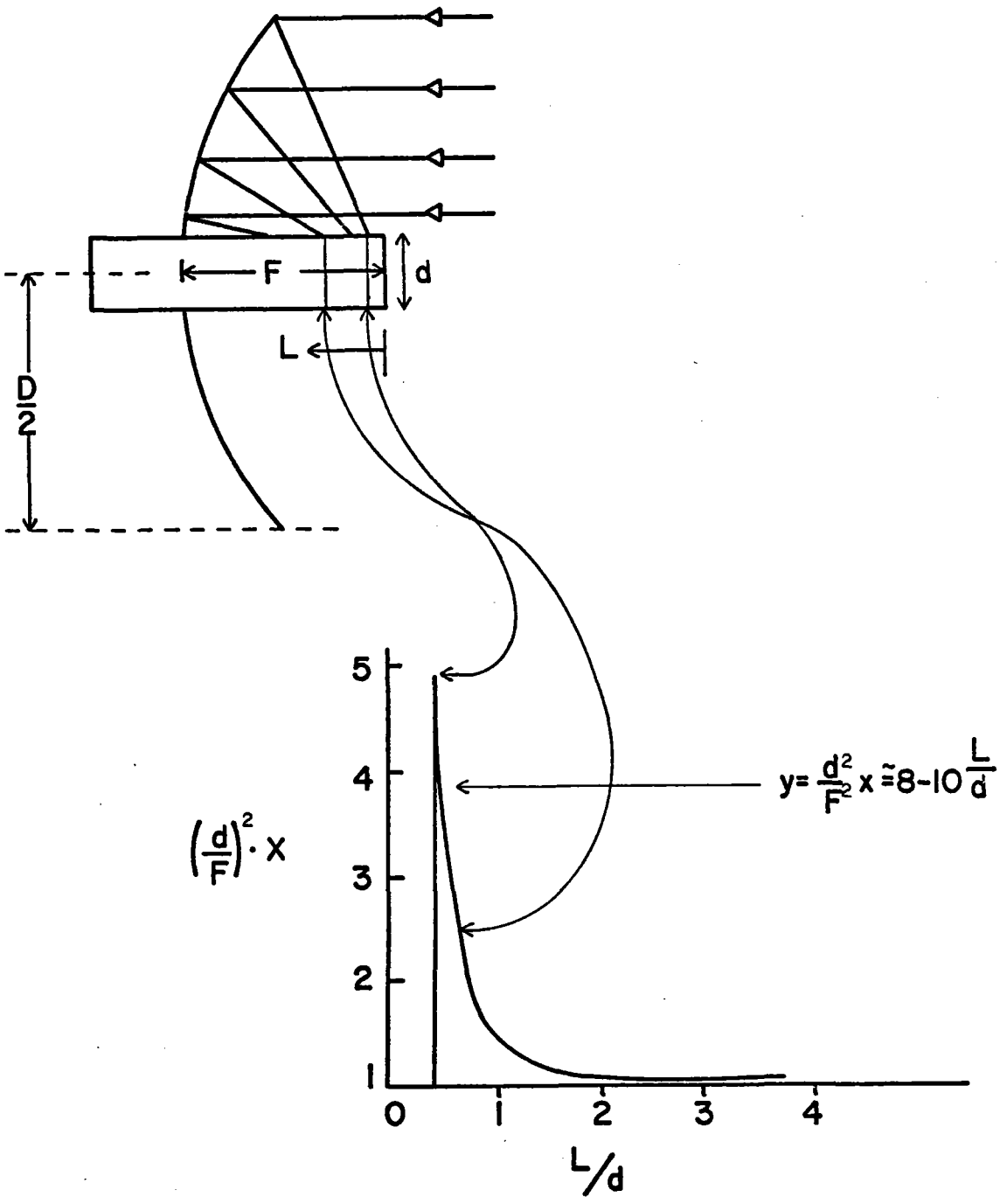

Figure 4.5. Concentration Expected Along the Receiver of a Heat Pipe Coupled to a Parabolic Dish.

with a SHE slipped over the condenser end of the heat pipe (Figure 4.5). In the graph accompanying the picture of the dish, X is the concentration of the dish, and the other parameters are identified in the figure. If the losses and other sources of the inefficiency could be suppressed, such a system might be an interesting and useful power conversion device in its own right.

The SHE is undergoing basic research both at Ford Motor Co. and at the University of Houston. The best source for information on the machine is Weber [3]. More recent work is in progress under DOE contract DE - AC02 - 79ER 10347, but no reports from this work are available.

REFERENCES

[1] J. T. Kummer and Neill Weber, U. S. patent 3,458,356 (1968), Assigned to Ford Motor Company.

[2] I. Langmuir, Phys. Rev. 2, 329, (1913).

[3] Neill Weber, Energy Conv., 14, 1-8 (1974).